Investigations of Organic Molecules Using Entangled Photons as a Novel Spectroscopic Tool

by

Audrey Veronne Eshun

A dissertation submitted in partial fulfillment
of the requirements for the degree of
Doctor of Philosophy
(Chemistry)
In the University of Michigan
2021

Doctoral Committee:

Professor Theodore Goodson III, Chair
Associate Professor Julie S. Biteen
Professor Herbert G. Winful
Associate Professor Dominika Zgid

Audrey Veronne Eshun

aeshun@umich.edu

ORCID: 0000-0001-6769-7082

DEDICATION

This dissertation is dedicated to all my family and friends who have been there for me along the way, and especially to my parents.

ACKNOWLEDGEMENTS

It is not an easy task to acknowledge all the people who have helped me on this journey, as there have been so many who have supported, helped and encouraged me to get to this point. I appreciate all that each and every one of you have contributed to my graduate degree in your own special ways. First of all, I would like to thank of course my parents Sam and Tina Eshun who never doubted me and provided support in every single way possible for me to attain my goals. They taught me no dream was too big for me to achieve and gave me constant affirmations. I know my mother is proud and I am very sure that although my father is no longer physically with me, he is very proud as well. I would like to thank my family who have always brought the fun and listening ears, especially my brother Kevin and my sister Korantema. To all my friends from Merton, SOS, MoHo, UMich and beyond who have contributed to my growth in greater ways than they could ever imagine, I truly appreciate you. Special thanks to Abena, Yaa, Regine and Omar who have talked me through almost every step of this PhD journey. To my colleagues in the Goodson Group, past and present, who have provided an enjoyable, supportive, collaborative and intellectual environment, I would not have made it through without you. I am grateful to my advisor, Professor Theodore Goodson III for his guidance and for bringing out the best scientist in me, to Dr. Oleg Varnavski who patiently assisted me through all my optics dilemmas and to Linda Van Blaircum for her keeping everything

together. Thank you to my dissertation committee for their feedback and discussions on my work. I would not be here without the support of so many people, thank you all.

Table of Contents

List of Figures

List of Tables

ABSTRACT

Entangled states have been utilized in a wide range of fields and their quantum properties have been taken advantage of across quantum information science to achieve outcomes that are not available through classical means. Despite being used in quantum computing, cryptography and communication, the use of entangled states of light in spectroscopy is a new area where a lot is still needed to be understood. The goal of this thesis is to expand on the understanding of quantum entanglement as it applies to spectroscopy of different types. Firstly, in entangled two-photon absorption (ETPA) spectroscopy measured via transmission (absorption) and fluorescence methods. Secondly, to experimentally realize the utilization of quantum entangled photons in the novel application of virtual state spectroscopy and finally to prove the viability of entangled photons in a Hong-Ou-Mandel interferometer for spectroscopic use.

In this thesis, the optical properties of a series of organic chromophores with differing structure-function properties were studied with classical and entangled light. It was observed that when used to excite some of these chromophores, entangled light causes enhancements in their nonlinear responses, which aids in our understanding of the structure-function relation to entangled light excitation, and the sensitivity of entangled light in resolving different absorption pathways. The experimental and molecular parameters necessary for the observation of entangled two-photon excited fluorescence signals were investigated, and it was found that in addition to high dipole moments and good quantum yields, there is a strong dependence on the detuning energies between the

molecule's intermediate states and the entangled photons; small detuning energies lead to a resonance effect and coupling between the intermediate states and the photons leading to higher fluorescence signals. This makes the transition pathway preferred for fluorescence measurements and enables enhancements in the fields of imaging and microscopy.

The idea of using quantum entangled light as a source to measure the intermediate or virtual energy levels of molecular transitions has been theorized but this work will be an expanded experimental achievement. ETPA signals are measured at different interbeam delay times for a pair of organic trimers that differ in their planarity. By using this data to obtain an energy spectrograph and comparing the information to results obtained via classical nonlinear spectroscopic methods, a broader picture of the compounds' excitation processes is attained. This is a step towards greater employment of this specialized virtual state spectroscopy technique. Additionally, Hong-Ou-Mandel (HOM) interferometry has been used primarily for metrology, but in this research the quantum interference properties of entangled light interacting with an organic sample's electronic states is used to determine information about the coherent excitation of organic molecules. This is the first time an HOM interferometer is being used to excite an organic sample and obtain information about optical molecular properties in this way. The dephasing time of the sample was extracted, and this proof-of concept experiment can now be expanded for further time-resolved and nonlinear spectroscopy with entangled photons.

Chapter 1

Introduction & Background

1.1. Scope

In recent years, scientists' interest in quantum applications and quantum information science has been on the rise. According to statistics from the Web of Science database,[1] publications in this area have risen almost exponentially over the past 10 years with 2020 having the most annual publications on the topic. There have been over 88,000 citations in a variety of fields, ranging from optics to applied physics, nanotechnology and physical chemistry. Our growing understanding of quantum mechanics have led to this shift, where numerous fields are taking advantage of purely quantum properties such as entanglement and superposition to expand our knowledge on research that has previously been viewed through a solely classical lens. While some are interested in utilizing quantum technology for creating devices for communication, computing and cryptography, many are working towards utilizing the properties of quantum light in sensing and imaging.

Quantum light via photon entanglement is therefore a promising area of study towards optical characterization of a vast array of materials. The burgeoning fields of ultrafast and nonlinear optical spectroscopy have enabled us to obtain a stronger understanding of the photophysical properties and dynamical processes of optical materials, yet with our expanding insight into quantum correlations, it is apparent that by combining the properties of quantum light with spectroscopy, we can develop methods to discover even more about these materials.

By harnessing the power of quantum light, researchers may advance experimental methods, solving unanswered questions and filling gaps in chemistry, material science and biology.

This dissertation focuses on different experimental approaches for using quantum entangled photon pairs generated by the process of spontaneous parametric downconversion (SPDC) for the spectroscopy of organic systems. One of the main schemes that has been theoretically suggested and experimentally realized is multiphoton absorption, specifically two-photon absorption (TPA) with entangled photon pairs. The high temporal and spatial correlations of the biphoton pair enable low intensity entangled two-photon absorption (ETPA) of chromophores. This thesis looks at measuring this ETPA via transmission methods as well as measuring the ETPA induced fluorescence, while studying the experimental and molecular parameters necessary to observe these fluorescence effects. In addition to the comparison of different ETPA measurement methods, these are also compared to classical TPA measurements and how these relate to structure-function relationships in molecules. ETPA is expanded on by using it as a way to characterize materials for photovoltaics. Furthermore, steps are taken towards developing new experimental methods for entangled photon spectroscopy via two-photon interferometry.

This work follows foundational theoretical reports on ETPA such as those by Saleh, Teich *et al*[2,3] Kojima and Nguyen[4] and Javaneinen and Gould[5] and expands on the preliminary ETPA experimental work conducted on molecules by the Goodson group[6–9]. A major component will be to gain a better understanding on the molecular response to ETPA excitation and a comprehensive analysis of ETPA induced fluorescence. Additionally, a new way to understand entangled light-matter interactions through Hong-Ou-Mandel interferometry will be

investigated. Thus, the aim of this dissertation is to critically explore different experimental methods using entangled light, to broaden the scope of spectroscopy in the quantum realm.

Although entanglement was initially thought of as counterintuitive as it seemed to leave quantum mechanics "incomplete"[10], it has since been well described mathematically and proven experimentally. Quantum entanglement is often simply described as a property of a system, where the quantum state of one object of the system cannot be described independently from another object within that system; that is, their quantum states cannot be factored into a product of single particle states. The classical description of the total state space of a system is the product of all its subsystem spaces, thus indicating that the total state should be the product state of all the separate systems. However, in the quantum description, the Hilbert space of the system is a tensor product of the subsystem spaces, and the superposition principle leads to a total state that is written in the form,[11]

$$|\psi\rangle = \Sigma_{i_1 \dots i_n} c_{i_1 \dots i_n} |i_n\rangle \otimes |i_2\rangle \otimes \dots \otimes |i_n\rangle \tag{1.1}$$

This cannot be described as the product of the states of the individual subsystems as $\psi \neq |\psi_1\rangle \otimes |\psi_2\rangle \otimes \dots \otimes |\psi_n\rangle$ and as such, a single state vector cannot be written for any one of the subsystems. This is a mathematical basis for quantum entanglement.

Entanglement is commonly expressed using the four "Bell States" (also referred to as EPR states) which form the basis of a bipartite state of a two-dimensional Hilbert space. The states are unique in that a measurement at system A has an equal and random probability of being in state 0 or state 1. However, the states exhibit perfect correlation because once system A is measured, the measurement at system B is known.

$$|\psi^+\rangle = \frac{1}{\sqrt{2}}\left(|01\rangle_{AB} + |10\rangle_{AB}\right)$$

$$|\psi^-\rangle = \frac{1}{\sqrt{2}}\left(|01\rangle_{AB} - |10\rangle_{AB}\right)$$

$$|\phi^+\rangle = \frac{1}{\sqrt{2}}(|00\rangle_{AB} + |11\rangle_{AB})$$

$$|\phi^-\rangle = \frac{1}{\sqrt{2}}(|00\rangle_{AB} - |11\rangle_{AB})$$

The Bell states violate Bell's inequality which predicts that classically, the outcome of a correlation measurement cannot exceed 2. Quantum mechanics deviates from this and predicts that the maximal value for a correlation measurement is limited by the degree of entanglement, P_E, within a system and therefore the maximum violation of the inequality is $2\sqrt{1 + {P_E}^2}$.[12] The Bell states lead to this value, therefore they are maximally entangled states. Entangled states of the Bell state form can be produced in various ways and one extensively studied method is through the generation of entangled photons. These quantum correlated photons can be produced by a non-linear optical process known as spontaneous parametric down-conversion (SPDC). In the SPDC process, a pump interacts with a non-linear crystal and is converted into an entangled photon pair. An essential quantity that characterizes the interactions of the generated entangled photon pairs with matter are higher order field correlations, sometimes referred to as a second-order field correlation,

$$\langle {E_s}^*(t){E_i}^*(t+\tau)E_i(t+\tau)E_s\rangle. \tag{1.2}$$

This function describes the degree of spatiotemporal correlation between the entangled photons. Numerous theoretical and experimental studies have been conducted on these correlation functions[13–15] because an integral aspect of what researchers seek to understand is how these correlations affect interactions between entangled photons and matter.

Researchers in the Goodson Group have contributed greatly to investigations on how non-classical light interacts with organic media. Classical non-linear optical spectroscopy of

organic materials has been largely explored and is well understood, yet the same cannot definitively be said for spectroscopy using entangled light. While it has been established that quantum entangled photon pairs do probe electronic states in organic molecules, a better understanding is needed on how ETPA cross-section measurements scale on the same sets of molecules using different detection methods, i.e. transmission versus fluorescence. This is important as accurate and in-depth knowledge of this entangled two-photon excited fluorescence scheme is necessary for major advancements in entangled fluorescence spectroscopy and quantum imaging and microscopy. Such studies present challenges due to the difficulties in measuring ETPA fluorescence and the few studies that have done. Furthermore, much has not been realized on the spectroscopic nature of ETPA and fully utilizing it to determine the optical properties of materials for specific optical uses. Thus, this work seeks to provide answers to these open questions. This introduction will continue with an overview of classical two-photon absorption, an introduction to entanglement and entangled two-photon absorption and an outline of the subsequent chapters of the dissertation.

1.2. Classical Two-photon absorption

Two-photon absorption (TPA) is a third-order non-linear optical process that involves the sequential absorption of two low energy photons via a short-lived virtual state to an excited state at an energy the sum of the two photons. The two-photon absorption process was first hypothetically defined by Maria Göppert-Meyer in 1931, when she theorized that an atom in the ground state can absorb two photons of energy hv_a and hv_b to an excited state of energy v_{ab}, where $v_{ab} = v_a + v_b$. As the TPA process requires the simultaneous absorption of both photons, the TPA rate is dependent on the intensity of both photons and thus is proportional to the square of the light intensity. That is, $\boldsymbol{R_r = \delta_R \emptyset^2}$ where R_r is the random TPA rate, δ_R is

the random TPA cross-section (sometimes referred to as classical TPA cross-section) and $\emptyset$ is the photon intensity. In order for this quadratic dependence to be experimentally observed, very high intensities of light are needed, making TPA initially unfavorable. The invention of pulsed lasers led to the realization of the hypothesized TPA phenomenon as they are able to deliver the high density and power of photons needed.

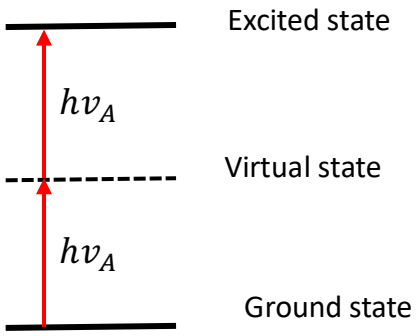

Figure 1.1*. Jablonski diagram of two-photon absorption process.*

TPA is a non-linear optical (NLO) effect related to the higher order polarizability of molecules, thus, TPA measurements provide information on state energies and transition dipole moments of the two-photon absorbing material under study. As such TPA has been used to elucidate the structure-function relationship of molecules and gain information about charge transfer strength and changes in dipole moments. A molecule's TPA is quantitatively analyzed by calculating its TPA cross-section (δ_R). The TPA cross-section takes into account the absorption of both photons within a given area and time. Therefore, the unit of the cross-section is in cm^4's'$photon^{-1}$ and are typically on the order of 10^{-50} $cm^4 \cdot s \cdot photon^{-1}$ and referred to in units of GM (in honor of Göppert-Meyer) where 1GM = 10^{-50} $cm^4 \cdot s \cdot photon^{-1}$. TPA cross-sections are sensitive to molecular properties and thus increase or decrease with molecular structure.[16,17]

Due to the higher order polarizability, specifically the third-order polarizability (γ), and third order susceptibility, ($\chi^{(3)}$), of the TPA process, it differs in selection rules from one-photon absorption (OPA). For instance, the ground to final state transition in non-centrosymmetric molecules is electric dipole allowed in both one and two-photon absorption. Alternatively, the OPA allowed and TPA allowed transitions in centrosymmetric molecules are mutually exclusive. Therefore, researchers have been keen to learn what parameters affect a molecule's TPA and what can be tuned in order to design molecules with large NLO properties. The molecular dipole polarization can be expressed as contributions of the molecular linear and nonlinear optical responses to an external electric field, E[18]:

$$P_i^{NLO} = \mu + \alpha_{ij}E_j + \beta_{ijk}E_jE_k + \gamma_{ijkl}E_jE_kE_l + \cdots \quad (1.3)$$

where μ is the permanent molecular dipole moment, and α, β and γ are the tensor elememts of the microscopic polarizabilities, or hyperpolarizabilities. These microscopic polarizabilities altogether dictate the macroscopic optical properties of the molecule. The structure-property relationships for γ have been studied in the past. [18–20] Generally, values of γ are known to depend on extended π-conjugation.[18] However, Marder et al.[19] found that it also has a strong dependence on other molecular parameters such as the charge transfer and bond order alternation. The charge transfer excited state gives a significant contribution to γ as it is dependent on bond order alteration (BOA) which is in turn tuned by donor-acceptor (D-A) moieties[21].

The real part of the second order molecular polarizability can be experimentally determined by third harmonic generation, four-wave mixing as well as quadratic electro-optical measurements. The imaginary part of γ can be measured by two-photon absorption experiments. The two photon cross-section is connected to γ by:[22,23]

$$\delta = \frac{4\times\pi^2\times\hbar\omega}{n^2c^2} \times L^4 \times Im\gamma(-\omega;\omega\omega-\omega,\omega) \tag{1.4}$$

$$\gamma_{Im} = \frac{4}{5} \times \mathrm{Im}\left[\frac{{\mu_{ge}}^2\times\Delta\mu^2}{(E_{ge}-\hbar\omega-i\Gamma_{ge})^2(E_{ge}-2\hbar\omega-i\Gamma_{ge})} + \sum_{e\prime}\frac{{\mu_{ge}}^2\times{\mu_{ee\prime}}^2}{(E_{ge}-\hbar\omega-i\Gamma_{ge})^2(E_{ge}-2\hbar\omega-i\Gamma_{ee\prime})} - \right.$$

$$\left.\frac{{\mu_{ge}}^4}{(E_{ge}-\hbar\omega-i\Gamma_{ge})^2(E_{ge}-2\hbar\omega-i\Gamma_{ge})}\right] \tag{1.5}$$

From Eqs. 1.4 and 1.5, it is clear that the random or classical TPA cross-section has a dependence on the transition dipole moments μ and the permanent dipole moment difference $\Delta\mu$ and this becomes apparent in the TPA cross-section equation obtained from second-order perturbation theory:[9]

$$\delta_R = \frac{\pi}{2}\omega_1^0\omega_2^0\delta(\varepsilon_f-\varepsilon_i-\omega_1^0-\omega_2^0) \times \left|\sum_j\left[\frac{D_j}{\Delta_j^{(1)}-i\kappa_j/2}+\frac{D_j}{\Delta_j^{(2)}-i\kappa_j/2}\right]\right|^2. \tag{1.6}$$

In this equation, ω_1^0 and ω_2^0 represent the photon energies, ε_f and ε_i the final and initial energy levels respectively, D_j give the transition matrix dipole elements, κ_j are the excited state linewidths and $\Delta_j^{(k)} = \varepsilon_j - \varepsilon_i - \omega_k^0$ which is the energy mismatch. In order to better understand the TPA cross-section in terms of dipole moments and the different TPA mechanisms, Upton *et al* rewrote the random TPA equation as:[9]

$$\delta_R = \frac{B}{\hbar^2\varepsilon_0^2}\omega_0^2\omega_2^0\delta(\varepsilon_f-\varepsilon_g-2\omega_0)\left|\frac{1}{(\omega_0+\varepsilon_g-\varepsilon_e)-i\kappa_e/2}\mu_{fe}\cdot e\mu_{eg}\cdot e+\frac{1}{\omega_0-\frac{i\kappa_g}{2}}\mu_{fg}\cdot e\mu_{gg}\cdot\right.$$

$$\left. e+\frac{1}{\omega_0-\frac{i\kappa_f}{2}}\mu_{ff}\cdot e\mu_{fg}\cdot e\right|^2. \tag{1.7}$$

Here, the dependence of δ_R on the transition dipole moment and permanent dipole moment difference becomes more apparent. The first term in equation 1.7 describes TPA through an intermediate level. Alternatively, terms 2 and 3 describe TPA through the permanent dipole

pathway where the ground and final states are strongly coupled to each other. Therefore, in the permanent dipole pathway intermediate states are not involved. This understanding of classical TPA will be beneficial in studying entangled TPA.

1.3. Entanglement

1.3.1. Non-classical fields

Entangled states are also referred to as Einstein-Podolsky-Rosen or EPR states, due to the famous EPR paper[10] that looked at whether the description of reality described by quantum mechanics is correct. The unique property of entangled states is that while the correlations of two subsystems of a state are known with certainty and provide complete information, the values of physical observables for either of the two individual subsystems are completely random. As a result, the measurement of a physical observable of one subsystem allows the value of the other subsystem to be 100% determined. Einstein, Podolsky and Rosen suggested this with the following state[10]

$$|\Psi\rangle = \sum_{a,b} \delta(a + b - c_0)|a\rangle|b\rangle, \tag{1.8}$$

where a and b are the momentum or position of two different particles respectively, and c_0 is a constant. This EPR state follows the above feature, where measuring neither observable a nor b are initially known, but measuring one determines the value of the other. This can be seen by the delta function in equation 1.8.

Nonclassical or quantum light, is light whose properties make it such that it cannot be described with classical electromagnetism and must be described by the quantized electromagnetic field. As such, quantum light and classical light differ in terms of their statistics, correlations and fluctuations. In terms of statistics, light can be divided into three categories: Poissonian, super-Poissonian and sub-Poissonian. Photon statistics of light can

be defined as a relation between its mean photon number $\langle \hat{n} \rangle$ and the variance in photon number $\langle (\hat{n})^2 \rangle$.[24] Classical light with fluctuating intensity such as thermal light is considered to have super-Poissonian distribution where $\langle (\hat{n})^2 \rangle > \langle \hat{n} \rangle$. Coherent light, such as laser light which can still be described with semi-classical theory, lies on the boundary and is defined by Poissonian distribution where $\langle (\hat{n})^2 \rangle = \langle \hat{n} \rangle$. On the other hand, non-classical light is described with a sub-Poissonian distribution of $\langle (\hat{n})^2 \rangle < \langle \hat{n} \rangle$. Looking at photon statistics in terms of light fluctuations, it is clear that if the variance is smaller than the mean photon number, the sub-Poissonian nature of non-classical light allows for much lower fluctuations in photon number which becomes useful in enhancing signal to noise rations (SNR) in measurements.[25]

These distribution statistics can in turn be correlated to the coherence properties of light. The second-order correlation function, $g^{(2)}$, is a normalized intensity correlation that characterizes photon number fluctuations by considering the position and time of the photons from a source.[26,27] This function depends on a time delay, τ, between the photons and thus the temporal correlation $g^{(2)}(\tau)$ is often referred to. For super-Poissonian behavior where the variance of the photon number is larger than the mean, $g^{(2)} > 1$ (Figure 2). For Poissonian light sources, $g^{(2)} = 1$ and from this, it is apparent that classical light fields are limited to $g^{(2)} \geq 1$. Sub-Poissonian behavior is therefore described by the parameter $g^{(2)} < 1$ and only describable in quantum terms.[28] For coherent (classical) light, photon modes are statistically independent while for non-classical light, the temporal correlations ensure that the arrival of one photon is followed by the arrival of the second photon. Therefore classical, coherent and quantum light can be described in terms of their degree of correlation with thermal light on one end with 0 correlation and quantum light

on the other with a 100% degree of correlation. The relationship of classical, coherent and quantum light with their photon statistics, second order correlation function as a function of time and degree of correlation is shown in Figure 1.2. It is these correlations that allow entangled photons to be useful for measurements via interference, coincidence detection, quantum reconstruction and entangled two-photon absorption.[29]

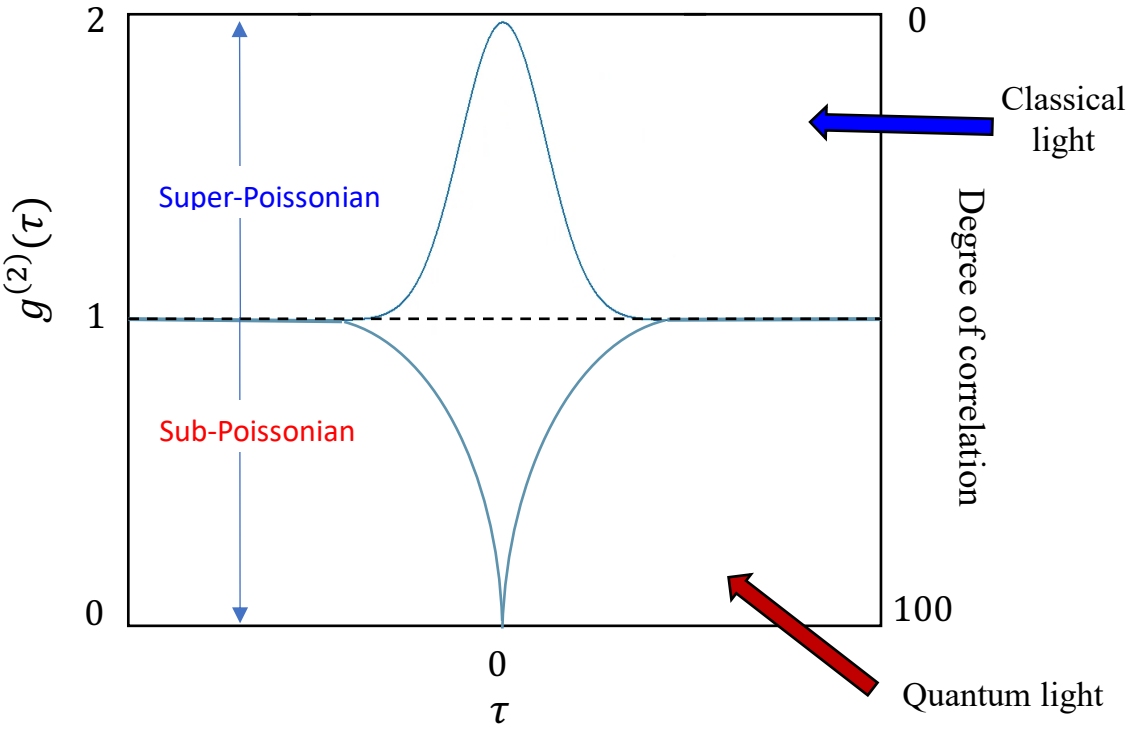

Figure 1.2. *Photon statistics of Super-Poissonian (thermal) light, Poissonian (coherent) light and Sub-Poissonian (quantum) light. Left axis shows relationship with the temporal correlation function* $g^{(2)}(\tau)$ *against time delay* τ. *The right axis shows the degree of correlation of photons from thermal and coherent (non-classical) light to quantum light.*

Gerd Leuchs examined the photon statistics and correlations of non-classical properties of light and deduced that certain aspects of the radiation fields of these anti-bunched or squeezed states cannot be described in classical terms.[30] The correlation function, $g^{(2)}(\tau)$, has become a standard way to describe radiation fields and involves

taking an ensemble average of the electric field amplitudes at particular space-time points. The first order correlation function $g^{(1)}$, describes amplitude characteristics of a radiation field and considers the electric field amplitude at two different space-time points.

$$g^{(1)}(r_1, t_1, r_2, t_2) = \langle \varepsilon^*(r_1, t_1)\varepsilon(r_2, t_2)\rangle \text{ [30]} \tag{1.9}$$

At the point where $r_1 = r_2$ and $t_1 = t_2$, the function $g^{(1)}$ is proportional to the field intensity, therefore, it is first order in intensity. Higher order correlation fields are needed to more thoroughly determine the temporal correlations and photon statistics of a light source. In the classical case, the general form of $g^{(2)}$, the second-order correlation function is[30]

$$g^{(2)}(r_1t_1, r_2t_2r_3t_3r_4t_4) = \langle \varepsilon^*(r_1, t_1)\varepsilon^*(r_2, t_1)\varepsilon(r_3, t_3)\varepsilon(r_4, t_4)\rangle. \tag{1.10}$$

This $g^{(2)}$ function relates to the intensity of the field being measured at two different space-time points. An ensemble average of the multiplied intensities gives:

$$g_I{}^{(2)}(\tau) = 4\langle I(t_1)I(t_2)\rangle = \langle \varepsilon^*(t_1)\varepsilon(t_1)\varepsilon^*(t_2)\varepsilon(t_2)\rangle \tag{1.11}$$

where $\tau = (t_2 - t_1)$ and $g_I{}^{(2)}(\tau)$ represents the temporal intensity correlation function. Alternatively, the second-order correlation function for a two-photon absorber is given as

$$g_I{}^{(2)}(\tau) = \langle \varepsilon^*(t_1)\varepsilon^*(t_1)\varepsilon(t_2)\varepsilon(t_2)\rangle. \tag{1.12}$$

In the above descriptions of $g^{(2)}$, the fields are ordered as intensity terms but the same cannot be done in the quantum description with non-classical light.

In the quantum description, operators replace the electric field amplitudes. However, due to commutation rules and since the field operators do not commute, the photon creation and annihilation operators, $\hat{a}^+$and $\hat{a}$ respectively must be appropriately ordered. Since the second-order correlation function represents the detection of two-photons at times t and t' and this process describes the destruction of the two photons at

the detectors, it can be written as the matrix element $\langle f|\,\hat{a}\,(t')\hat{a}^{+}(t)|i\rangle$. The two photons from the initial state, $\langle i|$, destruct at the detectors and are therefore not in the final state $\langle f|$. The correlation function $g^{(2)}(t'-t)$ is therefore the square of this matrix summed over all final states:[30]

$$g^{(2)}(t'-t) \propto \sum_f \langle i|\hat{a}^{+}(\mathrm{t})\hat{a}^{+}(t')|f\rangle\langle f|\,\hat{a}(t')\,\hat{a}(t')|i\rangle \tag{1.13}$$

where $\sum_f |f\rangle\langle f| = \hat{I}$ and with correct ordering (creation operators to the left of annihilation operators), the $g^{(2)}$ becomes

$$g^{(2)}(t'-t) = \langle i|\hat{a}^{+}(t)\hat{a}^{+}(t')\,\hat{a}\,(t')\,\hat{a}\,(t)|i\rangle. \tag{1.14}$$

To further evaluate the statistics of these we can use the properties of photon number states, $|n\rangle$. The photon annihilation and creation operators can be rewritten by how they act on the photon number states as the following:

$$\hat{a}|n\rangle = \sqrt{n}\,|n-1\rangle \tag{1.15}$$

$$\hat{a}^{+}|n\rangle = \sqrt{n+1}\,|n+1\rangle$$

The correlation function in Equation 1.11 can be re-evaluated under the assumption that the initial state is a pure photon number state, so

$$\langle n|\hat{a}^{+}\hat{a}^{+}\,\hat{a}\,\hat{a}|n\rangle = n^2 - n. \tag{1.16}$$

This expectation value provides a quadratic and a linear term, and it is clear that as the average number of photons expectation value is increased, the linear contribution, that is the quantized effect is less and less pronounced.

Beck utilized a different formalism to understand the temporal correlations of classical and entangled light sources.[31] The famous Hanbury Brown and Twiss (HBT) experiment (as shown in Figure 3) involves a field impinging on a beam splitter and the intensities from the two output ports measured by photon-counting detectors to determine

the correlation (and anti-correlation) effects between the reflected and transmitted output intensities.[32] A time delay, t, is introduced in one arm after the beam splitter, and the measurement provides the second order (temporal) coherence, $g^2(\tau)$. The "simultaneous" measurement, where $\tau = 0$, is of particular importance as it distinguishes between classical and quantum fields from their correlations. The classical value for $g^2(\tau)$ is evaluated by the normalized correlations of the transmitted (T) and reflected (R) output beams and can also be written in terms of the incident intensity:[31]

$$g^{(2)}(\tau) = \frac{\langle I_T(t+\tau) I_R(t)\rangle}{\langle I_T(t+\tau)\rangle\langle I_R(t)\rangle} = \frac{\langle I_I(t+\tau) I_I(t)\rangle}{\langle I_I(t+\tau)\rangle\langle I_I(t)\rangle} \tag{1.17}$$

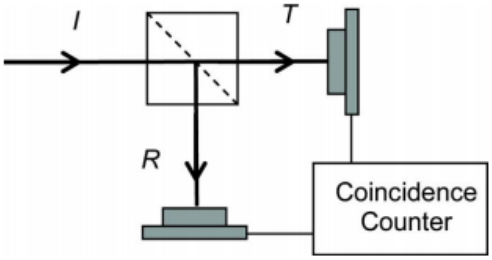

Figure 1.3. *Hanbury Brown Twiss Interferometer. Incident beam impinges on a 50/50 beam splitter and separates into the transmitted (T) and reflected (R) beam and are measured by photon detectors in coincidence.*[31]

For the important case where $\tau = 0$, the correlation function in equation 1.17 becomes $g^{(2)}(0) = \frac{\langle {I_I}^2(t)\rangle}{\langle I_I(t)\rangle^2}$ and applying the Cauchy-Schwartz inequality to this expression yields the following expression for a classical light source $g^{(2)}(0) \geq 1$. As stated previously, the quantum expression must utilize the appropriately ordered operators. In the quantum case, the expression is given as:[31]

$$g^{(2)}(\tau) = \frac{\langle :\hat{I}_T(t+\tau)\hat{I}_R(t):\rangle}{\langle \hat{I}_T(t+\tau)\rangle\langle \hat{I}_R(t)\rangle} \tag{1.18}$$

where the colons represent the time ordering of the operators and it can be shown that for a quantized or Fock state, $g^{(2)}(0) = (n-1)/n$, and as previously mentioned for non-

classical light $g^{(2)}(0) < 1$. This violates the inequality for classical light, $g^{(2)}(0) \geq 1$, and there is a clear difference in the correlations of classical and non-classical light.

1.3.2. Entangled light generation

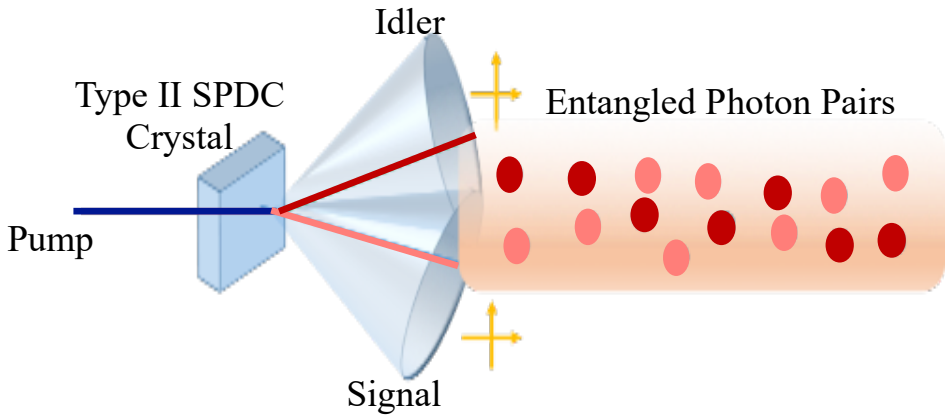

***Figure 1.4**. Diagram of Type-II SPDC process.*

The most popular way of generating entangled states is via quantum entangled photon pairs and this is most commonly carried out through spontaneous parametric downconversion (SPDC). SPDC is a nonlinear optical process where a single pump beam interacts with a nonlinear crystal and creates a pair of down-converted photons, i.e. the signal and idler photon, which can be entangled in frequency, time, space and/or polarization. A schematic of SPDC is shown in Figure 1.4. The efficiency of this process is roughly on the order of 10^{-7} – 10^{-11}. The process is governed by energy and momentum conservation, thus, the interaction of the pump beam with the nonlinear material leads to the annihilation of a high frequency pump and the simultaneous creation of two lower frequency photons that satisfy the phase matching conditions:

$$\omega_p = \omega_s + \omega_i, \qquad k_p = k_s + k_i \tag{1.19}$$

where ω is the frequency, k is the wave vector and p, s and i represent the pump, signal and idler respectively. The signal and idler photon energies must add up to the energy of the pump and the vector addition of the signal and idler wave vectors must add up to that of the pump. The SPDC photons are produced in a cone-like arrangement that is altered by the angle of the nonlinear crystal with respect to the pump beam. We can look more closely at the math of the SPDC process as analyzed by Yanhua Shih in order to determine the entangled two-photon state. The SPDC process is governed by the nonlinear susceptibility properties of the crystal. The polarization (dipole moment per unit volume) of the crystal is given by:[33]

$$P_i = \chi^{(1)}_{i,j} E_j + \chi^{(2)}_{i,j,k} E_j E_k + \chi^{(3)}_{i,j,k,l} E_j E_k E_l + \cdots, \tag{1.20}$$

where $\chi^{(m)}$ is the m^{th} order electrical susceptibility tensor and the main factor in SPDC is $\chi^{(2)}$, the second order nonlinear susceptibility. The interaction Hamiltonian for this tensor can then be written as follows with the integral taken over the interaction volume (V):[34]

$$H = \epsilon_0 \int_V d^3 r \chi^{(2)}_{i,j,k} E_i E_j E_k \tag{1.21}$$

The Fourier representation for the electrical fields,

$$E(\boldsymbol{r}, t) = \int d^3\boldsymbol{k} \left[\boldsymbol{E}^{(-)}(\boldsymbol{k}) e^{-i(\omega(\boldsymbol{k})t - \boldsymbol{kr}} + \boldsymbol{E}^{(+)}(\boldsymbol{k}) e^{i(\omega(\boldsymbol{k})t - \boldsymbol{kr}} \right] \tag{1.22}$$

is substituted into equation 1.21 in order to conveniently obtain the SPDC interaction Hamiltonian. Assuming an infinite volume and a plane and monochromatic pump field, this becomes:[33]

$$H_{int}(t) = \epsilon_0 \int d^3 k_s d^3 k_i \chi^{(2)}_{lmn} E^{(+)}_{p\,l} E^{(-)}_{s\,m} E^{(-)}_{i\,n} \delta\left(k_p - k_s - k_i\right) e^{-i\left(\omega_p - \omega_s(k_s) - \omega_i(k_i)\right)t} + h.c. \tag{1.23}$$

where h.c. is the Hermitian conjugate. As was done in the section on entangled light correlations, while the pump laser beam can be considered as a classical field, the signal and idler fields which are in single-photon level must be quantized and written in terms of operators:

$$E^{(-)}(k) = i\sqrt{\frac{2\pi\hbar\omega}{V}}\,\hat{a}^{\dagger}(k), \qquad E^{(+)}(k) = i\sqrt{\frac{2\pi\hbar\omega}{V}}\,\hat{a}(k). \tag{1.23}$$

These quantized fields are then utilized to obtain the entangled two-photon state. The two-photon state can be estimated using perturbation theory:[33]

$$\left|\Psi\right\rangle = -\frac{i}{\hbar}\int dt\; H_{int}(t)\,|0\rangle \tag{1.24}$$

In line with the SPDC process, initial state is in vacuum so there is no input radiation in either the signal or idler modes. We assume an infinite interaction time and evaluate the integral, substituting in the quantized electric fields and find the entangled two-photon state wavefunction:[33,35]

$$\left|\Psi\right\rangle = A\int d^3k_s d^3k_i\;\delta(\omega_p - \omega_s(k_s) - \omega_i(k_i))\;\delta(k_p - k_s - k_i)\;\hat{a}_s{}^{\dagger}(k_s)\hat{a}_i{}^{\dagger}(k_i)\,|0\rangle$$

or

$$|\Psi\rangle = \left(\frac{T_e\sqrt{2/\pi^3}}{l^2\Delta\omega_p}\right)^{1/2} l\iint d\omega_s d\omega_i \exp\left(-\frac{(\omega_s+\omega_i-\omega_p)^2}{\Delta\omega_p^2}\right) sinc\left(\frac{l}{2\pi}\left(k_s + k_i - k_p\right)\right)\hat{a}^{\dagger}(\omega_s)\hat{a}^{\dagger}(\omega_i)|0\rangle \tag{1.25}$$

where the first part of the wavefunction represents the temporal entanglement, with T_e being the entanglement time, the uncertainty in the arrival of one photon after the other and l is the length of the crystal. The second part of the wavefunction represents the energy conservation and the argument of the sinc function represents the momentum conservation and phase matching conditions of the signal-idler pair, thus, determining the frequency and

propagation direction of the biphoton. The creation operators of the signal and idler ($\hat{a}^{\dagger}$) are present to indicate the simultaneous creation of the photon pairs.

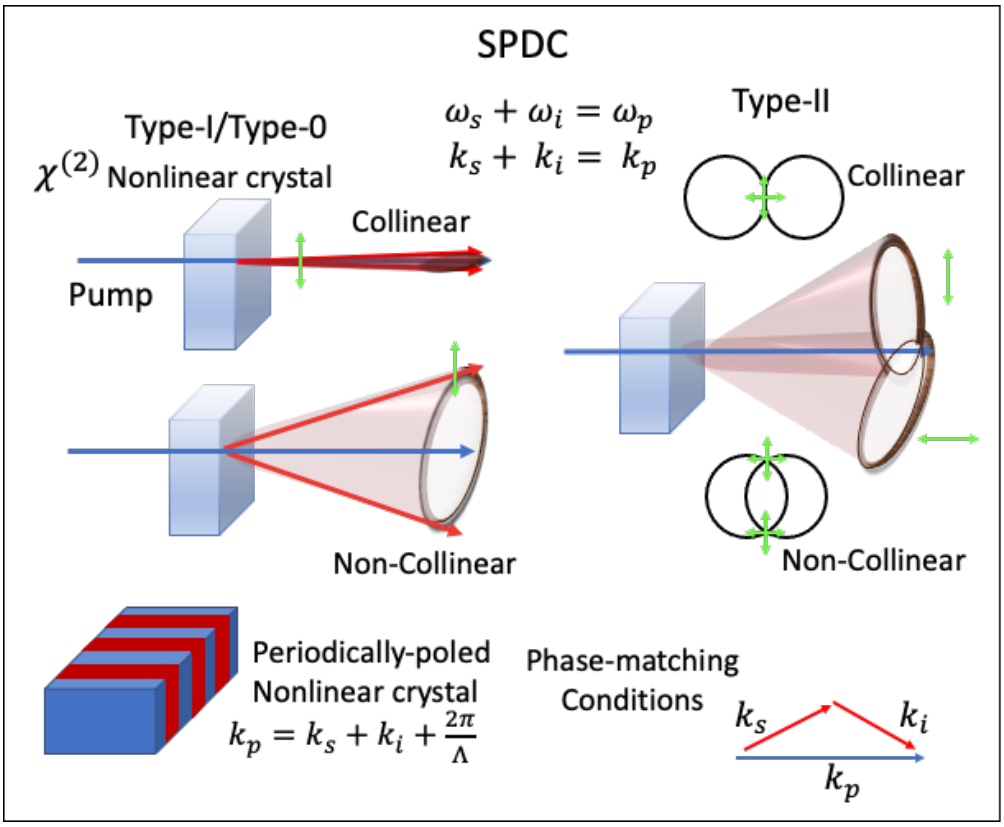

Figure 1.5. *Spontaneous Parametric Downconversion (SPDC) with a bulk crystal showing cone-like spatial arrangement of signal and idler photons for different types of SPDC. The spatial arrangements can be collinear or non-collinear as shown for Types –II, -I, and -0 phase-matching. SPDC can also be performed with a periodically-poled nonlinear crystal.*

SPDC occurs in different downconversion types resulting in particular polarizations of the emitted photons; for an extraordinary pump beam, Type-I SPDC produces two ordinary polarized beams, Type-0 produces two extraordinary polarized beams and Type-II produces two orthogonally polarized photon beams, one ordinary and one extraordinary (Figure 1.5). We are particularly interested in Type-II SPDC due to the polarization entanglement with the opposite polarizations. In Type-II SPDC, in a negative uniaxial crystal (such as β-Barium Borate (BBO)), the e-ray emerges from the crystal

before the o-ray and the maximum delay between the o- and e-ray is given by $\left(\frac{L}{u_o} - \frac{L}{u_e}\right) = DL$ [35], where L is the crystal length, u_o and u_e are the group velocity of the ordinary and extraordinary photons respectively. Therefore, $D \equiv {}^{1}/_{u_o} - {}^{1}/_{u_e}$ and the crystal thickness and polarization properties determine the optical delay between the photon pairs, i.e. the entanglement time and this leads to a rectangular shape of the two-photon wavefunction set by these time and polarization restrictions. This is portrayed in Figure 6 as depicted by Sergienko *et al*[35]

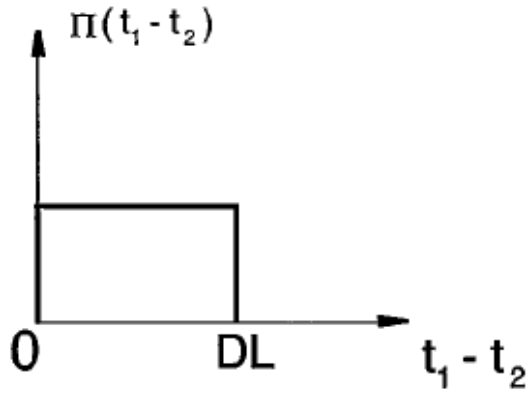

Figure 1.6. *Schematic of two-photon wave function*[35]

1.3.3. Entangled two-photon absorption

Due to the strong correlations and non-classical properties of entangled light, around 1990, Gea-Banacloche[36] and Javanainen and Gould[5] became interested in the possibility of multiphoton absorption, specifically two-photon absorption (TPA) with non-classical light. They theorized that one effect of entangled two-photon absorption would be the two-photon rate's linear (rather than quadratic) dependence on photon intensity at low input flux, despite TPA being a nonlinear process. Fei *et al* also considered this entangled TPA

(or ETPA) process.[3] The overall two-photon absorption rate contains both a linear and quadratic component:

$$R = R_e + R_r = \sigma_e \phi + \delta_r \phi^2. \tag{1.26}$$

Due to the linear dependence of the ETPA rate on intensity, it is clear this process only dominates when the photon flux is small. At higher intensities (ϕ), TPA is dominated by randomly arriving photons giving the random TPA rate, R_r. Assuming a simple probabilistic model of TPA, where one photon is absorbed to a virtual state of lifetime τ, and the second photon is then absorbed to the final state, R_r can be linked to the virtual state lifetime and the single-photon cross-section, σ, through their relationship with the two-photon random cross-section, $\delta_r = \sigma^2 \tau$. The entangled photon pair however, which are emitted from the SPDC crystal within the time T_e and within the area A_e, have a flux density of $\phi/2$ photon pairs / cm^{2}s and must arrive at the absorbing material within τ and within σ. Therefore the absorption rate of the pair depends on the probabilities ξT_e and ζA_e and the ETPA rate $R_e = \sigma_e \phi$ with the entangled cross-section, $\sigma_e = \sigma \xi T_e \zeta A_e$ /2.[3] The intensity at which there is a crossover between random and entangled TPA and the processes are equal is the critical flux, $\phi_c = \sigma_e / \delta_r$. A probabilistic way of comparing the ETPA and random TPA cross-sections can be deduced, in the case where $T_e \gg \tau$ and $A_e \gg \sigma$,

$$\sigma_e = \delta_r / 2 A_e T_e. \tag{1.27}$$

The full entangled-two photon absorption cross-section was then derived using second-order time-dependent perturbation theory. The entangled two-photon state, $|twin\rangle$, (Eq. 1.25) interacts with the atomic or molecular system which is in its initial state, providing the initial state of the entire system,

$$|\Psi_i\rangle = |\psi\rangle \otimes |twin\rangle. \tag{1.28}$$

The system is excited through some intermediate state $|\psi_j\rangle$ before it reaches its final state, $|\psi_f\rangle$. In the final state of the entire system, the light is in vacuum, $|0,0\rangle$ as the photons have been absorbed, therefore, the final state of the system is

$$|\Psi_f\rangle = |\psi_f\rangle \otimes |0,0\rangle \tag{1.29}$$

The absorption rate can then be derived using the interaction picture. The Hamiltonian is $H = H_0 + H_I$ where the interaction Hamiltonian is $H_I = e\mathcal{E}(r,t).r$. A time evolution operator, $|\Psi(t)\rangle = U_I(t)|\Psi_i\rangle$, is projected onto the final state of the system to derive the probability amplitude of the system:[3]

$$S_{fi} = \frac{\pi N l}{2A_q}\sqrt{\omega_1^0 \omega_2^0}\, exp\left[-\frac{(e_f - e_i - \omega_p)^2}{\Delta\omega_p^2}\right] \tag{1.30}$$

$$\times \sum_j \left\{ D_{21}^{(j)} \frac{1 - exp\{-i[T_e(e_j - e_i - \omega_1^0) + (T_0 - T_e/2)(e_f - e_i - \omega_1^0 - \omega_2^0)] - T_e\kappa_j/2\}}{T_e(e_j - e_i - \omega_1^0) + (T_0 - T_e/2)(e_f - e_i - \omega_1^0 - \omega_2^0) - iT_e\kappa_j/2} \right\}$$

$$+ D_{12}^{(j)} \frac{1 - exp\{-i[T_e(e_j - e_f + \omega_1^0) - (T_0 - T_e/2)(e_f - e_i - \omega_1^0 - \omega_2^0)] - T_e\kappa_j/2\}}{T_e(e_j - e_f + \omega_1^0) - (T_0 - T_e/2)(e_f - e_i - \omega_1^0 - \omega_2^0) - iT_e\kappa_j/2}$$

where $D_{kl}^{(j)} = \langle\psi_f|d_k|\psi_j\rangle\langle\psi_j|d_l|\psi_i\rangle$ are the transition matrix elements with material electric-dipole moment components d_k, d_l (with $k, l = 1,2$); $T_0 = (T_1 + T_2)/2$ (where T_1 and T_2 are the mean transit times determined by the group velocities of the signal and idler photons), κ_j is the intermediate state linewidth and A_q is the quantization area. This probability amplitude has a complex dependence on material terms and entangled two-photon terms. The ETPA cross-section can be written in terms of S_{fi}:

$$\sigma_e = |S_{fi}|^2 {A_q}^2 / A_e. \tag{1.31}$$

This equation can be simplified with a few assumptions; firstly that the pump beam is monochromatic such that $\Delta\omega_p \to 0$ and $\omega_p = \omega_1^0 + \omega_2^0$. With this, the energy mismatch can be determined to be ${\Delta_k}^{(j)} = e_j - e_i - \omega_k^0$ and Eqs. 1.30 and 1.31 can be reduced to[3]

$$\sigma_e = \frac{\pi}{4A_eT_e}\omega_1^0\omega_2^0\delta\left(e_f - e_i - \omega_1^0 - \omega_2^0\right) \tag{1.32}$$

$$\times \left|\sum_j \left| D_{21}^{(j)} \frac{1 - exp\left[i{T_e\Delta_1}^{(j)} - \frac{T_e\kappa_j}{2}\right]}{{\Delta_1}^{(j)} - \frac{i\kappa_j}{2}}\right.\right.$$

$$\left.\left. + D_{21}^{(j)} \frac{1 - exp\left[-i{T_e\Delta_2}^{(j)} - \frac{T_e\kappa_j}{2}\right]}{{\Delta_2}^{(j)} - \frac{i\kappa_j}{2}}\right|\right.$$

Using this famous ETPA equation (1.32) from Fei *et al*[3] we can begin to see that there is a complex dependence on T_e and due to the interference between the intermediate states of the molecule and the entangled photons, there is constructive and destructive interference that leads to an oscillating, nonmonotonic behavior of σ_e as a function of the entanglement time. The ETPA cross-section is dependent on the material electronic states as well as the material dipole moments. A more in-depth analysis of this ETPA cross-section was carried out by Upton *et al* in a 2013 study.[9] They considered the different pathways of two-photon absorption and the role these pathways play in entangled two-photon absorption. For some molecules there is an intermediate state close to resonance with the absorbed photon, and as a result, the TPA process occurs through this intermediate with coupling of the intermediate state and the entangled photon. Here, σ_e is dependent on the transition dipole moments between the ground and intermediate states and between the intermediate and final states. Alternatively, molecules with intermediate states that are further off from resonance undergo TPA through the permanent dipole pathway. In this

case, the intermediate states are directly coupled to the ground and final states and σ_e depends on the change in permanent dipole between the ground and final states. Equation 1.32 was therefore modified in this study to reflect the different pathways and was given as:[9]

$$\sigma_e = \frac{A}{\hbar^2 {\varepsilon_0}^2 A_e T_e} {\omega_0}^2 \delta\left(e_f - e_g - 2\omega_0\right) \qquad \text{Eq. 1.33}$$

$$\left| \frac{1 - e^{i(\omega_0 + \varepsilon_g - \varepsilon_e)T_e - \kappa_e T_e/2}}{\left(\omega_0 + \varepsilon_g - \varepsilon_e\right) - i\kappa_e/2} \mu_{fe}.e_i \mu_{eg}.e_s + \frac{1 - e^{i\omega_0 T_e - \kappa_g T_e/2}}{\omega_0 - i\kappa_g/2} \mu_{fg}.e_i \mu_{gg}.e_s \right.$$

$$\left. + \frac{1 - e^{i\omega_0 T_e - \kappa_f T_e/2}}{-\omega_0 - i\kappa_f/2} \mu_{ff}.e_i \mu_{fg}.e_s \right|^2$$

where e_i and e_s are the polarization of the signal and idler, In Eq. 1.33 the first term describes ETPA via the transition dipole pathway and the second and third terms describe ETPA through the permanent dipole. It can be seen that the first term involves the transition dipole moments, μ_{fe} and μ_{eg} while the second and third terms have the dipole moments of the ground and final states μ_{ff} and μ_{gg} and the ground to finale state transition moments μ_{fg}.

Javanainen and Gould also looked at the theory of the linear intensity dependence of a two-photon transition rate with light generated by parametric down conversion.[5] They considered both pathways; one where there is a two-step process and the field populates the intermediate state and immediately after populates the excited state (what we refer to as the transition dipole pathway) and the other route which is a two-photon process, and proceeds via a coherent superposition between the ground and final states (the permanent dipole pathway). They were able to suggest a model that estimates the two-photon transition rate in a three-level atomic system excited with down-converted light at

frequencies close to resonance with the two-photon transition. Considering the decay rates of the intermediate and final states as Γ and γ respectively, the total two-photon transition rate of both pathway contributions is given as[5]

$$R = \left|\frac{d_{01}d_{12}}{\hbar^2}\right|^2 \left[\frac{E^4\tau^2}{\Gamma} + \frac{\gamma/2}{\delta^2+(\gamma/2)^2}\frac{E^2\hbar\omega\tau}{\epsilon_0 cA}\right]. \quad \text{Eq. 1.34}$$

In this equation, d_{ij} represent the transition dipole elements, τ and A are the coherence time and area respectively and E represents the electric field where the intensity, I, is $I = c\epsilon_0 E^2/2$. We can see that in Eq. 1.34, at low intensities the two-photon rate is linearly dependent on the intensity and that as intensity increases, the crossover to a quadratic dependence on intensity takes over. In this intensity range and with higher photon densities, it is more likely to find uncorrelated photons in a coherence volume interacting with the atom.[5] In order to experimentally observe this two-photon phenomenon, there are some requirements that Javanainen and Gould brought up that must be met. One requirement is that there should be a nearly resonant intermediate state with the photon field. The second requirement considers the two-photon rate below the critical flux where there is linear intensity dependence. In the limit where Γ and γ are equal and the detuning energy is zero, the linear intensity rate is

$$R = \frac{1}{\gamma}\left[\frac{4\pi d_{01}d_{12}}{\hbar\lambda\epsilon_0 A}\right]^2 \quad \text{Eq. 1.35}$$

with A being the area of the focus and the down-converted light having a Gaussian beam profile.

1.3.4. Experimental Observations of Entangled Two-Photon Absorption

Since the early proposals of ETPA in the 1990s, work has been done to experimentally realize the phenomenon. The first experimental realization of this linearly dependent two-photon transition was carried out by Georgiades *et al.* when they were successful in using down-converted pairs to produce a two-photon excitation in atomic cesium.[37] *Georgiades et al* measured the photocurrent from the fluorescence of atomic Cs which had been excited with squeezed pairs generated by non-degenerate parametric conversion. They observed a dependence of the excited state population that deviates from quadratic and instead has a fit which has linear plus quadratic function. The log-log plot of this data recorded a slope of 1.3. This experiment was repeated with coherent light and with this they observed the typical classical quadratic behavior. Hence, their experiment provided the framework for the experimental observation of processes caused by excitation with non-classical fields.

Additionally, Dayan *et al* later demonstrated TPA with broadband down-converted light, exciting a Rb cell and measuring the resulting fluorescence with a photomultiplier tube.[38] They found that there were phase-sensitive modulations related to the correlation function of the nonclassical light. This work presented the opportunity for quantum coherent control with the TPA process, and that TPA can be induced with down-converted photon pairs at orders of magnitude lower peak power than fs pulses.

In 2006, Dong-Ik Lee in the Goodson Group at the University of Michigan was successful in experimentally observing the linear ETPA rate as a function of intensity for an organic porphyrin molecule.[39] In addition to this, he attained varying ETPA rates with different delay times, confirming the nonmonotonic behavior of ETPA cross-sections as a function of time. A large ETPA cross-section on the order of $\sim 10^{-17}$ cm^2 was measured,

which is comparable to the single photon absorption cross-section ($\sim 10^{-16}$ cm^2). It is important to note that the ETPA cross-section and classical TPA cross-section cannot be directly compared due to the different units.

Since then, more work has been done to determine trends and comprehend the processes of ETPA in organic chromophores. A systematic study was done on the effect of increasing thiophene dendrimer generation on TPA and ETPA, as dendrimers are known for their efficient intramolecular energy transfer and hence good TPA properties.[40] Interestingly, whereas ETPA is performed with an input flux of $\sim 10^7$ photons/s while classical TPA utilizes input fluxes on the much higher order of $\sim 10^{20}$ photons/s, the trend of increasing ETPA cross-section with increased thiophene units matched trends in cross-sections measured with classical TPA. This discovery suggested that both entangled and non-entangled light were probing the same states in these materials. Additionally, ETPA measurements were performed both in solution and in film. Enhanced cross-section of the dendrimer films compared to their corresponding solutions indicated better detection of entangled photons and opened a gateway to more solid phase experiments with entangled light. Another important area of research has been finding methods to control the ETPA process. Entanglement time variation has been greatly studied[4] but Guzman et al. further examined degree of entanglement by controlling ETPA with phase-matching conditions of SPDC.[8] It was shown that the non-collinear orientation yielded the greatest ETPA, followed by the collinear orientation then the spatially-separated conditions which showed no absorption at all. ETPA has been conducted in other popular two-photon dyes, and was found to be sensitive to molecular aggregation at high molecular concentrations ($\geq$ 1mM).[41] ETPA measurements have also been extended to biological systems, and have

found to be sensitive to the environments of fluorescence proteins which has great implications towards using entangled photons for biological sensing.[42]

Many ETPA methods utilized a transmission method to detect absorption via attenuation, but in 2013, an observation of fluorescence emission in an organic dendrimer upon two-photon excitation by entangled photon pairs was made.[9] The ability to characterize fluorescence generated with such low input flux is truly exciting application-wise with implications in imaging and microscopy, and further ETPEF experiments have been conducted.[43,44] The ETPEF study by Varnavski *et al* yielded results showing ETPA fluorescence has a nonmonotonic dependence on the delay between signal and idler beams.[43] Multiple chromophores were probed in this study and each exhibited different intensities of ETPA fluorescence that correlate to their measured ETPA cross-sections, implying differences in selective biphoton absorption and the ETPA origin of this emission. This is motivation to further understand the mechanisms that govern the interaction of entangled photon pairs with matter.

1.4. Quantum Interferometry with Entangled Photon Pairs

While there has been a lot of interest in the topic of entangled two-photon absorption spectroscopy, researchers have also been interested in other methods that take advantage of the photon correlations of quantum light in spectroscopy. Quantum interferometry is one such avenue to be exploited and as a result there has been great enthusiasm towards the possibility of using the quantum interference of entangled light as a means to obtain further spectroscopic information about organic and biological molecules. Optical interferometry in general is a useful technique for measuring optical phases and has been employed for numerous

applications from white light interferometry for measuring chromatic dispersion[45], medical imaging with optical coherence tomography[46] and laser interferometer gravitational-wave detectors for precise measurements of minute distances.[47] These methods usually rely on classical interference making them single photon processes, but when correlated photons are employed, quantum advantages can be achieved leading to higher sensitivity, limiting systematic errors and providing enhanced resolution.[48,49]

Quantum interferometry with entangled light states has been thoroughly studied and is now commonly employed in quantum optics particularly for metrology and quantum light characterization. Nonclassical light states can be used in different interferometric regimes such as the Hanbury-Brown-Twiss (HBT) and Hong-Ou-Mandel (HOM) interferometers. As was discussed in section 1.3.1, the HBT interferometer is used to determine the correlation and anticorrelation effects of a light source and connects these to the spatial and temporal coherence properties of the source.[50] Thus, HBT experiments have become a standard for measuring the quantum nature of the field and the purity of the single photon source. The HOM interferometer consists of a two-photon interference effect that measures the indistinguishability of photon pairs.[51] After its initial demonstration by Hong, Ou and Mandel in 1987[51], this two-photon interference effect has since been implemented in quantum information protocol for Bell state tests[52] and quantum logic operations.[53]

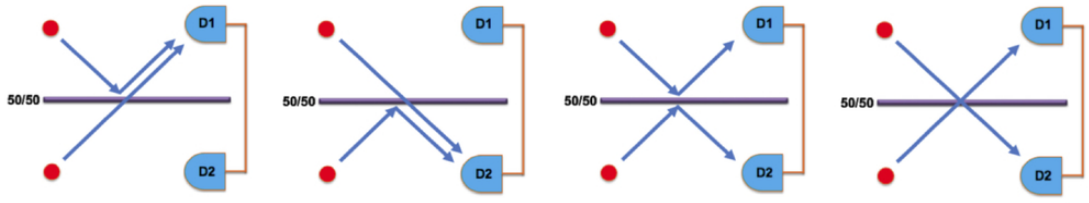

Figure 1.7. *Four possible pathways that photons from opposite arms in the interferometer can take at a 50/50 beamsplitter. Photons will interfere with each other if they are indistinguishable and destructively interfere.*[54]

An HOM interferometer measures the quantum interference resulting from the interference of probability amplitudes of 4 different two-photon Feynman paths, when indistinguishable photons are incident on a 50/50 beam splitter as shown in Figure 1.7. In the latter two pathways, where both photons are transmitted (TT) or both photons are reflected (RR), the indistinguishability of the pathways causes pathway entanglement. Hence, these two pathways destructively interfere and only the first two pathways where both photons exit the same port are measurable, leading to null coincidence counts. This HOM interference dip can be explained mathematically considering the beam splitter operators as given by Szoke *et al*.[55] The beam splitter operators, $\hat{B}_a$ and $\hat{B}_b$, act on the bosonic creation operators $\hat{a}^\dagger$ and $\hat{b}^\dagger$(for photons at ports a and b) to give the unitary transformation of an input state at input ports a/b of the beam splitter to the output states in ports, c/d:[55]

$$\hat{a}^\dagger \xrightarrow{\hat{B}_a} \frac{1}{\sqrt{2}}\left(\hat{c}^\dagger + i\hat{d}^\dagger\right), \qquad \hat{b}^\dagger \xrightarrow{\hat{B}_b} \frac{1}{\sqrt{2}}\left(i\hat{c}^\dagger + \hat{d}^\dagger\right), \tag{Eq. 1.36}$$

$$\hat{B}_a|1\rangle_a = \hat{B}_a\hat{a}^\dagger|0\rangle_a = \frac{1}{\sqrt{2}}(|1\rangle_c|0\rangle_d + i|0\rangle_c|1\rangle_d) \tag{Eq. 1.37}$$

$$\hat{B}_b|1\rangle_b = \hat{B}_b\hat{b}^\dagger|0\rangle_b = \frac{1}{\sqrt{2}}(i|1\rangle_c|0\rangle_d + |0\rangle_c|1\rangle_d). \tag{Eq. 1.38}$$

Where $\hat{a}^\dagger$, $\hat{b}^\dagger$, $\hat{c}^\dagger$ and $\hat{d}^\dagger$ are the creation operators for photons in ports a, b, c and d respectively, acting on the vacuum state $|0\rangle$ and the beam splitter introduces a phase shift of $\pi/2$ in the output state of the reflected photons. If a pair of entangled photons is introduced at input ports a and b:

$$\hat{B}_a\hat{B}_b|1\rangle_a|1\rangle_b = \frac{1}{2}\left(\hat{c}^\dagger + i\hat{d}^\dagger\right)\left(i\hat{c}^\dagger + \hat{d}^\dagger\right)|0\rangle_c|0\rangle_d).$$

$$= \frac{1}{2}\left(i\hat{c}^{\dagger 2} + \hat{c}^\dagger\hat{d}^\dagger - \hat{d}^\dagger\hat{c}^\dagger + i\hat{d}^{\dagger 2}\right)|0\rangle_c|0\rangle_d). \tag{Eq. 1.39}$$

As a result of the phase shift, there is a commutator term in the middle of equation 1.39. Since the photons are indistinguishable, the commutation for these creation operators at the beam splitter output is equals to zero,

$$\left[\hat{c}^{\dagger}, \hat{d}^{\dagger}\right] = \left[\hat{c}^{\dagger}\hat{d}^{\dagger} - \hat{d}^{\dagger}\hat{c}^{\dagger}\right] = 0. \qquad \text{Eq. 1.40}$$

Thus, the first and last terms of equation 1.39 remain, that is, where both photons are at output c or both photons are at output d (RT and TR terms). The state that remains is:

$$= \frac{1}{2}\left(i\hat{c}^{\dagger 2} + i\hat{d}^{\dagger 2}\right)|0\rangle_c|0\rangle_d) = \frac{1}{\sqrt{2}}(i|2\rangle_c|0\rangle_d + |0\rangle_c|2\rangle_d). \qquad \text{Eq. 1.41}$$

Such a state is commonly referred to as a N00N state where $|N\rangle|0\rangle + |0\rangle|N\rangle$ i.e. a superposition of N particles in mode c and 0 particles in mode d, and N particles in mode d and 0 particles in mode c. As such, only one of the two detectors will measure a detection and there will therefore be no coincidence count reading. These leads to the signature HOM interference "dip" in the coincidence counts. This effect can only be seen with a 50/50 beam splitter, as an asymmetric beam splitter would result in an interference that is not completely destructive.

The pathway entanglement is created in the commutator in Eq. 1.39 because the photons are indistinguishable. Entangled photons are indistinguishable when they have the same defining quantum states such as frequency and polarization. Thus, if the photons become more distinguishable due to a change in parameters, the interference will decrease and the commutation relation will no longer be equal to zero, resulting in a change in the depth of the dip. Furthermore, any modification to the photons or light-matter interaction will lead to a modification in the commutator. This phenomenon of HOM interferometry can be better understood by considering photons which are distinguishable via some parameter, for example polarization. Assume these two photons are identical in other properties such as time and

frequency but have orthogonal polarizations, H and V. If $\hat{c}_j^\dagger$ and $\hat{d}_j^\dagger$ are bosonic creation operators in beam splitter output modes, c and d, the output state of the photons after exiting the beam splitter is[56]

$$\left|\psi^{out}\right\rangle_{cd} = \frac{1}{2}\left(\hat{c}_H^\dagger \hat{c}_V^\dagger + \hat{c}_V^\dagger \hat{d}_H^\dagger - \hat{c}_H^\dagger \hat{d}_V^\dagger - \hat{d}_H^\dagger \hat{d}_V^\dagger\right)|0\rangle_{cd} \quad \text{Eq. 1.42}$$

$$= \frac{1}{2}(|1;H\rangle_c|1;V\rangle_c + |1;V\rangle_c|1;H\rangle_d - |1;H\rangle_c|1;V\rangle_d - |1;H\rangle_d|1;V\rangle_d). \quad \text{Eq. 1.43}$$

The first term in Eq. 1.43 contains both photons in mode c similar to the fourth term which contains both photons in mode d. Therefore, the first and fourth terms will lead to null coincidences as both photons arrive at the same detector. The second and third terms contain only one photon in each mode c and d, but each with a either a horizontal or vertical polarization and $\left[\hat{c}_V^\dagger \hat{d}_H^\dagger - \hat{c}_H^\dagger \hat{d}_V^\dagger\right] \neq \left[\hat{c}^\dagger \hat{d}^\dagger - \hat{d}^\dagger \hat{c}^\dagger\right]$. The coincidence probability can be computed from the probability amplitudes in front of these middle terms with only one photon at each output port. The coincidence probability of detecting one photon in each output mode then becomes $p = |1/2|^2 + |-1/2|^2 = 1/2$.[56] Therefore, there is a 50% chance of both counters detecting a photon.

On the other hand, two photons with the same polarization would result in a different outcome. If all other properties of the two photons are the same and they have the same polarization, H, these photons would be indistinguishable. Therefore, their output state would be:[56]

$$|\psi^{out}\rangle_{cd} = \left(\hat{c}_H^\dagger \hat{c}_H^\dagger + \hat{c}_H^\dagger \hat{d}_H^\dagger - \hat{c}_H^\dagger \hat{d}_H^\dagger - \hat{d}_H^\dagger \hat{d}_H^\dagger\right)|0\rangle_{cd} \quad \text{Eq. 1.44}$$

$$= \left(\hat{c}_H^\dagger \hat{c}_H^\dagger - \hat{d}_H^\dagger \hat{d}_H^\dagger\right)|0\rangle_{cd} \quad \text{Eq. 1.45}$$

$$= \frac{1}{\sqrt{2}}(|2;H\rangle_c - |2;H\rangle_d) \quad \text{Eq. 1.46}$$

In this case, the two middle terms of the output state equal zero because the commutator $\left[\hat{c}_H^\dagger \hat{d}_H^\dagger - \hat{c}_H^\dagger \hat{d}_H^\dagger\right] = 0$, but the state comes out normalized since $(\hat{a}^\dagger)^n|0\rangle = \sqrt{n!}\,n\rangle$. In equation 1.45, the first tern has both photons in mode c and the second term has both photons in mode d, while there are no terms containing one photon in each mode due to the commutator $\left[\hat{c}_H^\dagger, \hat{d}_H^\dagger\right]$. Since all photons were of the same polarization and the remaining terms are shown in Eq. 1.46, the coincidence probability of detecting a photon at each detector now is $p = 0$. Clearly, it is not possible to detect coincidence counts and this leads to the coincidence counts dropping to zero and creating an HOM "dip".

Grice and Walmsley described the HOM process theoretically using the electric fields. The field operators at the two detectors can be described as given by Grice and Walmsley by [57]

$$\hat{E}_1^{(+)}(t) = \frac{1}{\sqrt{2}}\left[\hat{E}_o^{(+)}(t) + \hat{E}_e^{(+)}(t+\delta\tau)\right]$$

$$\hat{E}_2^{(+)}(t) = \tfrac{1}{\sqrt{2}}\left[\hat{E}_o^{(+)}(t) - \hat{E}_e^{(+)}(t+\delta\tau)\right] \qquad \text{Eq. 1.47}$$

where the photons are o- and e- polarized, t represents time and $\delta\tau$ is the relative delay between the two photons of the entangled pair. Therefore the probability of detecting one photon at the first detector at some time t_1 and one photon at the second detector at time t_2 becomes [57]

$$P_{12}(t_1, t_2; \delta\tau) = \langle \hat{E}_1^{(-)}(t_1)\hat{E}_2^{(-)}(t_2)\hat{E}_2^{(+)}(t_2)\hat{E}_1^{(+)}(t_1)\rangle \qquad \text{Eq. 1.48}$$

and the average coincident counting rate (as a function of the relative delay) at the detectors is then[57]

$$R_c(\delta\tau) = \tfrac{1}{T}\int\int_0^T dt_1 dt_2 P_{12}(t_1, t_2; \delta\tau) \qquad \text{Eq. 1.49}$$

where T is the coincidence module detection window. This can be written in terms of the pump envelope function $\alpha(\omega_o + \omega_e)$ and the phase matching function $\Phi(\omega_o, \omega_e)$ which symbolize the energy and momentum conservation of the SPDC process:[57]

$$R_c(\delta\tau) \propto \int\int d\omega_o d\omega_e |\alpha(\omega_o + \omega_e)|^2 \left[|\Phi(\omega_o, \omega_e)|^2 - \Phi(\omega_o, \omega_e)\Phi^*(\omega_e, \omega_o) e^{-i(\omega_e - \omega_o)\delta\tau}\right]. \quad \text{Eq. 1.50}$$

This expression considers the change in the coincidence count rate as a function of the relative delay. The first term is an integration over the two-photon probability distribution and is proportional to the probability of observing photons from the SPDC process. The second term changes depending on the magnitude of $\delta\tau$. With large $\delta\tau$, the second term makes no contribution to the integral and the coincidence rate is set by the first term. Therefore, at large relative delay times between the photons of the entangled pair, the coincident count rate is constant. However, as $\delta\tau$ goes to zero, the second term increases and the coincidence rate drops, approaching zero as $\delta\tau$ approaches zero. Since the two-photon wave function is rectangular in time due to the sine cardinal frequency spectrum of the SPDC photons, the convolution of the two rectangular wave functions (one for each photon) results in a triangle. This gives the resulting coincidence drop, known as the HOM dip, its signature triangular shape, a depiction of which is shown in Figure 1.8.

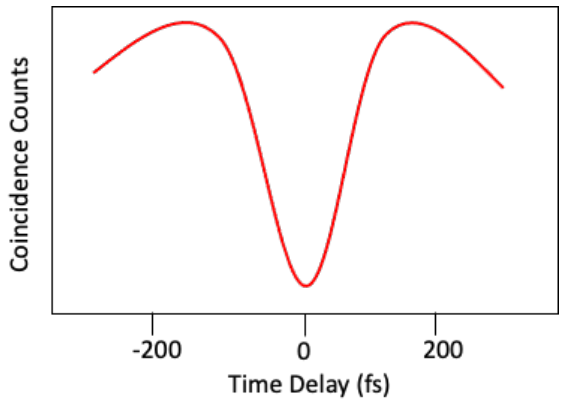

Figure 1.8. *Diagram of HOM signal showing coincidence count rate as a function of delay time.*

Due to its unique properties, researchers have grown interested in exploiting quantum interference in HOM setups towards further optical characterization of a variety of systems.

Dispersion cancellation effects of the HOM phenomenon have been paramount to methods such as quantum optical coherence tomography and quantum metrology.[58] In these methods, the laws of quantum mechanics are used to maximize the information extracted from a material under study.[48] Typically, interferometric techniques are utilized throughout physics to estimate optical phases (ϕ). By using quantum light in the form of N00N states, the precision and resolution of these methods are improved by the reduction of statistical errors due to quantum noise and the ability to beat the shot noise limit. Quantum methods usually allow a precision enhancement equivalent to the square root of the number N of entangled particles.[59] Therefore using two entangled photon states, quantum interferometry measurements can be enhanced by a factor of $\sqrt{2}$.[59]

So far, studies involving quantum interferometry with samples have been employed mainly in metrology and tomography. For instance, quantum optical coherence tomography (QOTC) utilizes the quantum effects of entangled pairs to provide resolution enhancements in measuring optical sections and thicknesses of samples. In QOTC, reflective samples are placed in one arm of the interferometer and a reflection coefficient or sample reflectivity function is obtained as the interferometer reflects off the layers of the sample.[60] As such, HOM dips are obtained at different positions for different reflections of the sample and provide the sample thickness and refractive index. A drawback to this technique is that it can only be used with reflective samples and as a result in order to measure non-reflective materials, they must be coated with thin reflective substances such as gold nanoparticles to enhance reflectivity.[60]With QOTC, the measurement involves physical penetration of the sample as opposed to excitation of the sample's energy levels. As such the wavelength used to probe the material is not tailored to the material's excitation wavelengths and is solely chosen to reduce scattering effects. Since

the QOTC technique does not involve exciting the sample, it does not involve the sample's electronic states and therefore only measures physical properties, but not electronic properties.

1.4.1. HOM Interferometry for Spectroscopy

As further studies have been carried out on quantum beatings observed in HOM oscillations[61,62] and the influence additional phases acquired by the photons have on HOM shapes,[63] proposals have been made for using HOM interferometers for spectroscopy.[29,64] It is of importance to consider what the effects are of exciting samples placed in an HOM interferometer path, how this alters the observed HOM dip if at all and what information can be gained from this interaction. A light-matter interaction with one photon of the biphoton pair will affect the indistinguishability of the photon pathways. Therefore, the HOM dip should carry a signature of the light-matter interaction that has been experienced and measuring the modifications should be able to offer spectroscopic information.[55] While proposals and previous studies have shown that exciting narrow linewidth, non-sensitive inorganic materials with entangled photons in an HOM interferometer can be achieved,[64] the question remains whether this can be extended to more sensitive organic and biological chromophores which typically have broader linewidths. Due to the higher sensitivity of quantum interferometers compared to classical, such spectroscopy could lead to measurements with better precision from this quantum advantage. As such, we wish to explore this by employing HOM interferometry to determine molecular properties of organic systems. With this experiment, I seek to determine whether the low intensity of photons in an HOM interferometer can indeed excite a sample placed in its path and result in an observable alteration to the HOM signal. Furthermore, I wish to look at what this

interference between the molecular states and the photons of half the entangled pair will result in when the photons recombine with their analog photons from the opposite path.

In addition to properly setting up the HOM interferometer, it is important to understand how this process of spectroscopy will work both experimentally and theoretically. The experiment involves a resonant absorbing medium being placed in one arm of the interferometer for transmission of the propagating signal photons. As the sample is resonant with the entangled photons, the transmission will result in a coherent excitation of the sample related to its susceptibility, ($\chi^{(1)}$). This light-matter interaction will cause a modification to the signal photons determined by the susceptibility, resulting in a phase shift for the different frequency components of the sample. At the beam splitter, the idler beam will experience the aforementioned $\pi/2$ phase shift, which is independent of frequency. This compensates for the shift caused by the molecular interaction in the opposite path and introduces a time shift to the HOM dip when photons from both paths recombine at the beam splitter. However, the quantum interference between the signal photons and the molecular states leads to a frequency dependent shift in one arm while there is a non-frequency dependent shift in the other. Thus, the idler beam cannot fully compensate the acquired phase modification in the signal beam and the HOM dip loses its symmetry, resulting in a change to the shape of the dip. Since the asymmetry of the dip is caused by the group delay contribution from the sample's coherent excitation, the asymmetry lasts for a duration related to the dephasing time, T_2, of the resonant absorption. If the experiment captures this phase shift and asymmetry, the dephasing time of this excitation can then be extracted from the measurement.

With the correct theoretical formalism, the observed experimental HOM results can be appropriately analyzed to interpret the light-matter interaction and understand how it relates to the sample. We have worked closely with theorists from Professor Shaul Mukamel's group at the University of California, Irvine to interpret this experiment. By displaying how the light-matter interaction is encoded in the coincidence counting rate, the information pertaining to the sample in the dip can be extracted. The output modes of the beam splitter are given by the beam splitter unitary transformation and described by the photon operators, $c(\omega), d(\omega)$ as:[65]

$$\begin{pmatrix} c(\omega) \\ d(\omega) \end{pmatrix} = \frac{1}{\sqrt{2}} \begin{pmatrix} 1 & i \\ i & 1 \end{pmatrix} \begin{pmatrix} a_s{}'(\omega) \\ a_i{}'(\omega) \end{pmatrix}. \qquad \text{Eq 1.51}$$

These exiting beams travel to the photon detectors where they are measured in coincidence, giving the coincidence counting rate ($R_c(\tau)$) as a function of the optical delay, τ, between the two photon beams as follows:[65,66]

$$R_c(\tau) = A \int_{-T_w/2}^{T_w/2} dt \left\langle d^\dagger(t) c^\dagger(t+\tau) c(t+\tau) d(t) \right\rangle \qquad \text{Eq 1.52}$$

where T_w is the detection window and the constant A depends on the incoming photon flux, the efficiency of the photon detectors, and propagation losses. $c(\omega), d(\omega)$ ($c^\dagger(\omega), d^\dagger(\omega)$) are the boson annihilation (creation) operators corresponding to the photon modes detected by the two detectors which are joined in coincidence. Using the joint spectral amplitude, $f(\omega_s, \omega_i)$, which depends on the entangled biphoton state, and how it becomes modified by the sample's transmission, the coincidence counting rate can be rewritten to incorporate the features of the entangled light field and the molecule under study. The entangled biphoton twin state generated by SPDC can be written as[65]

$$|\Phi\rangle = \int \int d\omega_s d\omega_i f(\omega_s, \omega_i) a_s{}^\dagger(\omega_s) a_i{}^\dagger(\omega_i) |0_s, 0_i\rangle, \qquad \text{Eq 1.53}$$

where the joint spectral amplitude (JSA) is $f(\omega_s, \omega_i) = \alpha(\omega_s + \omega_i)\beta(\omega_s - \omega_i)$ with $\alpha(\omega_s + \omega_i)$ being the pump envelope and $\beta(\omega_s - \omega_i)$ the phase-matching conditions. In the twin state, ${a_s}^{\dagger}(\omega)$ and $a_s(\omega)$ $[({a_i}^{\dagger}(\omega), a_i(\omega)]$ are the creation and annihilation operators respectively for the signal [and idler] modes. When the signal beam propagates through the sample, it is modified by the sample's matter transmission amplitude $T(\omega)$, and the signal mode $a_s(\omega)$ becomes:[65]

$$a_s'(\omega) = T(\omega)a_s(\omega) + \eta(\omega) \qquad \text{Eq 1.54}$$

($\eta(\omega)$ is the quantum noise associated with the absorption process). This transmission function contains susceptibility, thus, the signal mode and subsequently, the effective JSA are modified by the light-matter interaction leading to an altered JSA of $f(\omega_s, \omega_i)T(\omega_s)$.

From Eq. 1.50, where the coincidence counting rate, R_c, is written in terms of the pump envelope and phase matching functions, it is clear that in the case of our experiment, the rate can similarly be written in these terms, i.e. including the JSA. Thus, $R_c(\tau)$ from equation 1.52 can be written as:[65,66]

$$R_c(\tau) = A\left(\frac{1}{2} - \frac{1}{2}\iint d\omega d\omega' f^*(\omega, \omega')\, f(\omega', \omega)T^*(\omega')T(\omega)e^{i(\omega - \omega')\tau}\right). \qquad \text{Eq. 1.55}$$

If there is no sample in place or there is a medium which is transparent to the entangled light, the transmission function $T(\omega) = 1$ and the HOM dip is symmetric around the zero delay as is generally expected. However, the introduction of a resonant sample into the interferometer path causes the JSA to be modified by the sample's transmission. Therefore, the coincidence rate in Eq. 1.55 depends not only on the JSA relating to the light field, but also on the sample's susceptibility. As it now contains matter information, specifically the full linear susceptibility of the molecule, it can be used to determine the optical properties of the molecule. For example, the linear susceptibility (χ) can be linked to the dephasing

time for a molecular response dominated by a single resonance with a Lorentzian model for a 2-level system as:

$$\chi(\omega) = \frac{\alpha}{\omega - \Omega - i/T_2}. \quad \text{Eq. 1.55}$$

In this equation, α is a constant related to the length and concentration of the sample and Ω is the frequency of the resonant transition. By connecting this to the coincidence rate, the HOM data can be modelled to extract the dephasing time parameter.

The goal of this work in the context of this dissertation is to setup a proof-of-concept experiment where the objectives are four-fold. First to confirm that the HOM signal is responsive to sensitive organic samples that typically have broader linewidths than inorganic structures with narrow resonances, and are more susceptible to inhomogeneous broadening which might make subtle changes to the signal harder to perceive. Secondly, the obtained HOM signal through the resonant sample should reproduce the shift and asymmetry that has been predicted by theory. Third, the experimentally obtained dip through the organic dye should be able to be fit with data pertaining to the sample to confirm it carries molecular information. Lastly, if the experimental data can be used to extract the dephasing time, it confirms that the experimental setup can be used for time-resolved measurements. All these will have much broader implications across spectroscopy as the experiment is applied in different fields and for nonlinear measurements.

By setting up a working experiment and properly analyzing these results, we may open doors to a new form of quantum spectroscopy. The experiment is increasingly promising for the opportunities of spectroscopy with quantum light it gives rise to. It can be used to study organic systems with interesting excitation properties or systems that undergo symmetry breaking such as quantum emitters. It can also be applied to sensitive

biological systems of interest to biologists and biophysicists, to study protein dynamics and molecular coherence. Mainly, the experiment can be extended to nonlinear spectroscopic measurements with quantum advantages. The experiment can be modified with the introduction of an external beam, causing a steady state excitation in the medium while the entangled photons are utilized as a probe. In essence, with an external beam exciting the sample in the HOM path, a highly sensitive pump-probe system can be devised adapting the setup into a non-linear experiment using entangled light and its advantages. Additionally, the experiment can be modified in such a way that the entire biphoton pair interacts with the sample, leading to an entangled two-photon excitation with entangled light that probes higher order interactions while employing the control knobs and sensitivity offered by quantum pairs, enabling us to characterize and manipulate a molecule's optical responses with extremely low probing power. The frequencies of the photons, $f(\omega_s, \omega_i)$ can be tuned to observe the molecular optical response to different wavelengths. In this dissertation, for the first time, interferometry with quantum entangled photons is used to provide a sensitive characterization of electronic properties of organic molecules. This experiment can be expanded to nonlinear measurements taking advantage of the strong correlations and high sensitivity of entangled photons, thus leading to more sensitive measurements in a variety of chemistry, biology and material science fields. Thus, this is an important contribution to this dissertation.

1.5. Overview of subsequent chapters

This dissertation looks at different methods involving quantum entangled photon pairs in the characterization and understanding of optical properties of organic molecules. In some

cases, this is combined with classical spectroscopy to gain a wider picture of the molecular properties and discern what enhancements quantum light may provide. Additionally, theoretical calculations are utilized to better understand and explain the experimental findings.

Chapter 2 has a comprehensive breakdown of most of the experimental and theoretical techniques that are used throughout this work along with their theory. The two experimental works that were developed more during the dissertation research will be in separate chapters. In chapter 3, I investigate the optical properties of thienoacene molecules with different central atoms and provide a basis for the comparison of the linear, two-photon and entangled two-photon properties in molecules with varying dipolar or quadrupolar character. Classical TPA cross-sections are compared to entangled TPA cross-sections obtained via both absorption and fluorescence experiments and it is shown that the transition pathway used upon excitation has an effect on the ETPA process and ETPA is more sensitive to excitation pathway, thus providing higher resolution than classical experiments.

Chapter 4 is an extensive analysis of the entangled two-photon excited fluorescence (ETPEF) process and the molecular and experimental parameters necessary to observe it. ETPEF was first suggested theoretically and over the past seven years, experimental realizations have been attained in various forms. ETPEF is an extremely difficult experimental method as the emission signals to be observed are low. Thus, it is important to understand what contributes to successful ETPEF experiments. In this chapter, an in-depth look at the ETPEF setup is given and the optimization of fluorescence signal observation above noise levels. Theoretical calculations are carried out to compare the molecular parameters of molecules that have and have not provided good ETPEF signals. These results show that in addition to high transition dipole properties, resonance between the excited states and entangled photons is

extremely important for observing ETPEF. With these results, future researchers can tailor either experimental or molecular parameters in order to achieve the quantum advantage offered by entangled photon fluorescence.

In Chapter 5, entangled two-photon spectroscopy in addition to classical spectroscopic methods are used to study the optical properties of organic molecules for photovoltaic applications. Here, we use the nonmonotonic behavior of entangled two-photon absorption to understand organic molecules' virtual-electronic-state interactions with entangled photons. Comparing this to classical time-resolved and non-linear spectroscopy, this permits us to obtain the energies of virtual states contributing to two-photon excitations and learn more about the dynamics of these materials.

In Chapter 6 we shift gears from entangled two-photon absorption and examine another avenue for using entangled photon pairs for spectroscopy via Hong-Ou-Mandel interferometry. The goal of this study is to utilize the coherent excitation of a sample placed in the HOM interferometer path to gain information about the sample's molecular properties, specifically, the sample's dephasing time. This can be deduced by studying how the presence of the sample changes the HOM coincidence dip position and shape and applying the necessary theoretical modeling to extract the dephasing time. The chapter involves a detailed description of the HOM interferometer and how it was built. This investigation offers a new opportunity for characterizing and controlling organic molecule's coherent response with high sensitivity, all at extremely low probing power. The final chapter, Chapter 7 ends the dissertation with a summary of the studies and conclusions as well as future prospects for expanding the investigations carried out in the field of entangled photon spectroscopy.

References

(1) Web of Science Citation Report on Quantum Information Science.

(2) Saleh, B. E. A.; Jost, B. M.; Fei, H. B.; Teich, M. C. Entangled-Photon Virtual-State Spectroscopy. *Phys. Rev. Lett.* **1998**, *80* (16), 3483–3486. https://doi.org/10.1103/PhysRevLett.80.3483.

(3) Fei, H. B.; Jost, B. M.; Popescu, S.; Saleh, B. E. A.; Teich, M. C. Entanglement-Induced Two-Photon Transparency. *Phys. Rev. Lett.* **1997**, *78* (9), 1679–1682. https://doi.org/10.1103/PhysRevLett.78.1679.

(4) Kojima, J.; Nguyen, Q. V. Entangled Biphoton Virtual-State Spectroscopy of the A 2Σ +- X 2Π System of OH. *Chem. Phys. Lett.* **2004**, *396* (4–6), 323–328. https://doi.org/10.1016/j.cplett.2004.08.051.

(5) Javanainen, J.; Gould, P. L. Linear Intensity Dependence of a Two-Photon Transition Rate. *Phys. Rev. A* **1990**, *41* (9), 5088–5091. https://doi.org/10.1103/PhysRevA.41.5088.

(6) Lee, D. I.; Goodson, T. Entangled Photon Absorption in an Organic Porphyrin Dendrimer. *J. Phys. Chem. B* **2006**, *110* (51), 25582–25585. https://doi.org/10.1021/jp066767g.

(7) Harpham, M. R.; Süzer, Ö.; Ma, C. Q.; Bäuerle, P.; Goodson, T. Thiophene Dendrimers as Entangled Photon Sensor Materials. *J. Am. Chem. Soc.* **2009**, *131* (3), 973–979. https://doi.org/10.1021/ja803268s.

(8) Guzman, A. R.; Harpham, M. R.; Süzer, Ö.; Haley, M. M.; Goodson, T. G. Spatial Control of Entangled Two-Photon Absorption with Organic Chromophores. *J. Am. Chem. Soc.* **2010**, *132* (23), 7840–7841. https://doi.org/10.1021/ja1016816.

(9) Upton, L.; Harpham, M.; Suzer, O.; Richter, M.; Mukamel, S.; Goodson, T. Optically Excited Entangled States in Organic Molecules Illuminate the Dark. *J. Phys. Chem. Lett.* **2013**, *4* (12), 2046–2052. https://doi.org/10.1021/jz400851d.

(10) Einstein, A.; Podolsky, B.; Rosen, N. Can Quantum-Mechanical Description of Physical Reality Be Considered Correct? *Phys. Rev.* **1935**, *47*, 777–780. https://doi.org/10.1007/s10701-010-9411-9.

(11) Horodecki, R.; Horodecki, P.; Horodecki, M.; Horodecki, K. Quantum Entanglement. *Rev. Mod. Phys.* **2009**, *81* (2), 865–942. https://doi.org/10.1103/RevModPhys.81.865.

(12) Abouraddy, A. F.; Saleh, B. E. A.; Sergienko, A. V.; Teich, M. C. Degree of Entanglement for Two Qubits. *Phys. Rev. A* **2001**, *64* (5), 4. https://doi.org/10.1103/PhysRevA.64.050101.

(13) Schlawin, F.; Mukamel, S. Two-Photon Spectroscopy of Excitons with Entangled Photons. *J. Chem. Phys.* **2013**, *139* (24). https://doi.org/10.1063/1.4848739.

(14) Muthukrishnan, A.; Agarwal, G. S.; Scully, M. O. Inducing Disallowed Two-Atom Transitions with Temporally Entangled Photons. *Phys. Rev. Lett.* **2004**, *93* (9), 1–4. https://doi.org/10.1103/PhysRevLett.93.093002.

(15) Kim, Y. H.; Grice, W. P. Measurement of the Spectral Properties of the Two-Photon State Generated via Type-II Spontaneous Parametric down-Conversion. *Opt. InfoBase Conf. Pap.* **2005**, *30* (8), 908–910.

(16) Fu, J.; Padilha, L. A.; Hagan, D. J.; Van Stryland, E. W.; Przhonska, O. V.; Bondar, M. V.; Slominsky, Y. L.; Kachkovski, A. D. Molecular Structure—Two-Photon Absorption Property Relations in Polymethine Dyes. *J. Opt. Soc. Am. B* **2007**, *24* (1), 56. https://doi.org/10.1364/josab.24.000056.

(17) Reinhardt, B. A.; Brott, L. L.; Clarson, S. J.; Dillard, A. G.; Bhatt, J. C.; Kannan, R.; Yuan, L.; He, G. S.; Prasad, P. N. Highly Active Two-Photon Dyes: Design, Synthesis, and Characterization toward Application. *Chem. Mater.* **1998**, *10* (7), 1863–1874. https://doi.org/10.1021/cm980036e.

(18) Cheng, L. T.; Tam, W.; Stevenson, S. H.; Meredith, G. R.; Rikken, G.; Marder, S. R. Experimental Investigations of Organic Molecular Nonlinear Optical Polarizabilities. 1. Methods and Results on Benzene and Stilbene Derivatives. *J. Phys. Chem.* **1991**, *95* (26), 10631–10643. https://doi.org/10.1021/j100179a026.

(19) Marder, S. R.; Perry, J. W.; Bourhill, G.; Gorman, C. B.; Tiemann, B. G.; Mansour, K. Relation Between Bond-Length Alternation and Second Electric Hyperpolarizability of Conjugated Organic Molecules. *Science (80-.).* **1993**, *261* (12), 186–189.

(20) Geskin, V. M.; Lambert, C.; Brédas, J. L. Origin of High Second- and Third-Order Nonlinear Optical Response in Ammonio/Borato Diphenylpolyene Zwitterions: The Remarkable Role of Polarized Aromatic Groups. *J. Am. Chem. Soc.* **2003**, *125* (50),

15651–15658. https://doi.org/10.1021/ja035862p.

(21) Bartkowiak, W.; Zaleśny, R.; Leszczynski, J. Relation between Bond-Length Alternation and Two-Photon Absorption of a Push-Pull Conjugated Molecules: A Quantum-Chemical Study. *Chem. Phys.* **2003**, *287* (1–2), 103–112. https://doi.org/10.1016/S0301-0104(02)00982-5.

(22) Meyers, F.; Marder, S. R.; Pierce, B. M.; Brédas, J. L. Electric Field Modulated Nonlinear Optical Properties of Donor-Acceptor Polyenes: Sum-Over-States Investigation of the Relationship between Molecular Polarizabilities (α,β, and γ.) and Bond Length Alternation. *J. Am. Chem. Soc.* **1994**, *116* (23), 10703–10714. https://doi.org/10.1021/ja00102a040.

(23) Ye, C.; Zhou, L.; Wang, X.; Liang, Z. Photon Upconversion: From Two-Photon Absorption (TPA) to Triplet-Triplet Annihilation (TTA). *Phys. Chem. Chem. Phys.* **2016**, *18* (16), 10818–10835. https://doi.org/10.1039/c5cp07296d.

(24) Mandel, L. Fluctuations of Photon Beams: The Distribution of the Photo-Electrons. *Proc. Phys. Soc.* **1959**, *74* (233–243).

(25) Basset, M. G.; Setzpfandt, F.; Steinlechner, F.; Beckert, E.; Pertsch, T.; Gr, M. Perspectives for Applications of Quantum Imaging. *Laser Photon. Rev.* **2019**, *13* (1900097), 1–24. https://doi.org/10.1002/lpor.201900097.

(26) Glauber, R. J. The Quantum Theory of Optical Coherence. *Phys. Rev.* **1963**, *130* (6), 2529–2539.

(27) Paul, H. Photon Antibunching. *Rev. Mod. Phys.* **1982**, *54* (4), 1061–1102.

(28) Stevens, M. J.; Characteristics, S. *Photon Statistics , Measurements , and Measurements Tools Chapter Outline*; Elsevier Inc., 2013; Vol. 45. https://doi.org/10.1016/B978-0-12-387695-9.00002-0.

(29) Li, H.; Piryatinski, Srimath Kandada, A.R.; Silva, C.; Bittner, E. R. Photon Entanglement Entropy as a Probe of Many-Body Correlations and Fluctuations. *J. Chem. Phys.* **2019**, *150* (184106), 1–10. https://doi.org/10.1063/1.5083613.

(30) Leuchs, G. Photon Statistics, Antibunching and Squeezed States. In *Frontiers in Nonequilibrium Statistical Physics*; Moore, G. T., Scully, M. O., Eds.; New York, 1986; p 329.

(31) Beck, M. Comparing Measurements of g(2)(0) Performed with Different Coincidence

Detection Techniques. *J. Opt. Soc. Am. B* **2007**, *24* (12), 2972–2978.

(32) Hanbury Brown, R.; Twiss, R. Q. Correlation between Photons in Two Coherent Beams of Light. *Nature* **1956**, *177*, 27–29. https://doi.org/10.1007/BF03010401.

(33) Shih, Y. Entangled Biphoton Source - Property and Preparation. *Reports Prog. Phys.* **2003**, *66*, 1009–1044.

(34) Shih, Y. H.; Sergienko, A. V.; Rubin, M. H.; Kiess, T. E.; Alley, C. O. Two-Photon Entanglement in Type-II Parametric down-Conversion. *Phys. Rev. A* **1994**, *50* (1), 23–28. https://doi.org/10.1103/PhysRevA.50.23.

(35) Sergienko, A. V.; Shih, Y. H.; Rubin, M. H. Experimental Evaluation of a Two-Photon Wave Packet in Type-II Parametric Downconversion. *J. Opt. Soc. Am. B* **1995**, *12* (5), 859. https://doi.org/10.1364/josab.12.000859.

(36) Gea-Banacloche, J. Two-Photon Absorption of Nonclassical Light. *Phys. Rev. Lett.* **1989**, *62* (14), 1603–1606. https://doi.org/10.1103/PhysRevLett.62.1603.

(37) Georgiades, N. P.; Polzik, E. S.; Edamatsu, K.; Kimble, H. J.; Parkins, A. S. Nonclassical Excitation for Atoms in a Squeezed Vacuum. *Phys. Rev. Lett.* **1995**, *75* (19), 3426–3429. https://doi.org/10.1103/PhysRevLett.75.3426.

(38) Dayan, B.; Pe'er, A.; Friesem, A. A.; Silberberg, Y. Two Photon Absorption and Coherent Control with Broadband Down-Converted Light. *Phys. Rev. Lett.* **2004**, *93* (2), 1–4. https://doi.org/10.1103/PhysRevLett.93.023005.

(39) Lee, D.; Goodson III, T. Entangled Photon Absorption in an Organic Porphyrin Dendrimer. *J. Phys. Chem. B* **2006**, *110*, 25582–25585. https://doi.org/10.1021/jp066767g.

(40) Harpham, M. R.; Goodson III, T. Thiophene Dendrimers as Entangled Photon Sensor Materials. *J. Am. Chem. Soc. Artic.* **2018**, No. 21, 973–979.

(41) Villabona-monsalve, J. P.; Caldero, O.; Portela, M. N.; Valencia, A. Entangled Two Photon Absorption Cross Section on the 808 Nm Region for the Common Dyes Zinc Tetraphenylporphyrin and Rhodamine B. *J. Phys. Chem. A* **2017**, 7869–7875. https://doi.org/10.1021/acs.jpca.7b06450.

(42) Villabona-monsalve, J. P.; Varnavski, O.; Palfey, B. A.; Goodson III, T. Two-Photon Excitation of Flavins and Flavoproteins with Classical and Quantum Light. *J. Am. Chem. Soc. Commun.* **2018**, *140*, 14562–14566. https://doi.org/10.1021/jacs.8b08515.

(43) Varnavski, O.; Pinsky, B.; Goodson, T. Entangled Photon Excited Fluorescence in Organic Materials: An Ultrafast Coincidence Detector. **2017**, 6–11. https://doi.org/10.1021/acs.jpclett.6b02378.

(44) Tabakaev, D.; Montagnese, M.; Haack, G.; Bonacina, L.; Zbinden, H.; Thew, R. T. Energy-Time Entangled Two-Photon Molecular Absorption. *Phys. Rev. A* **2021**, *103* (033701), 1–5.

(45) Lee, J. Y.; Kim, D. Y. Versatile Chromatic Dispersion Measurement of a Single Mode Fiber Using Spectral White Light Interferometry. *Opt. Express* **2006**, *14* (24), 11608. https://doi.org/10.1364/oe.14.011608.

(46) White, B. R.; Pierce, M. C.; Nassif, N.; Cense, B.; Park, B. H.; Tearney, G. J.; Bouma, B. E.; Chen, T. C.; de Boer, J. F. In Vivo Dynamic Human Retinal Blood Flow Imaging Using Ultra-High-Speed Spectral Domain Optical Doppler Tomography. *Opt. Express* **2003**, *11* (25), 3490. https://doi.org/10.1364/oe.11.003490.

(47) Abramovici, A.; Althouse, W. E.; Drever, R. W. P.; Gürsel, Y.; Kawamura, S.; Raab, F. J.; Shoemaker, D.; Sievers, L.; Spero, R. E.; Thorne, K. S.; Vogt, R. E.; Weiss, R.; Whitcomb, S. E.; Zucker, M. E. LIGO: The Laser Interferometer Gravitational-Wave Observatory. *Science (80-.).* **1992**, *256* (5055), 325–333. https://doi.org/10.1126/science.256.5055.325.

(48) Spagnolo, N.; Aparo, L.; Vitelli, C.; Crespi, A.; Ramponi, R.; Osellame, R.; Mataloni, P.; Sciarrino, F. Quantum Interferometry with Three-Dimensional Geometry. *Sci. Rep.* **2012**, *2*, 1–6. https://doi.org/10.1038/srep00862.

(49) Kaiser, F.; Vergyris, P.; Aktas, D.; Babin, C.; Labonté, L.; Tanzilli, S. Quantum Enhancement of Accuracy and Precision in Optical Interferometry. *Light Sci. Appl.* **2018**, *7* (3), 17163. https://doi.org/10.1038/lsa.2017.163.

(50) Hong, S.; Riedinger, R.; Marinkovi, I.; Wallucks, A.; Hofer, S. G.; Norte, R. A.; Aspelmeyer, M.; Gröblacher, S. Hanbury Brown and Twiss Interferometry of Single Phonons from an Optomechanical Resonator. *Science (80-.).* **2017**, *358*, 203–206.

(51) Hong, C.K.; Ou, Z.Y.; Mandel, L. Measurement of Subpicosend Time Intervals between Two Photons by Interference. *Phys. Rev. Lett.* **1987**, *59* (18), 2044–2046.

(52) Bouwmeester, D.; Pan, J. W.; Mattle, K.; Eibl, M.; Weinfurter, H.; Zeilinger, A. Experimental Quantum Teleportation. *Nature* **1997**, *390*, 575–579.

(53) Pittman, T. B.; Jacobs, B. C.; Franson, J. D. Demonstration of Nondeterministic Quantum Logic Operations Using Linear Optical Elements. *Phys. Rev. Lett.* **2002**, *88* (25), 4. https://doi.org/10.1103/PhysRevLett.88.257902.

(54) Serafini, J. R.; Spiecker, D.; Steidle, J.; Preble, S.; Hach, E.; Tisson, C.; Fanto, M.; Alsing, P.; Smith, M. On-Chip Demonstration of Hong-Ou-Mandel Effect Using Quantum-Optical Ring Resonators. *SPIE* **2019**, *10984*. https://doi.org/10.1117/12.2523582.

(55) Szoke, S.; Liu, H.; Hickam, B. P.; He, M.; Cushing, S. K. Entangled Light-Matter Interactions and Spectroscopy. *J. Mater. Chem. C* **2020**, *Advance Ar*. https://doi.org/10.1039/d0tc02300k.

(56) Brańczyk, A. M. Hong-Ou-Mandel Interference. *arXiv* **2017**, 1–17.

(57) Grice, W. P.; Walmsley, I. A. Spectral Information and Distinguishability in Type-II down-Conversion with a Broadband Pump. *Phys. Rev. A* **1997**, *56* (2), 1627–1634.

(58) Abouraddy, A. F.; Nasr, M. B.; Saleh, B. E. A.; Sergienko, A. V.; Teich, M. C. Quantum-Optical Coherence Tomography with Dispersion Cancellation. *Phys. Rev. A* **2002**, *65* (5), 6. https://doi.org/10.1103/PhysRevA.65.053817.

(59) Giovannetti, V.; Lloyd, S.; Maccone, L. Quantum-Enhanced Measurements : Beating the Standard Quantum Limit. *Science (80-.).* **2004**, *306*, 1330–1337.

(60) Graciano, P. Y.; Michel, A.; Martínez, A.; Lopez-mago, D.; Castro-olvera, G.; Rosete-aguilar, M.; Garduño-mejía, J. Interference Effects in Quantum- Optical Coherence Tomography Using Spectrally Engineered Photon Pairs. **2019**, No. February, 1–14. https://doi.org/10.1038/s41598-019-45088-0.

(61) Specht, H. P.; Bochmann, J.; Mücke, M.; Weber, B.; Figueroa, E.; Moehring, D. L.; Rempe, G. Phase Shaping of Single-Photon Wave Packets. *Nat. Photonics* **2009**, *3* (8), 469–472. https://doi.org/10.1038/nphoton.2009.115.

(62) Chen, Y.; Fink, M.; Steinlechner, F.; Torres, J. P.; Ursin, R. Hong-Ou-Mandel Interferometry on a Biphoton Beat Note. *npj Quantum Inf.* **2019**, No. February, 1–6. https://doi.org/10.1038/s41534-019-0161-z.

(63) Mazzotta, Z.; Cialdi, S.; Cipriani, D.; Olivares, S.; Paris, M. G. A. High-Order Dispersion Effects in Two-Photon Interference. *Phys. Rev. A* **2016**, *94* (6), 1–6. https://doi.org/10.1103/PhysRevA.94.063842.

(64) Kalashnikov, D. A.; Melik-gaykazyan, E. V; Kalachev, A. A.; Yu, Y. F.; Kuznetsov, A. I.;

Krivitsky, L. A. Quantum Interference in the Presence of a Resonant Medium. *Sci. Rep.* **2017**, *7*, 1–8. https://doi.org/10.1038/s41598-017-11694-z.

(65) Eshun, A.; Gu, B.; Varnavski, O.; Dorfman, K. E.; Asban, S.; Mukamel, S.; Goodson III, T. Investigations of Molecular Optical Properties Using Quantum Light and Hong-Ou-Mandel Interferometry". *Submitted* **2021**.

(66) Dorfman, K. E.; Asban, S.; Gu, B.; Mukamel, S. Hong-Ou-Mandel Interferometry and Spectroscopy Using Entangled Photons. *Submiss.*

Chapter 2
Experimental Techniques and Methods

2.1 Overview

In this chapter, the experimental and theoretical techniques that are used throughout this dissertation are discussed. These techniques were used to elucidate different optical properties of the materials investigated. By understanding the functions of these methods and what information they are used to obtain, the reader will be better familiarized with their purpose and the results provided throughout the dissertation. Additionally, the techniques here are discussed in detail such that the reader will be well-versed enough in them as they appear in subsequent chapters. Those techniques that were built or specially optimized for this work will be discussed more comprehensively in their separate chapters.

2.2 Steady State Spectroscopy

Steady state spectroscopic methods are used to understand the initial optical properties of the system under study. Two steady state spectroscopy techniques were used, UV-Visible absorption spectroscopy and fluorescence spectroscopy. These methods provide information on the basic linear optical properties of the molecule. UV-Visible absorption involves the measurement of the absorbed electromagnetic radiation as a function of wavelength/frequency. As the name suggests, this method considers absorption in the ultraviolet to visible (UV-vis) range of the electromagnetic spectrum which is from 200-800nm. Absorption spectroscopy in this region is commonly referred to as electronic spectroscopy. When a material interacts with

light of an energy that corresponds to the energy of a specific atomic or molecular orbital transition, this light will be absorbed, and the electrons of the atom or molecule are promoted from a low energy ground state to a higher energy excited state. As such, certain corresponding wavelengths of light are necessary to achieve these transitions. For the molecules I studied in this dissertation, all absorption occurs in the UV-vis range and can be measured by uv-vis spectrometers. Beer-Lambert's law (Eq. 2.1) gives an explanation of the transitions measured by steady state absorption.[1] This law states that there is a relationship between the attenuation of light of a substance and the properties of that substance. Specifically, the absorption of light by the sample (A) is the ratio of the absorbed light intensity, I, over the initial intensity of light that interacts with the sample I_0. This can be written in terms of the molecular properties, where the absorbance is proportional to the sample's concentration, $[C]$, its path length, l, and the molar extinction coefficient, ε, which is a sample dependent property that measures the extent of light absorption at a particular wavelength.

$$A = \log\left(\frac{I_0}{I}\right) = \varepsilon[C]l. \qquad \text{Eq 2.1}$$

The concentration of a sample in solution is given in M (L^{-1}), the extinction coefficient in $M^{-1}cm^{-1}$ and the path length in cm which gives a unitless absorption. The spectrophotometer measures the ratio between the initial input light intensity (I_0) and the absorbed or attenuated light (I). In order to determine whether the light was absorbed by the sample or lost to other light-matter interactions such as scattering, diffraction, refraction and reflection, a background scan is taken of the solvent in which the sample is dissolved.[1] This accounts for the refractive index and any additional interactions that could occur in the measurement medium. Absorption spectroscopy also provides qualitative information about the sample such as sample

degradation, as well as the interaction between the material and its environment, as charge transfer species are sensitive to the nature of the solvent.[2]

The absorption measurements done in this thesis were carried out with a *Agilent model 8453* spectrophotometer with deuterium-discharge and tungsten lamps, providing light in the range 200 – 1100 nm (UV to near infrared region). Lenses focus the light onto the sample, and again to collimate the transmitted light through the slit to the grating for detection by the diode array (Figure 2.1). The concave holographic grating is responsible for dispersion and spectral imaging and the photodiode array has a wavelength range from 190 to 1100 nm in order to capture the full UV-Vis absorption spectrum. The sample solution (and solvent) is held in a quartz cuvette manufactured by Starna cells, with a path length of 1cm x 0.4cm.

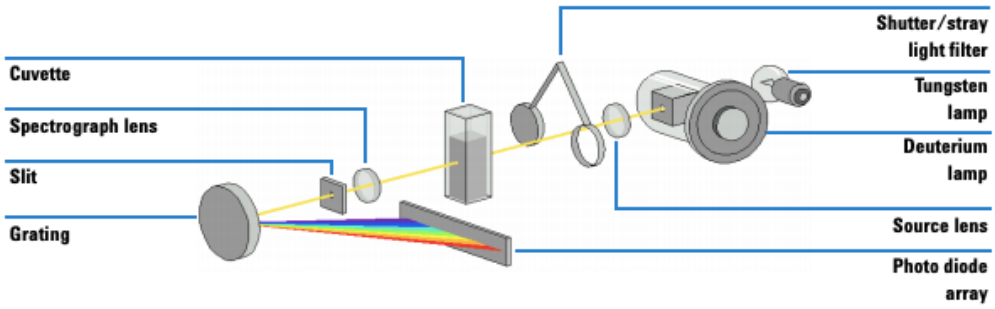

Figure 2.1. *Diagram of the Agilent 8453 UV-Vis spectrophotometer scheme (Agilent 8453 UV-Visible Spectroscopy System Service Manual).*

The second steady state absorption method that was used in this dissertation is fluorescence spectroscopy. The fluorescence is the process where a molecule in an excited state loses absorbed energy and relaxes to the lower energy vibrational levels of the ground state, resulting in the emission of photons. The re-emitted photons are of a longer energy (therefore longer wavelength) than the excitation photon due to energy loss to vibrational modes. Steady state fluorescence (or emission) measurements provide information about the quantum efficiency of

the material, that is the ratio of photons emitted to photons absorbed. As there are competing relaxation or energy radiation mechanisms in addition to fluorescence, knowing the quantum efficiency gives an idea of whether mostly emissive or non-emissive processes are taking place.[3–5] A material's quantum efficiency is measured by its quantum yield, Φ and the fluorescence intensity, I_{fl}, in terms of quantum yield is given by:

$$I_{fl} = I_0 \cdot \Phi \cdot l \cdot \mathcal{E} \cdot [C] \qquad \text{Eq. 2.2}$$

The fluorescence quantum yield can be determined by a method developed by Williams *et al*[6] now commonly referred to as the Williams comparative method. In this method, a standard with an already known quantum yield with similar steady state properties to the sample under study is used for comparison. The quantum yield can be calculated with the following equation:

$$\Phi_x = \Phi_{std} \frac{Grad_x}{Grad_{std}} \cdot \frac{{\eta_x}^2}{{\eta_{std}}^2}, \qquad \text{Eq. 2.3}$$

where the suffix std refers to the standard and x to the sample, η are the refractive indices and $Grad$ are the slopes of linear plots of the integrated area of fluorescence against concentration. In the quantum yield experiment, solutions of the sample and standard are prepared at decreasing concentrations and the emission of each sample is measured with a fluorimeter. It is these emission areas that are integrated to obtain the plots of fluorescence vs concentration. In order not to saturate the fluorimeter, optical densities of the sample are kept at 0.1 and below (low concentration).

The fluorescence spectra measurements in this dissertation were carried out with Spex Fluoromax-2 and Spex-Fluoromax 4 spectrofluoremeters by Horiba. In both systems, the excitation source is a xenon lamp which produces light from the 190 – 2000 nm range. An excitation spectrometer after the excitation source has a diffraction grating allowing for

selective single wavelength excitation and has adjustable excitation slits to select the intensity of light excitation on the investigated material. The sample is placed after this spectrometer in a Starna Cell quartz cuvette and the emission is collected with a photomultiplier tube (PMT) positioned at a 90∘ angle to the excitation source. Gratings on the emission spectrometer before the signal detection at the PMT are used to choose specific emission wavelengths to be monitored which is useful for efficient wavelength collection. A photon counting amplifier amplifies the signal and sends it to a computer to be recorded. The spectrum of emission intensity is given as a function of wavelength. This process is carried out for both the sample and standard at at least three concentrations and the emission spectra are integrated to calculate the sample quantum yield.

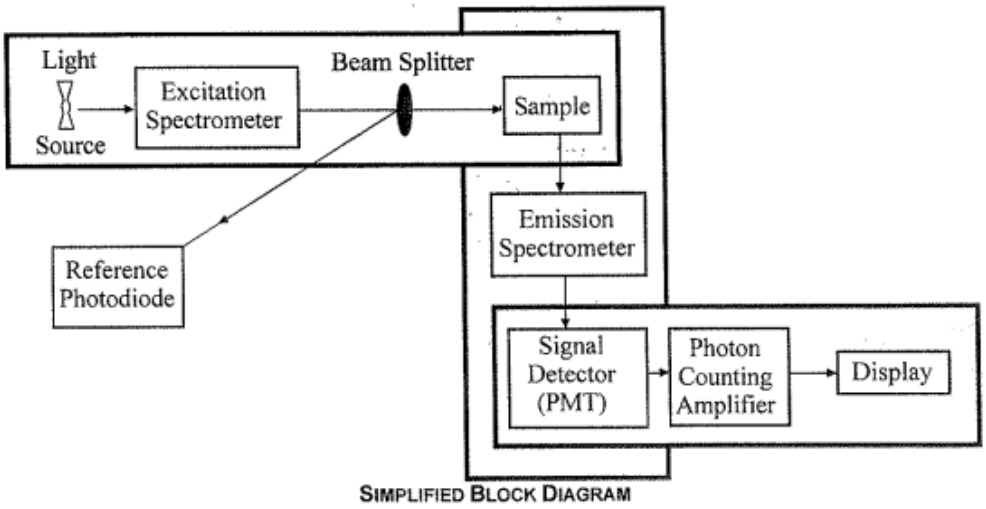

***Figure 2.2**. Block diagram schematic of the Spex Fluoromax-2* Spectrofluoremeter *(Horiba Scientific FluoroMax-2 with DataMax Manual).*

According to Kasha's rule, which has been applied to fluorescence spectroscopy, for most organic molecules, fluorescence will only occur from the lowest lying excited state irrespective of the electronic state the molecule has been excited to.[7] This is a result of the fast

internal conversion relaxation from higher-lying excited states. As such, even though the absorption mechanisms may differ for two-photon and one-photon absorption, the excitation results in the emission of fluorescence photons with the same fluorescence quantum yield that would be obtained with one-photon absorption. Additionally, Vavilov's rule states that the quantum yield of photoluminescence is generally independent of the excitation wavelength.[8] Thus, quantum yields measured with one-photon excitation are used for calculations with two-photon excitation in this work.

2.3 Classical Two-Photon Absorption

As discussed thoroughly in Chapter 1 Section 1.2, two-photon absorption (TPA) is the process whereby a molecule is excited from its ground state to a higher energy level excited state by the sequential absorption of two photons with energy the sum of the excitation. For instance, two photons of 800nm each are simultaneously absorbed by the material resulting in a 400nm absorption. The relaxation process from this two-photon excited state is similar to that from a single photon absorption as the emission occurs from the lowest lying excited state, therefore two-photon excited fluorescence is commonly used for TPA measurements.[9]

TPA cross-sections given in GM (Goeppert-Mayer) can be measured by two-photon excited fluorescence (TPEF) which entails measuring the fluorescence emission resulting from the TPA process. This experimental method takes advantage of the square intensity-dependence of TPA. In conducting TPEF measurements, the laser intensity is adjusted, and the subsequent fluorescence is measured. Due to the squared intensity dependence of the TPA rate, a log-log plot of log fluorescence intensity against log laser power intensity leads to a linear

plot with a slope of 2 and easily determines whether a material is TPA active or not. From this experiment, the TPA cross-section can be calculated using the following expression:

$$F(t) = \frac{1}{2}\eta\delta[C]\Phi\frac{g_p}{\pi f\lambda\tau}\varphi\langle P(t)\rangle^2. \quad \text{Eq. 2.4}$$

$F(t)$ is the emitted TPEF photons collected per second, η is the refractive index of the solvent, δ is the TPA cross-section, $[C]$ is the molecule's concentration, Φ is the sample's fluorescence quantum yield, $g_p$is the shape factor of the pulsed laser, f is the laser frequency, λ is the excitation wavelength, τ is the pulse duration, φ is the collection efficiency and $P(t)$ is the input intensity. The experiment is first conducted with a standard dye in order to calculate the relative TPA cross-section of the sample and this allows for the laser parameters to be removed from Eq. 2.4. The log of Eq. 2.4 is given as:

$$log[F(t)] = 2log[\langle P(t)\rangle] + log\left[\frac{1}{2}\eta\delta[C]\Phi\frac{g_p}{\pi f\lambda\tau}\varphi\right], \quad \text{Eq. 2.5}$$

which is now in the linear form $y = mx + b$ and the argument of the 3rd log term is the y-intercept, b, of the linear log-log plot. Since the standard (std) with known TPA cross-section is compared to the sample (x) both experiments utilize the same input power, i.e.

$$2log[\langle P(t)\rangle]_x = 2log[\langle P(t)\rangle]_{std}, \quad \text{Eq. 2.6}$$

The following equality can be obtained for the fluorescence intensities and y-intercepts of the sample and the standard:

$log[F(t)]_x - b_x = log[F(t)]_{std} - b_{std}$, Eq 2.7

Eq. 2.7 can be further simplified to obtain an exponential relationship that considers both sample and standard:

$\frac{[F(t)]_x}{[F(t)]_{std}} = 10^{(b_x - b_{std})}$ Eq. 2.8

If the log of the input power is zero, $F(t)$ is equal to b and it can be substituted into Eq. 2.8 to obtain an expression for calculating the classical cross-section (Eq. 2.11)

$$\frac{\left[\frac{1}{2}\eta_x\delta_x[C_x]\Phi_x\frac{gp}{\pi f\lambda\tau}\varphi\right]}{\left[\frac{1}{2}\eta_{std}\delta_{std}[C_{std}]\Phi_{std}\frac{gp}{\pi f\lambda\tau}\varphi\right]} = 10^{(b_x-b_{std})} \qquad \text{Eq. 2.9}$$

$$\frac{[\eta_x\delta_x[C_x]\Phi_x]}{[\eta_{std}\delta_{std}[C_{std}]\Phi_{std}]} = 10^{(b_x-b_{std})} \qquad \text{Eq. 2.10}$$

$$\delta_x = 10^{(b_x-b_{std})}\frac{\eta_{std}\delta_{std}[C_{std}]\Phi_{std}}{\eta_x[C_x]\Phi_x} \qquad \text{Eq. 2.11}$$

In equation 2.11, the TPA cross-section of the sample can be calculated with all the known variables for the sample and the standard, the refractive indices, η, concentrations $[C]$, fluorescence quantum yields, Φ, the cross-section of the standard, δ_{std} and the y-intercept obtained from the linear log (power) vs log (counts).

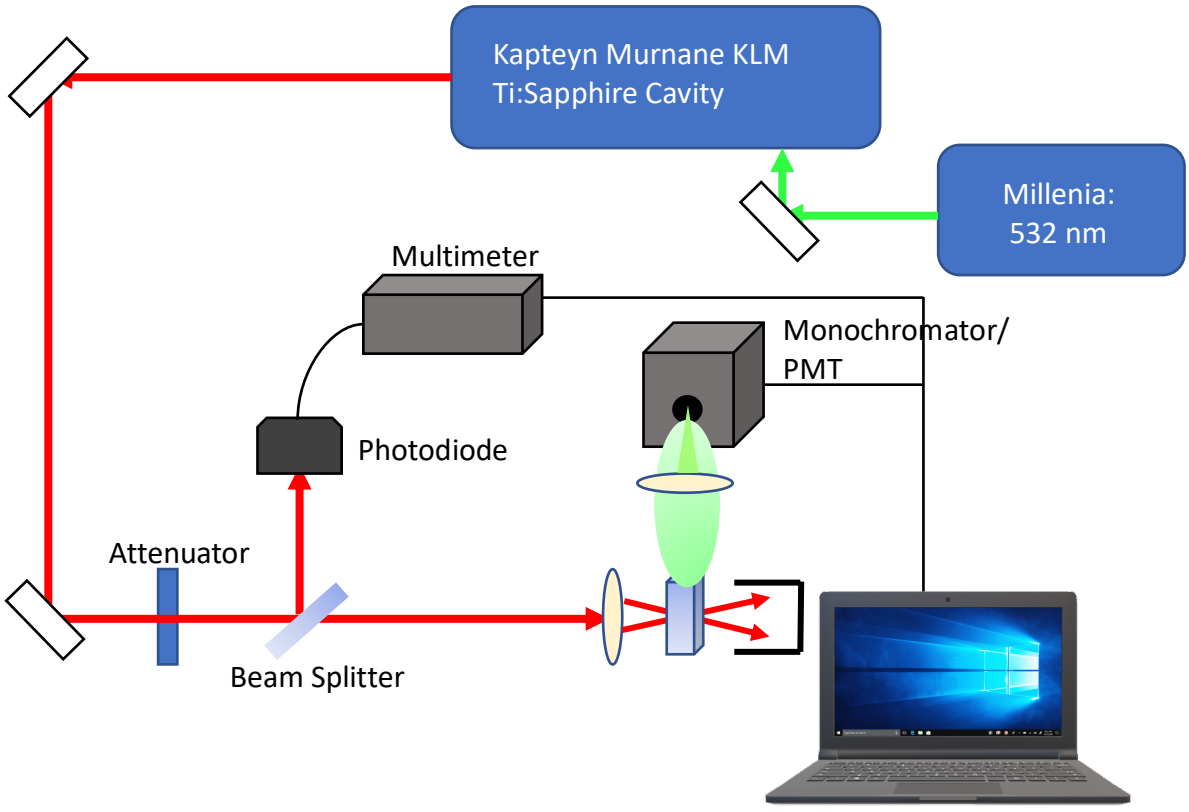

Figure 2.3 *Schematic of TPEF setup for classical TPA measurements.*

The TPEF setup (Fig. 2.3) uses a mode-locked Ti:Sapphire laser (Spectra-Physics Millenia) with 100fs pulses and a repetition rate of 80MHz. The laser is tuned to 800nm and focused on dilute solutions of the sample. Samples are placed in Starna Cells quartz cuvettes with a 1cm path length. A power dependence scan is performed by using a circular neutral density filter to adjust input power. A beam splitter after the neutral density filter reflects a percentage of the beam onto a photodiode which is connected to a multimeter for power reference measurements. The transmitted beam is focused onto the sample with a collimating lens and the resultant fluorescence collected perpendicular to the incident beam using a Hamamatsu photomultiplier tube and photocounting unit. The photocounting unit is set to the maximum emission wavelength of the sample by a Newport Oriel Cornerstone monochromator. The log of the emission intensity vs the log of the input power provides a linear plot with a slope of 2. Factors such as beam alignment and laser stability may affect the slope but, in most cases, the slope lies between 1.8 and 2.

2.4 Entangled Two-Photon Absorption

Entangled two-photon absorption (ETPA) was discussed in detail in Chapter 1 and was a major part of works in this dissertation. The linear dependence of ETPA was utilized in measuring the ETPA cross-section of different organic molecules. As ETPA employs low light intensities, ETPA measurements require precise alignment in order to detect ETPA signals and distinguish them from noise or other scattering mechanisms. In this dissertation, ETPA is measured via two methods, transmission and fluorescence. The fluorescence method will be explained more comprehensively in chapter 4. The total TPA absorption rate of a substance is given by:[10]

$$R_{TPA} = \sigma_e \phi + \delta_r \phi^2 \quad \text{Eq. 2.12}$$

where σ_e is the ETPA cross-section, δ_r is the classical or random TPA cross-section and ϕ is the input photon flux. At lower flux values, the ETPA term which is the linear term dominates. Therefore, by staying in the low photon flux regime, the ETPA rate can be measured by transmission through the sample, measuring the absorbed photon rate as a function of the input flux.

As there is a linear dependence of the ETPA rate on the input flux, the cross-section can be calculated from the linear absorption relation as follows:

$$I_{out} = I_{in} \times exp\left(-\frac{\sigma_e N_A [C] L}{1000}\right) \quad \text{Eq. 2.13}$$

where I_{in} and I_{out} are the input and output flux respectively, N_A is Avogadro's number, $[C]$ is the sample molar concentration and L is the path length in cm. The value I_{in} is the photon count rate through the solvent alone as this constitutes a background or blank reading of the intensity through the sample. I_{out} is the count rate through the sample dissolved in solvent. If the absorption is small, an approximation can be made and the absorption rate, A, can be calculated as:

$$A = I_{in} - I_{out} = I_{in} \times \frac{\sigma_e N_A [C] L}{1000} \quad \text{Eq. 2.14}$$

From Eq. 2.14, the ETPA cross-section is then:

$$\sigma_e = \frac{A}{I_{in}} = \times \frac{1000}{N_A [C] L}. \quad \text{Eq. 2.15}$$

In this equation, A/I_{in} is the relative absorption rate which is the slope of the linear fit of the absorption rate as a function of the input flux. Thus, the unit of ETPA cross-section is cm^2/molecule. This method of measuring ETPA cross-section was first used by Dong-Ik Lee[11] and later used in multiple studies.[12–15]

In our ETPA setup, entangled photons are generated using a mode-locked Ti:Sapphire laser with 100fs pulses at 80MHz repetition rate and a 12nm FWHM centered at 800nm. A 1mm thick β-Barium Borate (BBO) crystal is used for second harmonic generation (SHG) to produce a beam of 400nm. This beam is then focused onto a 0.5mm BBO crystal that is specifically designed for Type-II spontaneous parametric downconversion (SPDC). The phase-matching conditions for this SPDC are frequency degenerate, therefore entangled photon pairs of 800nm are generated from the 400nm pump ($\omega_1 = \omega_2 = \omega_p/2$). The input flux is altered using a variable neutral density filter with a photodetector as a reference for the input power. The entangled photon beam is focused on the 1mm x 1mm quartz cuvette with a collimating lens and the transmitted beam focused on for detection on a silicon avalanche photodiode (APD) single-photon counting module (Perkin-Elmer SPCM-AQR-13). A CCD camera is used to image SPDC spatial arrangement.

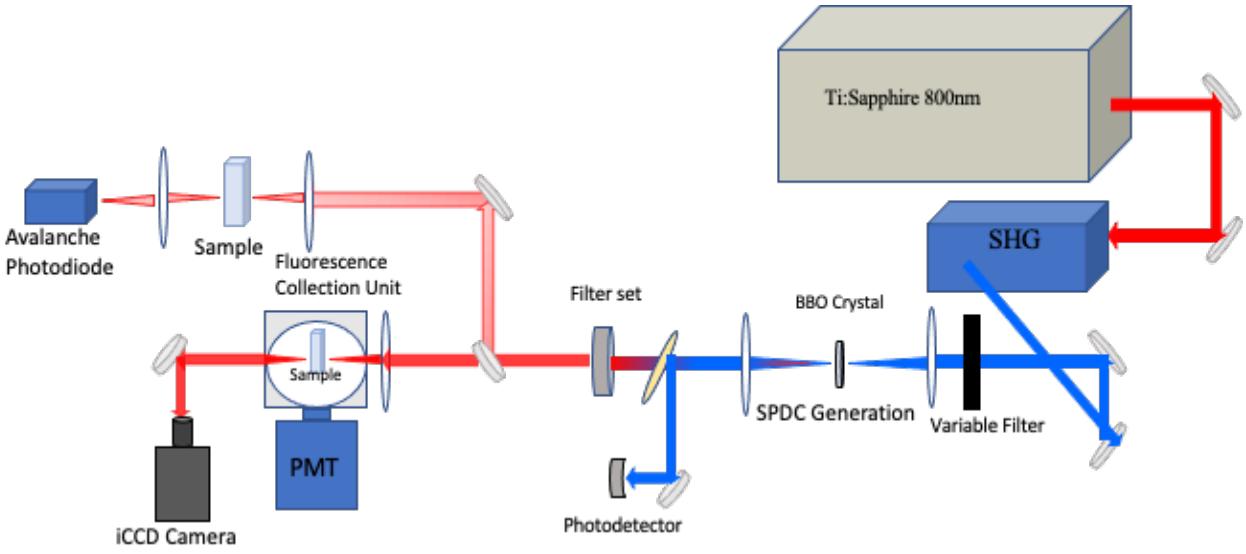

Figure 2.4 *ETPA setup diagram. 800nm pulsed laser pumps a nonlinear crystal for second harmonic generation, creating 400nm pump for SPDC process. The downconverted photons are filtered and use the upper path of the collection system for transmission through the sample for ETPA measurements. Lower path is used for fluorescence measurements.*

For this dissertation work, the transmission pathway was not in place at the start of the project. Therefore, it had to be re-incorporated into the system. The collimating lenses, cuvette holder and APD had to be aligned for transmission. The APD's photon detection efficiency at 800nm is 60% and at 400nm it is 7%. The low efficiency at 400nm aids in ensuring the detected signal is not spurious 400nm light that may not have been cut off by the dichroic mirror or interference filter. The dark count rate from the APD is ~300 photons/s. This accounts for any scattered light that may enter the collection compartment or spurious 400nm light. The active area of the detector is ~175 μm therefore precise focusing onto this spot is necessary. This is enabled by placing the detector on an Ultralign Precision XYZ linear stage and moving the stage as the photon counts are being measured.

Multiple transmission scans were taken with solvent to determine experimental noise and measurement errors. The neutral density filter was checked for thermal lensing and a linear neutral density filter from Thorlabs was decided as the best filter to remove thermal lensing issues. The residuals of solvent scans were kept low and random by aligning the APDs at specific points where residuals seemed systematic. The average raw counts to the APD are $3x10^5$ photons/s to $8x10^6$ photons/s. An instrument correction factor must be applied to the raw APD counts to determine the input flux rate for the absorption measurements. This correction is calculated using a method that was provided by Perkin Elmer in the counter datasheet and takes into consideration the module dead time. Additionally, there is a deviation from linearity that can be caused from saturation effects and this is also taken into consideration. Therefore the input flux rate is calculated as:

$$Corrected\ Rate = \frac{(Output\ Module\ Count\ Rate \times Correction\ Factor) - Dark\ count}{Photon\ Detection\ Efficiency}, \quad \text{Eq. 2.16}$$

where the correction factor has the APD deadtime, t_d and the module count rate, C_R, and can be given as,

$$Correction\ Factor = \frac{1}{1-(t_d \times C_R)}. \quad \text{Eq. 2.17}$$

The APD deadtime can be adjusted between 40 and 60ns and is chosen to be 55ns. Corrected photon count rate usually adjust the raw counts by a factor of ~1.8.

For ETPA measurements, a scan is taken with solvent to serve as the input flux measurement. Another solvent scan is performed to compare to the previous to determine the "background" measurement and confirm there is no extra scattering through the solvent. The change from solvent scan to solvent scan is on the order of ~0.02% of the input photon intensity. The solvent is carefully pipetted out of the cuvette and replaced with the sample in order to maintain the same alignment conditions. The slopes of the solvent and sample scans are different and are subtracted from each other to obtain the linear absorption rate. This is then used to calculate the ETPA cross-section according to equation 2.15.

2.5 Ultrafast Transient Absorption Spectroscopy

Ultrafast transient absorption is a powerful spectroscopic method that provides time-resolved measurements of the excited state dynamics of a system.[16,17] Unlike other spectroscopic methods that have been discussed, transient absorption spectroscopy (TAS) is able to probe dark (non-fluorescent) states. TAS is a pump-probe experiment.[18,19] A monochromatic pump beam excites the system under study and a white light probe beam measures the dynamics of the molecule in its excited state. The probe is delayed in time with respect to the pump in order to obtain time-resolved data. The probe measures the change in absorption of the system in its excited state compared to the initial absorption. This differential

absorption, ΔA, is the excited state absorption minus the ground state absorption.[19] ΔA is given as a function of wavelengths therefore shown as a spectrum. As such, transient data contains information pertaining to ΔA, wavelength and time.

Fast laser pulses allow for the characterization of the ultrafast processes that occur in molecules, usually in the femtosecond to picosecond range.[20] The pump beam excites the sample from the ground state, S_0, to an excited state, S_1. The probe which is delayed relative to the pump, further excites the sample from the S_1 state to higher excited states, S_n. Different signals can be detected via TAS and are observed as either positive or negative ΔA bands. A negative ΔA signal results from either a ground-state bleach (GSB) or stimulated emission (SE). The GSB occurs when there is strong steady state absorption and can be identified by comparing to the steady state absorption spectrum. SE occurs in the regions of the sample's fluorescence emission wavelengths and occurs for optically allowed transitions. A positive ΔA signal is due to excited state absorption (ESA) and is the result of optically allowed transitions from an excited state to higher excited states. Positive ΔA signals can also be due to reactions in the excited state, indicative of energy transfer reactions different species such as charge-separated, isomerized or triplet states.[18,19] These signals are commonly shifted relative to signals observed in the steady state absorption spectrum. The signals and their lifetimes aid in providing an understanding of the dynamic processes occurring in the sample.

In the ultrafast femtosecond transient absorption system, an amplified laser (Spectra Physics Spitfire) with pulse duration of ~100 fs, repetition rate of 1 kHz, and power of 800 mW is directed at a beam splitter to generate the pump (85%) and the probe beams (15%). The pump beam (~66 mJ per pulse) is generated from the second harmonic of the amplifier's output (~800 nm) using a BBO crystal and is focused onto the sample cell (l = 1 mm). The probe

beam is passed through a computer−controlled delay line and focused onto a 2 mm sapphire plate to generate the white light continuum (Helios by Ultrafast Systems Inc.). The white light is focused onto the sample and overlapped with the pump beam. The absorption difference (ΔA) of the signal is collected by a CCD detector (Ocean Optics). Data acquisition is performed with the software Helios by Ultrafast Systems Inc. The IRF is measured by the Raman scattering of water at 466 nm and is found to be 110 fs.

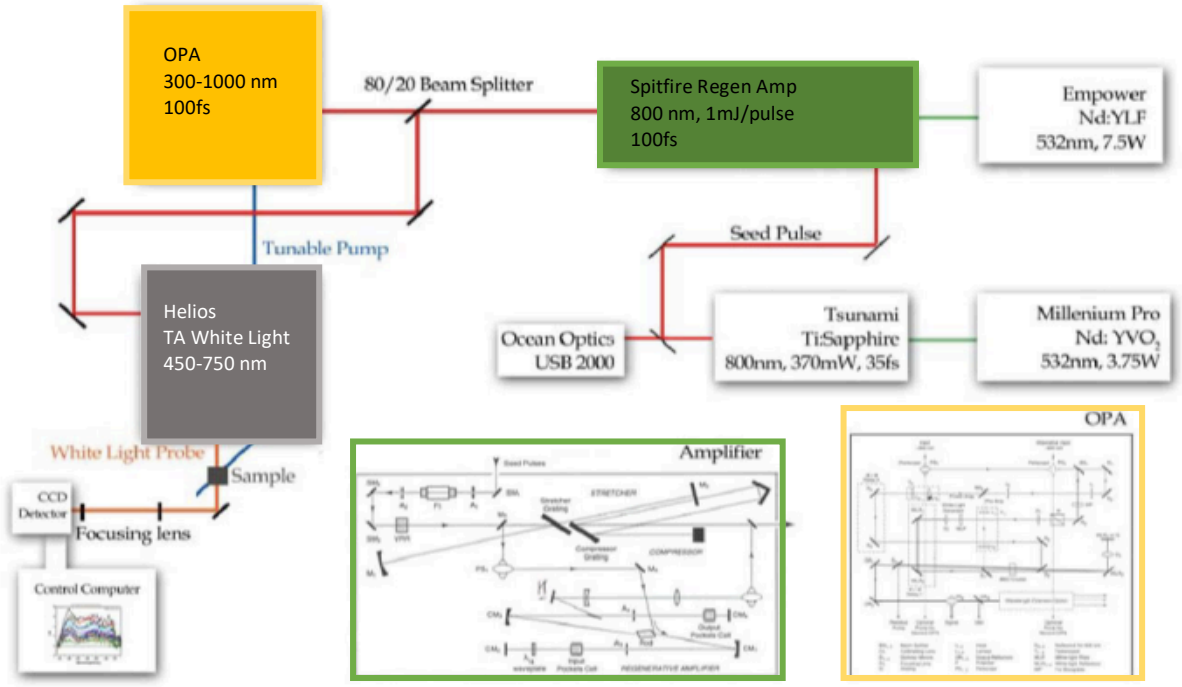

Figure 2.5. *Transient absorption experimental setup.*

2.6 Quantum Chemical Calculations

Density functional theory calculations were performed to determine the electronic structure and excitation properties of the compounds. To make the calculations easier to compute, the heavy side groups of compounds were replaced with methyl groups. These slight modifications were done to save computational time but had no significant effect on the electronic properties

of the compounds. Geometry optimizations and Time Dependent-Density Functional Theory (TD-DFT) calculations to obtain molecular orbitals, transition dipole moments, energy levels and two-photon cross-sections were carried out using the General Atomic and Molecular Electronic Structure Systems (GAMESS) program. Calculations were done with a B3LYP functional and 6-31G (D) basis set.

The geometries of the ground state (S_0) were optimized with the aforementioned basis set in order to perform further calculations. For one-photon absorption (OPA) oscillator strengths and two-photon absorption (TPA) cross-section computations, GAMESS utilized linear and quadratic response theory. These were done with chloroform as a solvent using the polarizable continuum model (PCM). The transition dipole moments from ground state to excited state and between excited states were obtained. The OPA oscillator strengths or transition probabilities from ground state to excited state were given by[21], $f_{OPA} = \frac{2\omega_f}{3}\sum_a |\langle 0|\mu_a|f\rangle|^2$ where ω_f is the excitation energy and μ_a is the dipole moment operator for which a is a Cartesian coordinate. TPA calculations were done assuming a source with linearly polarized light. To compute cross-sections, two-photon transition matrix elements were calculated using transition dipole moments and excitation energies. The two-photon transition matrix elements are:[21]

$$S_{\alpha\beta} = \sum_n \left[\frac{\langle 0|\mu_a|n\rangle\langle n|\mu_\beta|f\rangle}{\omega_n - \frac{\omega_f}{2}} + \frac{\langle 0|\mu_\beta|n\rangle\langle n|\mu_\alpha|f\rangle}{\omega_n - \frac{\omega_f}{2}} \right]$$

where n is an intermediate state between the ground state and final state, f. These elements are used to compute the TPA transition moment, $\delta^{TPA} = \sum_{\alpha\beta}\left[S_{\alpha\alpha}S^*_{\beta\beta} + 2S_{\alpha\beta}S^*_{\alpha\beta}\right]$. This is then used to compute the two-photon cross-section.[21]

References

(1) Swinehart, D. F. The Beer-Lambert Law. *J. Chem. Educ.* **1962**, *39* (7), 333–335. https://doi.org/10.1021/ed039p333.

(2) Kosower, E. M. A New Empirical Measure of Solvent Polarity : Z-Values. *J. Am. Chem. Soc.* **1958**, *80*, 3523–3260.

(3) Weber, G.; Teale, F. W. J. Determination of the Absolute Quantum Yield of Fluorescent Solutions. *Trans. Faraday Soc.* **1957**, *53*, 646–655. https://doi.org/10.1039/tf9575300646.

(4) Weber, G.; Teale, F. W. J. Fluorescence Ecxitation Spectrum of Organic Compounds in Solution. *Trans. Faraday Soc.* **1957**, 640–648.

(5) Würth, C.; Grabolle, M.; Pauli, J.; Spieles, M.; Resch-Genger, U. Comparison of Methods and Achievable Uncertainties for the Relative and Absolute Measurement of Photoluminescence Quantum Yields. *Anal. Chem.* **2011**, *83* (9), 3431–3439. https://doi.org/10.1021/ac2000303.

(6) Rhys Williams, A. T.; Winfield, S. A.; Miller, J. N. Relative Fluorescence Quantum Yields Using a Computer-Controlled Luminescence Spectrometer. *Analyst* **1983**, *108* (1290), 1067–1071. https://doi.org/10.1039/an9830801067.

(7) Kasha, M. Characterization of Electronic Transitions in Complex Molecules. *Discussions of the Faraday Society*. 1950, p 14.

(8) Klán, P.; Wirz, J. *Photochemistry of Organic Compounds : From Concepts to Practice*; John Wiley & Sons, 2009.

(9) Kaiser, W.; Garrett, C. G. B. Two-Photon Excitation in CaF2: Eu2+. *Phys. Rev. Lett.* **1961**, *7* (6), 229–231. https://doi.org/10.1103/PhysRevLett.7.229.

(10) Fei, H. B.; Jost, B. M.; Popescu, S.; Saleh, B. E. A.; Teich, M. C. Entanglement-Induced Two-Photon Transparency. *Phys. Rev. Lett.* **1997**, *78* (9), 1679–1682. https://doi.org/10.1103/PhysRevLett.78.1679.

(11) Lee, D.; Goodson III, T. Entangled Photon Absorption in an Organic Porphyrin Dendrimer. *J. Phys. Chem. B* **2006**, *110*, 25582–25585.

https://doi.org/10.1021/jp066767g.

(12) Harpham, M. R.; Süzer, Ö.; Ma, C. Q.; Bäuerle, P.; Goodson, T. Thiophene Dendrimers as Entangled Photon Sensor Materials. *J. Am. Chem. Soc.* **2009**, *131* (3), 973–979. https://doi.org/10.1021/ja803268s.

(13) Guzman, A. R.; Harpham, M. R.; Suzer, O.; Haley, M. M.; Goodson III, T. G. Spatial Control of Entangled Two-Photon Absorption with Organic Chromophores ¨. *J. Am. Chem. Soc. Commun.* **2010**, *132*, 7840–7841. https://doi.org/10.1021/ja1016816.

(14) Upton, L.; Harpham, M.; Suzer, O.; Richter, M.; Mukamel, S.; Goodson, T. Optically Excited Entangled States in Organic Molecules Illuminate the Dark. *J. Phys. Chem. Lett.* **2013**, *4* (12), 2046–2052. https://doi.org/10.1021/jz400851d.

(15) Villabona-monsalve, J. P.; Caldero, O.; Portela, M. N.; Valencia, A. Entangled Two Photon Absorption Cross Section on the 808 Nm Region for the Common Dyes Zinc Tetraphenylporphyrin and Rhodamine B. *J. Phys. Chem. A* **2017**, 7869–7875. https://doi.org/10.1021/acs.jpca.7b06450.

(16) Gustavsson, T.; Coto, P. B.; Serrano-Andŕs, L.; Fujiwara, T.; Lim, E. C. Do Fluorescence and Transient Absorption Probe the Same Intramolecular Charge Transfer State of 4-(Dimethylamino)Benzonitrile? *J. Chem. Phys.* **2009**, *131* (3). https://doi.org/10.1063/1.3173609.

(17) Kim, D.; Holten, D.; Gouterman, M. Evidence From Picosecond Transient Absorption and Kinetic Studies of Charge-Transfer States in Copper(Ii) Porphyrins. *J. Am. Chem. Soc.* **1984**, *106* (10), 2793–2798. https://doi.org/10.1021/ja00322a012.

(18) Ohkita, H.; Tamai, Y.; Benten, H.; Ito, S. Transient Absorption Spectroscopy for Polymer Solar Cells. *IEEE J. Slected Top. Quantum Electron.* **2016**, *22* (1).

(19) Berera, R.; van Grondelle, R.; Kennis, J. T. M. Ultrafast Transient Absorption Spectroscopy: Principles and Application to Photosynthetic Systems. *Photosynth. Res.* **2009**, *101* (2–3), 105–118. https://doi.org/10.1007/s11120-009-9454-y.

(20) van Amerongen, H.; van Grondelle, R. Understanding the Energy Transfer Function of LHCII, the Major Light-Harvesting Complex of Green Plants. *J. Phys. Chem. B* **2000**, *105*, 604–617. https://doi.org/10.1016/j.ocecoaman.2014.06.011.

(21) Salem, M. A.; Brown, A. Two-Photon Absorption in Fluorescent Protein Chromophores: TDDFT and CC2 Results. *J. Chem. Theory Comput.* **2014**, *10* (8), 3260–3269.

https://doi.org/10.1021/ct500028w.

Chapter 3
Entangled Two-Photon Absorption & Fluorescence in Thienoacene Molecules

This chapter was published as the following document

Eshun, A.; Cai, Z.; Awies, M.; Yu, L.; Goodson III, T. "Investigations of Thienoacene Molecules for Classical and Entangled Two-Photon Absorption" *J. Phys. Chem. A* **2018**, *122*, 8167–8182.

3.1. Abstract

Investigations of the optical effects in thienoacene chromophores with different central atoms were carried out. These chromophores provide a basis for the comparison of the linear, two photon, and entangled two photon properties in organic molecules with varying degree of dipolar or quadrupolar character. Linear absorption and emission as well as time-dependent density functional theory calculations were carried out for the chromophores investigated. Measurements of the classical two photon absorption entangled two photon absorption (ETPA) as well as entangled two photon fluorescence were experimentally carried out for the four chromophores. Electronic structure calculations were utilized in order to provide estimates of the classical two photon absorption coefficients. The results of the measured entangled two photon cross-sections were compared with theoretical estimates for the molecules investigated. It is found that the dipole (transition or permanent) pathway can have an effect on the trends in the entangled photon absorption process in dipolar organic chromophores. This study helps predict the properties of the entangled two photon effect in chromophores with different dipolar and quadrupolar character.

3.2. Introduction

The use of organic materials for the purposes of nonlinear optical (NLO) applications has enjoyed broad interest over more than fifty years.[1–5] These applications with organic NLO effects include the possibility of optical communications, frequency doubling and tripling effects, as well as photorefractive effects.[6–8] Research in this area focused previously on the details of the correlation of the electronic nonlinearities in the polarization with the molecular structure.[9,10] Through a rigorous degree of investigations, many in the field of organic NLO believe the basic structural characteristics in organic molecules which give rise to large NLO effects in has been established.[11–13] There is still great interest in providing new materials for NLO (and electro optical) effects in the far infra-red (off resonance) wavelengths which would make these materials great candidates for optical communications applications. An interesting development in the last decade has been the possibility of utilizing these organic materials with strong NLO effects for the purpose of demonstrating quantum optical effects. In particular, there has been new interest in organic materials to demonstrate NLO effects that are particularly sensitive to the use of entangled photons.[14,15] This suggests the interesting possibility of a new set of selection rules (structure-function relationships) for organic molecules which show NLO effects but are respondent to a pathway involving the interaction with entangled photons.

The study of quantum entanglement is now a fairly broad area of research involving its use in cryptography, spin polarized memory, as well as possible long lived coherences in natural biological light harvesting systems.[16–20] However, under the context of this investigation it involves the use of quantum entangled photons to probe electronic states in organic molecules. In general, the two entangled photons that are generated by the process of spontaneous parametric downconversion share a coupled eigenstate where the properties of each of the

photons cannot be isolated separately.[21] The connection between the NLO effects mentioned above and entangled photons is the possibility of using these entangled photons to do NLO spectroscopy at very small intensities.[15,22,23] One such example is the process of two photon absorption in organic molecules.[24] In the case of the general (classical) two-photon absorption effects one observes an increase in the absorption rate with an increase in the input intensity. This is a third order NLO effect. Molecules possessing this property have a nonzero third order molecular polarizability ($\boldsymbol{\gamma}$). The molecular dipole polarization can be expressed as contributions of the molecular linear and nonlinear optical responses to an external electric field, E.[25]

Generally, values of γ are known to depend on extended π-conjugation.[25] However, Marder et al.[26] found that it also has a strong dependence on other molecular parameters such as the charge transfer and bond order alternation. The charge transfer excited state gives a significant contribution to γ as it is dependent on bond order alteration (BOA) which is in turn tuned by donor-acceptor (D-A) moieties.[27] Charge resonance of D-A molecules causes them to be in either a neutral or charge separated form. The mixing of the resonance forms determine the BOA, which is the difference between the average pi bond orders of the same sets of bonds.[28] The imaginary part of γ can be measured by two-photon absorption experiments. The two-photon cross-section (δ_R) can be obtained using second-order perturbation theory and is given by:[29]

$$\delta_R = \frac{B}{\hbar^2 \varepsilon_0^2} \omega_0^2 \delta\left(\varepsilon_f - \varepsilon_g - 2\omega_0\right) \qquad \text{Eq. 3.1}$$

$$\left| \frac{1}{(\omega_0 + \varepsilon_g - \varepsilon_e) - i\kappa_e/2} M_{ee\prime}.eM_{ge}.e + \frac{1}{(\omega_0 - i\kappa_g/2)} M_{ge\prime}.e\mu_{gg}.e + \frac{1}{(-\omega_0 - i\kappa_{e\prime}/2)} \mu_{e\prime e\prime}.eM_{ge\prime}.e \right|^2$$

where ω_0 is the central frequency, e is the polarization, ε_g, ε_e and $\varepsilon_{e\prime}$ are the energy

eigenvalues of the ground, intermediate and excited states. μ_{ii} and M_{ij} denote the permanent dipole and transition dipole matrix elements respectively and κ_j are the state linewidths. One observes that the third order molecular polarizability and the two photon cross-section depend on the transition moments between final and ground states as well as the damping terms related to the linewidth.

There have been different approaches employed toward achieving enhancements in δ_R values.[30,31] One such design strategy is to create dipolar dyes with donor or acceptor groups linked by a π-conjugated bridge[32,33] because the π-conjugation provides a pathway for charge transfer while the donor and acceptor units provide ground state charge asymmetry.[34] Further research established that centrosymmetric chromophores also exhibited high TPA cross-sections due to the effective electronic delocalization.[35] Specific functional groups can be attached to ladder-type molecules[36] to form D-A type-molecules and these structural alterations have been shown to have enhancing effects on the TPA cross-section.[37] This improvement is suggested to emerge from the better coupling between the donor-acceptor junctions, that is a result of the now higher transition dipole moments. Furthermore, it is interesting to look at the effect of changing atoms within the heteroacene chain to integrate these adjustments in transition dipole moment.[38] Therefore, changing the central atoms on these ladder-type molecules may result in significant effects on their electronic properties and charge transfer character.

These important lessons have been learned for the case of the "classical" two photon absorption cross-section. There have been investigations of entangled two photon absorption processes in organic molecules where the strong temporal and spatial correlations of the entangled photon pair lead to the simultaneous absorption of the two photons. We have

previously successfully demonstrated ETPA and have attained the linear variation of ETPA rate at different input intensities with different molecular systems[39–43] and these findings have been essential in leading researchers towards photochemistry and photoluminescence applications that can be carried out on sensitive biological and organic samples using non-damaging low input flux levels. However, the interesting question as to whether the structure-function relationships obtained for the classical two-photon absorption cross-sections, δ_R, are the same for the entangled two-photon absorption cross-sections, σ_E, remains. The contribution of virtual state excitations in the case of entangled two photon absorption has been theoretically predicted to be different from that of the classical situation and this may play a role in looking at the structure-function relationships in these systems. In this paper, a series of ladder-type thienoacene molecules are characterized using both classical and entangled two-photon spectroscopic techniques. The molecule structures are established from a set of benzo[1,2-b:4,5-b′]dithiophene (BDT) units, fused together to form a **9**-**R**inged compound (**9R**). From knowledge that making atomic modifications to the heteroacene chain can be employed to change the photophysical properties of the material, the **9R** compound was subsequently used as the principle structure for three derivatives, **9R-N**, **9R-S** and **9R-Se** (structures shown in Figure 3.1). Investigations of the linear and nonlinear properties were carried out to characterize the impact of changing the central atom in the ladder which changes the quadrupolar and dipolar character in these molecules. Calculations of the classical TPA effect as well as the ETPA effect are compared with experiment.

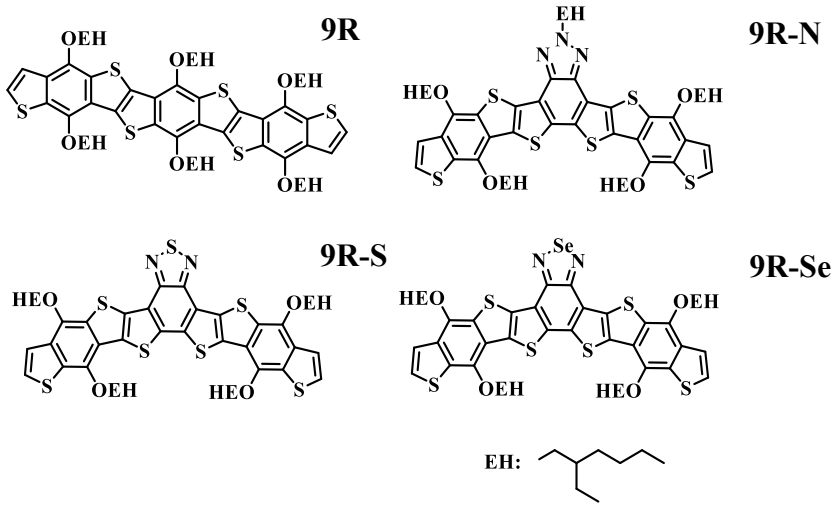

Figure 3.1. *Molecular structures of benzodithiophene derivatives (**9R**, **9R-N**, **9R-S**, **9R-Se**).*

3.3. Materials

Synthesis and Characterization of Molecules Investigated

Benzodithiophene (BDT) donor groups were prepared as previously reported, using short oligomer precursors which were coupled to thiophene groups containing triisopropylsilyl (TIPS) end capping groups.[36,37] An intramolecular electrophilic reaction was used to form aromatic C-S bonds for cyclization of the ladder-type donor units and **9R**. 5,6-difluoro-2-(2-ethylhexy)-benzo-1,2,3-triazole, 5,6-difluoro-2,1,3-benzothiathiadiazole and 5,6-difluoro-2,1,3-benzoselenadiazole were used to synthesize the acceptor starting material with boron groups attached for reaction with BDT donors.[44] A palladium-mediated Stille coupling method was employed to prepare a precursor of the acceptor and BDT units in a 4:5 ratio. These were cyclized to form **9R-N**, **9R-S** and **9R-Se**. All of the molecules prepared were characterized by NMR and MALDI-TOF mass spectrometry.

3.4. Results

3.4.1. Steady State Absorption

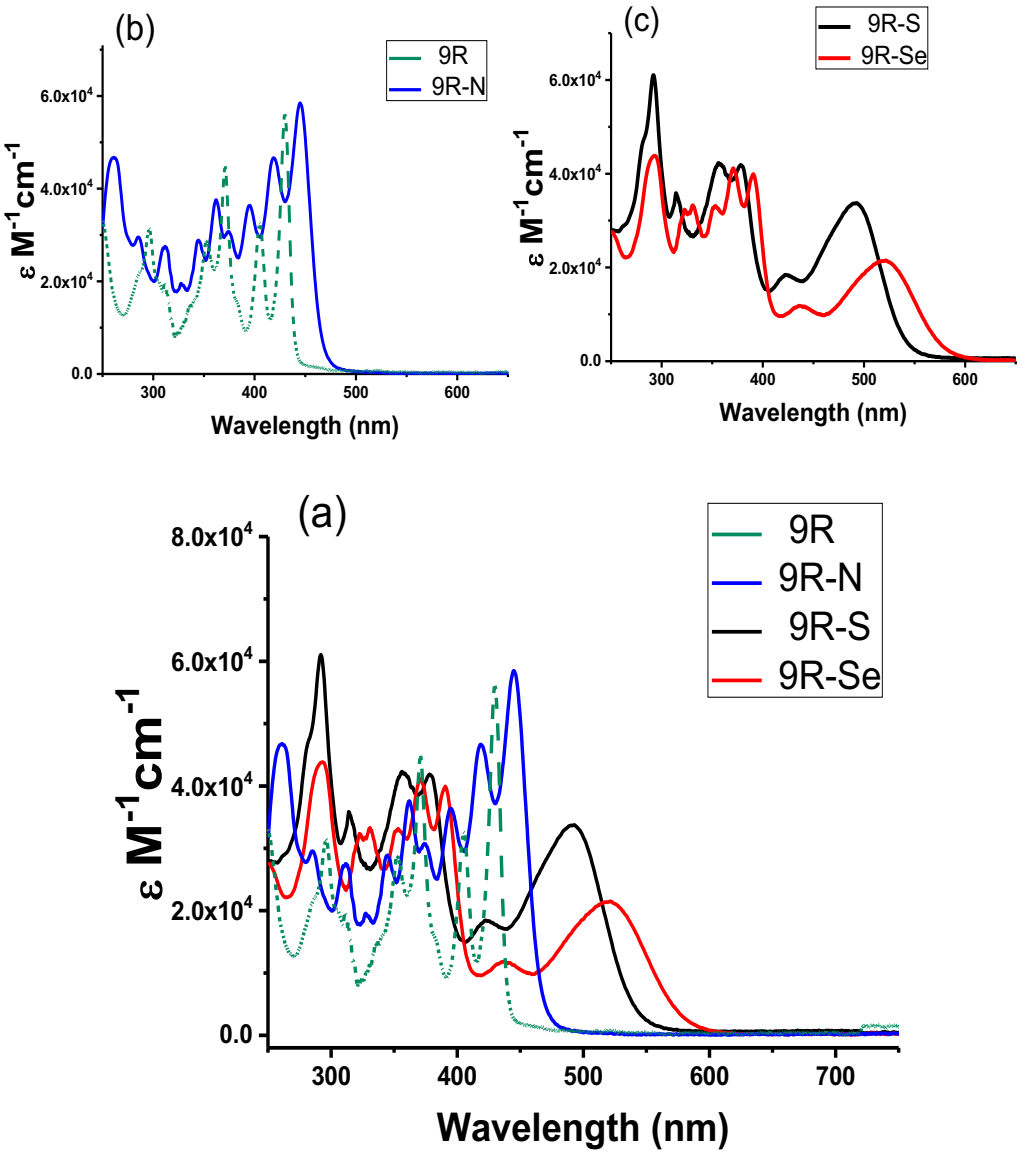

Figure 3.2. *(a) Absorption spectra of all four benzothiophene molecules in dilute chloroform solution (b)* ***9R*** *an* ***9R-N*** *(c)* ***9R-S*** *and* ***9R-Se***[37,44]

Steady state measurements for the compounds were taken in chloroform ($CHCl_3$) solutions and are depicted in Figure 3.2 (a, b and c). The molar extinction coefficients (ε) of the compounds were on the order of 10^4 M^{-1} cm^{-1} (Table 3.1). All of the investigated

molecules absorb in the 300-400nm range with narrow transition peaks in this region. These vibronic features are independent of added substituent suggesting that the excitations in this region are localized on the 9-ringed frame. These features have been observed in similar acene-type molecules.[36,45–47] The absorption spectra in a study of annulene derivatives contained similar vibrational progressions, where the rigid molecules showed absorption peaks that were present as a result of exciton and vibronic coupling to some fundamental excitation. These were attributed to a fundamental $\pi \rightarrow \pi^*$ transition.[48] As the different substituent atoms were added, a shoulder peak in the absorption was seen that was not observed in the absorption for the parent **9R** molecule. Specifically, a red shift in the absorption shoulder peak was observed as the size of the substituted atom was increased (**9R-Se**>**9R-S**>**9R-N**). It is suggested that the substituted atoms behaved as acceptors, forming Donor-Acceptor-Donor (D-A-D) structures. As such, the absorption behavior of the red-shifted shoulder peaks is consistent with absorption due to intramolecular charge transfer.[49] **9R** has a λ_{max} at 430nm compared to the shifted λ_{max} of **9R-N** at 450nm. **9R-S** and **9R-Se** showed a much greater shift and a pronounced broadening on the red side of the spectra. Cao et al.[50] observed such red shifts in a donor-acceptor polymer by incorporating selenium in place of sulfur.

Table 3.1. Steady state spectral properties of benzothiophene molecules

	λ_{abs}	λ_{em}	ε (M^{-1} cm^{-1})
9R	430	460	55950
9R-N	450	490	58500
9R-S	490	610	33650
9R-Se	515	655	21250

The calculated excitation energies and corresponding oscillator strengths are shown in Table 3.2. For **9R**, the first excitation energy of 2.85 eV was close to the experimental value and had a high oscillator strength of 1.246 which translates well to the high intensity peak seen in the absorption spectrum. The second and fourth excitations had oscillator strengths of almost zero, which suggests that the absorption of the molecule is confined to particular transitions. The narrow intense transition peaks with zero oscillator strengths may be dipole forbidden but may gain intensity as a result of vibronic and exciton coupling with other vibrational modes.[48] The excitation energies calculated for **9R-N** were also in fair agreement with the transitions in the experimentally obtained spectrum. The large oscillator strength of the lowest energy transition accounts for the high intensity seen for this peak. The subsequent transitions had comparatively lower oscillator strengths which justify the distribution of intensity seen for the higher energy region of the spectrum. The trend in oscillator strengths was similar for **9R-S** and **9R-Se** and they indicate that there is an appreciable amount of absorption in the lower energy charge transfer bands with absorption distributed throughout the higher energy peaks.

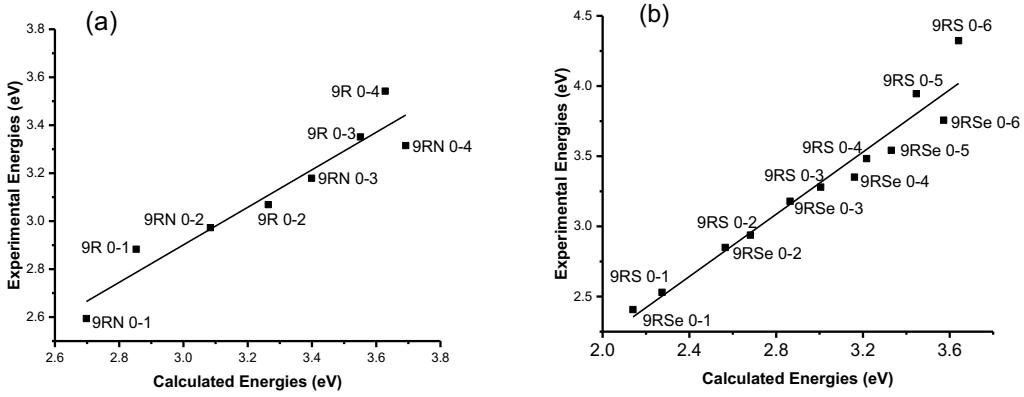

Figure 3.3. *Comparison of calculated vs experimental transition energies for (a)* ***9R*** *and* ***9R-N*** *and (b)* ***9R-S*** *and* ***9R-Se****.*

Figure 3.3 shows experimental transition energies plotted against the energies calculated by TD-DFT methods. The graph on the left (Figure 3.3a) has energies for **9R** and **9R-N** and that on the right (Figure 3.3b) has those for **9R-S** and **9R-Se**. Transitions for the two molecules with the heavier atoms begin at lower energies. The linear relationships exhibit that overall there is good agreement between calculated and experimental values. TD-DFT is known to be accurate for computing excitations from the ground state for large molecular systems.[48] As can be seen from the graph, all key spectral features of the absorption are predicted as well as the corresponding oscillator strengths. It appears that for these calculations the general electronic properties of the molecule are taken into consideration by this theoretical method. This gives rise to the good prediction of spectral shifts from one acene molecule to another.

Table 3.2. Excitation energies, wavelengths and transition dipole moments calculated for the singlet states of the benzothiophene molecules

Compound	State	Energy (eV)	λ_{1PA} (nm)	Transition Dipole Moment, M_{ge}	Oscillator Strength, f	λ_{2PA} (nm)	δ_{TPA} (GM)
9R	S_1	2.853	434	10.72877	1.2456	868	0.000175
	S_2	3.264	380	0.114117	0.0002	760	45.7
9R-N	S_1	2.698	460	10.74194	1.1809	920	0.425
	S_2	3.084	402	3.827594	0.1714	804	38.8
9R-S	S_1	2.274	545	8.3313	0.5986	1090	1.36
	S_2	2.681	463	3.718332	0.0961	926	36.6
9R-Se	S_1	2.140	579	7.830609	0.4977	1150	1.47
	S_2	2.565	483	3.680208	0.0910	966	36.1

The lower energy excitations seen for the substituted molecules may be indicative of a decrease in the optical energy band gap (HOMO-LUMO gap) because the donor/acceptor relationship affects the HOMO and LUMO energy levels. Therefore, electronic structure DFT calculations were carried out. These calculations verified that there was a narrowing of the HOMO-LUMO gap as predicted from the absorption spectra. Figure 3.4 visually represents the HOMO-LUMO levels and the band gaps of the chromophores calculated using TD-DFT. There was a decrease in energy band gap of 0.65 eV and 0.52 eV relative to the parent structure with the incorporation of selenium and sulfur respectively, compared to a smaller decrease of 0.14 eV with the nitrogen substitution.

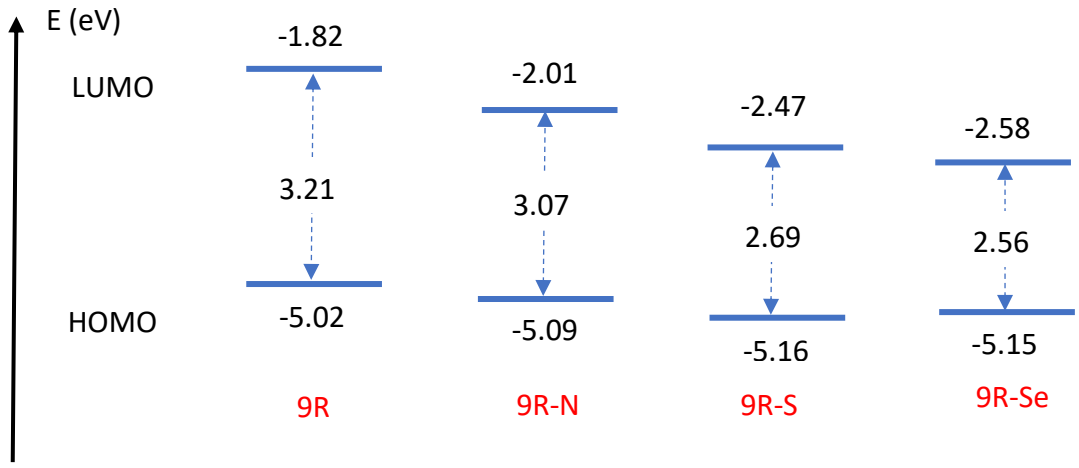

Figure 3.4. *Measured energy levels of the HOMO and LUMO energy levels and band gaps of the benzodithiophene molecules calculated using TD-DFT.*

To further understand the HOMO-LUMO energy levels and the possibility of charge transfer, the frontier orbitals of these molecules were analyzed using their ground state optimized geometry. The molecular orbitals are shown in Figure 3.5. The HOMOs of all four molecules were fairly delocalized along the entire molecular backbone. The

LUMOs of **9R** and **9R-N** also showed delocalization along the molecule. Although the LUMO of **9R-N** was mainly delocalized along the molecule, it showed a higher density around the substituted nitrogen than was observed in the HOMO. This suggests small charge transfer towards the nitrogen substituent. For **9R-S** and **9R-Se** the LUMOs were much more localized. In the LUMO of **9R-S** and **9R-Se**, there was clearly visible charge transfer from the donor ends towards the central sulfur and selenium acceptors.

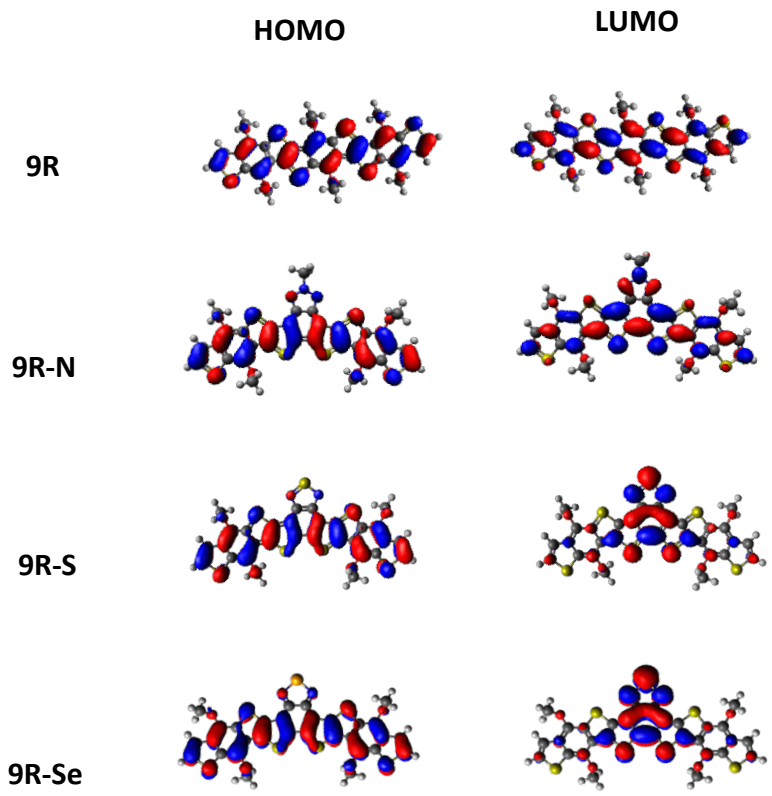

Figure 3.5*. Contour plots of molecular orbitals for all benzodithiophene molecules.*

3.4.2. Steady State Emission

Steady-state emission of the compounds was also measured and is shown in Figure 3.6. There is a distinct difference in emission between the parent structure and the substituted derivatives which is believed to result from the electronic effects of the

substituents on the benzothiophene frame. **9R** had a narrow emission band at 460nm with small shoulder peaks at 493nm and 530nm. The vibrational progressions of the absorption of **9R** were clearly reflected in its emission. In organic π-conjugated molecules with a rigid backbone such as oligoacenes and polyphenylene ladder-type oligomers, these well-resolved vibronic progressions are seen in the emission spectrum due to coupling between electronic and vibrational degrees of freedom.[51] The coupling results in structural distortions upon excitation, which affect the potential energy surfaces of the excited state relative to the ground state of the molecule, leading to pronounced spectral peaks.[52] However, molecules that are less planar and have more degrees of freedom, are prone to exhibit a lack of the mirror-image behavior from absorption to emission, and instead show homogenous broadening.[52] This is the case with the substituted benzodithiophene derivatives, which had single broadened emission peaks with λ_{Em} centered at 490nm, 610nm and 655nm for **9R-N**, **9R-S** and **9R-Se** respectively. As opposed to in **9R,** the substituted compounds most likely have different structural configurations and geometries in the excited state and ground state. This is known to occur for quadrupolar molecules with charge transfer, where there is a more pronounced difference in geometry and charge displacement of the excited state than in non-quadrupolar or dipolar molecules.[53] These conformational changes between the different states may lead to the broad spectra observed. There may also be possible twists caused by the bonds to the substituted atoms, and these are not present in the parent structure. The same shift seen in absorption (Figure 3.2) was seen with emission.

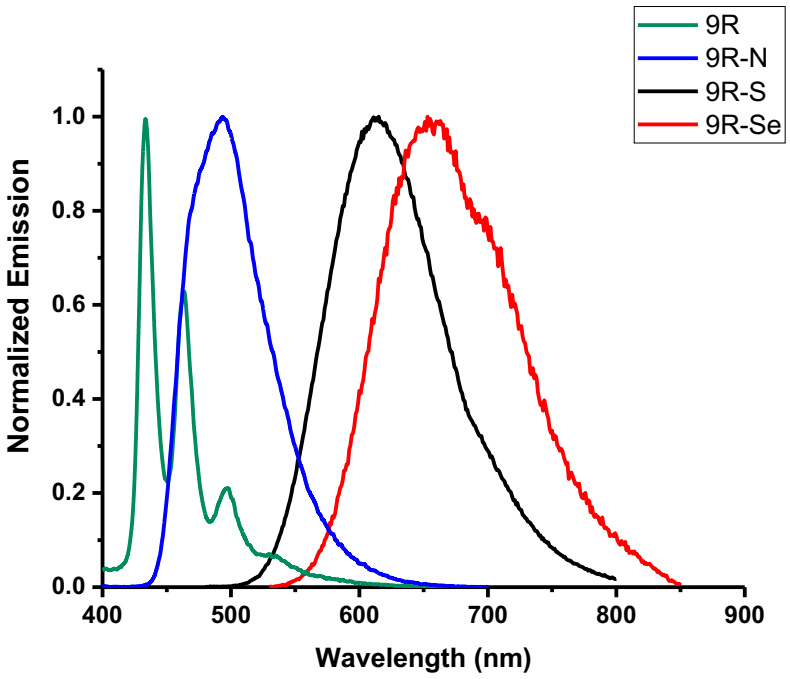

Figure 3.6. *Emission spectra of the benzothiophene molecules in dilute chloroform solution.*

The fluorescence quantum yield (Φ) of the investigated molecules was calculated to be 0.21, 0.77, 0.65 and 0.038 for **9R**, **9R-N**, **9R-S** and **9R-Se** respectively (Table 3.3). This shows that the molecular substitutions have a significant effect on the emissive properties of the molecule. The addition of selenium to the benzothiophene rings leads to a distinct drop in quantum yield in contrast to the increase obtained by adding nitrogen and sulfur. The small Φ of **9R-Se** can be explained by the heavy atom effect. There has been evidence of heavy atoms activating non-radiative pathways, where the singlet-triplet transitions are enhanced due to spin-orbit coupling. This has a detrimental impact on the emissive properties of the molecule and can result in a lower quantum yield.[54–56] A study of internal heavy atom effects showed that a sulfur substituted benzoperylene derivative had a quantum yield of 0.70 while a selenium derivative of the same compound had a much lower quantum yield of 0.025[57]. In that work, the strength of the intra-annular internal heavy-

atom effect (K) was measured as a function of the spin-orbit coupling constant of the heteroatom and the Hückel AO coefficients of the parent compound into which substitutions were made. The selenium containing compound showed ten times stronger intra-annular internal heavy atom than its sulfur counterpart. The observed decrease in fluorescence was proportional to this increase in K. Although sulfur and selenium are both considered heavy atoms, these results reported that the heavy-atom effect of selenium can be much stronger than for sulfur.[57]

3.4.3. Classical Two-Photon Excited Fluorescence

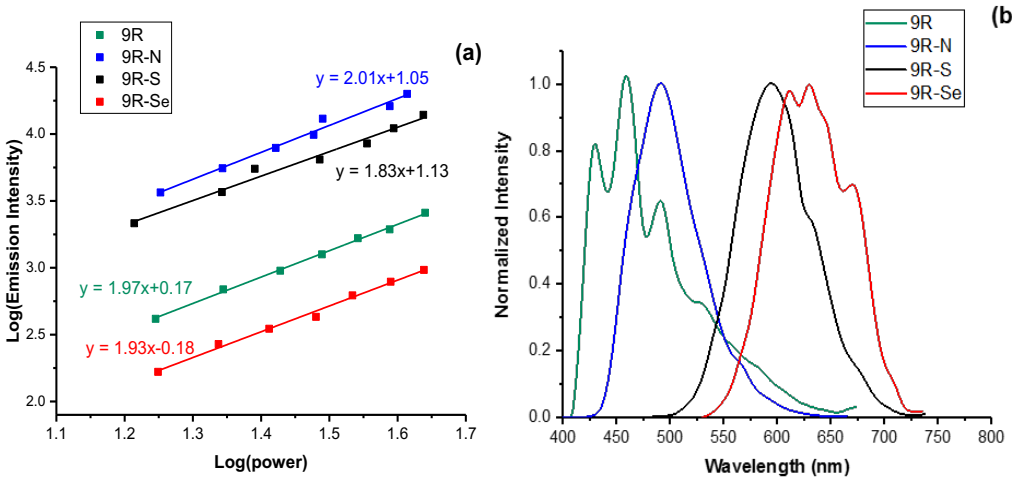

Figure 3.7 *(a) Intensity Dependence of two-photon excited fluorescence and (b) two-photon emission spectra*

Shown in Figure 3.7a is the measured two photon fluorescence for the ladder-type molecules investigated. The results are summarized in Table 3. The slopes of ~2 signify a two-photon excited emission. There were distinct differences in the intensity dependence of each compound. The TPA cross-sections (δ_R) of the compounds were calculated from the obtained intercepts of the intensity plots with respect to the reference compounds. The two-photon excited fluorescence spectra are shown in Figure 3.7b. The **9R** TPEF curve

includes the same peaks seen with one photon excitations. However, the curve seems broader towards the red region of the two-photon emission spectrum than for the emission observed with one photon excitations. This effect is most likely a result of the high intensity of this shoulder relative to the peak emission. TPEF curves of the substituted compounds were fairly similar to one-photon emission. Irregular shoulder peaks were observed for TPEF of **9R-Se**. This is due to the low quantum yield of the molecule, leading to the inability to obtain a smooth curve. It must be noted that the one-photon emission curves shown were performed with an excitation wavelength of the maximum one-photon absorption, while the two-photon excitation was 800nm. The different excitation wavelengths may also contribute to any small differences in emission seen.

Table 3.3. Summary of optical properties of benzothiophene molecules

Compound	Quantum Yield (Φ_f)	TPA Cross-Section (δ_R) (GM)
9R	21%	29.5
9R-N	77%	82.5
9R-S	66%	27.9
9R-Se	3.8%	9.01

The calculated cross-sections of the molecules at 800nm were 29.5, 82.5, 27.9 and 9.01 GM for **9R**, **9R-N, 9R-S** and **9R-Se** respectively. The δ_R value of **9R** agrees with previously studied benzodithiophene compounds.[36] Benzodithiophene compounds with 11, 15 and 21 rings had δ_R values of 64, 72 and 83 GM respectively. It was found that a decrease in conjugation length of the molecule led to a decrease in TPA cross-section. This was as a result of reduced effective conjugation and reduced intramolecular charge transfer over the shorter molecular distance.[36,58] Therefore the decrease in conjugation length from 11 to 9 rings led to the decrease in cross-section from 64 to 29.5 GM. The inclusion of nitrogen caused an enhancement of **9R**'s δ_R to 82.5 GM for **9R-N**. This suggests higher

charge transfer character in the nitrogen substituted compound. The inclusion of sulfur and selenium caused a decrease of **9R**'s δ_R to 27.9 and 9.01 GM for **9R-S** and **9R-Se.** For centrosymmetric chromophores, the main two-photon absorption peak does not correspond to the maximum one-photon absorption peak.[59] The main TPA peak coincides with a two-photon allowed transition that is blue-shifted with respect to the one-photon absorption spectrum. This was observed in our two-photon calculations for these molecules (Table 3.2). Due to this two-photon spectral shift, it is possible that the two-photon transitions excited for **9R-S** and **9R-Se** were far from the two-photon absorption maxima.

D-A molecules have been extensively studied and expressions for γ exhibit that it depends on the change in dipole moment, transition dipole moment and the energies between different excited states.[60] Therefore, it becomes important to look at how γ is affected for multipolar molecules. Specifically, we consider quadrupolar molecules. The degree of ground state polarization of the molecule can be modulated by changing D-A strength and properties, so it is necessary to investigate molecules of different polarity. Quadrupolar-type molecules are usually centrosymmetric in contrast to asymmetric dipolar molecules. This change in symmetry affects the charge transfer properties of the molecule which subsequently affect the values of γ. Marcano et al.[61] found that γ has a relation to the ratio between antibonding and bonding orbitals in quadrupolar-type molecules which resulted in γ being up to 1.6 times higher in these compounds than in dipolar-type compounds.[61] Another study suggested that the alternation from donor to acceptor blocks in multipolar molecules forms a quantum well structure. Quantum confinement of electrons within these wells leads to an enhancement of γ.[62] Since the behavior of γ is roughly periodic with respect to BOA, slight changes in BOA can have large effects on the value

of γ. It follows that the different donor-acceptor strength and molecular structure will affect the polarity of the molecules and the resulting δ_R values. This can be seen in our varying cross-section results.

In the molecules studied here, substituted derivatives of **9R-S**, **9R-N** and **9R-Se** can be described as benzothiadiazole**,** benzotriazole and benzoselenadiazole units fused to benzothiophene moieties. Consequently, these heteroatoms behave as fused acceptors in the molecules under investigation. Benzothiadiazole and benzotriazole are often covalently linked to electron donors as they are good electron withdrawing units.[63–65] This linkage is commonly executed via a single, double or even triple bond. We recently showed that the incorporation of fused acceptors into the conjugation system has benefits over bond linkages. The fusion enhances the molecule's NLO properties as it minimizes the possibility of bond twisting and keeps the compound's coplanar conformation.[37] The lack of a carbon-carbon double bond also eliminates the likelihood of cis-trans photoisomerization which would impair the stability of the compound.[66] The D-A-D motif of our substituted compounds suggests they are quadrupolar-type molecules. These are favorable as TPA materials because of their intrinsic intramolecular charge-transfer from the periphery donors to the central acceptor upon excitation.[67] The symmetrical charge distribution between the center and the ends of the molecule have been highly correlated to large two-photon cross-sections.[68] Altering the acceptor strength from nitrogen to sulfur to selenium can modulate the excited state properties of the molecules and affect γ, therefore affecting TPA cross section of the compound.

With regard to **9R-N**, the electronegativity of the nitrogen atom, placed adjacent to the π-system, causes inductive effects to occur.[69] There is bond polarization as a result of

the transmission of charge which increases its electron withdrawing character and makes it a strong acceptor. This was viewed in the enhancement of δ_R to 82.5 GM for **9R-N** compared to δ_R of **9R**. Similar results were reported in a study of TPA cross-sections of a benzothiophenyl compound with furan (central oxygen) and thiophene (central sulfur) interchanged as the central group.[70] This arrangement for the furan-containing compound can be viewed as a D-A-D type structure. It was documented that the difference in electronegativity between the oxygen of the furan and the sulfur atoms in the thiophene donor groups caused some photoinduced electron transfer. This resulted in a higher TPA cross-section for the molecule with the furan acceptor than for that with the central thiophene. This suggests that for **9R-N**, the inclusion of the highly electronegative central nitrogen to the nine ringed frame causes an enhancement in the effective conjugation and hence, enhances the charge transfer character. It has already been discussed that resonance forms of D-A-D molecules and the donor-acceptor strength are able to modulate the γ values of the molecule which influences two-photon absorbing effects. Previous studies have also reported that nitrogen atoms used as linkers are able to extend π-conjugation due to their sp^2-hybridization.[71] In the case of **9R-N**, there is an interaction between the π-electrons of the neighboring conjugated units and the unpaired electrons in the substituted nitrogen atom, which enhances the overall effective conjugation in the molecule. This leads to the much higher TPA cross-section calculated for **9R-N** than for **9R**.

Our experimental data showed that for the excitation examined, the sulfur substituted compound and the parent structure had similar δ_R values and therefore exhibited similar two-photon effects. This cannot be attributed to quantum yield effects, since the quantum yield of **9R-S** and **9R** were of the same magnitude. Therefore, the experimentally

measured cross-sections of either compound was not significantly enhanced. Furthermore, **9R-S** had a higher δ_R than **9R-Se**. This may be due to the greater charge transfer in the state probed for the sulfur substituted compound compared to the selenium substituted compound. A previous computational study by Zhang et al.[72] looked at atomic substitutions of sulfur and selenium in a molecule and the subsequent electron-withdrawing effects. It was reported that the amount of intramolecular charge transfer for sets of monomers decreased for selenium-based molecules compared to sulfur-based molecules.[72] Due to the large size of selenium compared to sulfur, the C_2—Se bonds (1.886 Å) were longer than C_2—S bonds (1.758 Å) and this led to stronger electron withdrawing ability of the sulfur-based molecules and higher calculated intramolecular charge transfer values. Similarly, our optimized geometries show that the N—Se bonds (1.821 Å) were longer than the N—S bonds (1.654 Å). This confirms that the longer selenium bond lengths may lead to the decreased electron withdrawing ability of selenium-based compounds. Therefore, there may be less charge transfer towards the selenium acceptor. This translates to the observed lower δ_R for **9R-Se** than **9R-S.** The different bond lengths will also have an effect on BLA which changes the γ values and subsequent NLO properties. Thus, it follows that **9R-S** may have more intramolecular charge transfer and hence larger two-photon cross section compared to **9R-Se**.

To obtain a more detailed depiction of the two-photon absorption for all four molecules, two-photon cross-sections for different transitions were calculated via TD-DFT using the GAMESS package. By computing two-photon transition tensors based on calculated energies and transition dipole moments, the two-photon cross-section is estimated. For many symmetric chromophores, the lowest energy transition which is one-

photon allowed is two-photon forbidden.[59] This is reflected in the low two-photon cross sections for the S_1 states of all four molecules (Table 3.2). Since an 800nm wavelength was used to determine TPA cross-section experimentally, it is important to consider the near 800nm theoretically obtained values. For these excitations, the computed cross-sections of **9R**, **9R-N**, **9R-S** and **9R-Se** were 45.7GM, 38.8GM, 1.33GM and 2.37 GM respectively. The computed TPA wavelengths for the nitrogen and sulfur substituted compounds are close to 800nm. The calculated values at these excitations confirm that the cross-section of **9R-N** is much higher than that of **9R-Se** at the 800nm excitation. This agrees with experimental results.

3.4.4. Entangled Two-Photon Absorption & Fluorescence

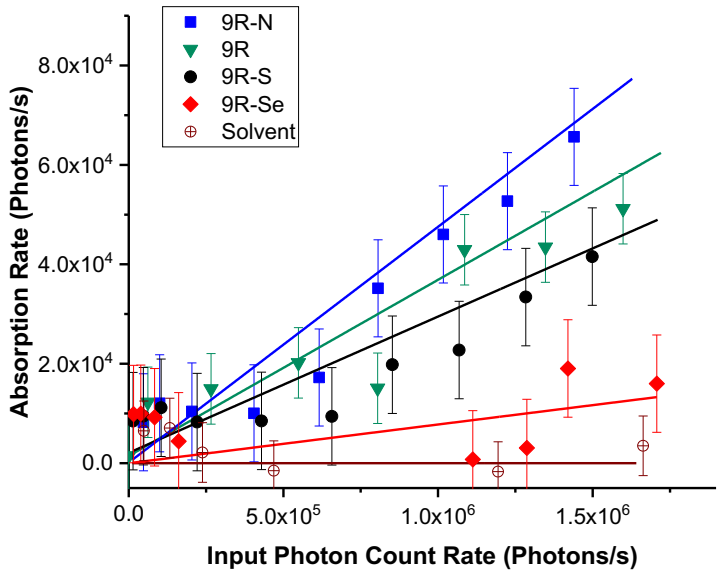

Figure 3.8. *Entangled two-photon absorption rate of the molecules investigated.*

Shown in Figure 3.8 are the entangled two-photon absorption plots for the molecules investigated. The general rate of NLO absorption of a molecule is a summation

of both the non-entangled or random TPA rate and the ETPA rate, $R = R_r + R_e$.[15] The random TPA rate was described above. Entangled photons at 800nm generated by type II SPDC were employed in these ETPA experiments. ETPA was observed in all compounds studied in this work. There were however, variations in how much entangled light each compound could absorb, and this can be viewed clearly in the graph of ETPA rate (Figure 3.8). The extent of two-photon absorption for each molecule changes greatly with each substituent. This implies that entangled photons are responsive to the nonlinear optical changes caused by adjustments in molecular structure. Figure 3.8 shows the absorbed photon rate against input flux for the benzodithiophene derivatives and the solid lines represent linear fits of the data. ETPA and the subsequent linear ETPA character were measured with an entangled photon flux of 10^6 photons/s. Only the linear dependence of ETPA was observed and excitation intensity was not high enough for the quadratic nonlinear dependence of classical TPA to be seen. The ETPA cross-sections were calculated from the linear ETPA rates (Table 3.4). **9R** had an ETPA cross-section of 4.76×10^{-19} cm^2/molecule which is somewhat smaller than ETPA cross-sections for other chromophores that have been reported.[39–42] However, here we are interested in the trends in σ_E for the thienoacene substituted ladder molecules. Compared to the parent structure, **9R-N** had a higher ETPA cross-section of 5.96×10^{-19} cm^2/molecule. **9R-S** and **9R-Se** had cross-sections of 2.69×10^{-19} cm^2/molecule and 0.679×10^{-19} cm^2/molecule respectively. Interestingly, the relative trend in cross-section for the substituted derivatives (**9R-N** > **9R-S** > **9R-Se**) remained the same in both the classical and entangled two-photon absorption cases. It is also interesting to note that there was an enhancement of the entangled photon cross-section of the 9R chromophore relative to its classical two photon cross-section.

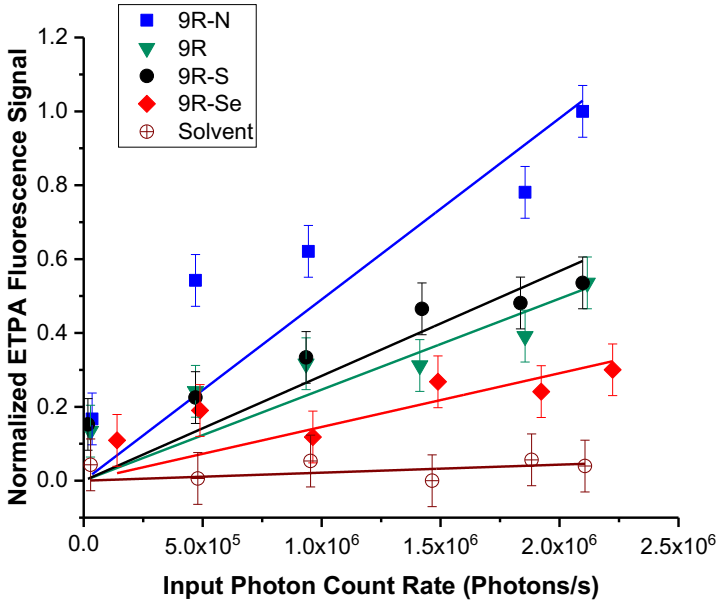

Figure 3.9. *Entangled two-photon excited fluorescence as a function of photon flux.*

Table 3.4. Entangled two-photon absorption cross-sections measured via transmission and fluorescence methods

Compound	σ_E (10^{-19} cm^2/molecule), via Transmission	σ_E (10^{-19} cm^2/molecule), via Fluorescence
9R	4.76	8.10
9R-N	5.96	5.25
9R-S	2.69	2.02
9R-Se	0.679	1.64

Two-photon excited fluorescence measurements were also carried out using entangled photons to excite the compounds (ETPEF) and the linear ETPEF of the different chromophores shown in Figure 3.9. It was previously reported that the entangled fluorescence intensity was roughly in agreement with a product of the ETPA cross-section measured by the absorption method and the fluorescence quantum yield of the molecule.[43] This approximation holds for the thienoacene molecules studied. There is a linear dependence of the fluorescence signal with input flux intensity as a result of the nonclassical properties of the ETPA process. The ETPA cross-sections calculated from

ETPEF are shown in Table 4. This is the first systematic comparison with multiple chromophores, of the ETPA transition method and ETPEF collection method to measure entangled cross-sections. There is very good correlation between the two sets of entangled cross section values. It was expected that the absorption and fluorescence detection methods would not provide the exact same entangled cross-section values, as different measurement methods are subject to different experimental errors, however, the values from both methods are generally within error of each other. Similar to results from TPA and ETPA experiments, **9R-Se**'s cross-section of 1.64×10^{-19} cm^2/molecule was smaller than those of the other three molecules. However, for ETPEF data there is again an enhancement in the entangled two photon cross-section for the **9R** chromophore.

3.5. Discussion

Figure 3.10 shows the normalized classical TPA cross-sections compared to normalized ETPA and ETPEF cross-sections for all four molecules investigated. The graph shows that with TPA and ETPA, the values for the substituted derivatives scale equivalently when the substituent is changed from nitrogen to selenium. There is a clear trend for **9R-Se**, **9R-S** and **9R-N**, with a similar increasing progression in that order. This corresponds with data from a previous study that looked at a set of thiophene dendrimers.[40] For similar compounds with systematic changes, classical TPEF and ETPA techniques can both be used to get correlation data for different molecules. There is a moderate change in trend when the substituent is changed to sulfur. However, **9R** shows a drastic ~45% increase in relative cross-section for entangled TPA compared to classical TPA. It is interesting that the three D-A-D substituted molecules exhibited a comparable trend in cross-section values going from classical to entangled TPA, despite the small difference seen for **9R-S**. Alternatively, the D-π–D **9R**

molecule showed a large enhancement of ~45% from classical to entangled TPA. For cross-sections measured via ETPEF, **9R** had the highest cross-section, followed by **9R-N**, **9R-S** and **9R-Se**. The enhancement for cross-section of **9R** seen with ETPA is more pronounced with ETPEF. Moreover, although **9R-S** still has a higher cross-section than **9R-Se**, the values for ETPEF are closer in magnitude.

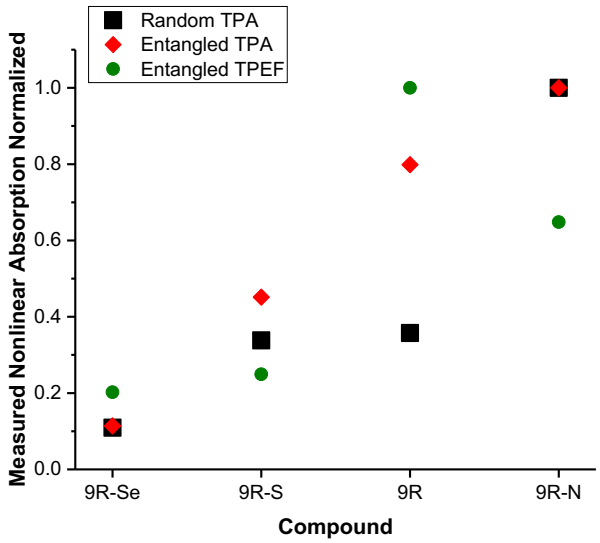

***Figure 3.10**. Graph showing normalized random TPA cross-sections and normalized ETPA cross-sections.*

To properly understand the differences in cross-sections seen in Figure 3.10, it is important to consider the possible two-photon absorption pathways, that is, the permanent dipole transition and the virtual state transition.[73] An extensive theoretical and experimental analysis on the selectivity of entangled photon absorption was done to exhibit how the particular excitation pathway of a molecule affects the observed non-classical NLO effects.[29] To compare the different absorption mechanisms, it is best to examine the equation for the entangled two-photon absorption cross-section, σ_e. This is given as:[29]

$$\sigma_e = \frac{A}{\hbar^2 \varepsilon_0^2 A_e T_e} \omega_0^2 \delta(\varepsilon_{e\prime} - \varepsilon_g - 2\omega_0) \times \left| \frac{1-e^{-i(\omega_0+\varepsilon_g-\varepsilon_e)T_e-\kappa_e T_e/2}}{(\omega_0+\varepsilon_g-\varepsilon_e)-i\kappa_e/2} M_{ee\prime}.e_i M_{eg}.e_s + \right.$$

$$\left. \frac{1-e^{-i\omega_0 T_e-\kappa_g T_e/2}}{(\omega_0-i\kappa_g/2)} M_{ge\prime}.e_i \mu_{gg}.e_s + \frac{1-e^{-i\omega_0 T_e-\kappa_{e\prime} T_e/2}}{(-\omega_0-i\kappa_{e\prime}/2)} \mu_{e\prime e\prime}.e_i M_{ge\prime}.e_s \right|^2 \quad \text{Eq. 3.2}$$

The first term describes absorption through intermediate levels, while the second and third term describe absorption via permanent dipole transitions. ω_0 is the signal and idler photon frequency, A_e and T_e are the entanglement area and entanglement time respectively, e_s and e_i are the polarization of the signal and idler photons, and ε_g, ε_e and $\varepsilon_{e\prime}$ are the frequency of the ground, intermediate and excited states. μ_{ij} and M_{ij} denotes the permanent dipole and transition dipole matrix elements respectively, and κ_j are the state linewidths. It was predicted by Fei et al[15] that the quantum interference between the entangled photon pair and the intermediate states produce a nonmonotonic behavior of the ETPA cross-section as a function of the entanglement time. These cause entanglement induced transparencies and this behavior can be seen by the oscillatory term $e^{-i\Delta\omega T_e}$. The period of these oscillations vary with the absorption pathway.[29] It was found that intermediate states that are off resonance with the laser (photon energy) did not contribute to the ETPA cross-section.[29] This is the case for absorption mechanisms through the permanent dipole pathway. Thus, it was found that using particular entanglement times, molecules excited via solely the permanent dipole transition where the ground and excited states are directly coupled, did not show ETPA signal.

An example of such interesting ETPA characteristics was seen with a trans-stilbene derivative, which had a bis(styryl)benzene structure with methoxy side groups and dialkyl amino end groups.[29,74] This molecule has very high classical TPA cross-section, on the order of 300 GM. However, it showed no entangled two-photon absorption.[29] This was intriguing because the classical two-photon absorption results suggest that this molecule exhibits strong

nonlinear optical effects. Examining the structure of the compound, the alkoxy chains on the central phenyl unit serve as additional donors on the conjugated chain, but have different polarity compared to the molecule's end groups. This enhances the dipole character of the molecule, which causes the dipole pathway to dominate absorption. Due to the high charge-transfer character of the compound and difference in dipole moments of the ground and excited states, the primary absorption mechanism is the permanent dipole pathway. This overshadows the transition dipole pathway and no ETPA was observed with a particular entanglement time. Therefore, it becomes necessary to understand how the symmetry and multipolar character of the molecule plays a role in observed ETPA signals.

Comprehensive investigations of conventional TPA have shown that for molecules that have non-zero permanent dipoles and existing virtual states, both two-photon excitation mechanisms are operational and compete in classical two-photon absorption.[73] Anderson *et al*[75] studied the different states involved in two-photon absorption of quadrupolar centrosymmetric molecules and dipolar non-centrosymmetric molecules.[75] For quadrupolar molecules, the three states involved in TPA are the $1A_g$ ground state, $1B_u$ intermediate state and an A_g final state. A study of TPA for a set of quadrupolar π-conjugated molecules also showed that TPA occurred from the $1A_g$ ground state to a TPA active A_g state, but TPA was forbidden in B_u states.[76] Furthermore, these forbidden TPA $1B_u$ states were one photon allowed. Thus, in quadrupolar molecules, the $S_0 \rightarrow S_1$ transition is allowed for one photon absorption, while the $S_0 \rightarrow S_2$ ($1A_g \rightarrow 2A_g$) is allowed for TPA, and the $1B_u$ state plays the role of an intermediate state.[77] Strehmel and co-workers also investigated how classical two-photon absorption occurs in quadrupolar compounds compared to their dipolar counterparts.[91] This highlighted how the structural polarity of the molecule is important in determining the two-

photon absorption mechanism and the resulting two-photon absorption cross-section. Due to the centrosymmetric nature of quadrupolar molecules, the change in dipole moment from S_0 to S_1, $\Delta\mu$, is close to zero.[78] As a result, the $\Delta\mu$ term in either the classical or entangled two-photon equation is minor for quadrupolar compounds. It has been found that there is strong electronic coupling between the excited states, thus the $S_1 \rightarrow S_{e'}$ is an important parameter for the TPA of quadrupolar compounds. This implies that the transition dipole moments, from ground to excited state, M_{ge}, and between excited states, $M_{ee'}$, determine the TPA cross-section for quadrupolar molecules. The relationship between γ and δ previously introduced shows that δ_R for centrosymmetric quadrupolar compounds would depend on parameter for the transition between excited states ($M_{ee'}$). This would imply that σ_E of quadrupolar molecules should depend primarily on the first term of Equation 3.2.

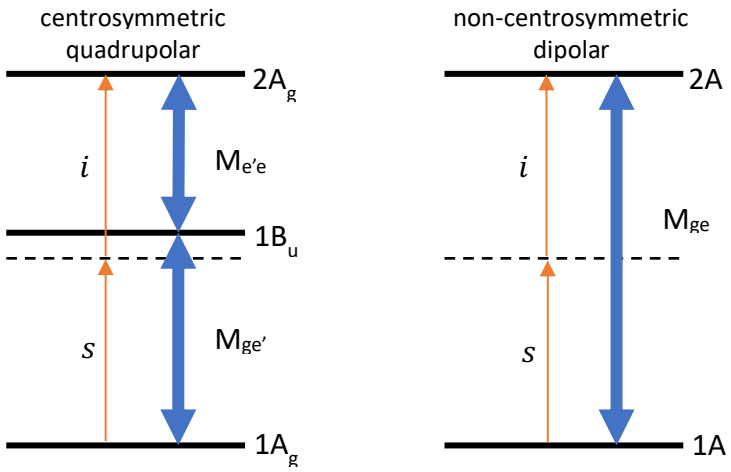

Figure 3.11. *Energy level diagram showing two-photon absorption mechanisms in centrosymmetric quadrupolar molecules and non-centrosymmetric dipolar molecules, i and s represent the signal and idler photons.*

On the other hand, TPA in dipolar molecules is more controlled by the change in dipole between the ground state and excited state ($\Delta\mu$) and the transition dipole moment between these states (M_{ge}). As a result, classical TPA of dipolar molecules is highly dependent on the parameters that are involved in one-photon absorption. Rather than a coupling between

intermediate states, this absorption pathway depends on the difference in permanent dipole moment of the ground and final state. A comparison of one-photon and two-photon excitation spectra for dipolar molecules, shows this dependence.[79,80] Since TPA in dipolar molecules depends on the parameters involved in one-photon absorption (OPA), their OPA and TPA spectra overlap. Therefore, the low-energy one-photon allowed transitions can also be two-photon allowed.[75] This is only the case for non-centrosymmetric molecules. It follows that the symmetries probed for dipolar and quadrupolar molecules may not be the same. Certain symmetry states for quadrupolar molecules cannot be probed by classical light. As all the dipole terms and detuning energies are present in both classical TPA and ETPA cross-section expressions, they affect TPA in both cases. The ETPA cross-section of dipolar molecules would hence be affected primarily by the second and third terms of Equation 3.2.

Since the compounds in this work have D-A-D and D-π-D structures, they are all centrosymmetric and may be described as quadrupolar-type molecules. Therefore, they must have majority TPA contributions from the transition dipole pathway. It is known that changes in quadrupole moment affect the molecule's transition dipole moment.[81] Hence, the effects of transition dipole moment are considered to account for them. Furthermore, our theoretical calculations for classical TPA showed that the interband transition dipole moments (M_{ge}) alone did not fully correlate with the cross sections (Table 3.2). This implies that there was also a considerable contribution from the intraband transition dipole moments ($M_{ge'}$) to the computed classical TPA cross-sections and substantiates the reasoning that the TPA mechanism of these chromophores involves the intermediate excited states. It can be said for the molecules being investigated that because there is only one intermediate state for the transition being considered (for **9R** and **9R-N**), or one intermediate state is highly dominant (**9R-S** and **9R-Se**), so a one

intermediate state model can be used. Using the first term of Equation 3.2 for σ_E and the transition dipole moments obtained computationally (M_{g1} and M_{1e}, shown in Table 3.5), estimates of the ETPA cross-sections for the four molecules were calculated. These were estimated at an entanglement time of 100fs to match experimental conditions.

Figure 3.12 shows the normalized cross-sections from experimental ETPA as well as from calculations. Calculated values show very good agreement with experimentally obtained ETPA cross-sections, although the calculated **9R** value is relatively lower than experimental obtained values and does not show the enhancement. It must be noted that these calculations were carried out using the $S_1 \rightarrow S_2$ transition dipole moments and only the first term in equation 7 which is the transition dipole moment pathway. The transition probed experimentally by the 800nm entangled photons for **9R-S** and **9R-Se** was most likely the $S_0 \rightarrow S_4$ transition. Using the $S_1 \rightarrow S_4$ transition dipole moment for these two molecules, their computational values match their experimental results and there are no deviations.

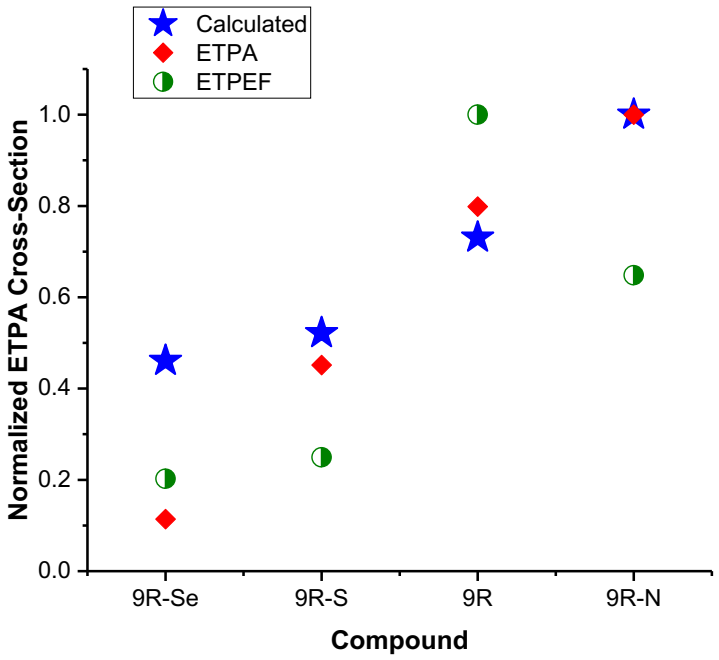

***Figure 3.12**. Graph showing calculated and experimental relative normalized ETPA cross-sections.*

Table 3.5. Quantum calculations for excitation energies, and transition dipole moments (M) for interband and intraband transitions

Compound	Energy (eV)	Transition	M_{g1} (D)	Energy (eV)	Transition	$M_{1e'}$ (D)	Detuning Energy (eV)
9R	2.853	$S_0 \rightarrow S_1$	10.728	0.411	$S_1 \rightarrow S_2$	20.300	1.304
9R-N	2.698	$S_0 \rightarrow S_1$	10.742	0.386	$S_1 \rightarrow S_2$	19.355	1.148
9R-S	2.274	$S_0 \rightarrow S_1$	8.3313	0.407	$S_1 \rightarrow S_2$	19.920	0.7242
9R-Se	2.140	$S_0 \rightarrow S_1$	7.8306	0.425	$S_1 \rightarrow S_2$	19.539	0.5902

Considering the centrosymmetric structure of all four molecules, it is intriguing that **9R** has an immensely different relative ETPA cross-section compared to classical TPA cross-section. It suggests that the difference in symmetry and structure, going from having a central acceptor to a central π-bridge, has an enhancement on ETPA that is not observed with classical

TPA. The parent **9R** structure does not have the charge transfer towards an acceptor that is seen in the substituted compounds. Thus, it does not have the strong quadrupolar character of the substituted molecules and can be considered as an analogue dipolar molecule. Therefore, it may have a non-zero dipole moment, giving this molecule some dipolar character. A low change in dipole moment, $\Delta\mu$, of 3D, is estimated to determine how ETPA cross-sections will be affected by contributions from the permanent dipole pathway.

Using the estimate of the permanent dipole moment, the second and third terms were included in the calculation of σ_E for **9R**. Calculations with the addition of the permanent dipole moment term lead to an increase in entangled two photon cross-section (by ~25%). Due to the complex oscillatory terms in the σ_E equation, it also affects the induced transparencies. With inclusion of $\Delta\mu$, we obtain an enhancement in the σ_E calculated. Although the two-photon absorption is dominated by the transition dipole pathway, contributions from the permanent dipole path are able to cause observable enhancements in ETPA and the trend of calculated ETPA becomes comparable to that obtained from ETPEF experiments. These contributions do not cause a detectable difference in classical TPA but due to the higher resolution and selectivity of ETPA, they are clearly seen using entangled photons. This explains the relative enhancement of the ETPA cross-section of **9R** compared to classical TPA. The substituted compounds have no permanent dipole contribution thus this enhancement is not seen. The small change in symmetry of the molecules by adjusting the donor/acceptor/π-bridge structure, causes changes in quadrupolar and dipolar character that is better elucidated with entangled photons.

These results suggest that the quantum interference between entangled photons and the interacting matter are able to provide changes to two-photon absorption signals that are not

observed classically. This improves the resolution of the non-linear optical signal for particular absorption pathways. For purely quadrupolar molecules, where only the transition dipole pathway is dominant for classical TPA, this remains the same for ETPA. For molecules that are centrosymmetric but have some dipolar character, both absorption mechanisms are involved and the small contributions from the permanent dipole pathway cause small enhancements to ETPA signal and changes to the ETPA nonmonotonic oscillations. Thus, ETPA is highly dependent on the symmetry and multipolar nature of the compound being investigated, as these determine the two-photon absorption mechanism that will be utilized. Donor-acceptor moieties of the molecule affect the BLA and BOA which in turn tune γ and the dipolar and quadrupolar character. It is clear that such adjustments will modify the dipole terms and influence possible pathway mechanisms. This introduces the opportunity to control the degree of ETPA by taking advantage of its dependence on molecular structure and absorption mechanism.

3.6. Conclusions

This comprehensive experimental and computational study of thienoacene molecules has shown that the electronic structure of each molecule provides different linear and nonlinear optical effects. These structural differences are based on the presence of atomic substitutions with different donor/acceptor and donor/π-bridge moieties. The absorption and emission spectra for the different molecules showed increasing red shifts with respect to the parent structure as the substituent was changed from nitrogen to sulfur to selenium. The absorption spectra was well predicted by computational methods and the observed red shifts were reflected in the narrowing HOMO LUMO band gaps. The atomic substitutions also had

significant effects on the emissive properties of the molecules. The nitrogen substituted compound, **9R-N**, showed strong nonlinear optical effects with its high classical two-photon absorption, followed by **9R**, **9R-S** and **9R-Se**. Measurements of the entangled photon absorption of the Thienoacene chromophores showed a strong correlation with the classical two photon experiments. However, the **9R** chromophore showed an enhancement for the case of the entangled two photon cross-section. Similarly, there was good agreement with the entangled photon fluorescence measurements and the classical two photon results. Again, there was also a strong enhancement observed in the **9R** chromophore for the entangled two photon fluorescence results. Calculations of the entangled cross-sections showed that inclusion of the permenant dipole pathway could result in an enhancement of the entangled cross section for the **9R**. This pathway is not accessible for the other quadrupolar chromophores studied in the series. The enhancements in the **9R** ETPA cross-section were experimentally observed due to the high resolution of the quantum processes involved and the strong correlations of entangled photons. These experimental and theoretical results provide the basis for developing organic NLO molecules that can be selectively synthesized based on multipolar character and to demonstrate strong absorption and fluorescence with low intensity nonclassical light.

References

(1) Morley, J. O.; Docherty, V. J.; Pugh, D. Non-Linear Optical Properties of Organic Molecules. Part 2. Effect of Conjugation Length and Molecular Volume on the Calculated Hyperpolarisabilities of Polyphenyls and Polyenes. *J. Chem. Soc. Perkin Trans. II* **1987**, No. 6, 1351–1355.

(2) Wu, E.-S.; Strickler, J. H.; Harrell, W. R.; Webb, W. W. Two-Photon Lithography for Microelectronic Application. *Opt. Microlithogr. V* **1992**, *1674* (June 1992), 776. https://doi.org/10.1117/12.130367.

(3) Maruo, S.; Nakamura, O.; Kawata, S. Three-Dimensional Microfabrication with Two-Photon-Absorbed Photopolymerization. *Opt. Lett.* **1997**, *22* (2), 132–134.

(4) Helmchen, F.; Denk, W. Deep Tissue Two-Photon Microscopy. *Nat. Methods* **2005**, *2* (12), 932–940. https://doi.org/10.1038/nmeth818.

(5) Gaus, K.; Gratton, E.; Kable, E. P. W.; Jones, A. S.; Gelissen, I.; Kritharides, L.; Jessup, W. Visualizing Lipid Structure and Raft Domains in Living Cells with Two-Photon Microscopy. *Proc. Natl. Acad. Sci. U. S. A.* **2003**, *100* (26), 15554–15559. https://doi.org/10.1073/pnas.2534386100.

(6) Garmire, E. Nonlinear Optics in Daily Life. *Opt. Express* **2013**, *21* (25), 30532. https://doi.org/10.1364/oe.21.030532.

(7) Verbiest, T.; Persoons, A. Nonlinear Optical Properties of Polymeric Materials and Polymer Films : Recent Developments and Future Trends. *Macromol. Symp.* **1996**, *102*, 347–354. https://doi.org/10.1002/masy.19961020141.

(8) Sapaev, U. K.; Kutzner, J.; Finsterbusch, K. Optimization of Type-II Frequency Doubling of Spatial and Temporal Limited Laser Light in Nonlinear Crystals. *Opt. Quantum Electron.* **2005**, *37* (6), 515–527. https://doi.org/10.1007/s11082-005-3195-8.

(9) Kuebler, S. M.; Denning, R. G.; Anderson, H. L. Large Third-Order Electronic Polarizability of a Conjugated Porphyrin Polymer. *J. Am. Chem. Soc.* **2000**, *122* (2), 339–347. https://doi.org/10.1021/ja9922330.

(10) Blanchard-Desce, M.; Alain, V.; Bedworth, P. V.; Marder, S. R.; Fort, A.; Runser, C.; Barzoukas, M.; Lebus, S.; Wortmann, R. Large Quadratic Hyperpolarizabilities with Donor-Acceptor Polyenes Exhibiting Optimum Bond Length Alternation: Correlation between Structure and Hyperpolarizability. *Chem. - A Eur. J.* **1997**, *3* (7), 1091–1104. https://doi.org/10.1002/chem.19970030717.

(11) Castet, F.; Rodriguez, V.; Pozzo, J. L.; Ducasse, L.; Plaquet, A.; Champagne, B. Design and Characterization of Molecular Nonlinear Optical Switches. *Acc. Chem. Res.* **2013**, *46* (11), 2656–2665. https://doi.org/10.1021/ar4000955.

(12) Li, D.; Ratner, A.; Marks, T. J. Molecular and Macromolecular Nonlinear Optical Materials. Probing Architecture/Electronic Structure/Frequency Doubling Relationships via an SCF-LCAO MECI π Electron Formalism. *J. Am. Chem. Soc.* **1988**, *110*, 1707–1715.

(13) Marder, S. R.; Kippelen, B.; Jen, A. K. Y.; Peyghambarian, N. Design and Synthesis of Chromophores and Polymers for Electro-Optic and Photorefractive Applications. *Nature* **1997**, *388* (6645), 845–851. https://doi.org/10.1038/42190.

(14) Saleh, B. E. A.; Jost, B. M.; Fei, H. B.; Teich, M. C. Entangled-Photon Virtual-State Spectroscopy. *Phys. Rev. Lett.* **1998**, *80* (16), 3483–3486. https://doi.org/10.1103/PhysRevLett.80.3483.

(15) Fei, H. B.; Jost, B. M.; Popescu, S.; Saleh, B. E. A.; Teich, M. C. Entanglement-Induced Two-Photon Transparency. *Phys. Rev. Lett.* **1997**, *78* (9), 1679–1682. https://doi.org/10.1103/PhysRevLett.78.1679.

(16) Walther, P.; Resch, K. J.; Rudolph, T.; Schenck, E.; Weinfurter, H.; Vedral, V.; Aspelmeyer, M.; Zeilinger, A. Experimental One-Way Quantum Computing. *Nature* **2005**, *434*, 169–176.

(17) Naik, D. S.; Peterson, C. G.; White, A. G.; Berglund, A. J.; Kwiat, P. G. Entangled State Quantum Cryptography: Eavesdropping on the Ekert Protocol. *Phys. Rev. Lett.* **2000**, *84* (20), 4733–4736. https://doi.org/10.1103/PhysRevLett.84.4733.

(18) Sarovar, M.; Ishizaki, A.; Fleming, G. R.; Whaley, K. B. Quantum Entanglement in Photosynthetic Light-Harvesting Complexes. *Nat. Phys.* **2010**, *6* (6), 462–467. https://doi.org/10.1038/nphys1652.

(19) Altepeter, J. B.; Hadley, P. G.; Wendelken, S. M.; Berglund, A. J.; Kwiat, P. G.

Experimental Investigation of a Two-Qubit Decoherence-Free Subspace. *Phys. Rev. Lett.* **2004**, *92* (14), 1–4. https://doi.org/10.1103/PhysRevLett.92.147901.

(20) Togan, E.; Chu, Y.; Trifonov, A. S.; Jiang, L.; Maze, J.; Childress, L.; Dutt, M. V. G.; Sørensen, A. S.; Hemmer, P. R.; Zibrov, A. S.; Lukin, M. D. Quantum Entanglement between an Optical Photon and a Solid-State Spin Qubit. *Nature* **2010**, *466* (7307), 730–734. https://doi.org/10.1038/nature09256.

(21) Joobeur, A.; Saleh, E. A. B.; Teich, M. C. Spatiotemporal Coherence Properties. *Phys. Rev. A* **1994**, *50* (4), 3349–3361.

(22) Dorfman, K. E.; Schlawin, F.; Mukamel, S. Nonlinear Optical Signals and Spectroscopy with Quantum Light. **2016**, *88* (December), 1–67. https://doi.org/10.1103/RevModPhys.88.045008.

(23) Schlawin, F. Entangled Photon Spectroscopy. *J. Phys. B* **2017**, *50* (203001).

(24) Schlawin, F.; Mukamel, S. Two-Photon Spectroscopy of Excitons with Entangled Photons. *J. Chem. Phys.* **2013**, *139* (24). https://doi.org/10.1063/1.4848739.

(25) Cheng, L. T.; Tam, W.; Stevenson, S. H.; Meredith, G. R.; Rikken, G.; Marder, S. R. Experimental Investigations of Organic Molecular Nonlinear Optical Polarizabilities. 1. Methods and Results on Benzene and Stilbene Derivatives. *J. Phys. Chem.* **1991**, *95* (26), 10631–10643. https://doi.org/10.1021/j100179a026.

(26) Marder, S. R.; Perry, J. W.; Bourhill, G.; Gorman, C. B.; Tiemann, B. G.; Mansour, K. Relation Between Bond-Length Alternation and Second Electric Hyperpolarizability of Conjugated Organic Molecules. *Science (80-.).* **1993**, *261* (12), 186–189.

(27) Bartkowiak, W.; Zaleśny, R.; Leszczynski, J. Relation between Bond-Length Alternation and Two-Photon Absorption of a Push-Pull Conjugated Molecules: A Quantum-Chemical Study. *Chem. Phys.* **2003**, *287* (1–2), 103–112. https://doi.org/10.1016/S0301-0104(02)00982-5.

(28) Gieseking, R. L.; Risko, C.; Brédas, J. L. Distinguishing the Effects of Bond-Length Alternation versus Bond-Order Alternation on the Nonlinear Optical Properties of Conjugated Chromophores. *J. Phys. Chem. Lett.* **2015**, *6* (12), 2158–2162. https://doi.org/10.1021/acs.jpclett.5b00812.

(29) Upton, L.; Harpham, M.; Suzer, O.; Richter, M.; Mukamel, S.; Goodson, T. Optically Excited Entangled States in Organic Molecules Illuminate the Dark. *J. Phys. Chem. Lett.*

2013, *4* (12), 2046–2052. https://doi.org/10.1021/jz400851d.

(30) Furgal, J. C.; Jung, J. H.; Goodson, T.; Laine, R. M. Analyzing Structure-Photophysical Property Relationships for Isolated T8, T10, and T12 Stilbenevinylsilsesquioxanes. *J. Am. Chem. Soc.* **2013**, *135* (33), 12259–12269. https://doi.org/10.1021/ja4043092.

(31) Lahankar, S. A.; West, R.; Varnavski, O.; Xie, X.; Goodson, T.; Sukhomlinova, L.; Twieg, R. Electronic Interactions in a Branched Chromophore Investigated by Nonlinear Optical and Time-Resolved Spectroscopy. *J. Chem. Phys.* **2004**, *120* (1), 337–344. https://doi.org/10.1063/1.1630309.

(32) Reinhardt, B. A.; Brott, L. L.; Clarson, S. J.; Dillard, A. G.; Bhatt, J. C.; Kannan, R.; Yuan, L.; He, G. S.; Prasad, P. N. Highly Active Two-Photon Dyes: Design, Synthesis, and Characterization toward Application. *Chem. Mater.* **1998**, *10* (7), 1863–1874. https://doi.org/10.1021/cm980036e.

(33) Beverina, L.; Fu, J.; Leclercq, A.; Zojer, E.; Pacher, P.; Barlow, S.; Van Stryland, E. W.; Hagan, D. J.; Brédas, J. L.; Marder, S. R. Two-Photon Absorption at Telecommunications Wavelengths in a Dipolar Chromophore with a Pyrrole Auxiliary Donor and Thiazole Auxiliary Acceptor. *J. Am. Chem. Soc.* **2005**, *127* (20), 7282–7283. https://doi.org/10.1021/ja050688l.

(34) Varanasi, P. R.; Jen, A. K. Y.; Chandrasekhar, J.; Namboothiri, I. N. N.; Rathna, A. The Important Role of Heteroaromatics in the Design of Efficient Second-Order Nonlinear Optical Molecules: Theoretical Investigation on Push-Pull Heteroaromatic Stilbenes. *J. Am. Chem. Soc.* **1996**, *118* (49), 12443–12448. https://doi.org/10.1021/ja960136q.

(35) Ramakrishna, G.; Bhaskar, A.; Goodson, T. Ultrafast Excited State Relaxation Dynamics of Branched Donor-π-Acceptor Chromophore: Evidence of a Charge-Delocalized State. *J. Phys. Chem. B* **2006**, *110* (42), 20872–20878. https://doi.org/10.1021/jp063262h.

(36) Zheng, T.; Cai, Z.; Ho-Wu, R.; Yau, S. H.; Shaparov, V.; Goodson, T.; Yu, L. Synthesis of Ladder-Type Thienoacenes and Their Electronic and Optical Properties. *J. Am. Chem. Soc.* **2016**, *138* (3), 868–875. https://doi.org/10.1021/jacs.5b10175.

(37) Cai, Z.; Vázquez, R. J.; Zhao, D.; Li, L.; Lo, W. Y.; Zhang, N.; Wu, Q.; Keller, B.; Eshun, A.; Abeyasinghe, N.; Banaszak-Holl, H.; Goodson, T.; Yu, L. Two Photon Absorption Study of Low-Bandgap, Fully Conjugated Perylene Diimide-Thienoacene-Perylene Diimide Ladder-Type Molecules. *Chem. Mater.* **2017**, *29* (16), 6726–6732.

https://doi.org/10.1021/acs.chemmater.7b01512.

(38) Wong, K.; Chao, T.; Chi, L.; Chu, Y. Syntheses and Structures of Novel Heteroarene-Fused Coplanar π -Conjugated Chromophores. *Org. Lett.* **2006**, *8* (22), 5033–5036.

(39) Lee, D.; Goodson III, T. Entangled Photon Absorption in an Organic Porphyrin Dendrimer. *J. Phys. Chem. B* **2006**, *110*, 25582–25585. https://doi.org/10.1021/jp066767g.

(40) Harpham, M. R.; Goodson III, T. Thiophene Dendrimers as Entangled Photon Sensor Materials. *J. Am. Chem. Soc. Artic.* **2018**, No. 21, 973–979.

(41) Villabona-monsalve, J. P.; Caldero, O.; Portela, M. N.; Valencia, A. Entangled Two Photon Absorption Cross Section on the 808 Nm Region for the Common Dyes Zinc Tetraphenylporphyrin and Rhodamine B. *J. Phys. Chem. A* **2017**, 7869–7875. https://doi.org/10.1021/acs.jpca.7b06450.

(42) Guzman, A. R.; Harpham, M. R.; Suzer, O.; Haley, M. M.; Goodson III, T. G. Spatial Control of Entangled Two-Photon Absorption with Organic Chromophores ¨. *J. Am. Chem. Soc. Commun.* **2010**, *132*, 7840–7841. https://doi.org/10.1021/ja1016816.

(43) Varnavski, O.; Pinsky, B.; Goodson, T. Entangled Photon Excited Fluorescence in Organic Materials: An Ultrafast Coincidence Detector. **2017**, 6–11. https://doi.org/10.1021/acs.jpclett.6b02378.

(44) Cai, Z.; Zhang, N.; Awais, M. A.; Filatov, A. S.; Yu, L. Synthesis of Alternating Donor–Acceptor Ladder-Type Molecules and Investigation of Their Multiple Charge-Transfer Pathways. *Angew. Chemie* **2018**, *130* (22), 6552–6558. https://doi.org/10.1002/ange.201713323.

(45) Payne, M. M.; Parkin, S. R.; Anthony, J. E.; Kuo, C. C.; Jackson, T. N. Organic Field-Effect Transistors from Solution-Deposited Functionalized Acenes with Mobilities as High as 1 Cm2/V·s. *J. Am. Chem. Soc.* **2005**, *127* (14), 4986–4987. https://doi.org/10.1021/ja042353u.

(46) Xiao, K.; Liu, Y.; Qi, T.; Zhang, W.; Wang, F.; Gao, J.; Qiu, W.; Ma, Y.; Cui, G.; Chen, S.; Zhan, X.; Yu, G.; Qin, J.; Hu, W.; Zhu, D. A Highly π-Stacked Organic Semiconductor for Field-Effect Transistors Based on Linearly Condensed Pentathienoacene. *J. Am. Chem. Soc.* **2005**, *127* (38), 13281–13286. https://doi.org/10.1021/ja052816b.

(47) Mondal, R.; Tönshoff, C.; Khon, D.; Neckers, D. C.; Bettinger, H. F. Synthesis, Stability,

and Photochemistry of Pentacene, Hexacene, and Heptacene: A Matrix Isolation Study. *J. Am. Chem. Soc.* **2009**, *131* (40), 14281–14289. https://doi.org/10.1021/ja901841c.

(48) Anand, S.; Varnavski, O.; Marsden, J. A.; Haley, M. M.; Schlegel, H. B.; Goodson, T. Optical Excitations in Carbon Architectures Based on Dodecadehydrotribenzo[18]Annulene. *J. Phys. Chem. A* **2006**, *110* (4), 1305–1318. https://doi.org/10.1021/jp0539573.

(49) Vázquez, R. J.; Kim, H.; Kobilka, B. M.; Hale, B. J.; Jeffries-El, M.; Zimmerman, P.; Goodson, T. Evaluating the Effect of Heteroatoms on the Photophysical Properties of Donor-Acceptor Conjugated Polymers Based on 2,6-Di(Thiophen-2-Yl)Benzo[1,2-b:4,5-B′]Difuran: Two-Photon Cross-Section and Ultrafast Time-Resolved Spectroscopy. *J. Phys. Chem. C* **2017**, *121* (27), 14382–14392. https://doi.org/10.1021/acs.jpcc.7b01767.

(50) Yang, R.; Tian, R.; Hou, Q.; Yang, W.; Cao, Y. Synthesis and Optical and Electroluminescent Properties of Novel Conjugated Copolymers Derived from Fluorene and Benzoselenadiazole (Macromolecules (2003) 36:20 (7453-7460)). *Macromolecules* **2008**, *41* (22), 8951. https://doi.org/10.1021/ma802220y.

(51) Heimel, G.; Daghofer, M.; Gierschner, J.; List, E. J. W.; Grimsdale, A. C.; Müllen, K.; Beljonne, D.; Brédas, J. L.; Zojer, E. Breakdown of the Mirror Image Symmetry in the Optical Absorption/Emission Spectra of Oligo(Para-Phenylene)S. *J. Chem. Phys.* **2005**, *122* (5). https://doi.org/10.1063/1.1839574.

(52) Schweitzer, B.; Wegmann, G.; Hertel, D.; Mahrt, R. F.; Bässler, H.; Uckert, F.; Scherf, U.; Müllen, K. Spontaneous and Stimulated Emission from a Ladder-Type Conjugated Polymer. *Phys. Rev. B* **1999**, *59* (6), 4112–4118. https://doi.org/10.1103/PhysRevB.59.4112.

(53) Ricci, F.; Carlotti, B.; Keller, B.; Bonaccorso, C.; Fortuna, C. G.; Goodson, T.; Elisei, F.; Spalletti, A. Enhancement of Two-Photon Absorption Parallels Intramolecular Charge-Transfer Efficiency in Quadrupolar versus Dipolar Cationic Chromophores. *J. Phys. Chem. C* **2017**, *121* (7), 3987–4001. https://doi.org/10.1021/acs.jpcc.6b10629.

(54) Harriman, A. Luminescence of Porphyrins and Metalloporphyrins. *J. Chem. Soc. Farady Trans. 2* **1981**, *77*, 1281–1291.

(55) Rae, M.; Perez-Balderas, F.; Baleizão, C.; Fedorov, A.; Cavaleiro, J. A. S.; Tomé, A. C.; Berberan-Santos, M. N. Intra- And Intermolecular Heavy-Atom Effects on the

Fluorescence Properties of Brominated C60 Polyads. *J. Phys. Chem. B* **2006**, *110* (25), 12809–12814. https://doi.org/10.1021/jp061010a.

(56) Seybold, P. G.; Gouterman, M. Porphyrins. XIII: Fluorescence Spectra and Quantum Yields. *J. Mol. Spectrosc.* **1969**, *31* (1–13), 1–13. https://doi.org/10.1016/0022-2852(69)90335-X.

(57) Zander, M. The Intra-Annular Internal Heavy-Atom Effect on the Fluorescence and Phosphorescence Properties of Oxygen, Sulphur or Selenium Containing Heterocyclic Systems Related to Dibenzo[b,n]Perylene. *Zeitschrift fur Naturforsch. - Sect. A J. Phys. Sci.* **1989**, *44* (11), 1116–1118. https://doi.org/10.1515/zna-1989-1113.

(58) Cho, B. R.; Son, K. H.; Lee, S. H.; Song, Y. S.; Lee, Y. K.; Jeon, S. J.; Choi, J. H.; Lee, H.; Cho, M. Two Photon Absorption Properties of 1,3,5-Tricyano-2,4,6-Tris(Styryl)Benzene Derivatives. *J. Am. Chem. Soc.* **2001**, *123* (41), 10039–10045. https://doi.org/10.1021/ja010770q.

(59) Narayanan Nair, M.; Hobeika, N.; Calard, F.; Malval, J. P.; Aloïse, S.; Spangenberg, A.; Simon, L.; Cranney, M.; Vonau, F.; Aubel, D.; Serein-Spirau, F.; Lère-Porte, J. P.; Lacour, M. A.; Jarrosson, T. One- and Two-Photon Absorption and Emission Properties of an Oligo(Phenylenethienylene)s Series. *Phys. Chem. Chem. Phys.* **2014**, *16* (25), 12826–12837. https://doi.org/10.1039/c2cp44365a.

(60) Meyers, F.; Marder, S. R.; Pierce, B. M.; Brédas, J. L. Electric Field Modulated Nonlinear Optical Properties of Donor-Acceptor Polyenes: Sum-Over-States Investigation of the Relationship between Molecular Polarizabilities (α,β, and γ.) and Bond Length Alternation. *J. Am. Chem. Soc.* **1994**, *116* (23), 10703–10714. https://doi.org/10.1021/ja00102a040.

(61) Marcano, E.; Squitieri, E.; Murgich, J.; Soscún, H. Theoretical Investigation of the Static (Dynamic) Polarizability and Second Hyperpolarizability of DAAD Quadrupolar Push-Pull Molecules. A Comparison among HF (TD-HF), DFT (TD-B3LYP), and MP2 (TD-MP2) Methods. *Comput. Theor. Chem.* **2012**, *985*, 72–79. https://doi.org/10.1016/j.comptc.2012.02.001.

(62) Ohnishi, S. I.; Orimoto, Y.; Gu, F. L.; Aoki, Y. Nonlinear Optical Properties of Polydiacetylene with Donor-Acceptor Substitution Block. *J. Chem. Phys.* **2007**, *127* (8). https://doi.org/10.1063/1.2754683.

(63) Wu, Y.; Zhu, W. Organic Sensitizers from D–π–A to D–A–π–A: Effect of the Internal Electron-Withdrawing Units on Molecular Absorption, Energy Levels and Photovoltaic Performances. *Chem. Soc. Rev.* **2013**, *42* (5), 2039–2058. https://doi.org/10.1039/c2cs35346f.

(64) Rohwer, E. J.; Akbarimoosavi, M.; Meckel, S. E.; Liu, X.; Geng, Y.; Lawson Daku, L. M.; Hauser, A.; Cannizzo, A.; Decurtins, S.; Stanley, R. J.; Liu, S. X.; Feurer, T. Dipole Moment and Polarizability of Tunable Intramolecular Charge Transfer States in Heterocyclic π-Conjugated Molecular Dyads Determined by Computational and Stark Spectroscopic Study. *J. Phys. Chem. C* **2018**, *122* (17), 9346–9355. https://doi.org/10.1021/acs.jpcc.8b02268.

(65) Thomas, K. R. J.; Lin, J. T.; Velusamy, M.; Tao, Y. T.; Chuen, C. H. Color Tuning in Benzo[1,2,5]Thiadiazole-Based Small Molecules by Amino Conjugation/Deconjugation: Bright Red-Light-Emitting Diodes. *Adv. Funct. Mater.* **2004**, *14* (1), 83–90. https://doi.org/10.1002/adfm.200304486.

(66) Gopal, V. R.; Reddy, A. M.; Rao, V. J. Wavelength Dependent Trans to Cis and Quantum Chain Isomerizations of Anthrylethylene Derivatives. *J. Org. Chem.* **1995**, *60* (24), 7966–7973. https://doi.org/10.1021/jo00129a043.

(67) Lavanya Devi, C.; Yesudas, K.; Makarov, N. S.; Jayathirtha Rao, V.; Bhanuprakash, K.; Perry, J. W. Combined Experimental and Theoretical Study of One- and Two-Photon Absorption Properties of D-π-A-π-D Type Bis(Carbazolylfluorenylethynyl) Arene Derivatives: Influence of Aromatic Acceptor Bridge. *Dye. Pigment.* **2015**, *113*, 682–691. https://doi.org/10.1016/j.dyepig.2014.09.027.

(68) Ventelon, L.; Moreaux, L.; Mertz, J.; Blanchard-Desce, M. New Quadrupolar Fluorophores with High Two-Photon Excited Fluorescence. *Chem. Commun.* **1999**, *1* (20), 2055–2056. https://doi.org/10.1039/a906182g.

(69) Cornil, J.; Dos Santos, D. A.; Beljonne, D.; Brédas, J. L. Electronic Structure of Phenylene Vinylene Oligomers: Influence of Donor/Acceptor Substitutions. *J. Phys. Chem.* **1995**, *99* (15), 5604–5611. https://doi.org/10.1021/j100015a051.

(70) Pan, G. L.; Fan, M. G.; Fan, P.; Wang, H. Z.; Wei, Z. C. Enhancement of a Two-Photon Absorption Cross Section (TPACS) — Design and Synthesis of a Novel Class of Photochromic Molecules with Large TPACS. *Chem. Commun.* **2001**, *1* (18), 1744–1745.

https://doi.org/10.1039/b102876f.

(71) Drobizhev, M.; Rebane, A.; Suo, Z.; Spangler, C. W. One-, Two- and Three-Photon Spectroscopy of π-Conjugated Dendrimers: Cooperative Enhancement and Coherent Domains. *J. Lumin.* **2005**, *111* (4 SPEC. ISS.), 291–305. https://doi.org/10.1016/j.jlumin.2004.10.009.

(72) Zhang, L.; Shen, W.; He, R.; Liu, X.; Fu, Z.; Li, M. Computational Study on the Effects of Substituent and Heteroatom on Physical Properties and Solar Cell Performance in Donor-Acceptor Conjugated Polymers Based on Benzodithiophene. *J. Mol. Model.* **2014**, *20* (11), 1–10. https://doi.org/10.1007/s00894-014-2489-9.

(73) Jagatap, B. N.; Meath, W. J. On the Competition between Permanent Dipole and Virtual State Two-Photon Excitation Mechanisms, and Two-Photon Optical Excitation Pathways, in Molecular Excitation. *Chem. Phys. Lett.* **1996**, *258* (1–2), 293–300. https://doi.org/10.1016/0009-2614(96)00620-3.

(74) Albota, M.; Beljonne, D.; Bre, J.; Ehrlich, J. E.; Fu, J.; Heikal, A. A.; Hess, S. E.; Kogej, T.; Levin, M. D.; Marder, S. R.; Mccord-maughon, D.; Perry, J. W.; Ro, H. Design of Organic Molecules with Large Two-Photon Absorption Cross Sections. *Science (80-.).* **1998**, *281*, 1653–1657.

(75) Pawlicki, M.; Collins, H. A.; Denning, R. G.; Anderson, H. L. Two-Photon Absorption and the Design of Two-Photon Dyes. *Angew. Chemie - Int. Ed.* **2009**, *48* (18), 3244–3266. https://doi.org/10.1002/anie.200805257.

(76) Zojer, E.; Beljonne, D.; Pacher, P.; Brédas, J. L. Two-Photon Absorption in Quadrupolar π-Conjugated Molecules: Influence of the Nature of the Conjugated Bridge and the Donor-Acceptor Separation. *Chem. - A Eur. J.* **2004**, *10* (11), 2668–2680. https://doi.org/10.1002/chem.200305650.

(77) Salem, M. A.; Brown, A. Two-Photon Absorption in Fluorescent Protein Chromophores: TDDFT and CC2 Results. *J. Chem. Theory Comput.* **2014**, *10* (8), 3260–3269. https://doi.org/10.1021/ct500028w.

(78) Susumu, K.; Fisher, J. A. N.; Zheng, J.; Beratan, D. N.; Yodh, A. G.; Therien, M. J. Two-Photon Absorption Properties of Proquinoidal D-A-D and A-D-A Quadrupolar Chromophores. *J. Phys. Chem. A* **2011**, *115* (22), 5525–5539. https://doi.org/10.1021/jp2000738.

(79) Liu, Z. Q.; Fang, Q.; Wang, D.; Cao, D. X.; Xue, G.; Yu, W. T.; Lei, H. Trivalent Boron as an Acceptor in Donor - π - Acceptor-Type Compounds for Single- and Two-Photon Excited Fluorescence. *Chem. - A Eur. J.* **2003**, *9* (20), 5074–5084. https://doi.org/10.1002/chem.200304833.

(80) Hu, N.; Gong, Y.; Wang, X.; Lu, Y.; Peng, G.; Yang, L.; Zhang, S.; Luo, Z.; Li, H.; Gao, F. A Successful Attempt to Obtain the Linear Dependence between One-Photon and Two-Photon Spectral Properties and Hammett Parameters of Various Aromatic Substituents in New π-Extended Asymmetric Organic Chromophores. *J. Fluoresc.* **2015**, *25* (6), 1559–1566. https://doi.org/10.1007/s10895-015-1637-7.

(81) Collette, J. C.; Harper, A. W. Properties and Chemical Environment Effects of Alkylamino Styryl Pyrazine Two-Photon Fluorophores. *Proc. SPIE Linear Nonlinear Opt. Org. Mater. III* **2003**, *5212* (November 2003), 184. https://doi.org/10.1117/12.505065.

Chapter 4
Entangled Two-Photon Excited Fluorescence

The work in this chapter is being used towards a manuscript in preparation
"*Entangled Two-Photon Excited Fluorescence and Quantum Advantage for Microscopy*"
Audrey Eshun, Oleg Varnavski and Theodore Goodson III

4.1 Abstract

The attainment of entangled two-photon excited fluorescence (ETPEF) will lead to using non-invasive light intensities for microscopy, imaging and spectroscopy while exploiting the quantum nature of entangled photons. In this paper, we investigate the ETPEF process and the experimental and molecular parameters necessary to obtain ETPEF. We report the pathway dependence of ETPEF and pathway's effects on observed fluorescence signal. We find that the observed fluorescence depends on the detuning energy between the molecule's intermediate states and the entangled photons. Molecules with small detuning energies utilize the transition pathway, where the resonance between the electronic states of the molecule and the photons leads to strong interactions, enhancing ETPEF. Conversely, those with large detuning energies use the permanent dipole pathway and do not experience this resonance effect, thus this pathway is less favorable for ETPEF. One must consider the differences in entangled photon light sources when comparing results from different experiments.

4.2 Introduction

Quantum entanglement is a curious phenomenon that has intrigued scientists since the latter part of the past century. It is an interesting property of many-body quantum states, where

one object of the state cannot be described separately from another object within the state; that is, their quantum states cannot be factored into a product of single particle states. Although entanglement was initially thought of as counterintuitive since it seemed to leave quantum mechanics "incomplete"[1], it has since been well described mathematically and proven experimentally. Quantum entanglement was originally investigated for its physical properties, towards exploring quantum mechanics with Bell inequality violations and Hong Ou Mandel interferometers.[2,3] Entanglement can be established in different particles such as atoms, electrons and photons and within them, occur in different degrees of freedom including momentum, frequency, spin, polarization, time and space. These various entangled parameters allow the concept of entanglement to be utilized for numerous applications. Over time, the entanglement characteristics of these particles have been applied to several technologies like quantum communication, cryptography and other computation operations.[4–6]

The application we are most interested in is that of quantum sensing, mainly fluorescence measurements with entangled photon pairs. Quantum entangled light generated in the form of photon pairs has a high degree of temporal and spatial correlations that present it as a powerful sensing tool.[7,8] Quantum sensing has the capability of targeted coherent control,[9] unique low noise characteristics and extremely low photon toxicity due to the low intensity of entangled light needed for experiments.[10] Measurements may be achievable with sensitivity beyond the standard quantum limit and limitations of low signal to noise ratio and resolution can be overcome while exciting photosensitive materials. Entangled light has additional parameters that can be controlled to adjust the observed signal.[11,12] Researchers have found that the efficiency of absorbing entangled light is dependent on the degree of frequency correlations of the light and thus, it is possible to enhance signals with highly correlated entangled light.[13,14]

Furthermore, the momentum and polarization correlations can be exploited to conduct spectroscopy in new spectral ranges.

Recently, advances in our understanding and manipulation of quantum light have led to its growing use as a spectroscopic tool. We specifically want to look at the induced fluorescence from the entangled two-photon absorption (ETPA) process. Entangled two-photon excited fluorescence (ETPEF) is a new and promising field and in this article, we will be focusing on its potential and how best to achieve it. Classical fluorescence spectroscopy in general is more selective than UV/Vis absorption[15] and this reflects in different ways with entangled two photon excitation. As early as 1997, ETPEF was suggested.[16] Despite the early suggestion, ETPEF was not conducted until recently due to the initial challenges associated with it. Measuring ETPEF is not a trivial task. The use of low light intensities for excitation often result in low fluorescence counts that require specialized equipment for precise measurements. Accurate confinement of the experimental setup is necessary so as to improve signal to noise ratios and systems had to be designed to ensure the maximum fluorescence collection. ETPEF was first measured with non-classical light in atoms.[17,18] Since then, strides have been made in our understanding of entangled photon sources and fluorescence collection to lead to the first observation of ETPEF in a molecule[19], followed by multiple experimental realizations of ETPEF in various forms, with different entangled photon sources and different experimental setups.[20–23]

In this chapter, I looked at the process of ETPEF, optimizing our experimental setup for ETPEF measurements and conduct a study on EPTEF observations to understand the necessary parameters to observe ETPEF. I will include a detailed description of the ETPEF setup and data collection. I will discuss in-depth the experimental data on ETPEF and with the aid of

electronic structure calculations, determine the molecular and experimental parameters necessary for ETPEF.

4.3 Fluorescence process

The correlations exhibited by photon pairs led researchers to consider the prospects of using entangled light for TPA. Since entangled photon pairs are highly correlated in time, the arrival of one is almost simultaneously followed by the arrival of the next and as a result, absorbing material placed in the beam path would simultaneously absorb both photons of the biphoton pair and ETPA would occur. Due to these strong temporal correlations, the rate of ETPA, is linearly dependent on the photon intensity, i.e., $\boldsymbol{R_e} = \boldsymbol{\sigma_e}\emptyset$ where σ_e is the ETPA cross-section and $\emptyset$ is the photon flux density. The time within which this simultaneous absorption of photons can occur is known as the entanglement time T_e and it is dependent on the entangled light generation source. The interaction of the entangled light with the electronic states of the absorbing matter is evaluated with second-order perturbation theory and is given as:[19,24]

$$\sigma_e = \frac{A}{\hbar^2\varepsilon_0^2 A_e T_e}\omega_0^2\delta(\varepsilon_f - \varepsilon_g - 2\omega_0) \times \left|\frac{1-exp[-i(\omega_0+\varepsilon_g-\varepsilon_e)T_e-T_e\kappa_e/2]}{(\omega_0+\varepsilon_g-\varepsilon_e)-i\kappa_e/2}\mu_{ef}.e_i\mu_{ge}.e_s + \frac{1-exp[-i\omega_0T_e-T_e\kappa_g/2]}{\omega_0-i\kappa_g/2}\mu_{gf}.e_i\mu_{gg}.e_s + \frac{1-exp[-i\omega_0T_e-T_e\kappa_f/2]}{-\omega_0-i\kappa_f/2}\mu_{ff}.e_i\mu_{gf}.e_s\right|^2 \quad \text{Eq. 4.1}$$

Where A_e and T_e are the entanglement area and entanglement time, ω_0 is the frequency of the signal and idler photons, ε_g, ε_e and ε_f are the frequency of the ground, intermediate and final states respectively. Thus, $\Delta = \varepsilon_e - \varepsilon_g - \omega_0$ is the detuning energy, μ_{ij} are the transition dipole matrix elements with μ_{jj} referring to the permanent dipole of an energy level and κ_j the state linewidths. This analog to the equation derived by Fei et al shows that ETPA involves two different pathways. The first term of Equation 1 involves ETPA through the transition dipole pathway, where the detuning energy is small and ETPA occurs through an intermediate

level (Fig.4.1(b)). The second and third terms involve ETPA through the permanent dipole pathway, where there is a large detuning energy and the ETPA is dependent on the difference in dipole moment between the ground and final states (Fig.4.1(c)). The relaxation of the excited state leads to fluorescence emission as shown in Figure 4.1.

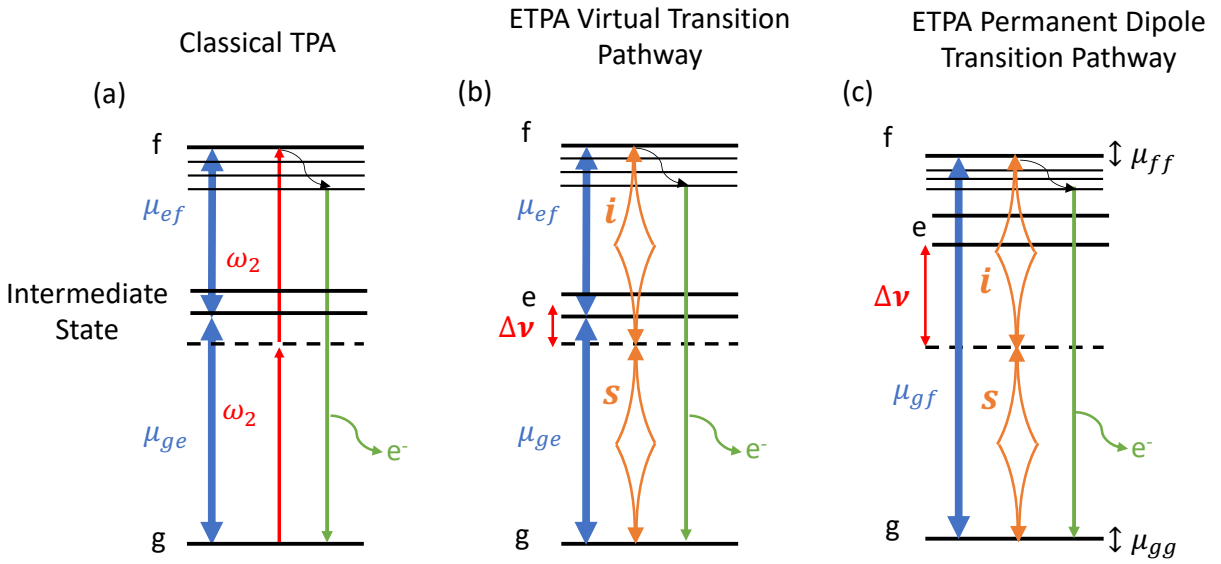

Figure 4.1. *Schematic of classical TPA showing classical photon pairs exciting a molecule from the ground state through an intermediate state to the final student. (a) Classical TPA diagram includes transition dipole moments and two-photon excited fluorescence. The detuning energy is extremely important for ETPA and less so for classical ETPA. (b) shows ETPA through the virtual transition pathway. The sample is excited with entangled signal and idler photon pairs through a virtual state which is in resonance with the pump energy thus, the transition dipole moments contribute significantly to the ETPA process. For ETPA through the permanent dipole pathway (c), there is a large detuning energy and the permanent dipole contributes significantly to the ETPA process. Both ETPA schematics show the resulting fluorescence emission.*

In the virtual transition pathway (Fig.4.1(b)), the intermediate states in resonance with the entangled photons leads to a strong interaction coupling between the molecule's states and the entangled photons. This perhaps causes an enhancement in the ETPEF signal and fluorescence is observed. On the other hand, molecules with larger detuning energies (Fig.4.1(c)) do not experience this interaction enhancement and ETPEF becomes less likely to be seen or will not

be seen at all. This will be explored and discussed later in this work. In addition, the linewidth of ETPA is dependent on the excited state lifetime, whereas that for classical TPA is assumed to be independent of the final state.[25]

Fluorescence in general is highly favorable for spectroscopic measurements due to the lack of intrinsic background and the good signal-to-noise ratio it provides. Similar to with classical excitation, fluorescence from ETPA originates from a relaxed excited state and the entanglement induced fluorescence detected is a measure of the state population created by the ETPA process. Fluorescence is vital in imaging through fluorescence microscopy, and with ETPEF, this critical imaging will be achievable for delicate materials by utilizing the low photon flux capabilities of quantum light. The strong correlations of entangled light allow for targeted excitation of particular pathways, resulting in enhanced signals with ETPEF.[26–28]

4.4 Experimental

4.4.1 Experimental Overview

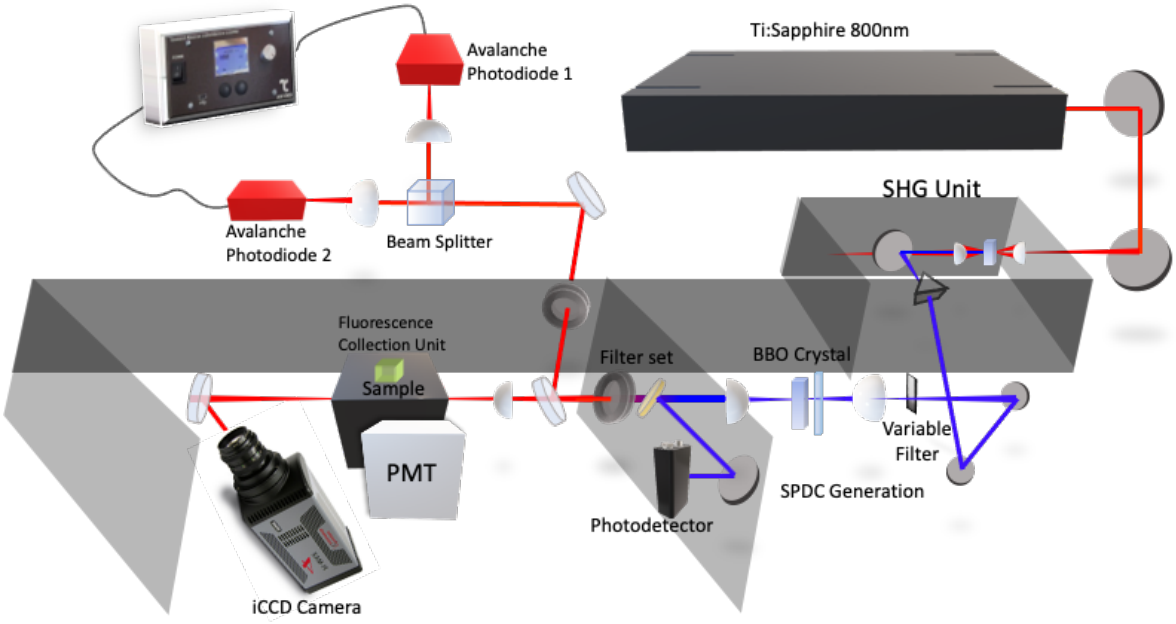

***Figure 4.2**. Experimental setup for entangled two-photon excited fluorescence.*

Our entangled two-photon excited fluorescence involves the entangled pairs generated by SPDC exciting a sample placed in a specialized unit and the resulting fluorescence measured with a photomultiplier tube (PMT). Our entangled photon setup is as seen in Figure 4.2. A mode-locked Ti:Sapphire 800nm laser with 100fs pulses and 80MHz repetition rate is used to pump a 1mm thick BBO crystal for second harmonic generation (SHG). The resulting 400nm beam pumps a 0.5 mm or 1 mm thick BBO crystal for frequency degenerate Type-II SPDC $\left(\omega_1 = \omega_2 = {}^{\omega_p}/_2\right)$. After down-conversion, a dichroic mirror and interference filter are utilized to separate all 400nm light before the measurement box which is adequately blocked off from all pump light. All fluorescence measurements are taken in a specifically designed fluorescence collection unit (FCU) as shown in the insert of Figure 4.3. The fluorescence collection unit has a hemispherical mirror and spherical cap that form an enclosed reflecting surface ensuring maximum fluorescence directed towards the cooled PMT (R7518P Hamamatsu) where fluorescence counts are taken in a photon counting mode. The sample cuvette is placed in the center of the collection unit for measurements. An iCCD camera is used to check the spatial arrangement of the SPDC cones. The input flux is measured with avalanche photodiodes (Perkin Elmer SPCM-AQR-13) either as singles or in coincidence.

4.4.2 Entangled Light Generation for ETPEF Experiments

Currently, the most commonly used method for generating quantum entangled photon pairs and the method we utilize is spontaneous parametric downconversion (SPDC). Decades of research on optical parametric processes for nonlinear optics have provided a great understanding of the spatial and spectral properties of the emitted light and developed our ability to control it. SPDC involves the interaction of a strong pump beam of frequency ω_p

with a $\chi^{(2)}$ nonlinear crystal, resulting in the emission of a pair of lower energy photons (the signal ω_s and idler ω_i photon) such that their energy adds up to that of the pump, $\omega_s + \omega_i = \omega_p$, due to energy conservation.[29] The pump beam must be intense enough to drive the process into the nonlinear regime, and these second order interactions cause the annihilation of the pump and the creation of the two downconverted photons.[30] In addition to energy conservation, there is also the total conservation of momentum defined by the phase-matching conditions of the propagation constants of the interacting constants, $k_s + k_i = k_p$. These phase-matching conditions determine the spatial arrangement and propagation direction of the generated photons, imparting spatial correlations between the photon pairs. These correlation properties govern the angular and temporal widths of the coherence function which in turn determines the coincidence rate of the signal and idler photons.[31] The nonlinear crystals used for SPDC such as β-barium borate (BBO), lithium niobite (LN) and potassium titanyl phosphate (KTP) differ in their birefringent properties which lead to different types of SPDC. The different phase-matching conditions of these SPDC types result in particular polarizations of the photon pairs. Periodically-poled SPDC utilizes ferroelectric crystals with very high nonlinearity that can be modulated. Periodically-poled crystals have quasi-phase matching with the conditions $k_p = k_s + k_i + \frac{2\pi}{\Lambda}$ (where Λ is the grating period).[32,33]

Alternatively, a source of entangled photon pair generation less commonly used for TPA experiments but has recently been used towards fluorescence measurements is squeezed light. These quantum correlated twin beams have low noise levels that can fall below zero point fluctuations and have been described as having "less noise than no light at all."[34] Squeezed light has a reduced quantum uncertainty compared to light in a coherent state. The uncertainty region is "squeezed", thus its width is reduced in one quadrature and increased in another,

usually these are the amplitude and phase quadratures. These highly correlated squeezed twin beams with high photon numbers can be generated through a process known as four wave mixing (FWM) in a $\chi^{(3)}$ nonlinear material.[35,36] Two photons from a strong pump field are mixed with a weak probe field to produce a 4th beam called the conjugate with phase-matching conditions $k_{pr} + k_c = 2k_p$ and with frequency $\nu_{pr} + \nu_c = 2\nu_p$ where the indices pr, c and p represent the probe, conjugate and pump beams respectively.

Table 4.1 Typical Photon Flux of Photons for Different Generation Method

Generation Method	**Typical Photon Flux per 100mW (photons/s)**
Type-II SPDC in BBO[37]	1x10^7
Type-I SPDC in BBO[38]	5x10^7
Type-0 SPDC in PPLN [39]	1x10^{15}
Squeezed light via FWM [40]	1x10^{16}

Different types of entangled pair generation result in different photon fluxes and typical values for SPDC types and 4WM are shown in Table 4.1. Squeezed light can generally be used to achieve orders of magnitude higher photon flux than SPDC. However, the typical 10^7 flux of type-II SPDC has been shown to be high enough to conduct spectroscopic experiments but low enough to avoid photodamage. While a source generating photons with a high flux may seemingly be beneficial for sensitivity and efficiency of interaction with the molecule under study, this may not necessarily be the ideal case. It is essential that while having a photon flux high enough for experimental results to be seen, the photon pairs should still maintain nonclassical properties. Dayan et al studied this flux boundary, where the photons can still be considered as exhibiting properties of entanglement. This critical maximal flux, Φ_{max}, was connected to the bandwidth (Δ) of the photon pair, and said to scale linearly with it as:[41]

$$\Phi_{max} \cong \Delta$$

After this Φ_{max} value is passed, the quantum effects of the photon pairs are no longer observed. The nonclassical properties exhibited in sum frequency generation (TPA in our case) are a result of the part of the TPA process that has linear intensity dependence.[42] $\boldsymbol{R = \sigma_e \emptyset + \delta_R \emptyset^2}$ As the overall rate of TPA shows, ETPA only occurs with a linear intensity of photon flux and as the intensity increases, random TPA takes precedence. As the ETPA process requires the simultaneous absorption of both photons within some entanglement time, it is sensitive to the relative time delay between the photons and this time scale is in turn inversely proportional to their bandwidth Δ. This is additionally written as the rate of TPA event being dependent on the photon number (n) and bandwidth:[41]

$$R \propto \Delta(n^2 + n)$$

From this dependence on Δ, it is apparent that the rate of TPA is inversely proportional to the temporal separation of the photons. Thus, narrow bandwidths of squeezed light may result in a lower Φ_{max}. The high photon flux of the squeezed light source can lead to observable spectroscopic events, but these could be beyond the linear region where quantum effects take place. Alternatively, while type-II SPDC may have a lower photon flux, it has been shown to be high enough to conduct spectroscopic experiments staying in the range of linear dependence.[37] In ETPEF measurements, there is therefore the compromise between high flux and maintaining the nonclassical effects of the photon pairs.[43]

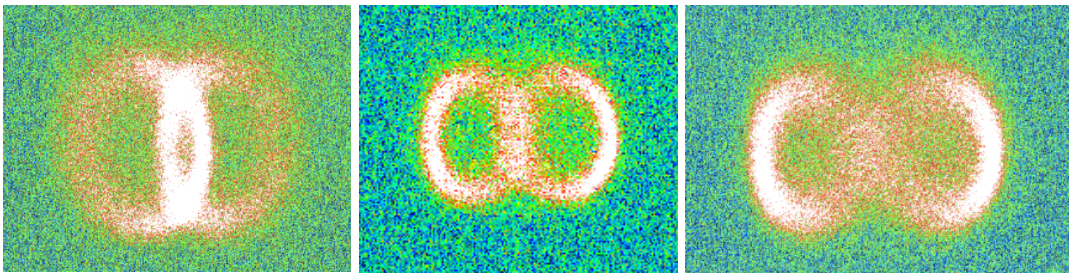

Figure 4.3. *SPDC Spatial arrangement imaged with the iCCD camera. From left to right: Non-collinear, collinear, spatially separated.*

Our SPDC photons are generated by pumping a BBO crystal placed in a rotating holder, such that the angle of the crystal with respect to the beam can be tuned to alter the phase-matching conditions. A focusing lens with focal length 6cm is placed in front of the BBO crsytal to focus the pump onto the crystal center. A blue filter, with transmission from ~380 – 480nm is placed in front of the BBO to ensure any leaked 800nm from the fs pump laser has been removed. Another lens is placed 6cm after the BBO crsytal for focusing of the SPDC photons. A 1 inch dichroic mirror with a 650nm cutoff, followed by an interference filter (12nm transmission centered at 800nm), are used to filter out any excess 400nm light after SPDC generation. In order to confirm the generation of SPDC photons and select the appropriate phase-matching conditions for experiment, the SPDC photons are directed to the iCCD camera for imaging. As the SPDC photons are not visible to the eye, the interference filter and dichroic mirror are removed for alignment to be done with the residue of 400nm light.

It is essential that for Type-II SPDC, the SPDC image is detected as rings as seen and not as a dot. The lack of rings signifies either a strong leak of pump light or incorrect alignment of the optics for SPDC generation. The image of the SPDC spatial arrangement from our experimental setup is shown in Figure 4.3 in 3 different phase-matching conditions namely non-collinear, collinear and spatially separated from left to right. From previous studies,[20] it was shown that the collinear phase-matching arrangement yielded the best entangled two-photon excited fluorescence intensity. Therefore, for experiments in this study, experiments were carried out with the rings arranged as shown in the second image of Figure 4.3. Furthermore, once this arrangement had been set, intensity scans ran changing angle slightly.

4.4.3 Fluorescence Collection & Measurements

For entangled two-photon excited fluorescence ETPEF measurements, the entangled photon beam is focused with a collimating lens onto a sample which is placed in a specially designed fluorescence collection unit (FCU) as shown in Figure 4.4(a). This unit was designed to increase for high geometric efficiency optical collection of fluorescence light from the sample which is held in a 1cm quartz cuvette cell at the assembly center. The FCU was manufactured by single-point diamond turning and consists of an Ag-coated hemispherical mirror and Ag-coated spherical cap mirror whose optical apertures are matched such that the assembly forms a spherically-enclosed reflecting surface with output ports allowing entry and exit of the entangled beam and an output port to which the fluorescence light is directed.[20,44] This unit was described in detail by Özgun Suzer in his dissertation work.[44] The mirror surface of the FCU is designed such that it is centered on the sample in a way that all the emitted light originates from the center of the mirror, and subsequently all the light is reflected towards the output port of the spherical cap. The interior of the FCU as well as a schematic of the fluorescence emission sample are shown in Figure 4.4. As seen in Figure 4.4(b), the emission is spread in all directions, therefore, the aim of the FCU is to efficiently direct this emission to the output port where the detector is placed. In the output port, a longpass filter cut on 435nm, is placed to ensure no leaking or scattered 800nm excitation light is read by the detector. In addition, a 1 inch focusing lens is placed in the output after the filters to collimate the fluorescence to the detection system. The collection effiency of the FCU was calibrated with blue light excitation and calculated to be 17% for fluorescence centered at 450nm.[20]

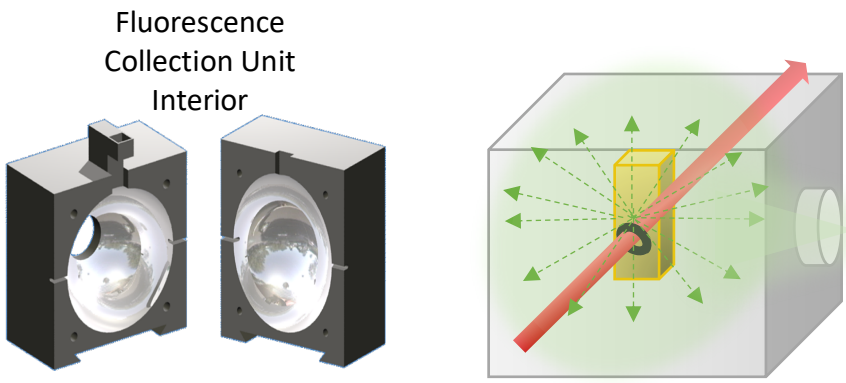

Figure 4.4. *(a) Interior of the fluorescence collection unit. (b) Schematic of sample emission after excitation in the FCU.*

The fluorescence that is collected by the FCU is detected by a photomultiplier tube (R7518P, Hamamatsu) in a photon counting mode. The quantum efficiency of the detector at 800nm is below 0.1%, ensuring no scattering of entangled photons is measured as it is not sensitive to light at this wavelength. The PMT regularly has a low dark count rate of ~ 10 photons/s, however, it is housed in a thermoelecrtic cooler. This reduces the thermal electrons emitted from the PMT photocathode and improves signal to noise ratio with a built in electrostatic and magnetic field. Thus, we are able to reduce dark count rate to as low as ~1 photon/s. The thermoelectric cooler (Hamamatsu C9144) is cooled down to 0ºC when ready to use and can be cooled down to -15 ºC for measurements. Fluorescence counts measurements are monitored with a LabView program written by Brian Pinsky for the work in Ref 20. In this program, manual collection of data can be chosen and for a typical scan, parameters can be entered as shown below:

Number of Large Steps - 1

Large Step Distance - 0.1

Number of Small Steps - 50 (to 100)

Small Step Distance - 0.0001

Photons/step - 10

The number of small steps can be increased to increase collection time. The small step distance is kept small to remain at the same input power. Photons/step determine how many photons should be counted before providing an average value of counts/s. This can also be changed to improve the data collection and is usually kept low when signal to noise levels are good.

For a molecule for which the ETPA cross-section has already been measured, a photon budget for fluorescence under entangled two-photon excitation can be calculated. The excitation rate can be estimated from the ETPA absorption rate, concentration, input flux and the number of excited molecules (proportional to the photon coincidence rate). With the excitation rate, collection effiency of the FCU (17%), efficiency of the interface connecting the FCU to the PMT (0.25%), the PMT quantum effiency at the emission wavelength and the losses from filters and reflective surfaces (0.62%), the detected fluorescence signal can be calculated. For a bisannulene molecule with ETPA rate of 3.6%, excited molecules at 6 x 10^5 pairs/s, quantum yield 45% and with the PMT quantum efficiency at its fluorescence wavelength being 23%, the estimated fluorescence counts are expected to be 5.8 counts/s. In experiments, counts for bowtie bisannulene have been detected in the signal range of 1-2.5 counts/s.[20] The smaller number in experiment versus the estimated value can be attributed to entanglement losses which are not considered in the calculation.

4.4.4 Experimental characterization

As experiments with ETPEF involve very low fluorescence counts, it is imperative to have a well characterized detection system. This is necessary for two purposes. Firstly, it ensures the dark count rate is low and there is a good signal to noise ratio. This is necessary for differentiating background counts from fluorescence signal. Secondly, characterization

measurements must be carried out with solvent at different intensities to ensure that the filters cut out any scattering effects and that the signal measured is indeed fluorescence. An example of signal measurements is shown in Figure 4.5. Initially, a dark count scan is run with the laser shutter closed to establish the background rate that the PMT may measure from the setup conditions. This is usually on the order of ~ 0.8 to 1.5 photons/s. Solvent is placed in the 1cm quartz cuvette and the laser shutter open for the beam to transmit through the sample. Multiple counts are taken by the PMT over a collection time that can be varied anywhere from 1 to 10 minutes. The counts are then averaged to obtain counts for that particular input photon rate. The counts around the blue line in Figure 4.5 show these counts that are used for averaging. For solvent scans, the filters should cut off any scattering such that the photon counts are close to the dark count rate. Furthermore, as the laser intensity is increased, counts from the solvent scan should stay relatively the same within the standard deviation and should not show a linear increase with laser intensity. The dark count rate is subtracted from the solvent counts to obtain the solvent baseline measurement.

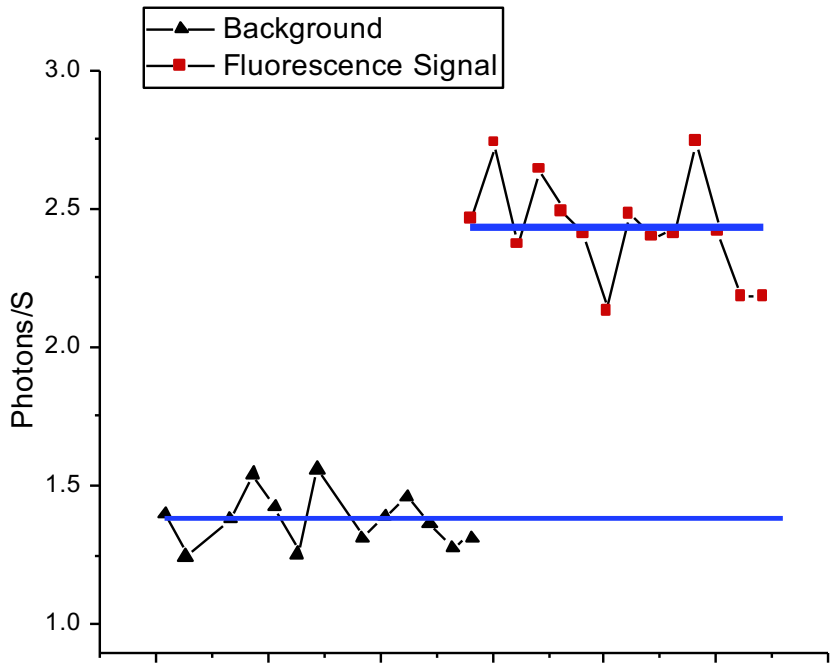

Figure 4.5 *Graph showing PMT counts for solvent (black) and for a triannulene compound (red) to be averaged to obtain signal at a specific input photon flux.*

The solvent can then be replaced with the sample under investigation. Unlike with solvent, ETPA active chromophores show an increase in counts when the entangled photons are transmitted through the cuvette and excite the sample. Fluorescence signal of a triannulene molecule is shown in red in Figure 4.5 and there is a clear distinction between the entangled two-photon induced fluorescence in a sample and the counts through solvent only. The dark count rate is also subtracted from the averaged fluorescence counts to obtain the actual fluorescence counts. In Figure 4.5, the signal from the excited sample is 1.05 photons/s compared to the 0.16 photons/s from the solvent. The standard deviation in a fluorescence scan is usually from 0.10 to 0.5 photons/s depending on the length of the collection time. The standard deviation for a reference solvent scan is used to determine the error bars for the measurements as it takes into consideration any scattering. The fluorescence rate is typically

three to seven times higher than the standard deviation in the reference solvent. Long scans are taking at different input intensities and the averages of these scans lead to the plot of ETPA fluorescence signal as a function of input photon flux as shown in Figure 4.6. This. Graph shows the linear ETPEF for a triannulene chromophore, the ETPA cross-section of which was measured previously.[45] It can clearly be seen that the fluorescence signal increases linearly as a the input photon flux is increased. With long collection times and optimal characterization of signal to noise ratio, signals of as low as 0.2 photons/s can be detected.

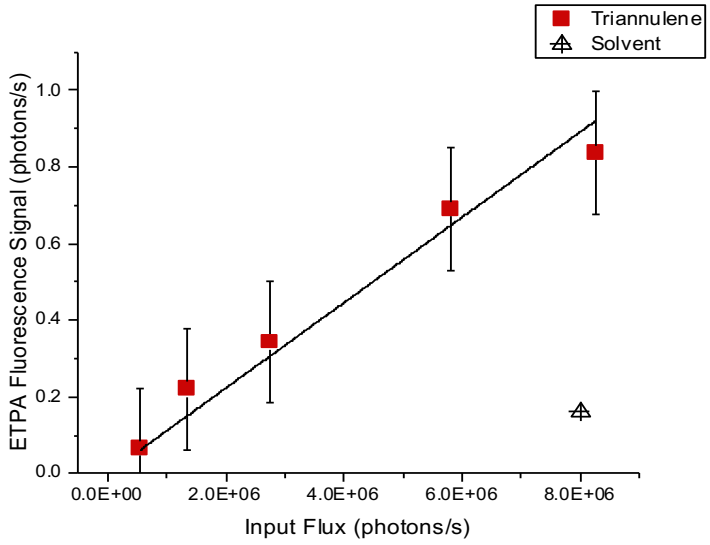

Figure 4.6. *Linear ETPEF signal of a triannulene compound. ETPA fluorescence signal shown as a function of input flux.*

4.5 Computational Methods

Computational methods were used to determine the electronic structure and excitation properties of the compounds. These quantum chemical calculations were carried out using the Gaussian g09 package in the 6-31G (D) basis set. Geometry optimizations and Time Dependent-Density Functional Theory (TD-DFT) calculations were performed to obtain transition dipole moments, permanent dipole moments and energy levels of the molecules under consideration. The geometries of the ground state (S_0) were optimized with the

aforementioned basis set in order to perform further calculations. All calculations were done taking into consideration the necessary solvent.

4.6 Results and Discussion

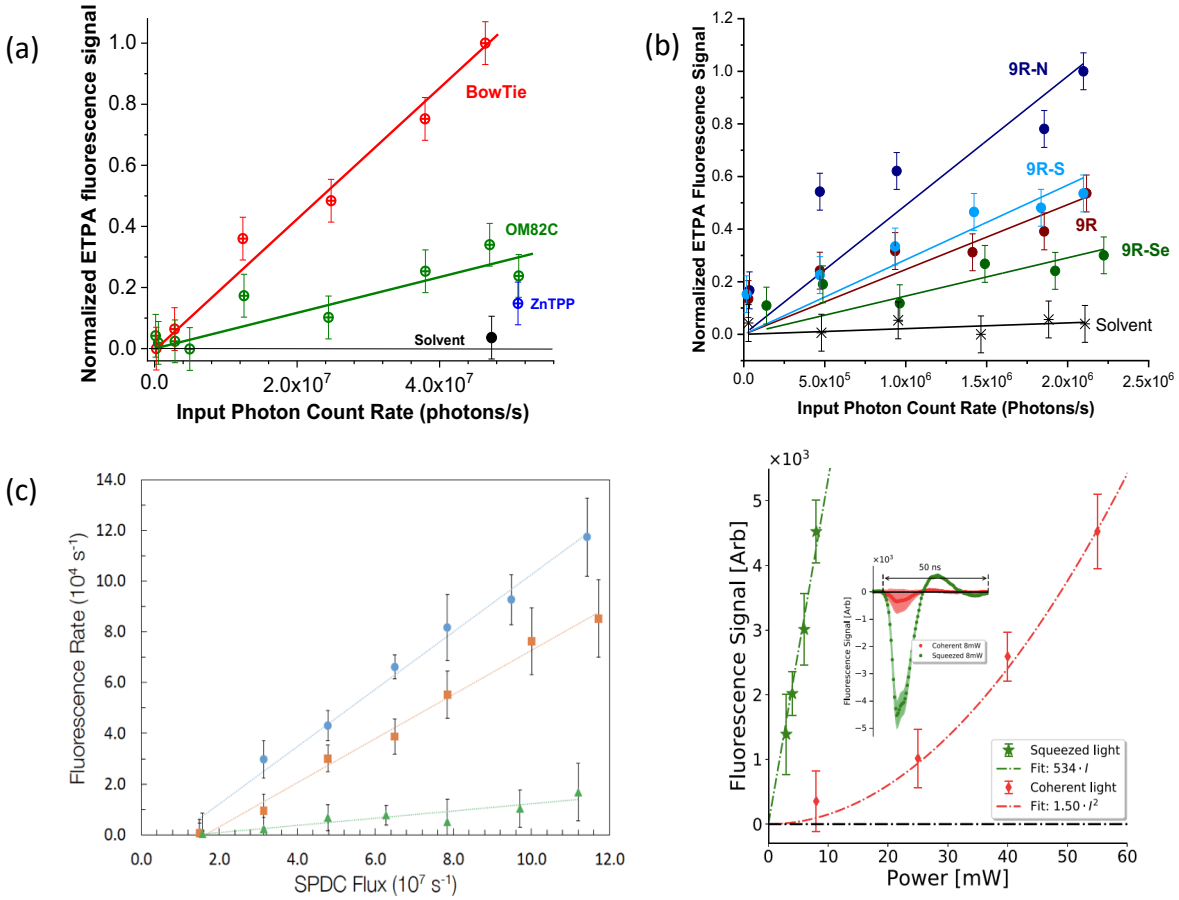

Figure 4.7 *ETPEF of (a) bisannulene, OM82C dendrimer and ZnTPP, (b) 9R-N, 9R-S, 9R and 9R-Se, (c) different concentrations of Rh-6G as a function of input photon rate. (d) ETPEF of DCM dye as a function of input power. Inset shows linear fit of ETPA dependence at lower input power*

Table 4.2. Properties of Molecules Studied with ETPEF

Molecule	Quantum Yield	Transition Energies (eV)	Transition Dipole Moments (D)	Detuning Energy Δ (cm^{-1}) /eV	μ_g (D)	μ_f (D)	Experimental TPA Cross-Section
Bowtie	0.45	2.4702 2.5325 2.7876 2.7924	7.912 27.98 0.000 91.36	7472 7965 10022 10060	0.0012	3.11	$3.2x10^{-17}$

		2.8843 2.9098	0.000 22.00	10802 11007			
9R	0.21	2.853 3.264	10.73 0.114	10549 13864	3.14	14.56	8.10×10^{-19}
18T [25]	0.08	2.42 2.62 2.72 2.72 2.82 2.94 3.01 3.03 3.11	14.31 0.072 0.411 6.587 0.044 7.842 4.427 0.051 0.574	7057 8670 9477 9477 10283 11251 11816 11977 12622	--	--	7.10×10^{-19}
Stilbene derivative[46]	0.88	3.49 4.10	13.1 9.3	15687 20607	--	--	$<< 1 \times 10^{-20}$
Fluorescein	0.97	3.134 3.186 3.902	9.510 2.665 0.022	12701 13120 18892	7.94	9.11	$>> 1 \times 10^{-17}$
DCM	0.43	2.549 3.419 3.6616	53.02 10.03 4.576	7982 14999 16954	5.6	26.3	1.30×10^{-18}

Quantum chemical calculations were carried out using the Gaussian g09 package in the 6-31G (D) basis set on some molecules that have been studied with ETPEF, along with values calculated in previous works.[25,46] Transition energies, transition dipole moments and detuning energies were calculated and are shown in Table 4.2 along with fluorescence quantum yield, and experimental ETPA cross-sections. Of the molecules shown, bowtie demonstrates very high ETPEF signals compared to most molecules we have studied. The two compounds 9R and thiophene dendrimer[37] show significantly measurable ETPEF while the stilbene derivative which we expected to show high ETPEF due to its huge classical cross-section, has a relatively weak ETPA response compared to other molecules[19] and no ETPEF has been detected with our experimental conditions in solution. The ETPEF of Fluorescein and DCM were measured with squeezed light.[40] Fluorescein showed linear ETPEF at all powers and the fluorescence of

DCM had a polynomial fit, with linear behavior at lower intensities. All molecules have relatively high fluorescence quantum yields, so although it is typically easier to conduct fluorescence measurements on molecules with higher quantum yields, this is not the deciding factor. In fact, ZnTPP and 9R-Se which had smaller quantum yields of 0.04 and 0.03 respectively, did show ETPEF.

Bowtie which has considerable ETPEF signal, has some transition energies with relatively small detuning energies of ~7500cm^{-1} as seen in Table 4.2. Many theoretical works have considered that the detuning energy plays a role in the ETPA process, but Burdick *et al* conducted a more comprehensive computational study of the effect different properties have on ETPA, including the detuning energy.[26] It was shown that based on the ETPA equation (Eq. 4.1), the inversely proportional relationship between the detuning energy and the cross-section results in higher cross-sections for smaller detuning energies,[26] but how does this reflect physically in the molecule and the observed ETPEF? A small detuning implies that there are some intermediate energies close to resonance with the entangled photons. Thus, these intermediate states are able to interfere with and interact strongly with the entangled photons. We suggest that this interaction causes a coupling between the intermediate and entangled states, and this quantum interference results in enhancements in the ETPEF response. With small detuning, the virtual transition pathway is dominant, and the transition dipole moments contribute significantly to the ETPEF. The high dipole moments of 7.9D, 27.9D and 91.3D, along with the small detuning energies make bowtie an ideal molecule for the virtual transition pathway and along with the high cross-section of 3.2x10^{-17} cm^2/molecule measured and its high quantum yield, lead to the high ETPEF observed. Furthermore it was reported that in the

virtual state pathway, there is an interference of the intermediate states causing a coupling of the transition moments and an enhancement to ETPEF.[26]

Conversely, 9R has higher detuning energies of ~10,500cm^{-1} suggesting the coupling between its intermediate states and the entangled photons is not as high as that for bowtie. It follows that there is not such an enhancement in its ETPEF signal due to coupling and a smaller cross-section of 8.1x10^{-19} cm^2/molecule is observed with the transition dipole moment of 10.7D. Interestingly, 9R has a significant permanent dipole difference (μ_f - μ_g), suggesting that the permanent dipole pathway may contribute and there will be an interference of the different pathways.[26] The difference between the magnitude of cross-sections of bowtie and 9R support the higher fluorescence signal seen for bowtie. However, it should be noted that the variation in fluorescence observed for the two compounds was not as large as their difference in cross-section magnitude. Similar to bowtie, 18T has smaller detuning energies ~7000cm^{-1} and we believe it would undergo ETPEF through the virtual transition pathway. Although this should result in some enhancement from the strongly coupled states leading to observable ETPEF, it is noted that the transition dipole moments for 18T are lower than those for bowtie so the ETPEF signal would be lower. This is in accordance with experimentally measured cross-section of 8.1x10^{-19} cm^2/molecule via the transmission ETPA method.

The ETPEF of DCM and Fluorescein were measured with squeezed light and therefore with a much higher flux than was used for the SPDC experiments. Different excitation powers were used for the two chromophores. A lower power, in the microwatt regime, was enough to reach the critical flux for DCM. The ETPEF curve has a polynomial fit, with the linear part of the curve corresponding to the quantum effects from the entangled photons. It is interesting that such low powers of squeezed light are enough to cause ETPEF and overcome the critical

flux. It could be that DCM has ideal electronic level properties for ETPEF, thus the fluorescence is observed early and not much power is needed for random TPA to supersede. The calculated values for DCM justify this hypothesis. DCM has a low detuning energy of ~8000 cm^{-1}, suggesting the virtual pathway is utilized and there is high coupling between the intermediate states and the entangled photons. This small detuning along with the high transition dipole moments of 53.02D and 10.03D would lead to good ETPEF signals, hence lower powers will be sufficient to achieve this. Additionally, the measured cross-section of DCM is $1.31x10^{-18}$ cm^2/molecule. Critical flux can also be considered as a ratio of the entangled and classical TPA cross-sections, $\Phi_{max} = {}^{\emptyset_e}/_{\delta_r}$. Thus the high classical TPA cross-section of 5100 GM[47], plays a role in lowering DCM's critical flux.

On the other hand, more power is utilized to obtain ETPEF signal from Fluorescein and to reach its critical flux, thus a full linear fit can be seen (Figure 4(d)). The classical TPA cross-section of Fluorescein (36 GM[48]) is orders of magnitude smaller than that of DCM which makes Fluorescein more likely to have a higher critical flux and subsequently a higher ETPA cross-section due to the critical flux ratio. From our calculations, the smallest detuning energy for Fluorescein is on the order of ~12700cm^{-1}. As such, there would not be as strong a coupling between the intermediate states and the entangled photons. This may be why a higher flux was needed for Fluorescein's ETPEF signal to be seen. However, the detuning energy is not large enough that there is no ETPEF observed. A compelling question is whether ETPEF would be observed for Fluorescein with a lower flux source such as SPDC.

While these molecules will justifiably show varying ETPEF responses, the stilbene derivative was shown to have no observable ETPEF response with the experimental conditions of SPDC excitation source and the sample in solution. For a molecule with such a high classical

TPA cross-section[19,46], this was not expected. In fact, the transition dipole moments have been shown to contribute to its high classical cross-section.[46] The detuning energies obtained from the calculated transition energies of this stilbene compound, at ~16,000 and ~20,000 are higher than those of the other compounds. The intermediate states being so far off from resonance from the entangled photons would result in the permanent dipole pathway being the dominant excitation pathway. Previous work showed that computationally, larger detuning energies would negatively affect ETPEF[26] but what would the physical manifestation of this be in the molecule? The further off the intermediate states are from resonance with entangled photons, the weaker their interaction is likely to be. This resonance effect is less prominent for classical light as extremely high photon intensities are used, so nonlinear behavior is still achievable through the permanent dipole pathway. Similar enhancements due to resonance effects are seen with classical light where the cross-section increases the closer to resonance.[49] However, this is not a requirement and a classical TPA response can still be easily observed without it. However, for the permanent dipole pathway in ETPEF, as the intermediate states are not in resonance with the entangled photons, we do not have great interaction between the molecule's intermediate states and the entangled light and without this, ETPEF is not observed with such low intensities of light. Javanainen *et al* noted that a nearly resonant intermediate state is necessary to experimentally observe the effects of excitation with down-converted light,[50] although the maximum number stated is much smaller than we have found to be needed experimentally. While a pathway may have a large transition probability, if it also has a large detuning there is a tradeoff between the two and the large detuning could negatively affect the observed signal. This we believe is the case for the stilbene derivative. It becomes apparent that with entangled light, the permanent dipole pathway is not ideal for ETPEF, and rather the

virtual transition pathway is preferred and takes precedence. We question whether the higher intensities of squeezed light excitation would cause the stilbene derivative to show ETPEF. Would this result in completely random TPA and a quadratic fit or will the flux of squeezed light be high enough for linear ETPEF to first be observed?

Interestingly, Burdick *et al* also computed that the cross-sections for the virtual transition pathway showed some deviation from a classical-like approximation while the permanent dipole pathway was closer to classical behavior.[26] As such it was proposed that in order to take advantage of quantum effects, the permanent dipole contribution should be minimized. Here we have provided experimental backing for this suggestion, where the permanent dipole pathway has been shown to be disadvantageous to ETPEF and molecules that experience ETPEF through this pathway are more difficult to obtain fluorescence from. The energy gap between the intermediate states and entangled photons impedes coupling and quantum interference, which in turn affects the observed fluorescence signal. For future experiments, we suggest that the electronic states of the compound be calculated in order to determine their detuning energies and identify those with small detuning that will be more likely to show ETPEF. This will be especially useful as we begin to make strides toward utilizing ETPEF towards novel applications such as microscopy.

4.7 Conclusion

Thus, it has been shown that entangled light can be used to successfully achieve ETPEF and the observed signal is dependent on the molecule's electronic states. The source determines the entangled properties of the light and the maximum photon flux achievable, which is useful for quantum measurements until Φ_{max}, after which the observed behavior becomes classical. ETPEF setups must be well isolated and incorporate efficient fluorescence collection methods.

ETPEF can be seen for a variety of molecules, however it is pathway dependent. For the molecules investigated, those with small detuning energies that absorb via the virtual transition pathway experienced ETPEF enhancements via the coupling between the intermediate states of the molecule and the entangled photons. Therefore, molecules with excitation via the virtual transition dipole pathway are favored for ETPEF. Those compounds with larger detuning energies that undergo excitation via the permanent dipole pathway only, most likely will not experience this resonance effect and as such, it is more difficult to observe ETPEF signals. Thus, for the molecules investigated, those with good cross-sections (order of 10^{-19} and above), high transition dipole moments and small detuning energies coupled with good quantum yield, showed observable ETPEF signals. ETPEF is not trivial and there is still more to be understood about factors affecting entangled fluorescence magnitude and what can be done to enhance it, but these are important steps toward our greater overall comprehension.

References

(1) Einstein, A.; Podolsky, B.; Rosen, N. Can Quantum-Mechanical Description of Physical Reality Be Considered Complete? *Phys. Reviw* **1935**, *47* (777), 2–5.

(2) Kiess, T.E.; Shih, Y.H.; Sergienko, A.V.; Alley, C. O. Einstein-Podolsky-Rosen-Bohm Experiment Using Pairs of Light Quanta Produced by Type-II Parametric Down-Conversion. *Phys. Rev. Lett.* **1993**, *71* (24), 3893–3897.

(3) Hong, C.K.; Ou, Z.Y.; Mandel, L. Measurement of Subpicosend Time Intervals between Two Photons by Interference. *Phys. Rev. Lett.* **1987**, *59* (18), 2044–2046.

(4) Ursin, R.; Tiefenbacher, F.; Weier, H.; Scheidl, T.; Zeilinger, A. Entanglement-Based Quantum Communication over 144 Km. *Nat. Phys.* **2007**, *3*, 481–486. https://doi.org/10.1038/nphys629.

(5) Jennewein, T.; Simon, C.; Weihs, G.; Weinfurter, H.; Zeilinger, A. Quantum Cryptography with Entangled Photons. *Phys. Rev. Lett.* **2000**, *84* (20), 4729–4732.

(6) Walther, P.; Resch, K. J.; Rudolph, T.; Schenck, E.; Weinfurter, H.; Vedral, V.; Aspelmeyer, M.; Zeilinger, A. Experimental One-Way Quantum Computing. *Nature* **2005**, *434*, 169–176.

(7) Huver, S. D.; Wildfeuer, C. F.; Dowling, J. P. Entangled Fock States for Robust Quantum Optical Metrology, Imaging and Sensing. *Phys. Rev. A* **2008**, *78* (063828), 1–5. https://doi.org/10.1103/PhysRevA.78.063828.

(8) Giovannetti, V.; Lloyd, S.; Maccone, L. Quantum-Enhanced Measurements : Beating the Standard Quantum Limit. *Science (80-.).* **2004**, *306*, 1330–1337.

(9) Gefen, T.; Rotem, A.; Retzker, A. Overcoming Resolution Limits with Quantum Sensing. *Nat. Commun.* **2019**, *10*, 1–9. https://doi.org/10.1038/s41467-019-12817-y.

(10) Richter, M.; Mukamel, S. Ultrafast Double-Quantum-Coherence Spectroscopy of Excitons with Entangled Photons. *Phys. Rev. A* **2010**, *82* (013820), 1–7. https://doi.org/10.1103/PhysRevA.82.013820.

(11) Schlawin, F.; Dorfman, K. E.; Mukamel, S. Entangled Two-Photon Absorption

Spectroscopy. *Acc. Chem. Res.* **2018**, *51*, 2207–2214. https://doi.org/10.1021/acs.accounts.8b00173.

(12) Dorfman, K. E.; Schlawin, F.; Mukamel, S. Nonlinear Optical Signals and Spectroscopy with Quantum Light. **2016**, *88* (December), 1–67. https://doi.org/10.1103/RevModPhys.88.045008.

(13) Leon-Montiel, R.; Svozilik, J.; Salazar-Serrano, L. J.; Torres, J. P. Role of the Spectral Shape of Quantum Correlations in Two-Photon Virtual-State Spectroscopy. *New J. Phys.* **2013**, *15* (053023), 1–15. https://doi.org/10.1088/1367-2630/15/5/053023.

(14) You, H.; Hendrickson, S. M.; Franson, J. D. Enhanced Two-Photon Absorption Using Entangled States and Small Mode Volumes. *Phys. Rev. A* **2009**, *80* (043823), 1–8. https://doi.org/10.1103/PhysRevA.80.043823.

(15) Lakowicz, J. R. *Principles of Fluorescence Spectroscopy*; Springer: Boston, 2006.

(16) Teich, M. C.; Saleh, B. E. A. Entangled-Photon Microscopy. **2014**, No. January.

(17) Georgiades, N. P.; Polzik, E. S.; Kimble, H. J. Atoms as Nonlinear Mixers for Detection of Quantum Correlations at Ultrahigh Frequencies. *Phys. Rev. A* **1997**, *55* (3), 1605–1608.

(18) Dayan, B.; Pe'er, A.; Friesem, A. A.; Silberberg, Y. Two Photon Absorption and Coherent Control with Broadband Down-Converted Light. *Phys. Rev. Lett.* **2004**, *93* (2), 1–4. https://doi.org/10.1103/PhysRevLett.93.023005.

(19) Upton, L.; Harpham, M.; Suzer, O.; Richter, M.; Mukamel, S.; Goodson, T. Optically Excited Entangled States in Organic Molecules Illuminate the Dark. *J. Phys. Chem. Lett.* **2013**, *4* (12), 2046–2052. https://doi.org/10.1021/jz400851d.

(20) Varnavski, O.; Pinsky, B.; Goodson, T. Entangled Photon Excited Fluorescence in Organic Materials: An Ultrafast Coincidence Detector. **2017**, 6–11. https://doi.org/10.1021/acs.jpclett.6b02378.

(21) Eshun, A.; Cai, Z.; Awies, M.; Yu, L.; Goodson III, T. Investigations of Thienoacene Molecules for Classical and Entangled Two-Photon Absorption Published as Part of The Journal of Physical Chemistry Virtual Special Issue " William M . Jackson Festschrift " . *J. Phys. Chem. A* **2018**, *122*, 8167–8182. https://doi.org/10.1021/acs.jpca.8b06312.

(22) Tabakaev, D.; Montagnese, M.; Haack, G.; Bonacina, L.; Zbinden, H.; Thew, R. T. Energy-Time Entangled Two-Photon Molecular Absorption. *Phys. Rev. A* **2021**, *103* (033701), 1–5.

(23) Li, T.; Li, F.; Altuzarra, C.; Classen, C.; Agarwal, G. S. Squeezed Light Induced Two-Photon Absorption Fluorescence of Fluorescein Biomarkers. *arXiv:1911.10239v2 [physics.optics* **2020**, 2–6.

(24) Saleh, B. E. A.; Jost, B. M.; Fei, H. B.; Teich, M. C. Entangled-Photon Virtual-State Spectroscopy. *Phys. Rev. Lett.* **1998**, *80* (16), 3483–3486. https://doi.org/10.1103/PhysRevLett.80.3483.

(25) Kang, G.; Avanaki, K. N.; Mosquera, M. A.; Burdick, R. K.; Villabona-monsalve, J. P.; Goodson III, T.; Schatz, G. C. Efficient Modeling of Organic Chromophores for Entangled Two-Photon Absorption. *J. Am. Chem. Soc.* **2020**, *10.1021/ja*. https://doi.org/10.1021/jacs.0c02808.

(26) Burdick, R. K.; Varnavski, O.; Molina, A.; Upton, L.; Zimmerman, P.; Iii, T. G. Predicting and Controlling Entangled Two-Photon Absorption in Diatomic Molecules Published as Part of The Journal of Physical Chemistry Virtual Special Issue " William M . Jackson Festschrift " . *J. Phys. Chem. A* **2018**, *122*, 8198–8212. https://doi.org/10.1021/acs.jpca.8b07466.

(27) Dorfman, K. E.; Schlawin, F.; Mukamel, S. Stimulated Raman Spectroscopy with Entangled Light: Enhanced Resolution and Pathway Selection. *J. Phys. Chem. Lett.* **2014**, *5*, 2843–2849. https://doi.org/10.1021/jz501124a.

(28) Svozilik, J.; Perina Jr., J.; León-montiel, R. D. J. Two-Photon Absorption Spectroscopy Using Intense Phase-Chirped Entangled Beams. *Chem. Phys.* **2018**, *510*, 54–59. https://doi.org/10.1016/j.chemphys.2018.05.013.

(29) Rubin, M. H.; Klyshko, D. N.; Shih, Y. H.; Sergienko, A. V. Theory of Two-Photon Entanglement in Type-II Optical Parametric Down-Conversion. *Phys. Rev.* **1994**, *50* (6), 5122–5133.

(30) Keller, T. E.; Rubin, M. H. Theory of Two-Photon Entanglement for Spontaneous Parametric down-Conversion Driven by a Narrow Pump Pulse. *Phys. Rev. A* **1997**, *56* (2), 1534–1541.

(31) Joobeur, A.; Saleh, B. E. A.; Larchuk, T. S.; Teich, M. C. Coherence Properties of Entangled Light Beams Generated by Parametric Down-Conversion: Theory and Experiment. *Phys. Rev. A* **1996**, *53* (6), 4360–4371.

(32) Manjooran, S.; Zhao, H.; Jr, I. T. L.; Major, A. Phase Matching Properties of PPKTP ,

MgO : PPSLT and MgO : PPcLN for Ultrafast Optical Parametric Oscillation in the Visible and Near Infrared Ranges with Green Pump 1. *Laser Phys.* **2012**, *22* (8), 1325–1330. https://doi.org/10.1134/S1054660X12080142.

(33) Fiorentino, M.; Kuklewicz, C. E.; Wong, F. N. C. Source of Polarization Entanglement in a Single Periodically Poled KTiOPO 4 Crystal with Overlapping Emission Cones. *Opt. Express* **2005**, *13* (1), 127–135.

(34) Lvovsky, A. I. Squeezed Light. *arXiv:1401.4118v2* **2016**, 1–21.

(35) Mccormick, C. F.; Marino, A. M.; Boyer, V.; Lett, P. D. Strong Low-Frequency Quantum Correlations from a Four-Wave-Mixing Amplifier. *Phys. Rev. A* **2008**, *78* (0413816), 1–5. https://doi.org/10.1103/PhysRevA.78.043816.

(36) Lahankar, S. A.; West, R.; Varnavski, O.; Xie, X.; Goodson, T.; Sukhomlinova, L.; Twieg, R. Electronic Interactions in a Branched Chromophore Investigated by Nonlinear Optical and Time-Resolved Spectroscopy. *J. Chem. Phys.* **2015**, *337* (December 2003). https://doi.org/10.1063/1.1630309.

(37) Harpham, M. R.; Goodson III, T. Thiophene Dendrimers as Entangled Photon Sensor Materials. *J. Am. Chem. Soc. Artic.* **2018**, No. 21, 973–979.

(38) Lounis, B.; Orrit, M. Reports on Progress in Physics Related Content Single-Photon Sources Single-Photon Sources. *Reports Prog. Phys.* **2005**, *58*, 1129–1179. https://doi.org/10.1088/0034-4885/68/5/R04.

(39) Boitier, F.; Godard, A.; Dubreuil, N.; Delaye, P.; Fabre, C.; Rosencher, E. Two-Photon-Counting Interferometry. *Phys. Rev. A* **2013**, *013844*, 1–14. https://doi.org/10.1103/PhysRevA.87.013844.

(40) Li, T.; Li, F.; Altuzarra, C.; Classen, A.; Agarwal, G. S. Squeezed Light Induced Two-Photon Absorption Fluorescence of Fluorescein Biomarkers Squeezed Light Induced Two-Photon Absorption Fluorescence of Fluorescein Biomarkers. *Appl. Phys. Lett.* **2020**, *116* (June), 1–5. https://doi.org/10.1063/5.0010909.

(41) Dayan, B.; Pe'er, A.; Friesem, A. A.; Silberberg, Y. Nonlinear Interactions with an Ultrahigh Flux of Broadband Entangled Photons. *Phys. Rev. Lett.* **2005**, *94* (043602), 2–5. https://doi.org/10.1103/PhysRevLett.94.043602.

(42) Fei, H. B.; Jost, B. M.; Popescu, S.; Saleh, B. E. A.; Teich, M. C. Entanglement-Induced Two-Photon Transparency. *Phys. Rev. Lett.* **1997**, *78* (9), 1679–1682.

https://doi.org/10.1103/PhysRevLett.78.1679.

(43) Pe'er, A.; Dayan, B.; Friesem, A. A.; Silberberg, Y. Temporal Shaping of Entangled Photons. *Phys. Rev. Lett.* **2005**, *94* (073601), 1–4. https://doi.org/10.1103/PhysRevLett.94.073601.

(44) Suzer, O. QUANTUM OPTICAL APPLICATIONS IN SPECTROSCOPY: INVESTIGATIONS OF ENTANGLED TWO-PHOTON ABSORPTION AND ENTANGLED TWO-PHOTON EXCITED FLUORESCENCE IN ORGANIC DENDRITIC SYSTEMS, 2010.

(45) Guzman, A. R.; Harpham, M. R.; Süzer, Ö.; Haley, M. M.; Goodson, T. G. Spatial Control of Entangled Two-Photon Absorption with Organic Chromophores. *J. Am. Chem. Soc.* **2010**, *132* (23), 7840–7841. https://doi.org/10.1021/ja1016816.

(46) Albota, M.; Beljonne, D.; Bre, J.; Ehrlich, J. E.; Fu, J.; Heikal, A. A.; Hess, S. E.; Kogej, T.; Levin, M. D.; Marder, S. R.; Mccord-maughon, D.; Perry, J. W.; Ro, H. Design of Organic Molecules with Large Two-Photon Absorption Cross Sections. *Science (80-.).* **1998**, *281*, 1653–1657.

(47) Chunosova, S. S.; Svetlichnyi, V. A.; Meshalkin, Y. P. Measurement of the Two-Photon Absorption Cross Sections of Dicyanomethylene-Pyrans by the z- Scan Method Measurement of the Two-Photon Absorption Cross Sections of Dicyanomethylene-Pyrans by the z-Scan Method. *Quantum Electron.* **2005**, *35*, 415–418. https://doi.org/10.1070/QE2005v035n05ABEH003405.

(48) Albota, M. A.; Xu, C.; Webb, W. W. Two-Photon Fluorescence Excitation Cross Sections of Biomolecular Probes from 690 to 960 Nm. *Appl. Opt.* **1998**, *37*, 7352–7356.

(49) Drobizhev, M.; Karotki, A.; Kruk, M.; Rebane, A. Resonance Enhancement of Two-Photon Absorption in Porphyrins. *Chem. Phys. Lett.* **2002**, *355* (March), 175–182.

(50) Javanainen, J.; Gould, P. L. Linear Intensity Dependence of a Two-Photon Transition Rate. *Phys. Rev. A* **1990**, *41* (9), 5088–5091. https://doi.org/10.1103/PhysRevA.41.5088.

Chapter 5

Evaluating the Photophysical Properties of Organic PDI Trimers with Classical Nonlinear Spectroscopy and Entangled Virtual State Spectroscopy

The work in this chapter is to be published in a manuscript currently under preparation "*Classical Nonlinear Spectroscopy and Entangled Virtual State Spectroscopy of Organic PDI Trimers*"

Eshun, A.; Carlotti, B.; Cai, Z.; Kim, H.; Yu, L.; Goodson III. T.

5.1 Abstract

Quantum entanglement is a rapidly growing research area, and the application of quantum entangled photons as a spectroscopic tool is one which is increasingly promising for providing new information about the photophysical properties of organic and biological materials that have optical applications. This work focuses on using the nonmonotonic behavior of entangled two-photon absorption to understand organic molecules' virtual-electronic-state interactions with entangled photons. Comparing this to classical time-resolved and non-linear spectroscopy, this permits us to obtain the energies of virtual states contributing to two-photon excitations and learn more about the dynamics of these materials.

5.2 Introduction

Over the years, organic molecules have been a major subject of study towards applications for organic electronic devices such as photovoltaics and organic light-emitting diodes

(OLED).[1–3] The excited states of these molecules dictate their optical properties from charge transfer to emission and singlet fission and these affect their suitability for electronic applications.[4–6] Researchers have aimed to tune these properties using a variety of different synthetic modifications such as creating highly conjugated aromatic ring structures, introducing structural changes by heteroatom replacements and geometric changes that affect the planarity of the molecule.[7–11]

A number of ultrafast spectroscopic methods are used to characterize the photophysical properties of such organic molecules. Transient absorption spectroscopy is a very useful time-resolved tool that gives an idea of the dynamic processes that occur upon a molecule's excitation, such as excited-state energy migration, charge transfer and intersystem crossing.[12,13] Transient absorption spectroscopy can be carried out on timescales spanning tens of femtoseconds to hundreds of picoseconds. Thus, it becomes an important technique for understanding different types of molecules that exhibit processes such as triplet formation in the femtosecond regime[14] and thermally activated delayed fluorescence that happens on a microsecond time scale.[15,16] Another interesting spectroscopic method used to analyze the photophysical properties of organic molecules and biological samples is two-photon absorption spectroscopy. This method allows researchers to probe excited states of molecules that may not be accessible with linear (one-photon) absorption and gain information about the polarization of the transition moments of these excitations.[17] TPA measurements have been used to determine how systematic changes such as an increase in conjugation affects dipole moments and hence charge transfer, how there can be strong dipole coupling between metal nanoclusters in solid state[18] and how molecules of different symmetry vary in their TPA dynamics. However, in order to obtain TPA spectra, TPA measurements must be obtained at

different wavelengths which requires expensive lasers with tunable frequencies or multiple laser sources. As such, researchers may face limitations when aiming to attain a molecule's TPA spectral resolution.

Recently, scientists have been excited about utilizing quantum entangled photons and the physical implication of their unique properties. This fairly new experimental area has applications from quantum computing to imaging and cryptography.[19,20] While it is being studied for these uses, questions have been raised about its employment in spectroscopy. It was originally theorized that the strong temporal and spatial correlations of the entangled photon pair would lead to entangled two-photon absorption within an entanglement time T_e, and the TPA rate would depend linearly on the input photon flux rather than quadratically as it does with random TPA, i.e. $\mathrm{Re} = \sigma_e \emptyset + \delta_R \emptyset$.[21,22] Experimentally, it has been shown that entangled photons can indeed be used similarly for two-photon absorption techniques and the excitations can remarkably occur with over a billion times less light intensity.[23–27] Ever more fascinating is the enhanced resolution that ETPA permits due to the strong interactions and correlations between photons of the entangled pair as well as the sensitivity to molecule's excitation pathway.[28–30] While this gives further information on molecular dipole moments, we seek to exploit the properties of quantum entangled light to learn even more about the molecules we study for photovoltaic applications and more.

Quantum interference between the signal and idler of the entangled biphoton pair, and the molecule undergoing two-photon absorption, allow for variations of the ETPA signal at different entanglement times. Thus, there is a nonmonotonic behavior of the ETPA signal with respect to T_e. This oscillating pattern was first discovered theoretically[22,31] and since then proof of its existence has been measured experimentally.[23,32] This interference empowers us to

extract information on the virtual states contributing to the two-photon excitation.[22,31] Entangled virtual-state spectroscopy is therefore an exciting and untapped approach to understanding new information about the dynamics of a molecule. The Fourier relationship between time and frequency permits us to realize spectral resolution of the states that contribute to the excitation of the medium under consideration. An adjustable time delay, τ, can be introduced between the signal and idler photons to reproduce the effects of altering the entanglement time within which the photon pair are simultaneously absorbed. Hence, we will gain a more comprehensive understanding of the dynamics involved in a molecule's excitation and how these can subsequently be tuned for its desired applications.

In this chapter, we consider perlyene diimide PDI trimers that differ in their structural orientation. One of these trimers, trimer $\boldsymbol{\beta}$, has three PDI monomers linked by benzodithiophene units with bonds such that its overall structure becomes twisted. Trimer $\boldsymbol{\beta C}$ has 3 PDI monomers fused with benzodithiophene units such that its structure is planar. The structures of the trimers are shown in Figure 5.1. By using different spectroscopic tools, including entangled light, we aim to obtain a more detailed picture of how the different geometries affect the photophysical properties of these molecules, and how virtual state spectroscopy can be incorporated as a new informative characterization method.

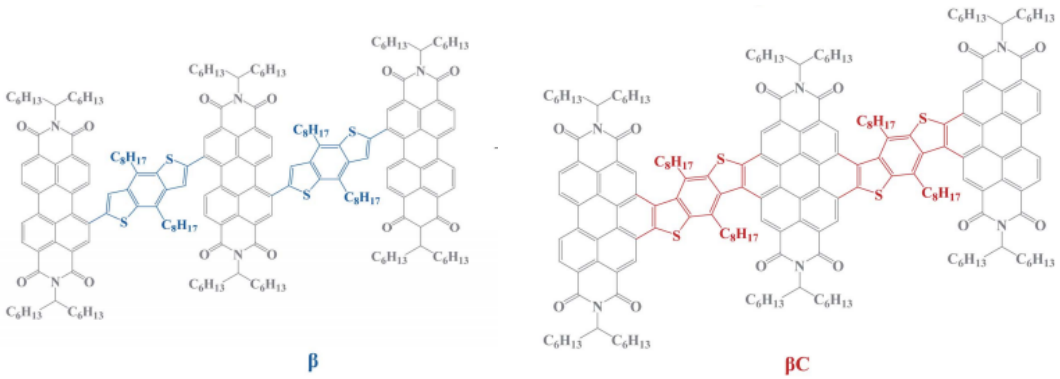

Figure 5.1*. Molecular structure of the investigated trimer compounds:* ***β,*** *twisted trimer and* ***βC****, planar trimer.*

5.3 Quantum Chemical Calculations

Theoretical investigations have been performed on molecular structures where the long alkyl chains are replaced by short chains (octyl and hexyl groups [C_8H_{17}, C_6H_{13}] attached to the PDI and the BDT linker are replaced by hydrogen atom and methyl groups, respectively) to save computational time without significant effect on the electronic properties. The ground state geometry of each compound was obtained by computations using density functional theory (DFT). The B3LYP functional and the 6−31G* basis sets have been employed. Excited state simulations using time−dependent DFT (TDDFT) were performed. The same functional and basis sets used in the ground state calculations, were employed for the geometry optimization of the first singlet excited state (S_1). Single−point energy calculations to evaluate the electronic property were performed using the system−dependent, nonempirically tuned version of long−range corrected functional ωB97X−D[33,34] which is known to significantly improve the charge delocalization problem in conventional DFT functionals and 6−31G* basis sets. The ω value is tuned to minimize the square sum of the difference between HOMO energy (ε_{HOMO}) and ionization potential (IP), and LUMO energy (ε_{LUMO}) and electron affinity (EA), $(\varepsilon_{HOMO}+IP)^2+(\varepsilon_{LUMO}+EA)^2$. The ω value is significantly affected by the environment,[4] and inclusion of the solvent (chloroform) dielectric field induces a reduced ω value. The optimal ω values of **1** and **2** are 0.004 and 0.003, respectively. The medium effect is included using polarizable continuum model with the dielectric constant of 4.31 for chloroform. Characters of excitations were described with natural transition orbitals (NTOs). All the quantum chemical simulations were conducted using Q−Chem 5.0.[35]

5.4 Results

5.4.1 Steady State Absorption and Fluorescence

The absorption spectra of compounds $\boldsymbol{\beta}$ and $\boldsymbol{\beta}$**C** in chloroform solution are shown in the left graph of Figure 5.2. The absorption spectra of the investigated samples are placed in the same region where the structured absorption of the parent PDI occurs. However, the relative intensities of the multiple peaks (or shoulders) exhibited by compounds **1** and **2** (see Table 1) are different with respect to those characteristics of the absorption of monomeric PDI. This spectral behavior has been reported in the literature for several PDI dimers[8,36] and is most likely related to intramolecular features of the molecules of the present study, and the fact that $\boldsymbol{\beta}$ and $\boldsymbol{\beta}$**C** are PDI trimers. In fact, no concentration effect on the absorption spectra was observed suggesting that no aggregation or intermolecular interaction are affecting the spectral shapes exhibited by the trimers.

It has to be noted that the absorption and emission spectra of $\boldsymbol{\beta}$ and $\boldsymbol{\beta}$**C** (Figure 5.2) appear to be extremely different, despite the structural similarity of the two molecules. Whereas the emission spectra of compound $\boldsymbol{\beta C}$ are peaked and structured, compound $\boldsymbol{\beta}$ shows broad structure−less spectra. These different spectral features, already visible in the absorption, become apparent in the fluorescence spectra. The emission of $\boldsymbol{\beta C}$ is peaked at 613 nm and shows a shoulder at 665 nm. On the other hand, compound $\boldsymbol{\beta}$ exhibits an extremely broad and bell−like shaped emission band, which results significantly red shifted with respect to $\boldsymbol{\beta C}$ and is centered around 790 nm. For the investigated compounds, no significant wavelength effect on the fluorescence spectra was observed and the excitation spectra well overlap the absorption.

A significant effect of solvent polarity was observed on the spectra of compounds ***β*** and ***β*C**, particularly on the emission (see Figures 5.13 and 5.13). When considering a low polar solvent such as toluene and a medium polarity solvent such as chloroform, a red shift (ca. 400 cm^{-1}) of the emission peak occurs upon increasing the solvent dielectric constant. These findings point to a certain intramolecular charge transfer character of the emitting state for these molecules containing electron donor and electron acceptor groups (A–π–D–π–A–π–D–π–A structures), for both compound ***β*** and ***βC***.

Fluorescence quantum yields were measured for the investigated molecular systems in chloroform solution (see Table 5.1). The fluorescence efficiency is 30 times lower in the case of compound ***β*** compared to ***βC*** (ϕ_F is 0.003 vs. 0.09). As a matter of fact, the fluorescence quantum yield of these PDI trimers is quite low (0.3 to 9 %). This is quite unusual for PDI derivatives which have been generally reported in the literature to be strongly fluorescent.[37]

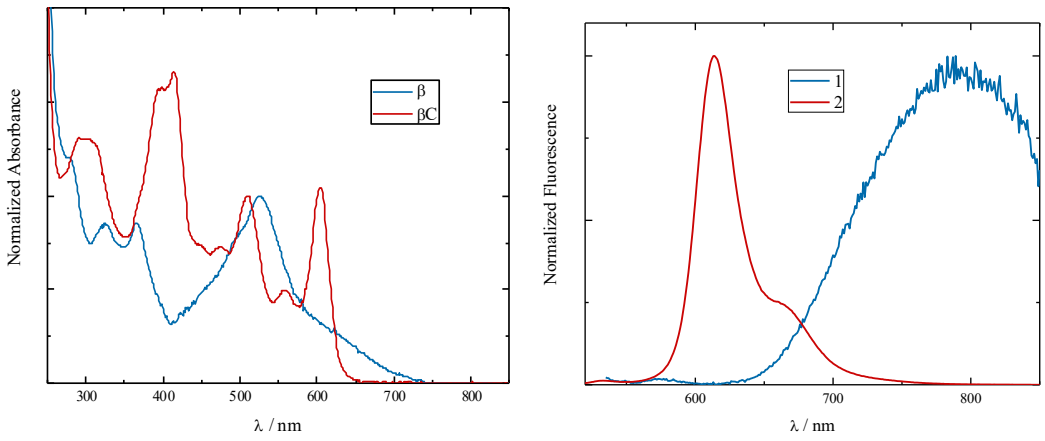

Figure 5.2. *Normalized absorption (right) and emission (left) spectra of compounds **1** and **2** in chloroform.*

Table 5.1. *Absorption and emission properties of compounds **1** and **2** in chloroform.*

Compound	λ_{abs} / nm	λ_{em} / nm	ε / $M^{-1}cm^{-1*}$	ϕ_F
$\boldsymbol{\beta}$	366, 450^{sh}, <u>526</u>, 630^{sh}	790	71100	0.003
$\boldsymbol{\beta C}$	394, 414, <u>510</u>, 605	613, 665$^{(sh)}$	58500	0.090

*at the underlined maximum wavelength

5.4.2 Femtosecond Transient Absorption

The ultrafast excited state dynamics of compounds $\boldsymbol{\beta}$ and $\boldsymbol{\beta C}$ in chloroform was investigated upon 400 nm laser excitation by femtosecond transient absorption. The obtained results, in terms of time resolved spectra, are shown in the left graphs of Figure 5.3. The transient spectra are shown for measurements carried out in both chloroform (left) and toluene (right). The transient spectra exhibit mostly positive signals due to excited state absorption. Negative peaks are revealed at ca. 520 nm for compound $\boldsymbol{\beta}$ and at ca. 510/605 nm for compound $\boldsymbol{\beta C}$. These spectral positions nicely match the steady state absorption maxima and thus these signals in the transient spectra are mainly due to ground state bleaching. However, for compound $\boldsymbol{\beta C}$, characterized by a small Stokes shift and a non−negligible fluorescence efficiency, a contribution of stimulated emission to the negative peak between 580 and 625 nm cannot be ruled out. The time resolved absorption spectra show several positive excited state absorption signals for the two samples: a band centered around 740 nm, another band at ca. 660 nm and peaks at ca. 540 and 570 nm, the last two peaks of which are particularly intense for compound $\boldsymbol{\beta C}$. The transient absorption at 740 nm has been repeatedly associated in the literature with the perylene diimide radical anion ($PDI^{\bullet-}$),[38–44] whereas signals in the region between 550 and 600 nm have been assigned to the perylene diimide radical cation ($PDI^{\bullet+}$).[40,42,43,45]

These transient absorptions were less apparent during the measurements carried out in a lower polar solvent such as toluene (see Figure 5.3, right graphs). This supports their assignment to charged transferred species produced after photoexcitation of the trimers. The spectral features observed during the ultrafast transient absorption experiments of ***β*** and ***βC*** in chloroform may therefore reflect the occurrence of intramolecular charge transfer in these molecules, particularly efficient in the case of compound ***βC***. No significant evolution of the absorption spectra was observed in time. Therefore, it is feasible that formation of the excited state with intramolecular charge transfer character occurs extremely fast, probably within the solvation in chloroform.[7]

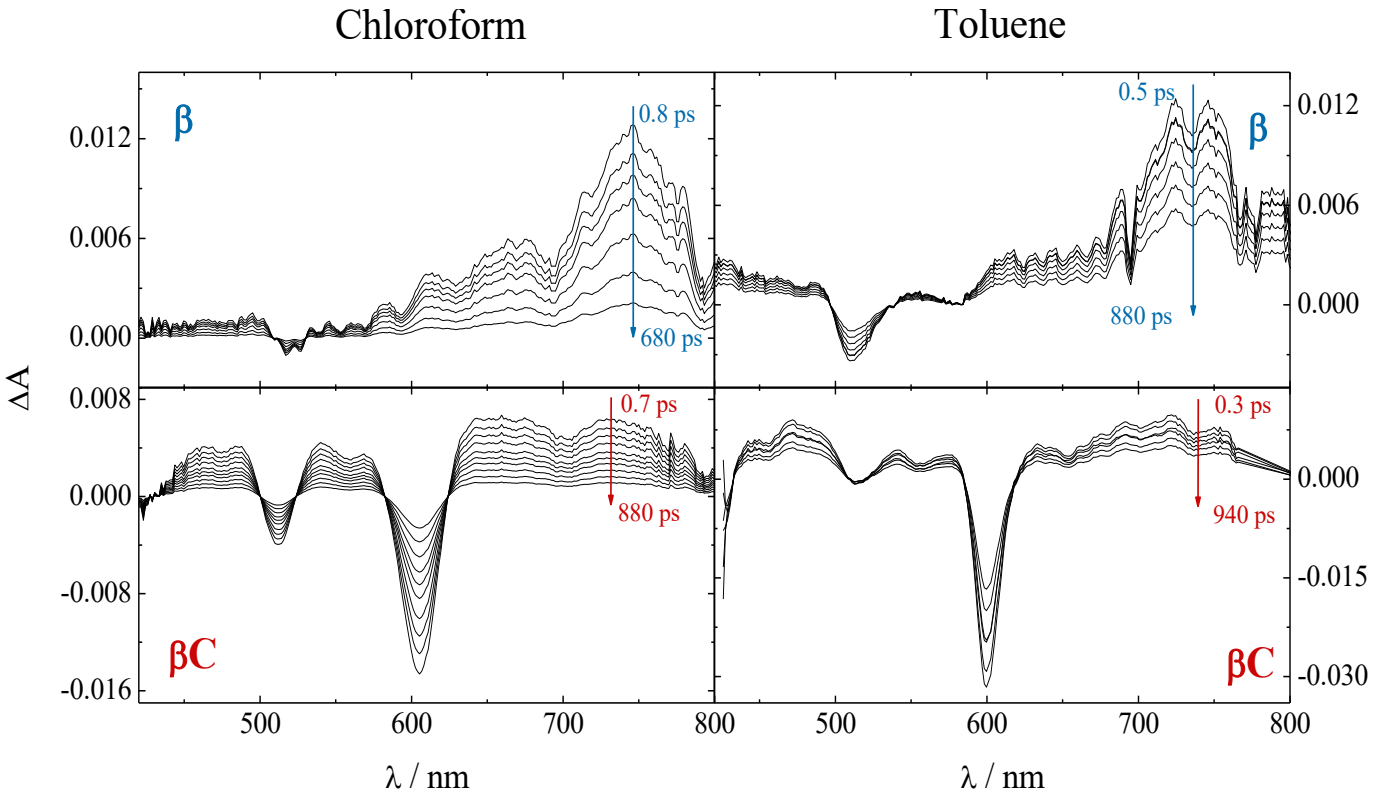

Figure 5.3. *Time−resolved absorption spectra obtained by femtosecond resolved transient absorption measurements of compounds* ***β*** *(top) and* ***βC*** *(bottom) in chloroform (left) and toluene (right).*

5.4.3 Quantum Chemical Simulations

A computational investigation of compounds $\boldsymbol{\beta}$ and $\boldsymbol{\beta C}$ was carried out by using density functional theory. The optimized geometry (Figure 5.15) computed for the trimer characterized by fused ring connectors (compound $\boldsymbol{\beta C}$) is almost planar. On the other hand, when the bridge between the PDIs and the BDTs is a single bond (compound $\boldsymbol{\beta}$), the optimized geometry is completely twisted.

The natural transition orbitals (NTOs) computed on the optimized S_0 geometry for the $S_0 \rightarrow S_1$ transition are shown in Figure 5.4. These orbitals represent the electron−hole pair of the excited state (which account for more than 95% of each transition's wave function). The hole and electron NTOs clearly indicate that the $S_0 \rightarrow S_1$ transition implies a charge transfer from the BDT electron donors toward the central PDI electron acceptor in the case of compound $\boldsymbol{\beta}$ (Figure 5.4). The planar geometry of $\boldsymbol{\beta C}$ allows the charge transfer associated to the $S_0 \rightarrow S_1$ transition to take place from the BDTs to all the three PDIs present in the molecular structure (Figure 5.4). Similar charge displacements are found to occur in the other NTOs which describe the main transitions relevant to the absorption spectra of compounds $\boldsymbol{\beta}$ and $\boldsymbol{\beta C}$. The computed transition energies remarkably agree with the experimental absorption maxima positions (see Table 5.8). To analyze $\boldsymbol{\beta}$ and $\boldsymbol{\beta}$**C** in detail, these compounds were divided into five subunits, considering their acceptor−donor−acceptor−donor−acceptor structure where the acceptors are the PDI and the donors the BDT fragments. The amount of charge transfer during absorption was quantified as the change in atomic charge of each fragment upon excitation (Table 5.2), where $0.76e^-$ and $0.63e^-$ migrated from the BDTs to the PDIs in $\boldsymbol{\beta}$ and $\boldsymbol{\beta C}$, respectively. Compound $\boldsymbol{\beta}$ absorption involves more charge displacement (0.76 e^-) than compound $\boldsymbol{\beta C}$

(0.63 e^-), which is consistent with the lower excitation energy of $\boldsymbol{\beta}$ experimentally observed and computationally predicted (Table 5.8). However, the symmetrical charge displacement taking place for both $\boldsymbol{\beta}$ and $\boldsymbol{\beta C}$ causes a dipole moment calculated for the ground state of these molecules close to zero (see Table 5.3).

The NTOs computed on the S_1 geometry which describe the $S_1 \rightarrow S_0$ transition are shown in Figure 5.5. The calculated orbitals show that the charge transfer accompanying emission involves the central PDI and one of the BDTs for compound $\boldsymbol{\beta}$; one of the lateral PDIs and one of the BDTs for compound $\boldsymbol{\beta C}$. In both compounds, the charge transfer excitation for S_1 appears to break the symmetry, because the hole and electron NTOs are largely localized on half of the molecular structure. The amount of charge transferred during emission, quantified by dividing the molecules in five subunits, is reported in Table 5.2. The charge transfer degree for the excited state of compound $\boldsymbol{\beta C}$ (0.80 e^-) is higher than for compound $\boldsymbol{\beta}$ (0.74 e^-). This computational result is consistent with the stronger solvent polarity effect experimentally observed on the emission spectra of $\boldsymbol{\beta C}$ and is in agreement with literature reports concerning planar vs. twisted PDI dimers.[7] The excited state dipole moment obtained from the calculations for the investigated trimers shows significant values (see Table 5.3) due to the excited state symmetry breaking observed for these molecules. In particular, the S_1 dipole moment for compound $\boldsymbol{\beta C}$ (ca. 33 D) is higher than for $\boldsymbol{\beta}$ (ca. 25 D), consistently with the higher charge transfer degree predicted for the excited state of this planar system.

	β	***βC***
Electron NTOs	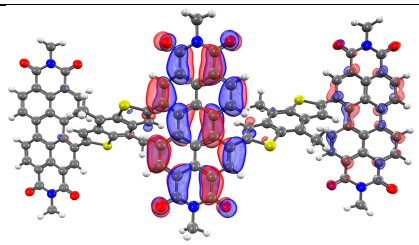	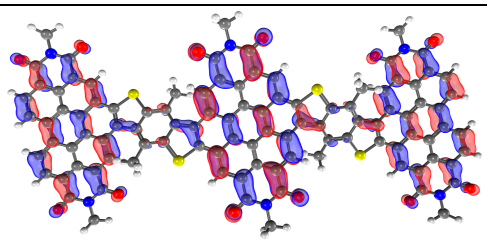
Hole NTOs	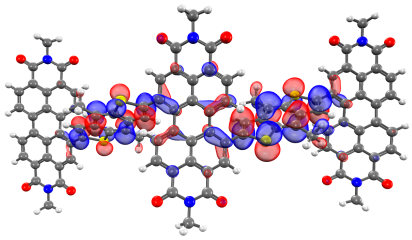	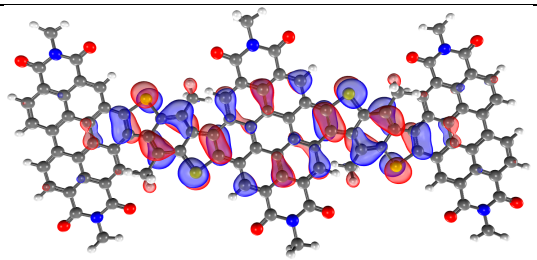

Figure 5.4. *Natural transition orbitals for the S_0 geometry ($S_0 \rightarrow S_1$ transition) of compounds* ***β*** *and* ***βC*** *(isodensity=0.05. Color scheme; Hydrogen—white, carbon—black, nitrogen—blue, oxygen—red, sulfur—yellow).*

	β	***βC***
Electron NTOs	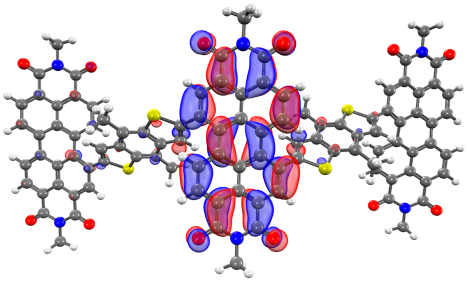	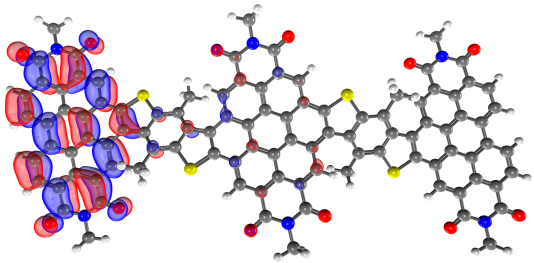
Hole NTOs	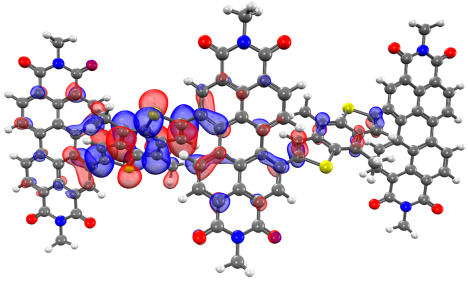	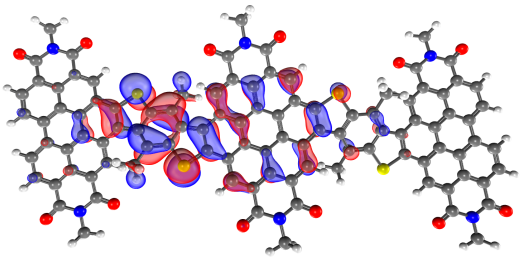

Figure 5.5. *Natural transition orbitals for the S_1 geometry ($S_0 \rightarrow S_1$ transition) of compounds* ***β*** *and* ***βC*** *(isodensity=0.05. Color scheme; Hydrogen—white, carbon—black, nitrogen—blue, oxygen—red, sulfur—yellow).*

Table 5.2. Change in atomic charge from S_0 to S_1 on the subunits of compound $\boldsymbol{\beta}$ and $\boldsymbol{\beta C}$.[a]

	$\boldsymbol{\beta}$					$\boldsymbol{\beta C}$				
	A	D	A	D	A	A	D	A	D	A
Absorption[b]	−0.07	+0.50	−0.66	+0.27	−0.03	−0.19	+0.32	−0.25	+0.32	−0.19
Emission[c]	+0.07	+0.64	−0.74	+0.03	0.00	−0.79	+0.61	+0.10	+0.08	−0.01

[a]Mulliken charge is given in e^-; [b]Calculated at S_0 geometry; [c]Calculated at S_1 geometry

Table 5.3. Dipole moments (μ) in Debye of ground and lowest excited singlet state for compounds $\boldsymbol{\beta}$ and $\boldsymbol{\beta C}$.

Compound	State	μ_x	μ_y	μ_z	μ_{tot}
$\boldsymbol{\beta}$	S_0	−0.10	0.08	0.01	0.13
	S_1	−22.65	0.35	−10.93	25.15
$\boldsymbol{\beta C}$	S_0	0.02	0.00	0.26	0.33
	S_1	32.89	1.55	4.13	33.18

5.4.4 Classical Two-Photon Absorption

Classical two photon excited fluorescence measurements were carried out on chloroform solutions of $\boldsymbol{\beta}$ and $\boldsymbol{\beta C}$ upon 820 and 875 nm laser excitation. A quadratic dependence of the fluorescence counts upon the laser power was verified during the measurements carried out at 875 nm in all cases and at 820 nm only in the case of compound $\boldsymbol{\beta C}$. In fact, a slope of two resulted from the linear fitting of the log(counts) vs. log (power) plots acquired during these experiments (Figures 5.6 and 5.14). Due to compound $\boldsymbol{\beta}$'s comparatively low linear absorption at ~410nm and low quantum yield, it showed very low two-photon excited fluorescence counts with an 820nm excitation. Coupled with scattering effects, a slope of 2 was not achieved for compound $\boldsymbol{\beta}$ at this wavelength. The classical two-photon excited emission spectra recorded for both trimer samples (Figure 5.6) resemble the steady state fluorescence spectra. This suggests that for

these compounds the excited state reached upon biphotonic excitation is the same populated by linear light absorption.

The classical TPA cross-sections of compounds ***β*** and ***βC*** show remarkable values of tens and hundreds of GM (see Table 5.4). In all cases, the two-photon absorption response of these PDI trimers is enhanced with respect to that exhibited by the monomeric PDI (ca. 1 GM).[8] This result is in agreement with the significant TPA ability discussed in the literature for symmetrical molecular structures containing electron donor and electron acceptor groups.[46,47] It has to be noted that the classical TPA cross-sections are enhanced by over one order of magnitude for the planar trimer ***βC*** (ca. 200−300 GM) with respect to the twisted trimer ***β*** (ca. 10 GM). This trend in the cross sections is consistent with the trend in the transition dipole moments of ***β*** and ***βC*** computed for the transitions experimentally probed upon the 875 nm excitation (see Table 5.8). Moreover, the increased two photon absorption cross section of compound ***βC*** compared to ***β*** reflects the higher charge transfer degree resulting from the calculations for the excited state of the fused ring connected planar molecule (***βC***) with respect to its single bond bridged twisted analogous (***β***).

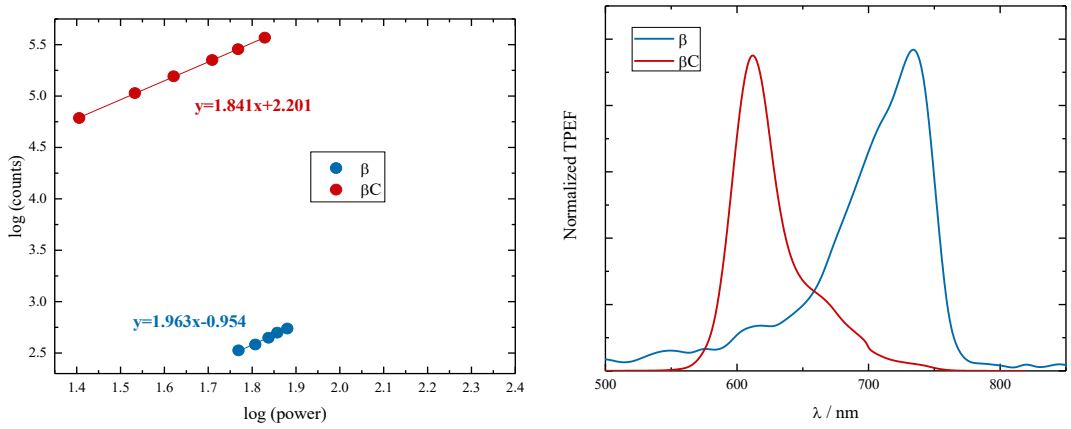

Figure 5.6. *Power dependence of the classical two−photon excited emission (left) and*

two−photon emission spectra (right) for compounds $\boldsymbol{\beta}$ *and* $\boldsymbol{\beta C}$ *in chloroform upon 875 nm excitation.*

Table 5.4. *Classical TPA cross-sections (δ) obtained by Two−Photon Excited Fluorescence measurements upon 820 nm or 875 nm laser excitation.*

Compound	δ / GM λ_{exc}=820 nm	δ / GM λ_{exc}=875 nm
$\boldsymbol{\beta}$	−	11.5
$\boldsymbol{\beta C}$	227	318

5.4.5 Entangled Two-Photon Absorption

Figure 5.7 shows the entangled two-photon absorption plots for the PDI trimers (Compounds $\boldsymbol{\beta}$ and $\boldsymbol{\beta C}$). The linear dependence of the entangled absorption rate on the input photon intensity is a result of the strong correlation of the photon pair and their ability to be simultaneously absorbed within a short time window, which is on the order of femtoseconds. The linear ETPA curves are measured using input photon intensity on the order of 10^6 photons/s. The used intensity was not high enough for the quadratic dependence of random two-photon absorption to be seen. As previously observed, there is a variation in the extent of absorption upon going from one molecule to another.[30] Using the slope of the ETPA curves obtained, the ETPA cross-section is estimated taking into consideration the concentration of the chromophore used and the cuvette path length.

The calculated ETPA cross-section values are shown in Table 5.5 and are similar to values measured for organic chromophores and biological samples in earlier studies.[24,27,28,30,48] Whereas classical two-photon signals could not be adequately observed for compound $\boldsymbol{\beta}$ at the wavelength closer to 800nm, ETPA measurements did not face the same challenges. The quantum interference of entangled photon pairs and their high correlation allows for large enhancements in the absorption rate of ETPA, as seen by the linear dependence as opposed to quadratic dependence on excitation intensity. Thus, ETPA

presents as a good alternative to classical TPA due to this enhancement in resolution. Results show that compound $\boldsymbol{\beta C}$ has an ETPA cross-section of 2.10×10^{-18} cm^2/molecule which is higher than that of $\boldsymbol{\beta}$, at 1.22×10^{-18} cm^2/molecule. This is in accordance with classical TPA data where$\boldsymbol{\beta C}$ had a higher classical TPA cross-section than $\boldsymbol{\beta}$. Additionally, this suggests that planar derivatives do indeed have higher charge transfer than their twisted analogues.

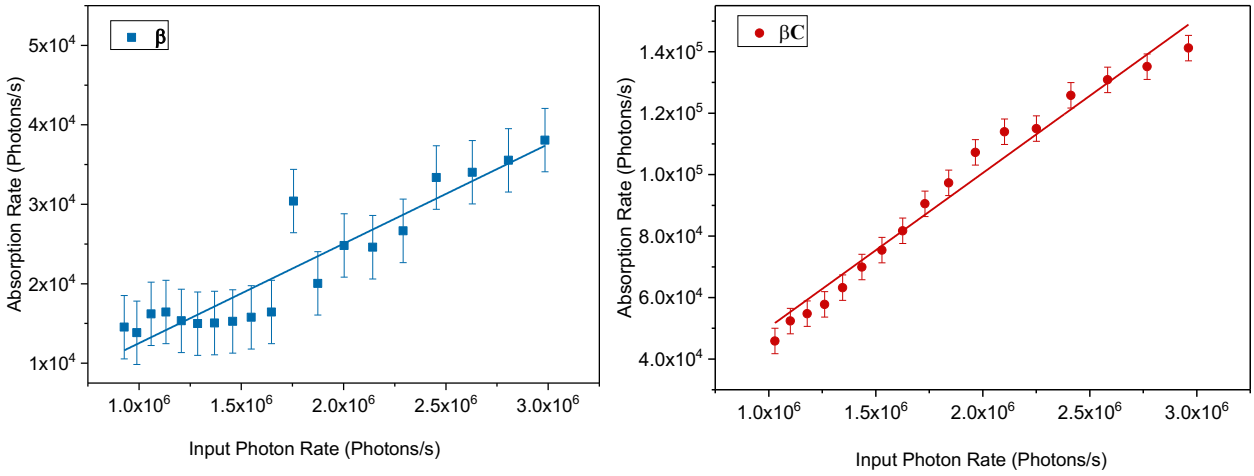

Figure 5.7*. Graphs showing entangled two-photon absorption rate of both dimers and trimers investigated; compounds* $\boldsymbol{\beta}$ *(left) and compound* $\boldsymbol{\beta C}$ *(right).*

Table 5.5. Entangled Two-Photon cross-sections (σ_E) of the investigated compounds

Compound	σ_E ($\times 10^{-18}$ cm^2/molecule)
$\boldsymbol{\beta}$	1.22
$\boldsymbol{\beta C}$	2.10

In addition to characterizing charge transfer properties of molecules under study, ETPA possesses the unique feature of determining the energy levels of virtual states that contribute to the excitation process of multiphoton absorption. Due to quantum optical properties of entangled photons, the ETPA signal oscillates as a function of entanglement time. A time delay, τ, between the signal and idler photons can be introduced in order to

reproduce this nonmonotonic behavior of the ETPA cross-section with respect to τ. The signal-idler mutual delay is introduced using quartz plates of different thicknesses. The quartz plates were placed such that the delay, τ, between the entangled photon pair allows the photons to arrive at different times but still within the entanglement time, T_E. Therefore, $-T_E < \tau < T_E$ and two-photon absorption of the entangled pair still occurs. The time delay drives the population of particular optical transitions and thus, ETPA signal becomes tunable without altering the incident photon frequency.

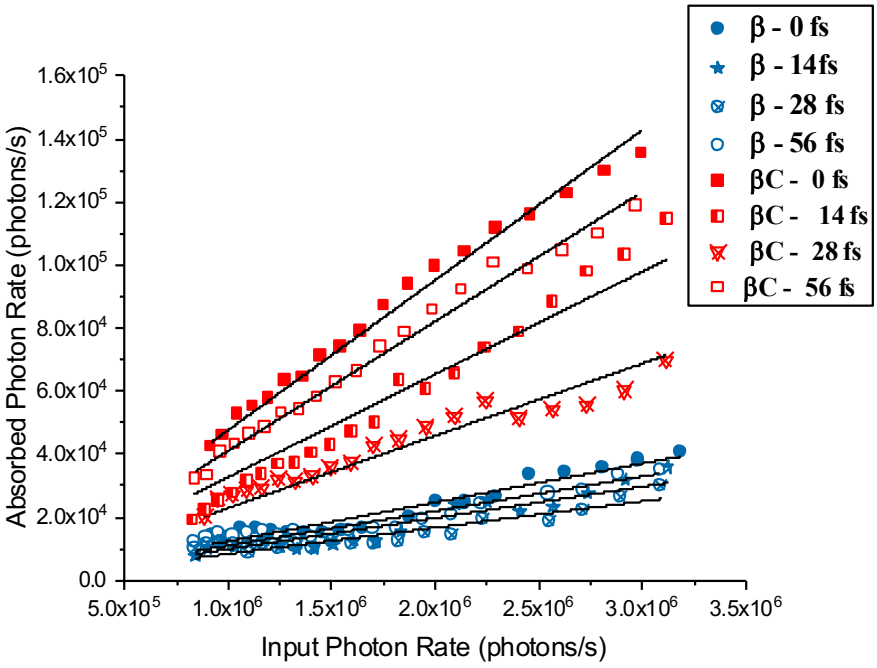

***Figure 5.8**. ETPA graphs of compound **β** (blue) and compound **βC** (red) varied by a time delay between the photon pair introduced by birefringent quartz crystals.*

Shown in Figure 5.8 are ETPA graphs of the same concentrations of compound ***β*** and ***βC***, measured with various time delays. At 800nm, a quartz plate of 1mm causes a delay of ~28fs between the signal and idler photon of the entangled pair. By orienting the plate with its fast axis perpendicular to the signal polarization plane of the BBO crystal, the

signal photon is delayed with respect to the idler photon. In this experiment, 0.5mm, 1mm and 2mm quartz plates were used which serve as a 14 fs, 28 fs and 56 fs time delay respectively. The entanglement time T_E, dictated by our specific light source and 0.5mm BBO crystal is 63 fs as previously estimated[32]. As can be seen in Figure 5.8, for both compounds there is an observable change in ETPA signal as the delay between the signal and idler photons is varied. Clearly, there is no direct increasing or decreasing trend between ETPA signal and the time delay and the pattern is indeed nonmonotonic. Using the linear slopes from Figure 5.8, the ETPA cross-sections were measured and are shown in Table 5.6. These cross-section values are displayed in Figure 5.9 as a function of the mutual time delay, τ. Here, the nonmonotonic behavior is distinctly seen. This shows that while the compound and the laser source wavelength are unchanged, the entanglement properties can be adjusted to obtain different signals for the same molecule.

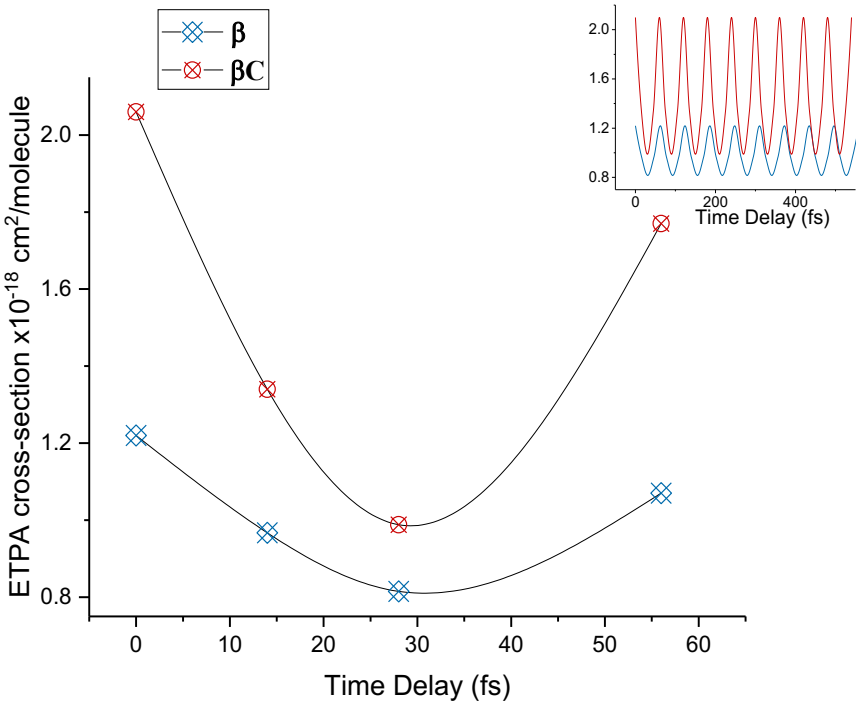

***Figure 5.9**. ETPA cross-sections of trimer **β** and **βC** as a function of the signal-idler mutual time delay, τ. Inset: Extrapolation of experimental results over 400fs delay time.*

***Table 5.6**. ETPA cross-sections for $\boldsymbol{\beta}$ and $\boldsymbol{\beta C}$ measured with a mutual delay between the signal and idler photons of the entangled photon pair.*

Time Delay τ (fs)	σ_E (1×10^{-18} cm^2/molecule)	
	$\boldsymbol{\beta}$	$\boldsymbol{\beta C}$
0 fs	1.22	2.10
14 fs	0.967	1.34
28 fs	0.815	0.988
56 fs	1.07	1.77

From Figure 5.9, the experimental data shows a period of ~65 fs for compound $\boldsymbol{\beta}$ and ~60fs for compound $\boldsymbol{\beta C}$ and it is apparent that the oscillation frequency in relation to time delay is different for different compounds. Another interesting feature is that the change in amplitude magnitude for compound $\boldsymbol{\beta C}$ is distinctly larger than that of compound $\boldsymbol{\beta}$. This is of interest as compound $\boldsymbol{\beta C}$ also has the overall stronger ETPA rate (Figure 5.8) and cross-section and thus the difference in molecular structure is playing a role in some way.

5.5 Discussion

Two PDI trimers which are analogous in structure but differ conformationally have been studied. Computational results reveal that due to variations in the bonding between PDI units and BDT units, from being connected by a single bond to being fused by ring connectors, the structures go from twisted (compound $\boldsymbol{\beta}$) to planar (compound $\boldsymbol{\beta}$**C**) respectively. This geometrical isomerism manifests in the steady state properties of the compounds. While the absorption spectra for both compounds cover the same wavelength range, the absorption peaks differ as a result of different intramolecular characteristics. Additionally, the emission of compound $\boldsymbol{\beta}$ is significantly red shifted (790nm) and the Stokes shift for compound $\boldsymbol{\beta}$ (264nm) is much larger than that of compound $\boldsymbol{\beta C}$ (103nm). This large difference in Stokes shift may suggest a large geometrical difference between the ground and excited state of the twisted

compound.[49] Furthermore, this is seen in how the broad structureless emission of compound $\boldsymbol{\beta}$ contrasts with the structured emission peak of the more rigid compound $\boldsymbol{\beta C}$. Despite the differences in planarity, solvatochromism studies show intramolecular charge transfer occurs in both compounds upon excitation as a result of the electron donor, electron acceptor groups. The extremely low quantum yield for compound $\boldsymbol{\beta}$ in comparison to compound $\boldsymbol{\beta C}$ (ϕ_F is 0.003 vs. 0.09) suggests some non-radiative pathways in compound $\boldsymbol{\beta}$, indicative that these compounds have different energetic properties. In fact, a recent study conducted by members of the Goodson group showed that while the stronger intramolecular charge transfer character in the planar $\boldsymbol{\beta}$**C** compound leads to triplet formation via conventional intersystem crossing (with a triplet yield of 16%), the entropic gain allowed by the twisted trimeric structure of compound $\boldsymbol{\beta}$ leads to a high triplet (170%) and fast intramolecular singlet exciton fission.[50]

In order to gain an understanding of the energetic and excited state dynamics of these compounds, we first investigated them via transient absorption spectroscopy. The distinct excited state absorption (ESA) signals observed in the time resolved transient absorption spectra give information about the charged species produced upon photoexcitation. Mainly, the 740nm ESA that is assigned to the negative PDI radical and the ESA in regions between 550 and 600nm which are assigned to the radical cation. Although the radical cation peak is very pronounced for compound $\boldsymbol{\beta}$, the radical anion peaks are much less so. In contrast, for compound $\boldsymbol{\beta C}$, the bands for both the cation and anion have equal prominence in the spectra. These results suggest that compound $\boldsymbol{\beta C}$ has more evenly distributed charge separation than its twisted derivative. The development of these charged species and proposed charge transfer are in line with computational results. Quantum chemical simulations reveal that in the case of compound $\boldsymbol{\beta}$, charge transfer occurs towards the center of the compound whereas in compound

$\boldsymbol{\beta C}$, the planarity of the compound leads to charge displacement throughout all PDI units of the trimer (Figure 5.4). Calculated charge transfer degree between acceptor fragments (PDI) and donor fragments (BDT), show higher charge transfer for compound $\boldsymbol{\beta C}$ than for compound $\boldsymbol{\beta}$, confirming previously obtained results that planar compounds have higher charge transfer than their twisted alternatives. These results give an idea of the excited state characteristics, but more information is needed to describe the dynamics of the transitions that lead from steady state to excited state.

Two-photon absorption measurements provide information about the molecule's dipole moments upon interaction with an optical field and determines the strength of the polarization changes for the transitions taking place.[51] Classical two-photon measurements are highly dependent on wavelength and the one-photon absorption of the molecule under consideration, as observed with our results. We were unable to obtain classical TPA cross-sections for compound $\boldsymbol{\beta}$ at one of the wavelengths utilized due to its linear absorption at this wavelength and low quantum yield. Compound $\boldsymbol{\beta}$ has relatively low two-photon signals, and this becomes more prevalent at wavelengths where linear absorption is less intense. For the 875nm excitation where TPA cross-sections could be measured for both compounds, the cross-section of compound $\boldsymbol{\beta C}$ is drastically higher than that of compound $\boldsymbol{\beta}$, with an order of magnitude difference. This is consistent with transition dipole moments computed for the corresponding transitions. ETPA has been shown to be a more sensitive TPA measurement method.[27,30] Furthermore, ETPA can be used to obtain a time delay dependent two-photon spectra, and thus energetic information about the transitions are provided without having to alter the wavelength used. In contrast to classical TPA, ETPA signals for compound $\boldsymbol{\beta}$ could be measured at a lower wavelength of ~800nm. Indeed, the ETPA absorption rates for compound $\boldsymbol{\beta}$ are smaller than

for compound $\boldsymbol{\beta C}$, however, whereas there is a difference of 20 times between the classical TPA values for compound $\boldsymbol{\beta}$ and $\boldsymbol{\beta C}$, with ETPA the cross-section for compound $\boldsymbol{\beta C}$ is only twice that of compound $\boldsymbol{\beta}$. This leads us to question why we see this enhancement in cross-section of the twisted molecule relative to the planar molecule in the entangled case. The ability of entangled light to discern such low signals at low photon flux and result in certain enhancements speaks to its advantage as a spectroscopic tool. Moreover, the time delay experiments aid in determining any difference in dynamics there may be that contribute to these responses.

To further examine the experimentally obtained time delay ETPA pattern, we use simulations to fit this data. From previous computational studies, it has been found that a modulating wave, which we will refer to as an envelope wave, that overlaps the molecule's more complex oscillation can be characterized.[29] The dominant pathways interfere to form the complex oscillations, while the difference between their frequencies is equivalent to the difference in frequency between the maxima of the envelope wave. It has also been stated that variations in σ_e can be greater than 2 orders of magnitude but would require tuning of τ with exact femtosecond precision to achieve all possible values. Thus, the experimental values obtained with the quartz plates are assigned as the upper limit of the envelope wave that contains the complex ETPA oscillation pattern and there may be oscillations within smaller time periods due to destructive interferences that were not observed experimentally due to the limited thicknesses of our quartz plates.

To determine the exact complex ETPA pattern of each compound, computational modelling of the ETPA cross-section, σ_e, to fit experimental data was carried out. σ_e can be expressed as:[32]

$$\sigma_e(T_e,\tau) = \frac{\pi\omega_p}{16A_eT_e}\delta\left(\varepsilon_f - \varepsilon_g - \omega_p\right) \times \left|\sum_j A_j\left\{2 - exp\left[-i\Delta_j(T_e - \tau)\right] - exp\left[-i\Delta_j(T_e + \tau)\right]\right\}\right|^2 \quad \text{Eq. 5.1}$$

where Ae and Te are the entanglement area and time respectively; ω_p is the pump frequency; ε_f and ε_g are the final and ground state energies respectively; Δ_j is the detuning energy $\left(\Delta_j = \varepsilon_j - \varepsilon_g - {}^{\omega_p}/_2\right)$, with *j* ranging over intermediate states; $A_j = {}^{D_j}/_{\Delta_j}$, and D_j being the dipole moment operator. In our case, D_j comprises of both transition dipole moments (μ_{gj}, μ_{jf}) and permanent dipole moments ($\Delta\mu$).[28] Thus, with all these parameters known, a Fourier analysis of the resultant graph of σ_e as a function of τ produces peaks that reveal Δ_j. From this, the exact values of virtual state energies (ε_j) that contribute to the ETPA can ultimately then be determined. To obtain accurate models, the experimental values are extrapolated over a greater delay time range as seen in the inset of Figure 5.9. Since the entanglement time and entanglement area are set and the pump frequency is known (where ε_f is in resonance with ω_p), the calculated excitation energies and dipole moments can be used over a range of τ to fit the precise oscillation pattern of each molecule. The periods of the envelope waves can be given as:[29]

$$\tau = \frac{2n\pi}{\|\omega_1| - |\omega_2\|} \quad \text{Eq. 5.2}$$

For our simulations, all energy levels, their permanent dipole moments and the transition dipole moments for each $S_0 \rightarrow S_n$ is known from quantum chemical TD-DFT calculations. The energy levels closest to the pump energy (sum of entangled photon energies) is chosen as the final state. Energy levels with frequencies in resonance with the entangled photon frequencies are initially assumed to be a dominant transition, and the frequency of the subsequent dominant transitions are determined from equation 5.2 using the oscillation period found experimentally

(65 and 60 fs). The ground state and final state dipole moments are known, so the permanent dipole moment difference, $\Delta\mu$ is known and included in simulations. For compound $\boldsymbol{\beta}$, the final state is the S23 transition. The difference between dominant pathway frequencies is 3380cm^{-1} or 0.419eV, and transitions with this energy difference along with their transition dipole moments are used to simulate the ETPA oscillations until the best fit is found. For compound $\boldsymbol{\beta C}$, the final state is the S20 state. The difference between dominant pathway frequencies is 3490cm^{-1} or 0.432eV. With our TD-DFT calculations, transition dipole moments from intermediate to final states cannot easily be calculated. However, since experimental values were obtained, we are able to infer these excited state transition dipole moments such that the resulting ETPA values fit our experimental data. Thus, we successfully combine experiment and computational work to produce a model of the ETPA pattern for each compound.

The resulting ETPA patterns are shown in Figure 5.10, overlaid with the experimentally obtained envelope wave. For compound $\boldsymbol{\beta}$, when the transitions closest to resonance with the entangled photons are used to compute the ETPA simulations, the resulting cross-section ranges are far greater which suggests that their contribution may be suppressed by some other process. The transition dipole moments of states with the appropriate energy difference dictated by equation 5.2 are used to compute the ETPA pattern for compound $\boldsymbol{\beta}$ until the best fit is found, resulting in an overlap of the upper portion of the oscillations with the experimentally obtained values (Figure 5.10). The upper values coincide well with the experimentally measured cross-sections and for the lower values, it is possible that these were not seen experimentally as we did not have smaller tuning of τ. The destructive interference from different energy levels is seen by the smaller peaks within the higher peaks that match

the experimental oscillation period. For compound ***βC***, the permanent dipole moments of the ground and final states as well as transition dipole moments for the dominant pathways were used to compute ETPA cross-section oscillations. As seen in Figure 5.10, this results in good correlation with experimental data. Again, destructive interferences are seen within the main period obtained experimentally.

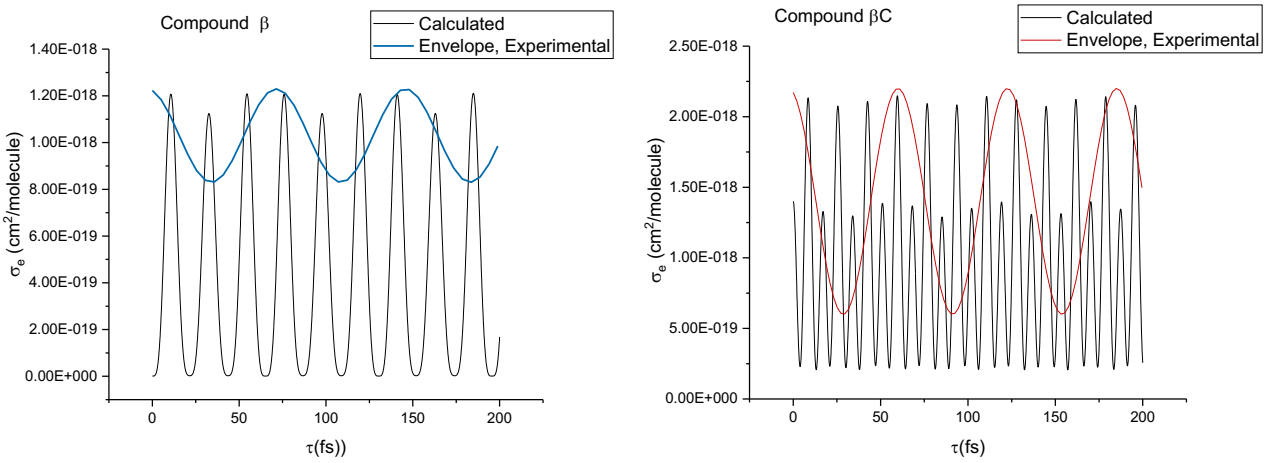

Figure 5.10*. Graphs showing calculated pattern of ETPA cross-section as a function of time delay (τ) for compound* ***β*** *(left) and compound* ***βC*** *(right), overlaid with experimentally obtained envelope wave*

A Fourier analysis is performed to determine the frequency spectra (ETPA spectrogram) from the calculated ETPA versus time delay graphs. This becomes the first use of experiment to fully realize virtual-state spectroscopy. To obtain such distinct peaks, the Fourier transform had to be carried out over a broad picosecond range of τ. Frequency spectra were first obtained using a very small range of τ (200fs) and this confirmed that the higher range indeed presented much higher resolution for frequency peaks. The graph shows distinct peaks for Δ_j of compound ***β*** (blue) and compound ***β*****C** (red). The energy of these states are given by, $\varepsilon_j = \pm\Delta_j + \left(\varepsilon_i + {}^{\omega_p}/_2\right)$. The compounds' ground state energy, ε_i, was set to 0 and ${}^{\omega_p}/_2$ is half of the pump photon energy. The amplitude of the peaks in the spectrogram are proportional to the

square of the term A_j which contains the dipole matrix elements D_j with rovibrational or electronic transition moments.[52] Therefore, only states with relatively significant contributions to the ETPA emerge in the spectrum.

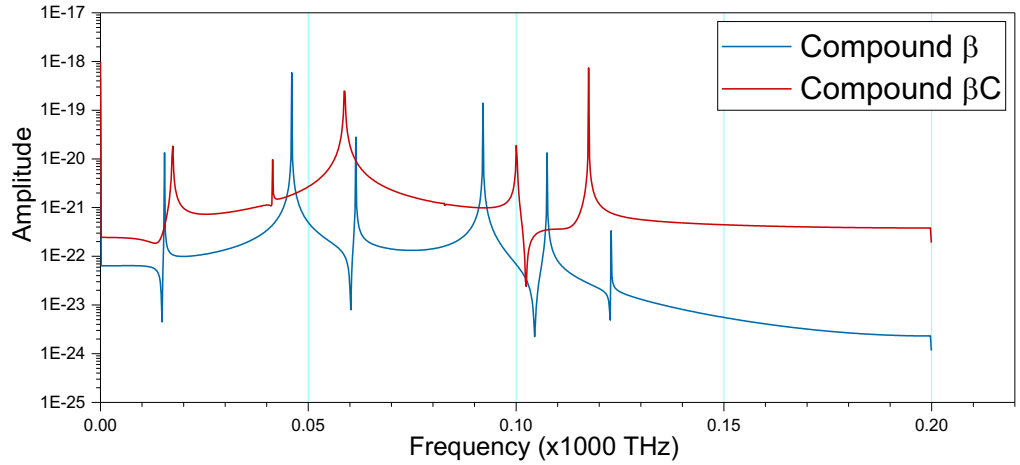

Figure 5.11. *ETPA Spectrogram from Fourier transform of ETPA cross-section as a function of time delay showing intermediate state energy peaks of compound* ***β*** *and* ***βC****.*

Table 5.7. *Virtual state energies for compounds* ***β*** *and* ***βC*** *attained from ETPA spectrogram.*

Compound ***β***			Compound ***βC***		
Δ_j (cm^{-1})	Virtual State energy (nm)		Δ_j (cm^{-1})	Virtual State energy (cm^{-1})	
	$\varepsilon_j +$	$\varepsilon_j -$		$\varepsilon_j +$	$\varepsilon_j -$
4096.17	589.67	1140.72	3915.8	616.11	1190.59
3582.48	608.09	1077.58	3335.7	638.95	1113.67
3068.79	627.69	1021.06	1959.9	700.53	965.7
2048.08	670.66	924.68	1380.98	730	914.5
1534.39	694.59	882.76	580	775.49	852.15
513.68	747.59	809.79	--	--	

It can be seen in Figure 5.11 that there is a blue shift in the frequencies of virtual states of compound ***β*** compared to compound ***β***C. Additionally, the spectrum of compound ***βC*** is at an overall higher amplitude than that of compound ***β***, with one peak with a comparatively high

amplitude. This is expected as compound $\boldsymbol{\beta}$**C** has the higher cross-section values, therefore the Fourier transform will result in higher amplitudes. The peaks of compound $\boldsymbol{\beta}$ although lower, occur over a broad amplitude range, suggesting high contributions of virtual states. We consider first $\varepsilon_j +$ and secondly $\varepsilon_j -$, which are low-lying energy levels. For compound $\boldsymbol{\beta}$, the $\varepsilon_j +$ of Δ_j 513.68 cm^{-1} corresponds to ~747nm which is the S1 transition, suggesting that the S1 state may be an intermediate state for entangled two-photon absorption or resonant with an intermediate state of ETPA. This position was also pronounced in the transient absorption spectra. In fact, the intermediate state energy peaks for compound $\boldsymbol{\beta}$ range from 747nm to 590nm, which is where the transient ESA behavior is most evident. As such, it seems virtual state energies can be correlated with transient species. Similarly, the $\varepsilon_j +$ of Δ_j 1534 cm^{-1} is 695nm which corresponds to the S4 transition. While these two intermediate transitions coincide very closely with the stationary Born-Oppenheimer (BO) transitions of S1 and S4, the other virtual states lie between the BO states and are indeed non-stationary virtual states. On the other hand, all the virtual states of compound $\boldsymbol{\beta C}$ are at lower energy levels than the BO states. Comparing this to the dynamics of compound $\boldsymbol{\beta}$, this suggests that the intermediate pathway is more prominent for the twisted trimer; the intermediate states are both virtual (non-stationary) and definite stationary states. This high contribution from BO intermediate states for compound $\boldsymbol{\beta}$ may lead to what is seen as an enhancement of its ETPA signal relative to compound $\boldsymbol{\beta C}$ compared with classical results.

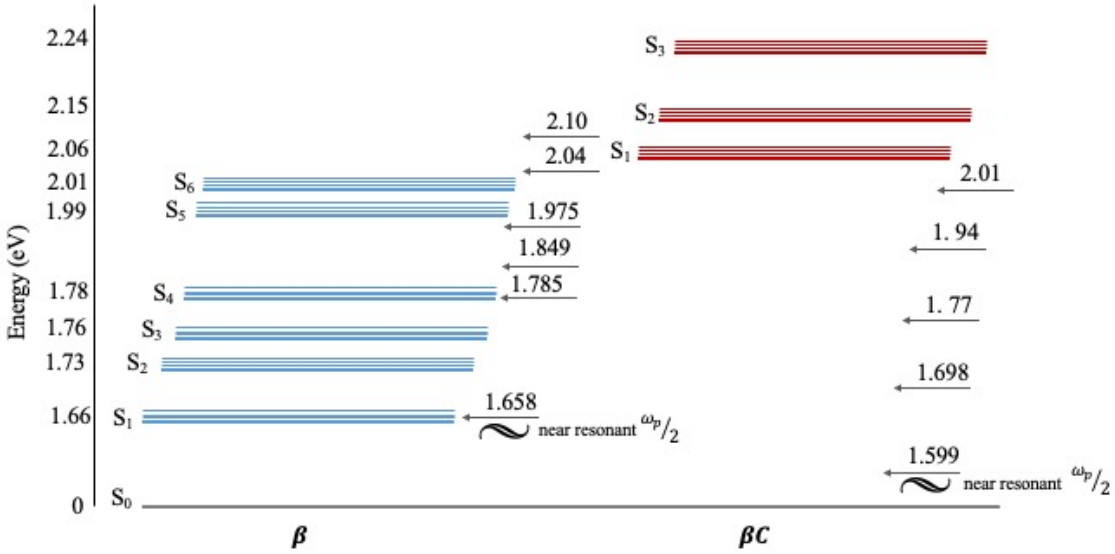

Figure 5.12. *Energy level diagrams of compound* ***β*** *(blue) and compound* ***βC*** *(red) with virtual state energies for each compound shown to the right of the energy levels with black arrows. The transition states near resonant with the entangled photons are indicated.*

The $\varepsilon_j \pm$ values for both compounds are lower than the pump photon energy and in some cases are resonant or close to resonance with the entangled photon energy (Figure 5.12). For compound ***β***, the $\varepsilon_j -$ value of 747nm is strongly resonant with the pump photon energy (800nm) with a low detuning energy of 876 cm^{-1} and thus will act strongly as an intermediate state. This again confirms that compound ***β*** undergoes ETPA via the intermediate or virtual pathway and speaks to the enhancement seen in its ETPA signal. However, such low detuning would ideally result in higher cross-sections and as was seen in our simulations, the full effect of this strong resonance was not observed experimentally. In fact, the peak of this intermediate state (farthest right on Figure 5.11) shows a relatively small contribution. From the previous study[50] which has shown that ultrafast processes such as intramolecular charge transfer compete with intramolecular singlet fission (iSEF), it is possible that the iSEF process that has been shown to be present for compound ***β***[50] may affects its ETPA cross-section. The double

triplet state (^{1}TT) is energetically accessible from the S_1 state. Therefore, it is possible that contribution from the S_1 state to ETPA is reduced as it competes with the formation of this double triplet state. There is still an enhancement of the cross-sections of $\boldsymbol{\beta}$ relative to $\boldsymbol{\beta}$**C** with ETPA compared to classical TPA because as has been shown previously, ETPA is highly sensitive so better able to resolve to small pathway contributions compared to classical TPA.[30]

On the other hand, while the intermediate energies of compound $\boldsymbol{\beta C}$ do not coincide with any stationary states of the compound and in fact lower in energy than any of the energy levels of $\boldsymbol{\beta C}$ (Figure 5.12), they are close to resonance with the entangled photons, therefore leading to the relatively high cross-section on the order of 10^{-18} compared to molecules showing cross-sections on the order of 10^{-19} and below.[27,30,53] With higher transition dipole moments or stationary states close to these virtual states, the cross-section may have been higher still.[29,53] Knowing information about these intermediate levels significantly modifies our understanding of their excitation processes. It shows that we may be able to probe different types of states and gives a broader picture of the energetics at play. If we are able to gain such information about other compounds with known useful applications, we will be able to implement this knowledge to more effectively synthesize materials with the necessary properties.

5.6 Conclusion

Our results show us spectral dynamics of the steady state, excited state (transient) and virtual intermediate states of both compounds. To the best of our knowledge, this is the first time entangled photons have experimentally been used to achieve virtual state spectroscopy. Our study demonstrates that intermediate states can correspond to virtual non-BO states or stationary BO states and this affects their significance to excitations and how they subsequently

determine properties such as charge transfer character. In cases where the experimental observations need to be better understood, a broader picture using virtual state spectroscopy may aid in understanding the energetics at play. Furthermore, these virtual states can be related to transient species observed with femtosecond transient absorption spectroscopy and other proposed mechanisms occurring in the compound. We believe that with fine tuning of the delay time, virtual state spectroscopy can be used done with better femtosecond precision and over a longer period of times. It can be used to better determine what states entangled photons may probe and learn more about these states. Thus, it can be applied to optical materials to learn more about their photophysical properties.

References

(1) Friend, R. H.; Gymer, R. W.; Holmes, A. B.; Burroughes, J. H.; Marks, R. N.; Taliani, C.; Bradley, D. D. C.; Santos, D. A. Dos; Brédas, J. L.; Lögdlund, M.; Salaneck, W. R. Electroluminescence in Conjugated Polymers. *Nature* **1999**, *397*, 121–128.

(2) Kippelen, B.; Brédas, J. L. Organic Photovoltaics. *Energy Environ. Sci.* **2009**, *2* (3), 251–261. https://doi.org/10.1039/b812502n.

(3) Kulkarni, A. P.; Tonzola, C. J.; Babel, A.; Jenekhe, S. A. Electron Transport Materials for Organic Light-Emitting Diodes. *Chem. Mater.* **2004**, *16* (23), 4556–4573. https://doi.org/10.1021/cm049473l.

(4) Zheng, Z.; Brédas, J. L.; Coropceanu, V. Description of the Charge Transfer States at the Pentacene/C 60 Interface: Combining Range-Separated Hybrid Functionals with the Polarizable Continuum Model. *J. Phys. Chem. Lett.* **2016**, *7*, 2616–2621. https://doi.org/10.1021/acs.jpclett.6b00911.

(5) Paci, I.; Johnson, J. C.; Chen, X.; Rana, G.; Popović, D.; David, D. E.; Nozik, A. J.; Ratner, M. A.; Michl, J. Singlet Fission for Dye-Sensitized Solar Cells: Can a Suitable Sensitizer Be Found? *J. Am. Chem. Soc.* **2006**, *128* (51), 16546–16553. https://doi.org/10.1021/ja063980h.

(6) Müller, A. M.; Avlasevich, Y. S.; Schoeller, W. W.; Müllen, K.; Bardeen, C. J. Exciton Fission and Fusion in Bis(Tetracene) Molecules with Different Covalent Linker Structures. *J. Am. Chem. Soc.* **2007**, *129* (46), 14240–14250. https://doi.org/10.1021/ja073173y.

(7) Carlotti, B.; Cai, Z.; Kim, H.; Sharapov, V.; Madu, I. K.; Zhao, D.; Chen, W.; Zimmerman, P. M.; Yu, L.; Goodson, T. Charge Transfer and Aggregation Effects on the Performance of Planar vs Twisted Nonfullerene Acceptor Isomers for Organic Solar Cells. *Chem. Mater.* **2018**, *30*, 4263–4276. https://doi.org/10.1021/acs.chemmater.8b01047.

(8) Cai, Z.; Vázquez, R. J.; Zhao, D.; Li, L.; Lo, W. Y.; Zhang, N.; Wu, Q.; Keller, B.; Eshun, A.; Abeyasinghe, N.; Banaszak-Holl, H.; Goodson, T.; Yu, L. Two Photon Absorption

Study of Low-Bandgap, Fully Conjugated Perylene Diimide-Thienoacene-Perylene Diimide Ladder-Type Molecules. *Chem. Mater.* **2017**, *29* (16), 6726–6732. https://doi.org/10.1021/acs.chemmater.7b01512.

(9) Vázquez, R. J.; Kim, H.; Kobilka, B. M.; Hale, B. J.; Jeffries-El, M.; Zimmerman, P.; Goodson, T. Evaluating the Effect of Heteroatoms on the Photophysical Properties of Donor-Acceptor Conjugated Polymers Based on 2,6-Di(Thiophen-2-Yl)Benzo[1,2-b:4,5-B′]Difuran: Two-Photon Cross-Section and Ultrafast Time-Resolved Spectroscopy. *J. Phys. Chem. C* **2017**, *121* (27), 14382–14392. https://doi.org/10.1021/acs.jpcc.7b01767.

(10) Wu, J. S.; Cheng, S. W.; Cheng, Y. J.; Hsu, C. S. Donor-Acceptor Conjugated Polymers Based on Multifused Ladder-Type Arenes for Organic Solar Cells. *Chem. Soc. Rev.* **2015**, *44* (5), 1113–1154. https://doi.org/10.1039/c4cs00250d.

(11) Rosenberg, M.; Dahlstrand, C.; Kilså, K.; Ottosson, H. Excited State Aromaticity and Antiaromaticity: Opportunities for Photophysical and Photochemical Rationalizations. *Chem. Rev.* **2014**, *114* (10), 5379–5425. https://doi.org/10.1021/cr300471v.

(12) Berera, R.; van Grondelle, R.; Kennis, J. T. M. Ultrafast Transient Absorption Spectroscopy: Principles and Application to Photosynthetic Systems. *Photosynth. Res.* **2009**, *101* (2–3), 105–118. https://doi.org/10.1007/s11120-009-9454-y.

(13) Gustavsson, T.; Coto, P. B.; Serrano-Andŕs, L.; Fujiwara, T.; Lim, E. C. Do Fluorescence and Transient Absorption Probe the Same Intramolecular Charge Transfer State of 4-(Dimethylamino)Benzonitrile? *J. Chem. Phys.* **2009**, *131* (3). https://doi.org/10.1063/1.3173609.

(14) Rao, A.; Friend, R. H. Harnessing Singlet Exciton Fission to Break the Shockley-Queisser Limit. *Nat. Rev. Mater.* **2017**, *2* (17063), 1–12. https://doi.org/10.1038/natrevmats.2017.63.

(15) Dias, F. B.; Santos, J.; Graves, D. R.; Data, P.; Nobuyasu, R. S.; Fox, M. A.; Batsanov, A. S.; Palmeira, T.; Berberan-Santos, M. N.; Bryce, M. R.; Monkman, A. P. The Role of Local Triplet Excited States and D-A Relative Orientation in Thermally Activated Delayed Fluorescence: Photophysics and Devices. *Adv. Sci.* **2016**, *3* (12), 1–10. https://doi.org/10.1002/advs.201600080.

(16) Vázquez, R. J.; Kim, H.; Zimmerman, P. M.; Goodson, T. Using Ultra-Fast Spectroscopy to Probe the Excited State Dynamics of a Reported Highly Efficient Thermally Activated

Delayed Fluorescence Chromophore. *J. Mater. Chem. C* **2019**, *7* (14), 4210–4221. https://doi.org/10.1039/c8tc05957h.

(17) Swofford, R. L.; Albrecht, A. C. Nonlinear Spectroscopy. *Annu. Rev. Phys. Chem.* **1978**, *29*, 421–440. https://doi.org/10.1126/science.178.4058.247.

(18) Ho-Wu, R.; Yau, S. H.; Goodson, T. Linear and Nonlinear Optical Properties of Monolayer-Protected Gold Nanocluster Films. *ACS Nano* **2016**, *10* (1), 562–572. https://doi.org/10.1021/acsnano.5b05591.

(19) O'Brien, J. Optical Quantum Computing. *Science (80-.).* **2007**, *318*, 1567–1570. https://doi.org/10.1109/ICNC.2015.7378022.

(20) Pirandola, S.; Andersen, U. L.; Banchi, L.; Berta, M.; Bunandar, D.; Colbeck, R.; England, D.; Gehring, T.; Lupo, C.; Ottaviani, C.; Pereira, J. L.; Razavi, M.; Shaari, J. S.; Tomamichel, M.; Usenko, V. C.; Vallone, G.; Villoresi, P.; Wallden, P. Advances in Quantum Cryptography and Relays. *Adv. Opt. Photonics* **2020**, *12* (4), 1012–1236. https://doi.org/10.1109/ecoc.2006.4801410.

(21) Fei, H. B.; Jost, B. M.; Popescu, S.; Saleh, B. E. A.; Teich, M. C. Entanglement-Induced Two-Photon Transparency. *Phys. Rev. Lett.* **1997**, *78* (9), 1679–1682. https://doi.org/10.1103/PhysRevLett.78.1679.

(22) Saleh, B. E. A.; Jost, B. M.; Fei, H. B.; Teich, M. C. Entangled-Photon Virtual-State Spectroscopy. *Phys. Rev. Lett.* **1998**, *80* (16), 3483–3486. https://doi.org/10.1103/PhysRevLett.80.3483.

(23) Lee, D. I.; Goodson, T. Entangled Photon Absorption in an Organic Porphyrin Dendrimer. *J. Phys. Chem. B* **2006**, *110* (51), 25582–25585. https://doi.org/10.1021/jp066767g.

(24) Harpham, M. R.; Goodson III, T. Thiophene Dendrimers as Entangled Photon Sensor Materials. *J. Am. Chem. Soc. Artic.* **2018**, No. 21, 973–979.

(25) Guzman, A. R.; Harpham, M. R.; Suzer, O.; Haley, M. M.; Goodson III, T. G. Spatial Control of Entangled Two-Photon Absorption with Organic Chromophores ¨. *J. Am. Chem. Soc. Commun.* **2010**, *132*, 7840–7841. https://doi.org/10.1021/ja1016816.

(26) Villabona-monsalve, J. P.; Caldero, O.; Portela, M. N.; Valencia, A. Entangled Two Photon Absorption Cross Section on the 808 Nm Region for the Common Dyes Zinc Tetraphenylporphyrin and Rhodamine B. *J. Phys. Chem. A* **2017**, 7869–7875. https://doi.org/10.1021/acs.jpca.7b06450.

(27) Villabona-monsalve, J. P.; Varnavski, O.; Palfey, B. A.; Goodson III, T. Two-Photon Excitation of Flavins and Flavoproteins with Classical and Quantum Light. *J. Am. Chem. Soc. Commun.* **2018**, *140*, 14562–14566. https://doi.org/10.1021/jacs.8b08515.

(28) Upton, L.; Harpham, M.; Suzer, O.; Richter, M.; Mukamel, S.; Goodson, T. Optically Excited Entangled States in Organic Molecules Illuminate the Dark. *J. Phys. Chem. Lett.* **2013**, *4* (12), 2046–2052. https://doi.org/10.1021/jz400851d.

(29) Burdick, R. K.; Varnavski, O.; Molina, A.; Upton, L.; Zimmerman, P.; Iii, T. G. Predicting and Controlling Entangled Two-Photon Absorption in Diatomic Molecules Published as Part of The Journal of Physical Chemistry Virtual Special Issue " William M . Jackson Festschrift " . *J. Phys. Chem. A* **2018**, *122*, 8198–8212. https://doi.org/10.1021/acs.jpca.8b07466.

(30) Eshun, A.; Cai, Z.; Awies, M.; Yu, L.; Goodson III, T. Investigations of Thienoacene Molecules for Classical and Entangled Two-Photon Absorption Published as Part of The Journal of Physical Chemistry Virtual Special Issue " William M . Jackson Festschrift " . *J. Phys. Chem. A* **2018**, *122*, 8167–8182. https://doi.org/10.1021/acs.jpca.8b06312.

(31) Kojima, J.; Nguyen, Q. V. Entangled Biphoton Virtual-State Spectroscopy of the A 2Σ +- X 2Π System of OH. *Chem. Phys. Lett.* **2004**, *396* (4–6), 323–328. https://doi.org/10.1016/j.cplett.2004.08.051.

(32) Varnavski, O.; Pinsky, B.; Goodson, T. Entangled Photon Excited Fluorescence in Organic Materials: An Ultrafast Coincidence Detector. **2017**, 6–11. https://doi.org/10.1021/acs.jpclett.6b02378.

(33) Chai, J.; Head-gordon, M. Long-Range Corrected Hybrid Density Functionals with Damped Atom – Atom Dispersion Corrections W. **2008**, 6615–6620. https://doi.org/10.1039/b810189b.

(34) Phys, J. C. Systematic Optimization of Long-Range Corrected Hybrid Density Functionals. **2010**, *084106* (January 2008), 0–15. https://doi.org/10.1063/1.2834918.

(35) Shao, Y.; Gan, Z. et al. Advances in Molecular Quantum Chemistry Contained in the Q-Chem 4 Program Package. *Mol. Phys.* **2014**, *8976*. https://doi.org/10.1080/00268976.2014.952696.

(36) Spenst, P.; Würthner, F. Journal of Photochemistry and Photobiology C : Photochemistry Reviews Based on Aromatic Bisimides. *"Journal Photochem. Photobiol. C Photochem.*

Rev. **2017**, *31*, 114–138. https://doi.org/10.1016/j.jphotochemrev.2017.03.002.

(37) Langhals, H. Emission Characteristics and Photostability Of. **1988**, No. 1, 4565–4568. https://doi.org/10.1021/j100326a062.

(38) Brown, K. E.; Veldkamp, B. S.; Co, D. T.; Wasielewski, M. R. Vibrational Dynamics of a Perylene − Perylenediimide Donor − Acceptor Dyad Probed with Femtosecond Stimulated Raman Spectroscopy. **2012**. https://doi.org/10.1021/jz301107c.

(39) Fron, E.; Pilot, R.; Schweitzer, G.; Qu, J.; Herrmann, A.; Klaus, M.; Hofkens, J.; Auweraer, M. Van Der; Schryver, F. C. De. Photoinduced Electron-Transfer in Perylenediimide Triphenylamine-Based Dendrimers : Single Photon Timing and Femtosecond Transient Absorption Spectroscopy †‡. **2008**, 597–604. https://doi.org/10.1039/b718479d.

(40) Giaimo, J. M.; Gusev, A. V; Wasielewski, M. R. Excited-State Symmetry Breaking in Cofacial and Linear Dimers of a Green Perylenediimide Chlorophyll Analogue Leading to Ultrafast Charge Separation. **2002**, 8530–8531. https://doi.org/10.1021/ja026422l.

(41) Blocks, B.; Boom, T. Van Der; Hayes, R. T.; Zhao, Y.; Bushard, P. J.; Weiss, E. A.; Wasielewski, M. R. Charge Transport in Photofunctional Nanoparticles Self-Assembled from Zinc. **2002**, No. 14, 9582–9590. https://doi.org/10.1021/ja026286k.

(42) Lukas, A. S.; Zhao, Y.; Miller, S. E.; Wasielewski, M. R. Biomimetic Electron Transfer Using Low Energy Excited States : A Green Perylene-Based Analogue of Chlorophyll A. **2002**, 1299–1306. https://doi.org/10.1021/jp014073w.

(43) Sung, J.; Nowak-kro, A.; Schlosser, F.; Fimmel, B.; Kim, W.; Kim, D.; Wu, F. Direct Observation of Excimer-Mediated Intramolecular Electron Transfer in a Cofacially-Stacked Perylene Bisimide Pair. **2016**, 13–16. https://doi.org/10.1021/jacs.6b04591.

(44) Vagnini, M. T.; Smeigh, A. L.; Blakemore, J. D.; Eaton, S. W.; Schley, N. D.; Souza, F. D.; Crabtree, R. H.; Brudvig, G. W.; Co, D. T.; Wasielewski, M. R. Ultrafast Photodriven Intramolecular Electron Transfer from an Iridium-Based Water-Oxidation Catalyst to Perylene Diimide Derivatives. **2012**, *109* (39). https://doi.org/10.1073/pnas.1202075109.

(45) Berberich, M.; Krause, A.; Orlandi, M.; Scandola, F.; Würthner, F. Toward Fluorescent Memories with Nondestructive Readout : Photoswitching of Fluorescence by Intramolecular Electron Transfer in a Diaryl Ethene-Perylene Bisimide Photochromic System **. **2008**, No. Scheme 1, 6616–6619. https://doi.org/10.1002/anie.200802007.

(46) Drobizhev, M.; Stepanenko, Y.; Dzenis, Y.; Karotki, A.; Rebane, A.; Taylor, P. N.; Anderson, H. L. ( ) - 2 (1). **2004**, *2* (1), 15352–15353. https://doi.org/10.1021/ja0445847.

(47) Gryko, D. T.; Anderson, H. L. Porphyrin Dimers : Torsional and Substituent. **2014**, 6802–6809. https://doi.org/10.1039/c4tc01120a.

(48) Lee, D.; Goodson III, T. Entangled Photon Absorption in an Organic Porphyrin Dendrimer. *J. Phys. Chem. B* **2006**, *110*, 25582–25585. https://doi.org/10.1021/jp066767g.

(49) Zhang, J.; Xu, B.; Chen, J.; Wang, L.; Tian, W. Oligo (Phenothiazine) S : Twisted Intramolecular Charge Transfer and Aggregation-Induced Emission. **2013**. https://doi.org/10.1021/jp405664m.

(50) Carlotti, B.; Madu, I. K.; Kim, H.; Cai, Z.; Jiang, H.; Muthike, A. K.; Yu, L.; Zimmerman, P. M.; Goodson, T. Activating Intramolecular Singlet Exciton Fission by Altering π-Bridge Flexibility in Perylene Diimide Trimers for Organic Solar Cells. *Chem. Sci.* **2020**, *11* (33), 8757–8770. https://doi.org/10.1039/d0sc03271a.

(51) Vivas, M. G.; De Boni, L.; Mendonça, C. R. Two-Photon Spectroscopy of Organic Materials. *Mol. Laser Spectrosc. Adv. Appl.* **2018**, No. 2, 165–191. https://doi.org/10.1016/B978-0-12-849883-5.00008-5.

(52) Kojima, J.; Nguyen, Q. Entangled Biphoton Virtual-State Spectroscopy of the A 2 R + – X 2 P System of OH. **2004**, *396*, 323–328. https://doi.org/10.1016/j.cplett.2004.08.051.

(53) Kang, G.; Avanaki, K. N.; Mosquera, M. A.; Burdick, R. K.; Villabona-monsalve, J. P.; Goodson III, T.; Schatz, G. C. Efficient Modeling of Organic Chromophores for Entangled Two-Photon Absorption. *J. Am. Chem. Soc.* **2020**, *10.1021/ja*. https://doi.org/10.1021/jacs.0c02808.

5.6. Supplementary Information

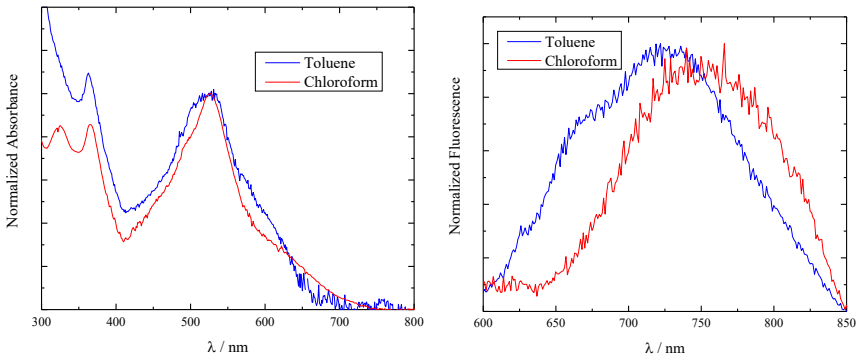

Figure 5.13 *Normalized absorption and emission spectra of compound* ***βC*** *in toluene (blue) and chloroform (red).*

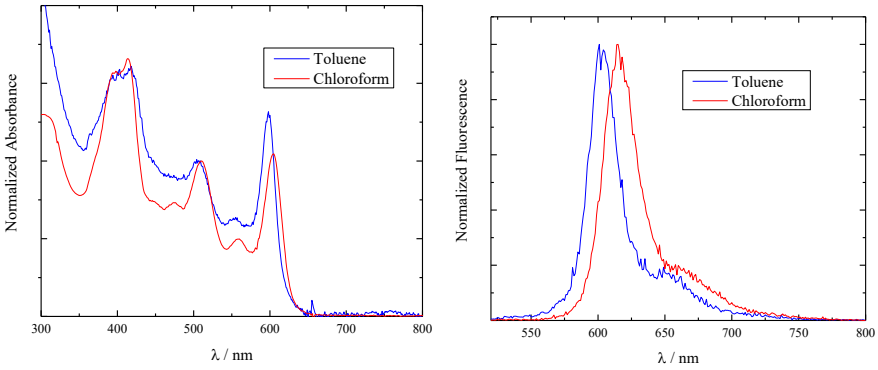

Figure 5.14. *Normalized absorption and emission spectra of compound* ***βC*** *in toluene (blue) and chloroform (red).*

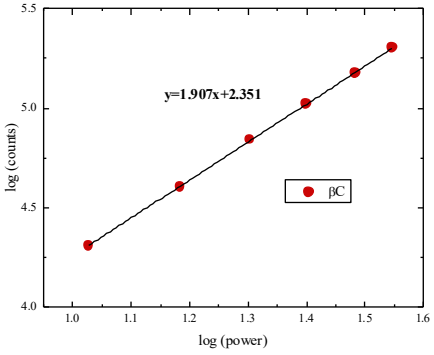

Figure 5.15 *Power dependence of the two−photon excited emission for compound* ***2*** *in chloroform upon 820 nm excitation.*

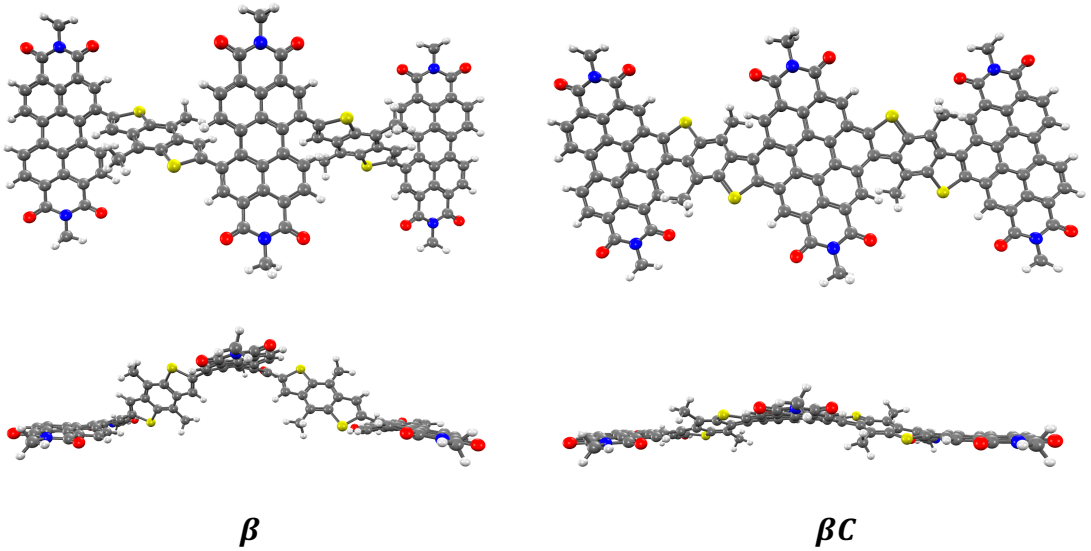

β ***βC***

Figure 5.16. *Ground state optimized geometry computed for compounds* ***β*** *and* ***βC*** *(top view for the upper panel, and side view for the lower panel. Color scheme: Hydrogen—white, carbon—black, nitrogen—blue, oxygen—red, sulfur—yellow).*

Table 5.8. Computed transition energy, nature and oscillator strength of the lowest excited singlet states of **1** and **2** in chloroform, together with the experimental absorption and emission maxima (λ_{exp}).

compound	transition	λ_{calc} / nm	f	λ_{exp} / nm
β	$S_0 \rightarrow S_1$	745	0.33	630^{sh}
	$S_0 \rightarrow S_7$	537	0.26	526
	$S_0 \rightarrow S_{17}$	452	1.06	450^{sh}
	$S_0 \rightarrow S_{29}$	374	0.18	366
	$S_1 \rightarrow S_0$	925	0.32	
	$S_2 \rightarrow S_0$	800	0.12	790
βC	$S_0 \rightarrow S_1$	602	1.02	605
	$S_0 \rightarrow S_5$	514	0.32	510
	$S_0 \rightarrow S_{15}$	436	0.53	414
	$S_0 \rightarrow S_{22}$	397	0.34	394
	$S_1 \rightarrow S_0$	646	0.45	613
	$S_2 \rightarrow S_0$	596	0.49	

Chapter 6
Investigating Molecular Optical Properties with Hong Ou Mandel Interferometry

This chapter is adapted from a manuscript

Eshun, A.; Gu, B.; Varnavski, O.; Dorfman, K.; Asban, A.; Mukamel, S.; Goodson III, T. "Investigations of Molecular Optical Properties Using Quantum Light and Hong-Ou-Mandel Interferometry"

which has been submitted for review for publication. Supporting Information is included in this chapter.

6.1 Abstract

Entangled photon pairs have been used for molecular spectroscopy in the form of entangled two-photon absorption and have been used in quantum interferometry for precise measurements of light source properties and time delays. Here we present an experiment that combines molecular spectroscopy and quantum interferometry, by utilizing the correlations of entangled photons in a Hong-Ou-Mandel (HOM) interferometer to study molecular properties. We show that the HOM signal is sensitive to the presence of a resonant organic sample placed in one arm of the interferometer and the resulting signal contains information pertaining to the light-matter interaction. With this effect, we are able to extract the dephasing time of the coherent response induced by the excitation on a femtosecond timescale. A dephasing time of 102fs is obtained, which is relatively short compared to times found with similar methods and taking into consideration linewidth broadening and the instrument entanglement time As the measurement is done with coincidence counts as opposed to simply intensity, it is unaffected

by dispersion effects, and since interactions with the molecular state affect the photon correlation, the observed measurement contains only these effects and no other classical losses. The experiments are accompanied with theory which predicts the observed temporal shift, and captures the entangled photon joint spectral amplitude and the molecule's transmission in the coincidence counting rate. Thus, we present a proof-of-concept experimental method based of entangled photon interferometry that can be used to characterize optical properties in organic molecules, which can be expanded to other fields in materials chemistry and biology, and can in the future be expanded on for more complex spectroscopic studies of non-linear optical properties.

6.2 Introduction

Our growing understanding of quantum light over the years has led researchers to utilize its unique properties towards advancements in quantum information science, in the fields of computing, cryptography, imaging and quantum sensing.[1–4] Of particular interest has been the subject of spectroscopy with quantum light, as it offers avenues to overcome classical Fourier limitations, the opportunity for enhanced light-matter coupling due to its distinct photon statistics, and novel control knobs defined by the quantum photon field wave function. So far, quantum light spectroscopy has been approached experimentally with entangled two-photon absorption studies[5–16] via absorption, fluorescence and microscopy. These measurements have provided great progress with enhanced resolution in two-photon cross-section measurements as well as the ability to conduct spectroscopy at extremely low light intensities, limiting the risk of damaging the studied sample. We now wish to develop experimental quantum light spectroscopy even further. In this work, by exploiting the correlations of entangled photon pairs via two-photon interferometry, we seek to illustrate a new method of spectroscopy to

study molecular properties using a Hong-Ou-Mandel (HOM) set up, which has not yet been used to probe molecules experimentally in such a way.

Due to the unique quantum interference properties of the HOM phenomenon, it presents itself as an interesting and robust outlet for investigating quantum light-matter interactions. We have designed and set up an experiment where, as a result of the quantum interference of the indistinguishable photons, we observe the effect the sample's presence in the interferometer path has on the light's photon statistics as opposed to simply the intensity, which provides information on the light statistics as well as features of the light-matter interactions. Being able to utilize interferometric schemes to detect linear and nonlinear susceptibilities with quantum light can improve the accuracy of our measurements of these material susceptibilities due to the increased sensitivity of quantum interferometers.[17,18] Furthermore, the susceptibilities can be connected to other physical properties of the matter such as coherence dephasing times, and in this article, we seek to make this connection through theory and extract the molecule's dephasing time from experimental data. This experimental scheme presents a novel and accessible way in which we can measure molecular optical properties with quantum light and serves as a model to be expanded on and adapted for future more complex spectroscopic studies. While the setup of an interferometer can be tedious, it is far less daunting and less involved than large expensive femtosecond laser systems usually used for time-resolved ultra-fast or high-resolution spectroscopy. Improvements have been made in the field of quantum optics making the building of such HOM interferometers accessible to many researchers.[19–22] Thus, this straightforward interferometric setup can be used in place of complex laser systems, to interrogate the dynamics of and interactions between molecular states with the advantages of quantum light.[23] As the interest in entangled light applications grows and more studies

consider the possibility of utilizing it for spectroscopy,[23–26] we present experimental confirmation of a method that can be expanded into various fields that require sensitive spectroscopy of molecules.

The phenomenon of quantum interference with entangled light states is well understood and has been utilized in quantum optics mainly for metrology and quantum light characterization.[27] The nonclassical properties of photon pairs generated from Spontaneous Parametric Downconversion (SPDC) allow them to be used for a variety of interferometric purposes such as the Hanbury-Brown-Twiss[28] (HBT) and Hong-Ou-Mandel (HOM) interferometers. The HOM interferometer is a two-photon interference effect that measures the indistinguishability of photon pairs.[29] This two-photon interference at a beam splitter was initially exhibited by Hong, Ou and Mandel in 1987[29] and Shih and Alley[30] and has been used in testing nonlocality, Bell-state measurements, quantum metrology and in building quantum optical logical gates.[31] An HOM interferometer measures the quantum interference resulting from the interference of probability amplitudes of 4 different two-photon Feynman paths, when indistinguishable photons are incident on a 50/50 beam splitter (Figure 6.1). When indistinguishable photons arrive simultaneously in time, they destructively interfere leading to null coincidence counts at two detectors connected in coincidence. The temporal width of the resulting dip, is the inverse of the bandwidth of the SPDC spectrum and the coherence time of the entangled photons.

While the presence of a simple refractive or birefringent material in the interferometer pathway can lead to polarization mode dispersion which degrades entanglement and causes temporal delays,[32] it is theorized that the presence of an absorbing material in an interferometer would result in a much more complex modification to the coincidence signal.[33,34] Such

experiments with entangled light interferometers have been proposed.[23,35,36] One study was carried out on inorganic crystals where Kalashnikov *et al*[37] used a similar experimental outlook to conduct time-resolved measurements focused on coherent dynamics of inorganic nanostructures.[37] The study's focus was on the ability to use entangled photons for measurements of a medium's dephasing time with the HOM dip. However, their work considered solid crystals and nanostructures which are much easier to probe. In our work, we assess the sensitivity of the experimental setup and possibility of expanding it into more fields by conducting measurements on organic molecular chromophores. Changes caused by molecules that are at unsaturated concentrations and do not have molecular aggregates will be more subtle, therefore, the HOM signal must be shown to be perceptible to these light-matter interactions. Furthermore, the inorganic crystals used in Ref. 35 have narrow resonances whereas the typical linewidths of organic and biological systems are much broader. For such crystals, homogeneous broadening dominates inhomogeneous effects and therefore it is easier to account for any slight changes caused by inhomogeneous broadening. By conducting the experiment with an organic chromophore, we show that the dephasing time can still be extracted despite the greater inhomogeneous broadening effects in organic molecules. In the case of our experiment, the SPDC spectrum is narrower than the molecule's linewidth. Thus, we show that subtle changes caused by organic chromophores can be perceived by our experiment and that information can be extracted even when the SPDC spectrum is narrower than the molecule's linewidth.

In our experiment, a resonant absorbing medium is placed in the signal arm of the interferometer. The signal beam transmits through the sample and subsequently becomes modified by its susceptibility ($\chi^{(1)}$), acquiring a phase shift for the different frequency

components which introduces a delay in the signal mode. The idler beam undergoes a frequency independent phase shift, compensating for the shift caused by the molecular interaction which introduces a time shift to the observed HOM dip upon recombination and interference of the signal and idler beams at the beam splitter. As there is quantum interference between the signal beam and the molecular states, the idler is not able to fully compensate the acquired modification and hence, there is a change in the shape of the HOM dip i.e. loss of its symmetry. The molecule-induced modifications to the signal mode are frequency dependent as encoded in ($\chi^{(1)}$), thus, the interaction with the sample breaks the exchange symmetry. Upon coherent excitation of the sample, the phase acquired by the propagating photons and corresponding group delay contribution leads to an asymmetry of the HOM dip that lasts for the duration related to T_2 for single resonance in absorption. Therefore, measuring the asymmetry caused by the group velocity may provide a measurement of the dephasing time. A longer asymmetric tail for the HOM picture will correspond to a longer T_2 for a single resonance.

The indistinguishable biphoton pair have a commutation relation which should equal zero at full indistinguishability.[38] As well described by Szoke *et al*[38]*,* spectroscopy using HOM interference should measure how entangled light-matter interactions from a sample in the interferometer path will modify the commutation relation.[38] In that regard, the correlations between the photon pair are affected; the time at which the photons of the entangled pair overlap is shifted, and our measurements taken as a function of time allow us to obtain time-resolved data pertaining to the sample. Moreover, measurements of coincidence counts take into account changes of one photon with respect to its conjugate photon. Therefore, we measure alterations caused by the material as the interaction affects the statistics and

indistinguishability of the photon pair. Since we measure the photon correlations, we are ensured that any observations are a result of the light-matter interaction only. Similar to advantages offered by entangled photons in other interferometric setups like quantum polarized light microscopy and quantum optical coherence tomography,[39] the two-photon N00N state is more phase sensitive[18] than classical counterparts, thus, our experimental HOM interference method should offer a quantum advantage with fewer sources of systematic errors with fewer photons.[18] In addition to the benefits of low intensity and lower noise that can be achieved using entangled photons, this quantum interferometry setup has the advantage of being able to probe optically thick samples and samples with intrinsically high optical densities for which conventional classical transmission spectroscopy techniques may show limitations. The role of dispersion compensation which is specific to HOM interferometers, is not found in classical spectroscopy, therefore HOM interferometers offer more accurate time-resolution without having to account for dispersion.

It is important to have the appropriate theoretical formalism to analyze the observed results from an HOM interaction and we believe the lack of understanding on how to interpret this light-matter interference signal has set back the implementation of this spectroscopic method. As the light-matter interactions are encoded in the field correlations, the entangled biphoton state and sample transmission are used to obtain electric field operators of the photon mode through the sample, and this along with the beam splitter transformation are used to determine the coincidence counting rate. The counting rate depends on the joint spectral amplitude (JSA) which relates to the pump pulse and phase-matching function of the SPDC photons. This joint spectral amplitude, $f(\omega_s, \omega_i)$, determined by the bandwidth and frequency of the pump and

the properties of the nonlinear crystal, encodes the correlation between the frequencies of the SPDC photon modes (ω_s and ω_i).

As depicted in Fig. 6.2, a femtosecond laser is used as the pump in SPDC generation with a Type-II SPDC BBO crystal. The entangled photon pair (signal and idler beams) are separated by a polarizing beam splitter. A molecular sample is placed in the signal photon beam and a delay line in the idler photon beam, before the two beams recombine at a beam splitter and coincidence is measured. A theoretical framework for linear spectroscopic signals with an HOM setup is presented and specialized to this setup, the coincidence counting rate ($R_c(\tau)$) as a function of the optical delay τ between the two photon beams is given by:[36]

$$R_c(\tau) = A\int_{-T_w/2}^{T_w/2} dt\,\langle d^\dagger(t)c^\dagger(t+\tau)c(t+\tau)d(t)\rangle$$

$$= A\left(\tfrac{1}{2} - \tfrac{1}{2}\iint d\omega d\omega' f^*(\omega,\omega')\, f(\omega',\omega)T^*(\omega')T(\omega)e^{i(\omega-\omega')\tau}\right), \qquad \text{Eq. 6.1}$$

where $f(\omega',\omega)$ is an amplitude of the two-photon wave function (see Eq. 6.4) and $T(\omega)$ is a matter transition amplitude, which contains susceptibility (see Eq. 6.5). T_w is the detection window and the constant A depends on the incoming photon flux, the efficiency of the photon detectors, and propagation losses. $c(\omega), d(\omega)$ $(c^\dagger(\omega), d^\dagger(\omega))$ are the boson annihilation (creation) operators corresponding to the photon modes detected by the two photon detectors of the coincidence signal. The transmission function, $T(\omega) \approx 1 + i\omega L\,\tilde{n}(\omega)/c$ for the signal photon arm encoding the matter influence on the transmitted field, with $\tilde{n}(\omega)$ the complex refractive index of matter, L the sample thickness and c the speed of light. Integrating over frequencies in Eq. 6.1 corresponds to "blind" detectors, which detect photons of all frequencies. Eq. 6.1 reveals how the matter modulates the coincidence count rate; an intuitive way to understand this is that the effective JSA after interacting with matter is $f(\omega_s,\omega_i)T(\omega_s)$.

In addition to the joint spectral amplitude which relates to the light field, the coincidence rate depends on the sample's susceptibility. Therefore, the coincidence rate contains matter information. From this connection between the matter properties and the HOM coincidence rate, it is possible to use the obtained HOM signal to determine optical properties of the molecule. As the signal contains the full linear susceptibility of the molecule, we utilize this to directly extract the molecule's dephasing time upon coherence excitation.

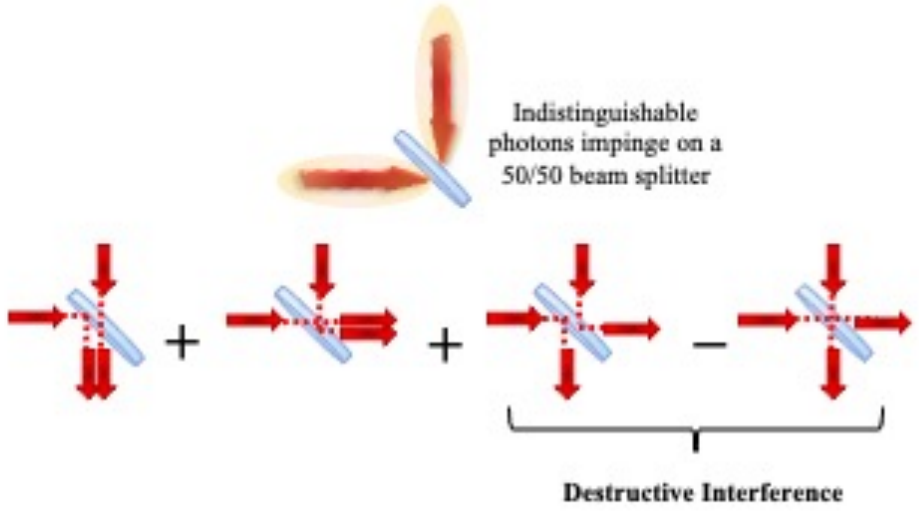

Figure 6.1. *Schematic of possible Hong-Ou-Mandel (HOM) interferometer pathways. Indistinguishable photons are incident on a 50:50 beam splitter from orthogonal directions and each photon is either reflected or transmitted. In the first two pathways, one photon is reflected, and one transmitted and coincidence counts detected. In the last two pathways, both photons are either transmitted or reflected, leading to destructive interference and null coincidence counts.*

6.3 Experimental Setup

Our experimental setup (Figure 6.2) consists of entangled photons generated using a mode-locked 800nm Ti:Sapphire laser (Spectra-Physics MaiTai) with 100 fs pulses at a repetition rate of 80MHz. A 400nm beam is produced via second harmonic generation

(SHG) with a 1mm thick β-Barium Borate (BBO) crystal. The power after SHG is set using a neutral density filter on a translation stage. This 400nm beam is subsequently used to pump a 1mm BBO crystal cut for Type-II SPDC. The generated photon pairs have orthogonal polarizations and are frequency degenerate ($\omega_s = \omega_i$) with a half opening angle of 5°. The SPDC crystal is placed in a rotating holder, such that the angle of the crystal with respect to the beam can be tuned to alter the phase-matching direction. The angle is then positioned to set the phase-matching orientation to collinear, such that the SPDC rings are "touching". A pinhole aperture is used to select the central overlap portion of the SPDC rings in the collinear phase-matching arrangement. Spatial arrangement of SPDC is confirmed by imaging with a CCD camera (Diffraction Limited STF-402M). After SPDC generation, any spurious 400nm light is filtered out with a dichroic mirror and interference filter (12nm transmission centered at 800nm). The 12 nm filter was used for initial scans to obtain the dip, since a narrower filter leads to better depth.[37] The blue box in Figure 6.2 represents the input to the interferometer.

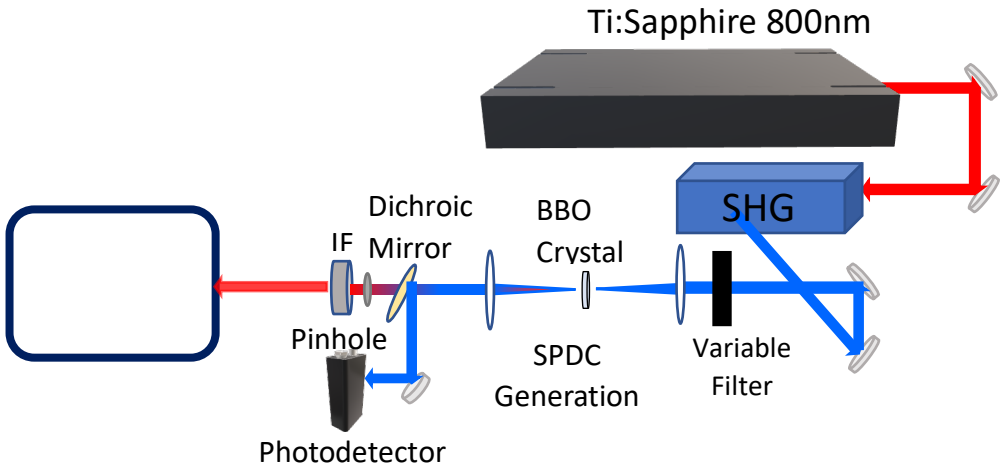

Figure 6.2. *Femtosecond laser and SPDC generation with Type-II SPDC BBO crystal.*

At the input of the HOM interferometer system (Figure 6.3) the entangled photons interact with a polarizing beam splitter creating two pathways; one for the signal photons and one for the idler. After the beams are separated, a time delay is created in one arm of the interferometer using parallel quartz wedges placed on a motorized translation stage (Thorlabs MTS25), with resolution < 0.5fs (0.1μm). This delay is adjusted by increasing the thickness of the quartz wedge through which the beam passes. A quartz plate is placed in the second arm of the interferometer to compensate any disparity in the lengths of the two paths. A sample (or solvent) in a 2mm path length quartz cuvette is placed in this second arm (which does not have the delay line). The mirror in arm 2 after the sample is mounted on a stepper motor controller translation stage (Thorlabs LNR25ZFS) to allow micrometer precise alignment of the length of the 2 beam paths. The entangled photon pairs from the two arms of the interferometer then recombine and interfere on a 50/50 beam splitter. After recombination, any information regarding polarization of the light is erased with polarization analyzers at the transmission and reflection output ports of the beam splitter, set at 45° relative to the incoming rays to maintain indistinguishability. The beams are focused onto the photosensitive area of single photon avalanche photodiodes (Perkin Elmer SPCM-AQR-13) which are connected to a coincidence counting module (Ortec NIM7400, 10ns coincidence window) in order to detect the photon rate in coincidences. Coincidence counts are measured as a function of time delay to obtain the HOM dip.

Since the 800nm SPDC light is in the infrared range and not visible to the eye, an external visible He-Ne laser (not shown) was used to aid the alignment process. It is necessary that the beams from both paths are aligned both spatially and angularly to ensure a perfect overlap (at the beam splitter and at the detectors) and indistinguishability. Using

the He-Ne laser, the reflection of the beams exiting the final beam splitter can be projected onto a note card or a wall and discrepancies in the beams' positions can be better observed. Once the beams overlap and the translation stage is set to the correct zero delay position, interference fringes should be discernable in order to confirm that the interferometer is well aligned. The He-Ne laser can then be removed for the SPDC light beam to travel through the setup to the detectors and coincidence scans to be measured as a function of time delay. Before HOM delay scans were performed, polarization visibility tests were carried out to determine the degree of polarization entanglement of the SPDC light to ensure that entanglement is high enough for indistinguishability to be seen in the HOM measurements.

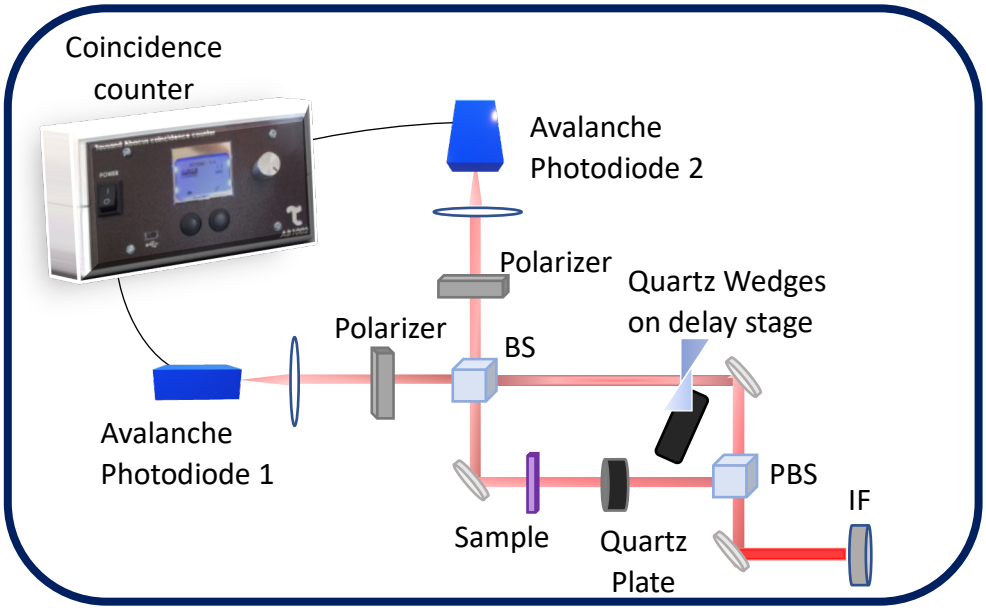

Figure 6.3. *Scheme of HOM interferometer. Entangled photon pair separated by a polarizing beam splitter. A molecular sample is placed in one arm and a delay line in the other, before beams recombine at a beam splitter.*

In this test, the polarization analyzer at one detector is kept constant while the other analyzer is adjusted, and coincidence counts are measured as a function of this polarizer

angle, showing where there is maximum entanglement. When the polarizer angle at detector A is orthogonal to that at detector B, the maximum coincidence counts are observed, confirming the polarization entanglement of the photon pairs. Alternatively, when the polarization angles are the same, no coincidences are detected since detector A does not register the twin photon of the entangled photon pairThe graph of polarization visibility is shown in Figure 6.4 and shows a visibility of 90 ± 2% which is an appropriate value for measurements.

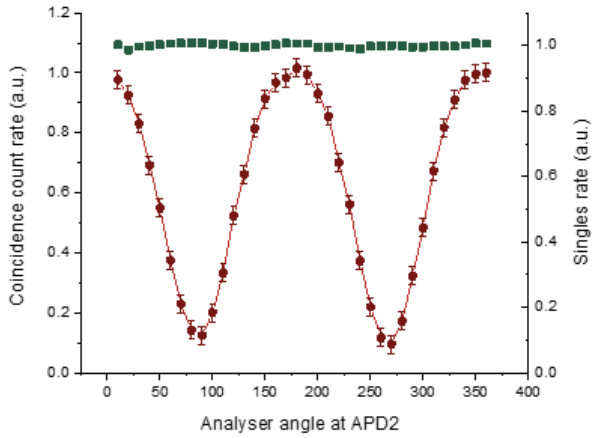

Figure 6.4 *Graph showing polarization visibility. Normalized coincidence count rate as a function of polarizer angle (red). Singles count rate as a function of polarizer angle (green).*

Two chromophores were used in this study; one with no one-photon absorption at 800nm and another with an absorption peak resonant with the 800nm entangled photons. The well-known and commercially available dye Coumarin 30(Fig. 6.5(c)) with absorption at ~415nm (Fig. 6.5(d)) is used as the off-resonant sample and a control measurement. The main molecular system investigated is the dye IR-140 (Fig. 6.5(a)) as its maximum absorption at 800nm (Fig. 6.5(b)) makes it an ideal resonant medium with the entangled photon spectrum. The sample has a single absorption peak with a broad spectrum, from ~700-850nm. While a 12nm interference filter was used for initial scans, due to the broad

absorption band of the molecule an interference filter with a 40nm transmission was used for scans with solvent and sample to ensure there is an adequate overlap between the spectra of the entangled photons and the sample.

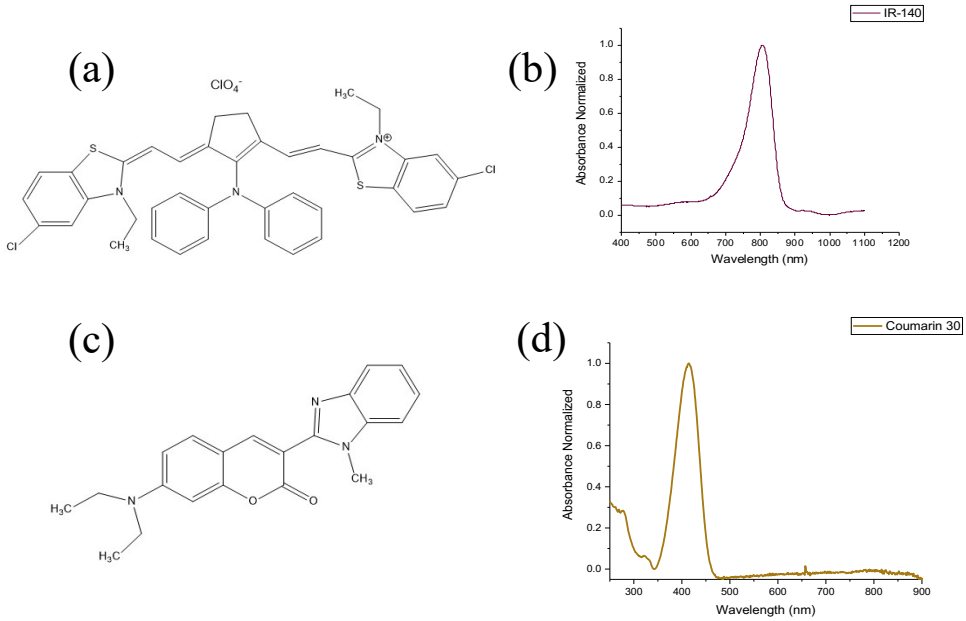

***Figure 6.5**. (a) Molecular structure of IR-140. (a) Normalized absorption spectra of IR-140 dye. Concentration 20µM. (c) Molecular structure of Coumarin 30. (d) Normalized absorption spectra of Coumarin 30 dye. Concentration 29 µM.*

6.4 Results

6.4.1 HOM Dip

The typically narrow bandwidth of the SPDC type-II photons[38] is on the order of ~10-20nm. In our experiments the spectrum of the SPDC field is determined by the transmission curve of the interference filter used after SPDC to block out the remaining pump beam. Furthermore, HOM depth is better with a filtered spectrum to reduce distinguishability.[39] Thus, to first observe the HOM dip, an interference filter centered at 800nm with FWHM of 12 nm is utilized for alignment. With this, the HOM dip is characterized as seen in Figure 6.6 showing the normalized coincidence counts as a

function of time delay. The photons of the SPDC entangled pair travel separate but equal pathways and impinge on the beam splitter from opposite sides. The probability amplitudes of the paths with both transmitted, "t-t", and both reflected, "r-r", have the same amplitude but different relative phases. Thus, because it is impossible to distinguish the photons in these paths, they destructively interfere, leading to a drop in coincidences at zero delay when the indistinguishable photons overlap perfectly in time. A unitary transformation (which will be discussed in more detail) occurs at the output channels of the beam splitter, and project the input state of the photons into a N00N state where both photons of the entangled biphoton pair exit the beam splitter from the same output port. This superposition of the biphoton pair causes the signature bunching effect as a result of the bosonic properties of photons.[40]

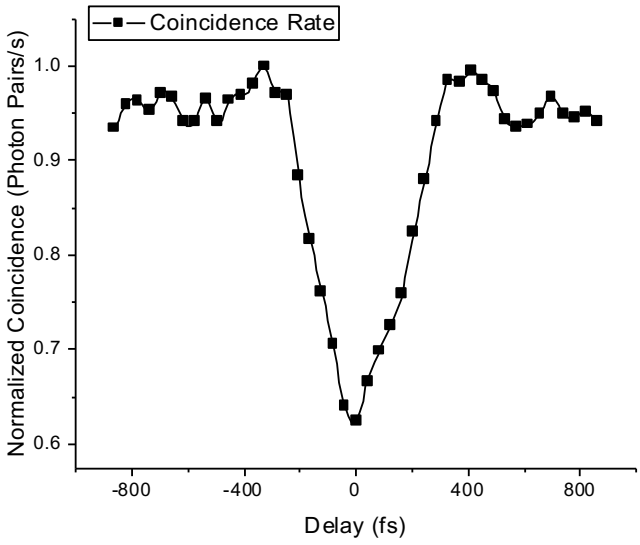

Figure 6.6. *HOM dip measured without sample. Coincidence counts shown as a function of time delay.*

Shown in Figure 6.6 are direct normalized coincidence counts measurements with no corrections or subtractions, shown as a function of the time delay. The visibility is on

the order of 40%. While imperfections in the visibility can be caused by factors in alignment and background events related to mixed states and two-photon components that do not interfere,[41] correlations have been drawn between the spectral properties of the SPDC photons and the resulting visibility. The broader joint spectrum width of type-II SPDC using ultrafast pulsed laser systems compared to pumping with CW lasers or using Type-I SPDC, has been shown both theoretically and experimentally to reduce the quantum interference visibility of the HOM dip due to the large range of frequencies and wave vector modes.[38,42–45] An investigation on the effect of spectral information and distinguishability in Type-II SPDC with a broadband pump showed that as the pump bandwidth is increased, the overlap between the pump envelope and the phase-matching function also increases, leading to a larger range of frequencies in the downconverted photons, therefore greater distinguishability and lower visibility.[46] They were able to integrate an equation for the coincidence rate of the HOM counts, where $R_c(\delta\tau) \propto \sigma$ (where σ is proportional to the pump bandwidth) shown in Eq. 2.[46] For the CW pump limit, $\sigma \to 0$, therefore the coincidence rate at the dip can go to zero. Alternatively, as σ increases and the beams become more distinguishable, the lowest coincidence rate also increases and the visibility is diminished. Using smaller crystal lengths (≤0.5mm) as well as narrow spectral filters can improve visibility[45] and their calculations showed visibility of ~20-25% with an 8nm filter, in line with our result with a 12nm filter. Previous experimental studies have obtained HOM visibilities with ultrafast pumped type-II SPDC photons in the range of 20-30% for SPDC crystal thicknesses greater than 0.5mm which is consistent with our results.[42–44] This equation that roughly estimates the dependence of HOM visibility based on pump bandwidth is,[46]

$$R_c(\delta\tau) \propto \frac{1}{\sqrt{2\pi}}\frac{\sigma}{\Omega_+} - \mathrm{erf}\left[\frac{1}{2\sqrt{2}}\frac{\sigma}{\Omega_+}(1 - |\delta\tau|\Omega_-)\right] \quad \text{Eq. 6.2}$$

where σ is proportional to the pump bandwidth and $\Omega_\pm$ relates to the crystal length and phase matching conditions. Using this relation, we simulated the coincidence rate as a function of relative time delay for different pump bandwidths; a narrow bandwidth for CW (Fig. 6.7(a)) and 8 times that bandwidth to simulate our femtosecond pump (Fig. 6.7(b)). The small bandwidth of CW produces a visibility of ~96%. However, for the wide femtosecond pump ($8\sigma_{CW}$), the visibility is much smaller and estimated to be ~40% (the erf function in Eq. 6.2 accounts for the shape). This in accordance with our own experimental results.

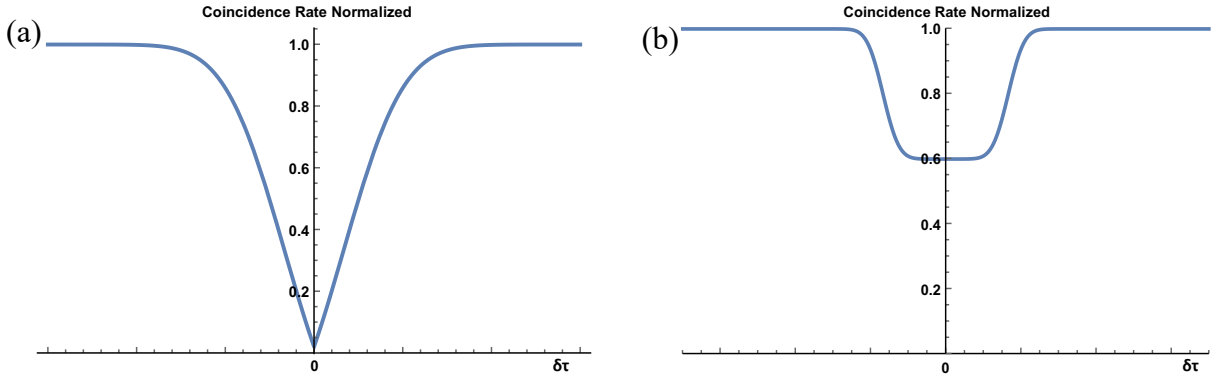

Figure 6.7. *Normalized coincidence rate as a function of time estimated using Eq. 6.2 for (a) a narrow CW pump bandwidth and (b) a larger femtosecond pump that is* $8\sigma_{CW}$.

The dip shown in Figure 6.6 has the characteristic symmetrical triangular or V-shape that is expected as described by theory.[47] The joint spectral function for type-II SPDC, $S(v)$, within the SPDC state is commonly written as[48,51]

$$S(v) = \left|sinc\left(\frac{vDL}{2}\right)\varepsilon_p(\omega_s + \omega_i)\right|^2 \quad \text{Eq. 6.3}$$

where $\varepsilon_p(\omega_s + \omega_i)$ is the pump envelope, D represents the group velocity difference of the o and e polarized photons in the crystal $\left(D = \frac{1}{u_o} - \frac{1}{u_e}\right)$, L is the thickness of the SPDC

crystal and ν is the detuning frequency of the signal and idler photons from half the pump frequency. The sinc function leads to the natural rectangular shape of the two-photon effective wave function, the Fourier transform of which produces the triangular shape of the HOM dip that can appear Gaussian from distortions due to the interference filter.[47] The experimental HOM dip (Figure 6.6) is clearly symmetrical, with steady coincidence counts from ~ ±800-400fs, which peak before starting to drop, referencing the zero-delay point and indistinguishability and temporal correlation of the photon pairs. The coincidence counting rate of the HOM dip can also be written as $R_c(\tau) = R_0[1 - V(\tau)]$ [48] where R_0 is the coincidence rate at long delay times beyond any region of quantum interference, and $V(\tau)$ has a dependence on DL. The parameters DL determine the entanglement time of the entangled photon pair, so it is expected that the width of the HOM dip should reflect this. A spectral filter with a bandwidth smaller than the bandwidths of the individual photons causes an increase in their coherence time[39] and thus the contribution of the spectral filtering can be used to estimate the broadened coherence time and subsequent dip width.[48] The FWHM of the dip (Figure 6.6) is on the order of ~370 fs which represents the inverse of the bandwidth of the SPDC spectrum and the coherence time of the entangled photons. The unfiltered entanglement time (T_e) with the 1mm BBO crystal is calculated as 126fs, but considering the 12nm interference filter in place, the filtered entanglement time is therefore estimated to be ~ 177fs.[48] The estimated coherence time of 2 times the entanglement time ($2T_e$) would be 354fs which agrees well with the coherence time obtained by the HOM dip width.

6.4.2. HOM Scans with Non-Resonant Sample

The HOM dip with solvent (methanol) placed in the interferometer path is measured and the normalized coincidence rate as a function of time delay is shown in Figure 6.8. Similar to the dip in Figure 6.6, the dip with solvent is symmetric and triangular, with steadily oscillating counts on both ends before counts drop, signifying the zero-delay position. The declining portion of the dip is smooth on both sides with no oscillations and any changes in amplitude as low as 1%. This reproduced symmetrical triangular shape confirms that the methanol does not absorb the photons or interfere with them and is not excited by them. Thus, methanol does not affect the two-photon quantum interference, and this serves as an accurate control scan.

Subsequently, the pure solvent in the interferometer arm was replaced with Coumarin 30 (dissolved in methanol). As Coumarin 30 has no absorption at 800nm, this was used to determine how the HOM dip would be affected by a non-resonant medium placed in the interferometer path. There was little to no change with the Coumarin 30 sample placed in the interferometer path (Figure 6.8). The HOM dip maintains its symmetric triangular shape, with steady coincidence counts oscillating at $\pm$ 2.5% on the ends before smoothly descending to the zero-delay position. In addition to the HOM dip maintaining its shape, the coincidence counts from the measurement with Coumarin 30 remain the same and display no attenuation compared to the counts with pure solvent. This indicates that the photons propagated through the non-resonant sample were not absorbed and did not interfere with the sample, thus there was no coherent excitation of the Coumarin 30 chromophore. The photons propagating through this dye experienced no new phenomena or phase change compared to the photons in the opposite path, therefore, upon recombining

at the beam splitter there is no difference in their interaction and the HOM dip is unchanged.

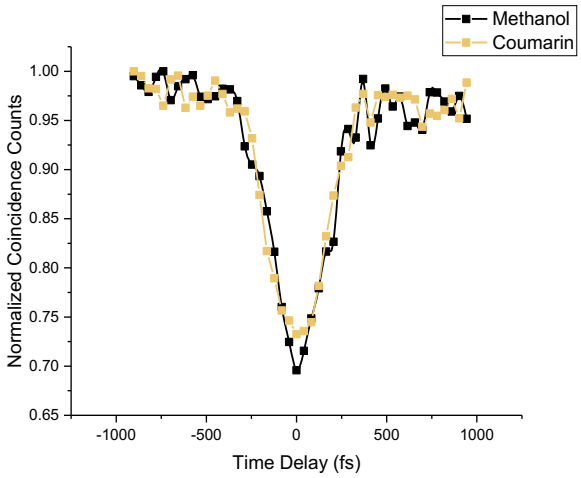

***Figure 6.8**. Normalized coincidence counts as a function of time delay showing the HOM dip with a solvent, Methanol, (shown in black) and with a non-resonant sample, Coumarin 30 (shown in yellow).*

6.4.3. HOM Scans with Resonant Sample

The experiment is carried out with a solvent (ethanol) as the control measurement and with IR-140 (dissolved in ethanol), a dye with strong absorption at 800nm, as the resonant sample. The solutions are held in a 2 mm quartz cuvette which is placed in the beam path in one arm. In both cases (solvent and sample), the broader interference filter with a transmission bandwidth of 40nm was used in order to overlap with the broad absorption band of IR-140. The HOM dip with solvent placed in the interferometer path is measured and the normalized coincidence rate as a function of time delay shown in Figure 6.9 (black curve). As the spectrum for this measurement is wider, the dip appears narrower (~350fs) as discussed in literature.[25] However, as the full SPDC spectrum falls within the 40nm spectral filter, we do not observe much spectral filtering which would cause greater narrowing. Again, the HOM dip with pure solvent is symmetric with a triangular almost

Gaussian shape. There are steady counts on both ends peaking before counts drop, signifying the zero-delay position. There is a smooth decline of the counts to the zero-delay point and the photons propagating through the ethanol do not get absorbed or experience interference with it.

The solvent is then replaced with the IR-140 dye and the HOM scan is performed. With the sample in place, the features of the dip change and the HOM dip becomes distorted as seen in Figure 6.9 (red curve). The left side of the dip is similar to that of the solvent scan, maintaining a Gaussian shape with coincidence counts peaking and then beginning to drop at ~400fs. However, the dip overall becomes narrower and gains an asymmetry on the right side. The right side of the dip becomes almost inverted compared to the solvent scan until it reverts to steady coincident count levels. The side of the dip is no longer smooth and there are multiple peaks or oscillations, with amplitude changes of ~7% within an 80fs time window. Furthermore, the center of the HOM dip with the sample is shifted to the left compared to the dip with the solvent. Since the sample absorbs at 800nm and interacts with only one photon of the entangled pair, this is a resonant one-photon process that involves linear excitation. As expected with the IR-140 dye, the photons that propagate through the resonant sample induce a coherent excitation that lasts for some time period. This interaction with the sample affects the phase of the photons that were transmitted through it and hence affects their quantum interference when recombined with the photons from the opposite path. As the light now possesses information related to the sample, this information is portrayed in the HOM dip and results in the subsequent shift, asymmetry and oscillations that are now observed. It is very interesting that the organic molecule in the interferometer path results in changes to the shape and symmetry

of the dip itself and not just a shift of the dip as a function of delay time. A simple shift in time with the same shape and symmetry is seen in polarization mode dispersion measurements to determine the refractive indices of optics. However, in this case the complexity of the distortions to the dip suggest more information about the molecule is accessed and present in the coincident count results. We are then interested in what molecular information can be extracted from the new shape and features obtained.

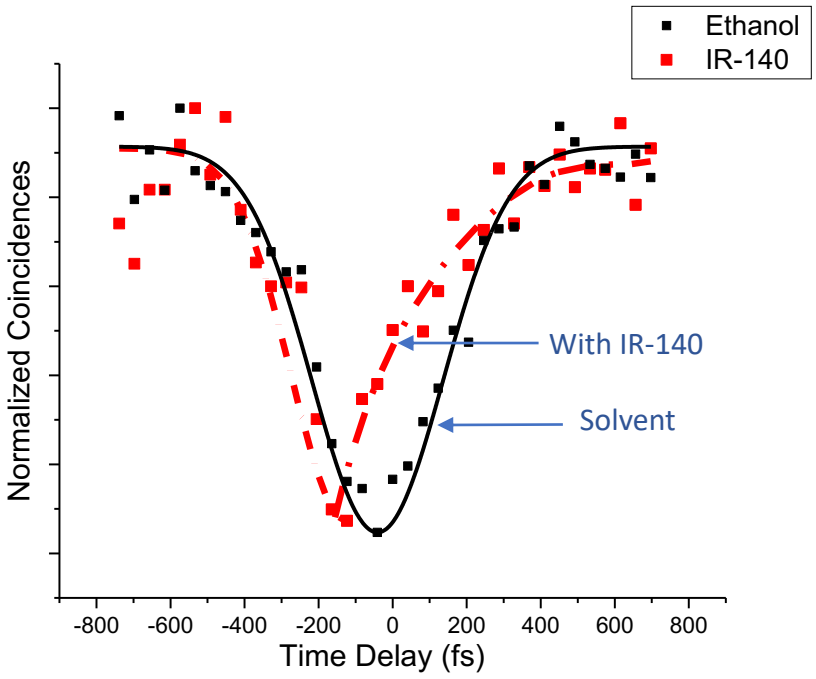

***Figure 6.9**. Normalized coincidence counts as a function of time delay showing HOM dip without sample (black) and HOM dip with IR-140 sample (red*

6.5 Discussion

To understand the HOM interference process and how it is affected by the introduction of a resonant medium, we develop a theoretical formalism to describe the experiment. We first consider the entangled biphoton twin state generated by SPDC. This can be described by

$$|\Phi\rangle = \int\int d\omega_s d\omega_i f(\omega_s, \omega_i) {a_s}^\dagger(\omega_s) {a_i}^\dagger(\omega_i) |0_s, 0_i\rangle, \quad \text{(Eq. 6.4)}$$

where $f(\omega_s, \omega_i) = \alpha(\omega_s + \omega_i)\beta(\omega_s - \omega_i)$ is the joint spectral amplitude with $\alpha(\omega_s + \omega_i)$ as the pump envelope, $\beta(\omega_s - \omega_i)$ as the phase-matching function, and where ${a_s}^\dagger(\omega)$, $a_s(\omega)$ [$({a_i}^\dagger(\omega), a_i(\omega)$] are the creation and annihilation operators respectively for the signal [and idler] modes. These satisfy the boson commutation relation $[a_j(\omega), {a_j}^\dagger(\omega')] = \delta(\omega - \omega')$. The signal mode is modified by interacting with the medium placed in the path, the modifications can be described by either a perturbative treatment or a continuum of lossy beam splitters[36,52]. After transmission through the sample, the signal mode operator $a_s(\omega)$ becomes:

$$a_s'(\omega) = T(\omega) a_s(\omega) + \eta(\omega), \quad \text{(Eq. 6.5)}$$

where $T(\omega)$ in the first term is the transmission function for the medium the light propagates through, and $\eta(\omega)$ is the quantum noise associated with the absorption process. This transmission function, $T(\omega) = e^{i\omega(n(\omega)+i\kappa(\omega))L/c}$ (L is the sample length and c the speed through vacuum), is determined by the dielectric constant (ϵ) (or linear susceptibility (χ)) of the medium. The complex refractive index of the sample satisfies the equality:

$$\big(n(\omega) + i\kappa(\omega)\big)^2 = \epsilon(\omega) = 1 + \chi(\omega). \quad \text{(Eq. 6.6)}$$

The real part of this complex index adds a phase to the signal operator while the imaginary part contains the absorption (attenuation) by the medium. A wave packet of modes transmits through the sample, causing a modulation of the signal as it propagates through the sample which leads to the subsequent phase shift. It is clear from the expression in Eq. 6.6 how the transmission function is related to the dielectric constant and linear susceptibility. For a non-resonant and non-absorbing medium that is transparent to the propagating photon, $T(\omega) \approx 1$

and the signal mode operator remains almost unchanged. However, for a resonant absorbing medium, the signal mode interferes with the sample, therefore, undergoes a phase shift and attenuation as dictated by the complex refractive index. For thin samples, the noise term in Eq. 6.5 can be neglected. Therefore, rewriting Eqs. 6.5 and 6.6 with the transmission function in terms of electric field operators, the electric field operators of the photon mode transmitted through the sample is:

$$E^{(+)}(\omega) \equiv T(\omega)E_0^{(+)}(\omega) = E_0^{(+)}(\omega) + \frac{i\omega L}{c}\tilde{n}(\omega)E_0^{(+)}(\omega). \qquad \text{(Eq. 6.7)}$$

After the signal beam is transmitted through the sample, it recombines with the idler beam (which passed through the other arm of the HOM interferometer) at the 50:50 beam splitter. The idler beam undergoes a controllable phase shift, $a_i{}'(\omega) = a_i(\omega)e^{i\omega\tau}$ due to the travel path difference of the two beams. The output modes of the beam splitter, described by the photon operators$c(\omega), d(\omega)$, after this recombination are given by the 50:50 beam splitter unitary transformation:

$$\begin{pmatrix} c(\omega) \\ d(\omega) \end{pmatrix} = \frac{1}{\sqrt{2}}\begin{pmatrix} 1 & i \\ i & 1 \end{pmatrix}\begin{pmatrix} a_s{}'(\omega) \\ a_i{}'(\omega) \end{pmatrix}. \qquad \text{(Eq. 6.8)}$$

This beam splitter unitary transformation introduces a $\pi/2$ phase shift in the reflected photons output state. The exiting beams travel to photodetectors and are measured in coincidence where the coincidence counting rate reads (Eq. 6.1):

$$R_c(\tau) = A\int_{-T_w/2}^{T_w/2} dt \left\langle d^\dagger(t)c^\dagger(t+\tau)c(t+\tau)d(t)\right\rangle$$

$$= A\left(\frac{1}{2} - \frac{1}{2}\iint d\omega d\omega' f^*(\omega,\omega')\, f(\omega',\omega)T^*(\omega')T(\omega)e^{i(\omega-\omega')\tau}\right). \qquad \text{(Eq. 6.1)}$$

where we have used Eq. 6.8 in the first line and Eq. 6.5 in the second line of Eq. 6.1. The detectors are blind to the frequency of the photons; thus, the counting rate is integrated over

frequency and the coincidence counts depends on the phase of the photons. Eq. 6.1 shows that the HOM signal provides a product of the spectral $f(\omega_s, \omega_i)$ and material $T(\omega_s)$ properties. This can be analyzed further by conducting a Fourier transform of Eq. 6.1. The Fourier transform of the signal in Eq. 6.1 yields

$$R(\Omega) = -\frac{1}{2}\beta^*(\Omega)\beta(-\Omega)T^*\left(\bar{\omega} - \frac{\Omega}{2}\right)T\left(\bar{\omega} + \frac{\Omega}{2}\right) \quad \text{Eq. 6.9}$$

where $\bar{\omega} = \frac{1}{2}(\omega_1 + \omega_2)$. Again, there is a product of the spectral and material properties. When the signal and idler modes are broadband, Eq. 6.9 builds a connection between the Wigner transform of the transmission function and the coincidence counting rate (see supporting information).

Due to the $T(\omega)$ function in the coincidence rate in Eq. 6.1, the resulting coincidence rate contains the full linear susceptibility of the absorbing medium in the interferometer path. Given that the beam transmitted through the sample is in resonance with some excited state of the sample, it creates a coherent excitation which must dephase over a time, T_2, governed by the group delay contribution. If the molecular response is dominated by a single resonance at Ω with dephasing time T_2, these can be linked to the linear susceptibility by a Lorentzian model for a 2-level system as,

$$\chi(\omega) = \frac{\alpha}{\omega - \Omega - i/T_2} \quad \text{(Eq. 10)}$$

where α is a constant related to the length and concentration of the sample. By connecting our understanding of the HOM experimental data to the theoretical formalism and the susceptibility, we will be able to model our data to extract this dephasing time.

For comparison with our experimental data from the HOM experiment, the full susceptibility can be computationally simulated from the absorption data using the Kramers-Kronig dispersion relation.[53] The imaginary part of the linear susceptibility $\chi''(\omega)$ is obtained

by a Hilbert transform of $\chi''(\omega)$, $\chi'(\omega) = \frac{1}{\pi}\mathcal{P}\int_{-\infty}^{\infty}\frac{\chi''(\omega')}{\omega'-\omega}\,d\omega'$ where $\mathcal{P}$ denotes the Cauchy principle value. A Gaussian joint spectral amplitude function,

$$f(\omega_1,\omega_2) = \left(2\pi\sigma_p\sigma_-\right)^{-\frac{1}{2}}\exp\left[-\left(\omega_s+\omega_i-\omega_p\right)^2/(16\sigma_p^2)\right]\exp[-(\omega_s-\omega_i)^2/(4\sigma_-^2)],$$

(Eq. 6.11)

is used to fit the experimentally obtained HOM spectrum, which, along with the linear susceptibility ensures the exact information the experimental data contains about the SPDC spectrum and the molecule studied. Here σ_p is the bandwidth of the pump laser and $\sigma_- \propto 1/T_e$. ω_s, ω_i and ω_p are the frequencies of the signal, idler and pump respectively.

With this study, we aim to provide the first step in illustrating that entangled photons in an HOM interferometer can be utilized for complex spectroscopy with organic, biological materials and more, as the interferometer is sensitive to their presence and the SPDC two-photon wave function experiences a transformation caused by the sample's transmission. Specifically, if our experiment can be modeled using the linear susceptibility as expected by simulation and with this our experimental data can be used to extract time-resolved data pertaining to the molecule, it substantiates the viability of the HOM interference as a spectroscopic method to be studied further. Our objective is to understand how our HOM scan can be connected to the coherent excitation of the sample, which will be useful towards testing the feasibility of this spectroscopic method in more complex designs, with possibilities for time-resolved nonlinear spectroscopy with entangled photons.

First, the full linear susceptibility is simulated using the Kramers-Kronig relation to fit to our signal from the HOM experiment. The computed linear susceptibility $\chi(\omega)$ of the IR-140 molecule from the absorption data is shown in supplementary Fig. 6.13 constructed by

computing a transformation on the imaginary part of the susceptibility. In order to fit the HOM dip obtained with the solvent in the interferometer arm, the coincidence counting rate in Eq. 6.1 and the Gaussian JSA in Eq. 6.11 are used setting the transmission function $T(\omega)$ equal to 1. In this limit, there is no absorption by the medium and hence no attenuation or change to the phase of the propagating photon. By fitting the HOM data without the sample, we are able to obtain the full joint spectral amplitude of our SPDC source using Eq. 11 with the pump central frequency, $\omega_p = 1.549$ eV, and bandwidth, $\sigma_p = 23$ meV. The central frequencies for the signal and idler photons are $\omega_s = \omega_i = \frac{\omega_p}{2}$. Hence with the fitting, the width σ_- is determined and found to be $\sigma_- = 4$ meV. This width, which is related to the SPDC photons as $\sigma_- \propto 1/T_e$ gives the diagonal of the JSA obtained (Figure 6.10(a)). The full JSA gives us a theoretical model of the SPDC two-photon amplitude and is shown in Figure 6.10(a). This is important as it provides the width of the difference of the two modes of the biphoton pair and thus, an understanding of the bandwidth and diagonal of the JSA and the frequency correlations of our SPDC source. As shown, the entangled signal and idler modes are correlated in their frequency. The width in the diagonal matches the pump bandwidth, where the off-diagonal width is determined by the phase-matching condition. Subsequently, the fitting of the HOM dip through solvent is simulated and the comparison between the experimental HOM spectrum with only the solvent and theoretical modelling is depicted in Figure 6.10(b). As shown, the fit produces a symmetric Gaussian shape through the HOM dip that descends towards the zero-delay position and peaks at ~ $\pm$ 500fs. The FWHM of this fit is ~375 fs which is very similar to that obtained directly from the experimental data. Thus, the theory is in good agreement with the experiment and can assuredly be used for further analysis with the data involving the sample.

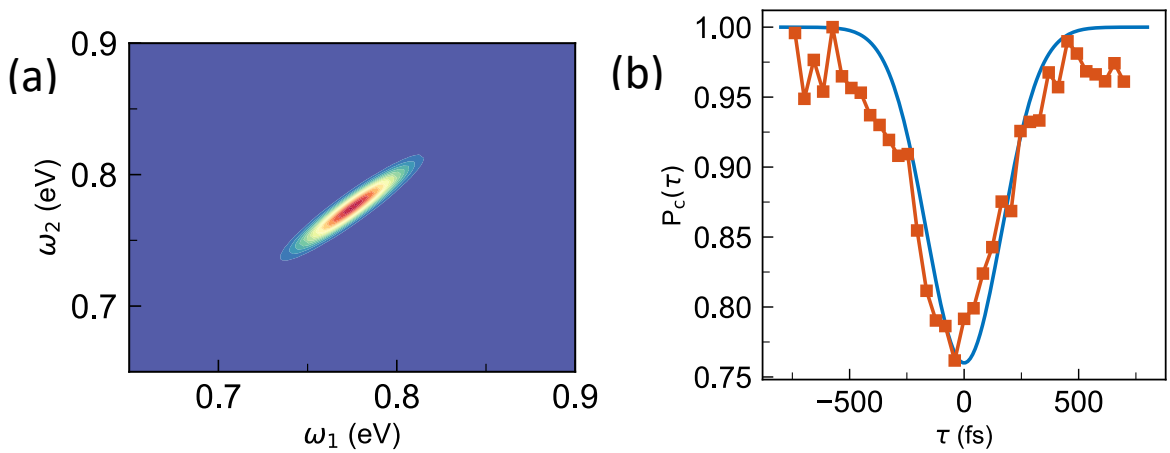

Figure 6.10. *(a) Joint spectral amplitude $|f(\omega_s, \omega_i)|$ obtained by fitting Eq. 6.11 to the experimental HOM coincidence counting rate with solvent only. (b) Comparison between theory and experimental data for the HOM coincidence counting rate for the solvent only. Theoretical modelling shown in blue.*

It is important to obtain a fitting of our experimental HOM data through the sample with the computed $\chi(\omega)$ and the full JSA of our entangled light source, to confirm that the experiment does indeed agree with and contain the full information about the real and imaginary linear susceptibility, dephasing and SPDC source. This will be necessary for extracting the dephasing time, T_2. The transmission function $T(\omega)$ in $R_c(\tau)$ is replaced with the real transmission from the linear susceptibility $\chi(\omega)$ of the sample. As the transmission through the resonant sample IR-140 showed attenuation of the coincidence counts while transmission through the non-resonant sample Coumarin 30 showed no attenuation at all, it is clear that there is absorption of the signal photons by the resonant IR-140 sample and a subsequent excitation of this sample despite the low entangled photon intensity. Conversely, Coumarin 30 is transparent to the light. The real transmission along with the full JSA obtained from fitting the solvent data are used to model the HOM spectrum with the IR-140 chromophore. Shown in Figure 6.11 is the theoretical fitting of the HOM coincidence count rate for the IR-140 molecule. Again, the theory is in good agreement with the experimental data. The theoretical fit reproduces the shift of the HOM dip, to the left of the original zero-

delay position. Intuitively, the molecules act as a frequency-dependent phase shifter, which induces a phase shift in the signal photon beam $a(\omega)e^{i\theta(\omega)}$. The interbeam time delay can either compensate or amplify the relative difference between the two beams depending on the relative sign of τ and $\theta(\omega)$. This leads to a shift of the center of the dip and it can be seen in Figure 6.11 that the dip with the sample is shifted to ~ -150fs compared to the dip with the solvent. As the light-matter interference cannot be completely compensated by only the delay in the idler, in addition to the shift, there is an asymmetry of the HOM signal. The right side of the dip becomes elongated and asymmetrical compared to the left, representing the change in phase of the photons propagated through the sample in comparison to those in the opposite arm of the interferometer. This elongation is a reflection of the additional oscillations caused by the induced polarization of the molecule and the resulting effect in the propagating photons leading to a change in shape of the HOM dip. Thus, the exchange symmetry between the arms is broken. Evidently, our experimental data accurately reflects what is expected from theory. The agreement between the theoretical fit, which contains the IR-140 transmission data, and the experimental HOM data, confirm that this IR-140 transmission information is indeed measured by the HOM interferometer.

The indistinguishability and temporal correlation of the photon pairs are advantageous, as the absorbing media in the interferometer path experience quantum interference with the signal photon of the entangled pair but not the idler. Therefore, due to its group velocity, the sample modulates the phase packet that propagates through it and upon recombination with the idler photons, the signal photons hold information about the absorbing media which translates to an alteration of the interference between the entangled photon pair at the beam splitter and a change in the observed HOM dip. This expected result is successfully obtained by our

experiment. As the signal measurements are conducted through coincidence counts and it is the statistics of the coincidences and not simply the photon intensity that is considered, they are a reflection of the entangled light photon statistics, therefore governed by non-classical properties. One may think to attribute these changes to some simple refractive distortion caused by placing an additional optical element in one path of the interferometer. However, by conducting scans using solvent and the off-resonant Coumarin 30 dye with the same experimental parameters and same cuvette, it is clear that the observed result is substance dependent. Additionally, coincidence counts remained the same for scans using solvent and using the Coumarin 30 dye signifying no absorption but dropped for the IR-140 dye, which confirms that there was one photon absorption taking place.

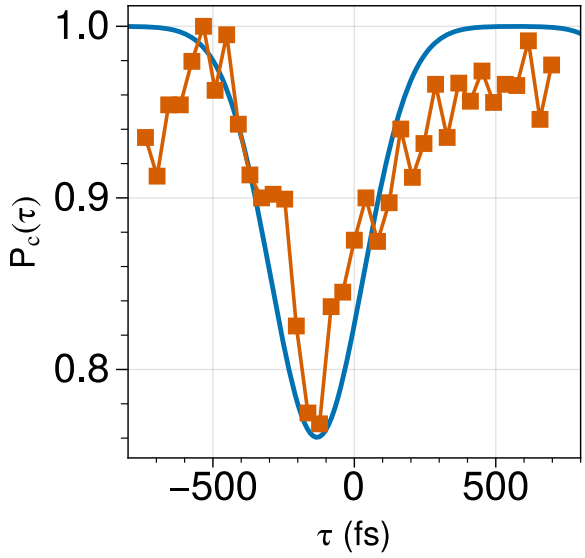

Figure 6.11*. Comparison between theory and experimental data for the HOM coincidence counting rate for the IR-140 molecule.*

Our main objective is to obtain molecular information from the data, specifically the dephasing time of the molecule's coherent excitation. As mentioned, the linear susceptibility can be connected to the dephasing time and the molecule's coherent excitation by the Lorentzian function in Eq. 6.10. Therefore, the HOM data can be exploited to obtain the

dephasing time as was similarly considered in a previous study with a crystal and nanostructures[37]. We fit our experimental data using the Lorentzian model in Eq. 6.10. This simulation was done for both the HOM scans with and without the sample. The simulation of the HOM dip without the sample (with solvent) is shown in Figure 6.12(a) with the transmission again set to 1 to signify no absorption through the medium. The resulting fit is similar to the theoretical fit of $R_c(\tau)$ in Figure 6.10(b), where the dip symmetrically descends to the zero-delay position with the ends flattening out at large delay times. The modeling provides the characteristic triangular almost Gaussian shape of the HOM dip, which confirms the width (time) and shape of the biphoton.

The graph in Figure 6.12(b) shows the Lorentzian modeling of the HOM data with the IR-140 sample in the interferometer path using Eq. 6.10, fit with the full linear susceptibility from transmission through the sample. This is very similar to the graph in Figure 6.11 simulated with $R_c(\tau)$ of Eq. 6.1. It is interesting that similar fittings can be achieved with Eq. 6.10 which contains mainly data pertaining to the sample such as the linear susceptibility, length, concentration and resonance frequency, as well as the frequency of the SPDC light. As the equation is heavily substance dependent, the ability to obtain a good fitting with it certifies that the experimental data through the sample contains molecular related information. The coherent excitation of the sample is successfully captured by the photons interferometric response and clearly seen in the alteration of the HOM dip and its simulated fitting.

The important aspect of this Lorentzian fitting is the ability to use it to connect the HOM data to time-resolved information pertaining to the sample. While current entangled light spectroscopy methods such as entangled two-photon absorption offer insights to nonlinear effects on dipole properties, many researchers across fields are interested in utilizing the

temporal correlations of entangled photon pairs to measure temporal photophysical properties of substances under study. From the fitting in Fig. 6.12(b), we are able to extract the dephasing time T_2. Using the best fit of Eq. 10, the dephasing time of the IR-140 molecule is extracted and found to be ~102 fs. The T_2 is a result of the dephasing of the transition dipole-dipole interactions between the nearest IR-140 molecules in solution excited by the beam. There is a static charge distribution upon excitation and this excitation propagates coherently through the molecule until these induced dipole moments dephase. Our experimental delay has sub-femtosecond precision, allowing for highly precise measurements of any changes with adjustments in time which should benefit our experimental analysis. From our measurements, we are able to infer that the dephasing time in the IR-140 molecule is ~102 fs. Considering the broad linewidth of the IR-140 absorption band, we did expect to see a short coherence time, on the order of tens of femtoseconds. 102fs is relatively short compared to times found with similar methods[37], thus, it is an adequate result taking into consideration the linewidth broadening and the instrument entanglement time. The group delay contribution from the sample does not last long as is evident by the width of the oscillating asymmetric tail in the modified HOM dip. As such, we did not expect a long dephasing time and the calculated T_2 adequately reflects this. Although our SPDC spectrum is much narrower than the molecule's absorption linewidth, we are able to provide a fitting that resolves a relatively short dephasing time. We suggest that in order to extract even shorter dephasing times for broad linewidth samples, the optical thickness of the sample could be adjusted as this may affect the linewidth and make extraction of coherence time more difficult. A smaller entanglement time (much shorter than the dephasing time) will also lead to simpler deconvolution of different broadening effects. Additionally, Type-I SPDC and continuous wave pump sources lead to higher HOM

visibilities, making it easier to deduce subtle changes in coincidence counts and leading to more accurate data extraction. We suggest a Type-I SPDC source may be applied in future investigations. In the future, we also hope to conduct experiments with thin film samples to overcome hindrances by sample optical thickness.

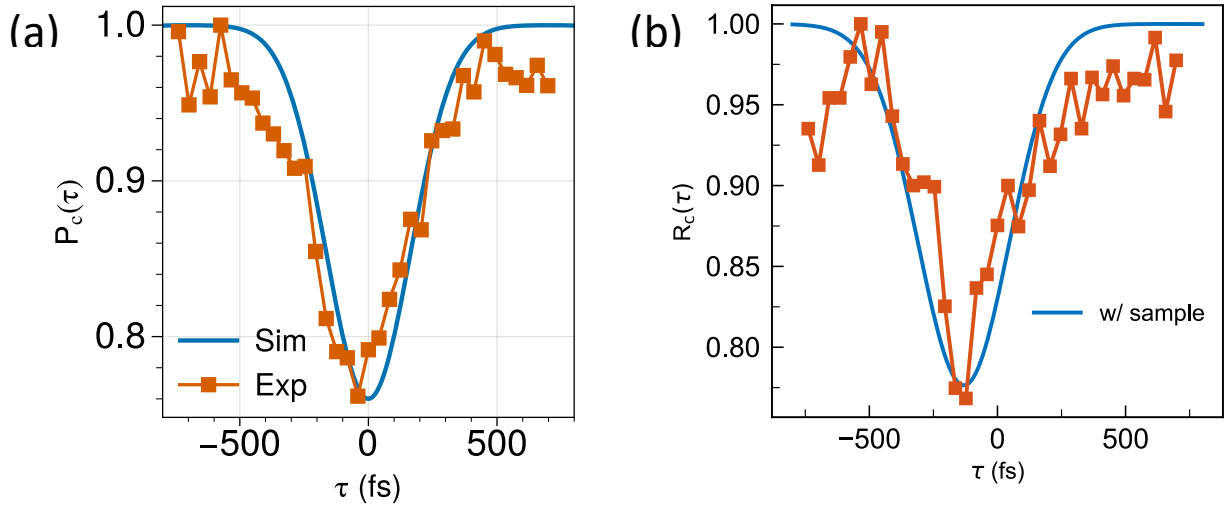

Figure 6.12. *(a) HOM dip with solvent (without substance) and (b) HOM dip using the Lorentzian model for the IR-140 sample. These fits were modelled using Eq. 6.10.*

Thus, our HOM interferometer is indeed sensitive to the presence of a resonant sample placed in its path. Our experiment provides a proof-of-concept illustration of an entangled photon spectroscopic method and is the first time this is illustrated with a chemical system. The experimental results along with theoretical fitting confirm that the coincidence counts measured by the HOM interferometer can be fit with the full (real and imaginary) linear susceptibility of a substance placed in its path and can be used to deduce the dephasing time T_2 of the chromophore even if it has a broad linewidth. The low photon flux of the entangled photons can induce an excitation in a resonant sample and our experimental method is sensitive to any observable changes. Therefore, this investigation of molecular properties using HOM interferometry presents itself as a viable method for conducting sensitive spectroscopy and opens the door for more complex spectroscopic design possibilities. The current setup can be

readily extended to measuring higher-order nonlinear response functions (susceptibilities) of materials by using additional external classical laser pulses. These pulses can interact with the sample before the final interaction with the signal beam of the quantum light such that the transmitted beam carries information of the nonlinear susceptibilities of matter. This information can then be extracted by the coincidence counting measurements as demonstrated here. The coincidence counts will be able to capture fast evolving macroscopic and microscopic processes as a function of the time delay. Time-resolved signals can then be studied by controlling the temporal delay between the laser pulses. As we have corroborated the ability of this method to detect light-matter interactions, the next step is to perform such higher order experiments to capture excited state dynamics on the samples under study, while taking advantage of the low flux, good signal to noise ratio and control parameters of entangled light. Similarly, the frequency correlations, $f(\omega_s, \omega_i)$, can be varied by using different types of quantum light and observing the effects this has on the resulting light-matter interactions; the strength of the interference and coupling with different frequency correlations and the change to the observed phase shifts. By shaping the photon entanglement, we can manipulate the optical signals for different material responses. A vast array of material substances may be probed with this technique, particularly substances with interesting characteristics such as biological systems and quantum emitters. Single photon emitters may be probed in a multiphoton interferometer regime to investigate higher order coherence characteristics using low photon flux and strong temporal correlations.[54,55] Moreover, the experimental setup can be made easier to assemble and more accessible using compact continuous wave lasers and Type-I SPDC, making this a highly resourceful experiment that many researchers can utilize across multiple fields. Nonlinear experiments that take advantage of the correlations and

interferences of entangled photons with molecules have been proposed, and with this work, our experiment with HOM interferometry may be the doorway towards achieving these ideas and bringing them into fruition. Now the possibility to investigate a series of chromophores by using HOM interferometry to probe dynamical behavior upon coherent excitation has become a reality.

6.6 Conclusions

We have successfully conducted an experiment to test the sensitivity of entangled photons in an HOM interferometer to the presence of resonant organic dyes. We have been able to confirm that the coincidence counts and HOM dip are responsive to a resonant dye placed in the interferometer path and that the sample causes an interference and phase shift to the propagating photons. In accordance with our theory, the resulting HOM dip contains molecular information pertaining to the linear susceptibility and absorption of the studied sample. Mainly, the coincidence measurements of the HOM signal obtained from experiment can be connected to molecular dephasing and used to measure the molecular coherence times which is an important factor for further time-resolved studies. With our HOM experiment, we were able to extract a dephasing time of the organic molecule of as low as 102 fs upon coherent excitation and quantum interference with a path of entangled photons in the interferometer. This affirms the viability of HOM interferometry as a spectroscopic method to be used across scientific fields to study optical properties using quantum advantages. There are numerous ways to advance this method for even more fascinating studies and with our work, we have set the stage for these possibilities.

References

(1) Jennewein, T.; Simon, C.; Weihs, G.; Weinfurter, H.; Zeilinger, A. Quantum Cryptography with Entangled Photons. *Phys. Rev. Lett.* **2000**, *84* (20), 4729–4732.

(2) Lemos, G. B.; Borish, V.; Cole, G. D.; Ramelow, S.; Lapkiewicz, R.; Zeilinger, A. Quantum Imaging with Undetected Photons. *Nature* **2014**, *512* (7515), 409–412. https://doi.org/10.1038/nature13586.

(3) Xu, W.; Wang, T.; Wang, C. Efficient Teleportation for High-Dimensional Quantum Computing. *IEEE Access* **2019**, *7*, 115331–115338. https://doi.org/10.1109/ACCESS.2019.2934408.

(4) Chuan, X.; Zhang, L.; Huang, S.; Ma, T.; Liu, F.; Yonezawa, H.; Zhang, Y.; Xiao, M. Sensing and Tracking Enhanced by Quantum Squeezing. *Photonics Res.* **2019**, *7* (6), 14–26. https://doi.org/10.1364/PRJ.7.000A14.

(5) Lee, D.; Goodson III, T. Entangled Photon Absorption in an Organic Porphyrin Dendrimer. *J. Phys. Chem. B* **2006**, *110*, 25582–25585. https://doi.org/10.1021/jp066767g.

(6) Guzman, A. R.; Harpham, M. R.; Suzer, O.; Haley, M. M.; Goodson III, T. G. Spatial Control of Entangled Two-Photon Absorption with Organic Chromophores ¨. *J. Am. Chem. Soc. Commun.* **2010**, *132*, 7840–7841. https://doi.org/10.1021/ja1016816.

(7) Harpham, M. R.; Goodson III, T. Thiophene Dendrimers as Entangled Photon Sensor Materials. *J. Am. Chem. Soc. Artic.* **2018**, No. 21, 973–979.

(8) Upton, L.; Harpham, M.; Suzer, O.; Richter, M.; Mukamel, S.; Goodson, T. Optically Excited Entangled States in Organic Molecules Illuminate the Dark. *J. Phys. Chem. Lett.* **2013**, *4* (12), 2046–2052. https://doi.org/10.1021/jz400851d.

(9) Varnavski, O.; Pinsky, B.; Goodson, T. Entangled Photon Excited Fluorescence in Organic Materials: An Ultrafast Coincidence Detector. **2017**, 6–11. https://doi.org/10.1021/acs.jpclett.6b02378.

(10) Eshun, A.; Cai, Z.; Awies, M.; Yu, L.; Goodson III, T. Investigations of Thienoacene

Molecules for Classical and Entangled Two-Photon Absorption Published as Part of The Journal of Physical Chemistry Virtual Special Issue " William M . Jackson Festschrift " . *J. Phys. Chem. A* **2018**, *122*, 8167–8182. https://doi.org/10.1021/acs.jpca.8b06312.

(11) Villabona-monsalve, J. P.; Varnavski, O.; Palfey, B. A.; Goodson III, T. Two-Photon Excitation of Flavins and Flavoproteins with Classical and Quantum Light. *J. Am. Chem. Soc. Commun.* **2018**. https://doi.org/10.1021/jacs.8b08515.

(12) Villabona-monsalve, J. P.; Caldero, O.; Portela, M. N.; Valencia, A. Entangled Two Photon Absorption Cross Section on the 808 Nm Region for the Common Dyes Zinc Tetraphenylporphyrin and Rhodamine B. *J. Phys. Chem. A* **2017**, 7869–7875. https://doi.org/10.1021/acs.jpca.7b06450.

(13) Tabakaev, D.; Montagnese, M.; Haack, G.; Bonacina, L.; Zbinden, H.; Thew, R. T. Energy-Time Entangled Two-Photon Molecular Absorption. *arXiv:1910.07346v4 [quant-ph]* **2020**, 1–5.

(14) Varnavski, O. Two-Photon Fluorescence Microscopy at Extremely Low Excitation Intensity: The Power of Quantum Correlations. *J. Am. Chem. Soc.* **2020**, *142*, 12966–12975. https://doi.org/10.1021/jacs.0c01153.

(15) Kaiser, F.; Vergyris, P.; Aktas, D.; Babin, C.; Labonté, L.; Tanzilli, S. Quantum Enhancement of Accuracy and Precision in Optical Interferometry. *Light Sci. Appl.* **2018**, *7* (3), 17163. https://doi.org/10.1038/lsa.2017.163.

(16) Israel, Y.; Rosen, S.; Silberberg, Y. Supersensitive Polarization Microscopy Using NOON States of Light. *Phys. Rev. Lett.* **2014**, *103604* (March), 12–15. https://doi.org/10.1103/PhysRevLett.112.103604.

(17) Armendáriz, G.; Cravioto-Lagos, J.; Velázquez, V.; Grether, M.; López-Moreno, E.; Galvez, E. J. Teaching Quantum Mechanics with the Hong-Ou-Mandel Interferometer. *SPIE* **2014**, *9289* (July 2014), 928908. https://doi.org/10.1117/12.2070280.

(18) Thomas, P. J.; Cheung, J. Y.; Chunnilall, C. J.; Dunn, M. H. The Hong-Ou-Mandel Interferometer: A New Procedure for Alignment. *Rev. Sci. Instrum.* **2009**, *80* (3). https://doi.org/10.1063/1.3080559.

(19) Atatüre, M.; Sergienko, A. V.; Saleh, B. E. A.; Teich, M. C. Entanglement in Cascaded-Crystal Parametric down-Conversion. *Phys. Rev. Lett.* **2001**, *86* (18), 4013–4016. https://doi.org/10.1103/PhysRevLett.86.4013.

(20) Jachura, M.; Chrapkiewicz, R. Shot-by-Shot Imaging of Hong–Ou–Mandel Interference with an Intensified SCMOS Camera. *Opt. Lett.* **2015**, *40* (7), 1540. https://doi.org/10.1364/ol.40.001540.

(21) Li, H.; Piryatinski, A.; Jerke, J.; Ram, A.; Kandada, S.; Silva, C. Probing Dynamical Symmetry Breaking Using Quantum-Entangled Photons Probing Dynamical Symmetry Breaking Using Quantum-Entangled Photons. *Quantum Sci. amd Technol.* **2018**, *3* (015003).

(22) Schlawin, F. Entangled Photon Spectroscopy. *J. Phys. B* **2017**, *50* (203001).

(23) Saleh, B. E. A.; Jost, B. M.; Fei, H. B.; Teich, M. C. Entangled-Photon Virtual-State Spectroscopy. *Phys. Rev. Lett.* **1998**, *80* (16), 3483–3486. https://doi.org/10.1103/PhysRevLett.80.3483.

(24) Yabushita, A.; Kobayashi, T. Spectroscopy by Frequency-Entangled Photon Pairs. *Phys. Rev. A* **2004**, *69* (013806), 3–6. https://doi.org/10.1103/PhysRevA.69.013806.

(25) Dauler, E.; Jaeger, G.; Muller, A.; Migdall, A. Tests of a Two-Photon Technique for Measuring Polarization Mode Dispersion With Subfemtosecond Precision. *J. Res. Natl. Inst. Stand. Technol.* **1999**, *104* (1), 1–10.

(26) Hong, S.; Riedinger, R.; Marinkovi, I.; Wallucks, A.; Hofer, S. G.; Norte, R. A.; Aspelmeyer, M.; Gröblacher, S. Hanbury Brown and Twiss Interferometry of Single Phonons from an Optomechanical Resonator. *Science (80-.).* **2017**, *358*, 203–206.

(27) Hong, C.K.; Ou, Z.Y.; Mandel, L. Measurement of Subpicosend Time Intervals between Two Photons by Interference. *Phys. Rev. Lett.* **1987**, *59* (18), 2044–2046.

(28) Walborn, S. P.; Oliveira, A. N. de; Padua, S.; Monken, C. H. Multimode Hong-Ou-Mandel Interference. *Phys. Rev. Lett.* **2003**, *90*, 1–4. https://doi.org/10.1103/PhysRevLett.90.143601.

(29) Lim, H. T.; Hong, K. H.; Kim, Y. H. Effects of Polarization Mode Dispersion on Polarization-Entangled Photons Generated via Broadband Pumped Spontaneous Parametric down-Conversion. *Sci. Rep.* **2016**, *6* (April), 1–7. https://doi.org/10.1038/srep25846.

(30) Dorfman, K. E.; Schlawin, F.; Mukamel, S. Stimulated Raman Spectroscopy with Entangled Light: Enhanced Resolution and Pathway Selection. *J. Phys. Chem. Lett.* **2014**, *5*, 2843–2849. https://doi.org/10.1021/jz501124a.

(31) Mukamel, S.; Freyberger, M.; Schleich, W.; Bellini, M.; Zavatta, A.; Leuchs, G.; Silberhorn, C.; Boyd, R. W.; Sánchez-soto, L. L. Roadmap on Quantum Light Spectroscopy. **2020**.

(32) Chen, Y.; Fink, M.; Steinlechner, F.; Torres, J. P.; Ursin, R. Hong-Ou-Mandel Interferometry on a Biphoton Beat Note. *npj Quantum Inf.* **2019**, No. February, 1–6. https://doi.org/10.1038/s41534-019-0161-z.

(33) Dorfman, K. E.; Asban, S.; Gu, B.; Mukamel, S. Hong-Ou-Mandel Interferometry and Spectroscopy Using Entangled Photons. *Submiss.*

(34) Kalashnikov, D. A.; Melik-gaykazyan, E. V; Kalachev, A. A.; Yu, Y. F.; Kuznetsov, A. I.; Krivitsky, L. A. Quantum Interference in the Presence of a Resonant Medium. *Sci. Rep.* **2017**, *7*, 1–8. https://doi.org/10.1038/s41598-017-11694-z.

(35) Szoke, S.; Liu, H.; Hickam, B. P.; He, M.; Cushing, S. K. Entangled Light-Matter Interactions and Spectroscopy. *J. Mater. Chem. C* **2020**, *Advance Ar*. https://doi.org/10.1039/d0tc02300k.

(36) Graciano, P. Y.; Michel, A.; Martínez, A.; Lopez-mago, D.; Castro-olvera, G.; Rosete-aguilar, M.; Garduño-mejía, J. Interference Effects in Quantum- Optical Coherence Tomography Using Spectrally Engineered Photon Pairs. **2019**, No. February, 1–14. https://doi.org/10.1038/s41598-019-45088-0.

(37) Tanida, M.; Okamoto, R.; Takeuchi, S. Highly Indistinguishable Heralded Single-Photon Sources Using Parametric down Conversion. *Opt. Express* **2012**, *20* (14), 134–140.

(38) Kim, Y.; Grice, W. P. Measurement of the Spectral Properties of the Two- Photon State Generated via Type II Spontaneous Parametric Downconversion. *Opt. Lett.* **2005**, *30* (8), 908–910.

(39) Grice, W. P.; Erdmann, R.; Walmsley, I. A.; Branning, D. Spectral Distinguishability in Ultrafast Parametric Down-Conversion. *Phys. Rev. A* **1998**, *57* (4), 2289–2292.

(40) Kambs, B.; Becher, C. Limitations on the Indistinguishability of Photons from Remote Solid State Sources Limitations on the Indistinguishability of Photons from Remote Solid State Sources. *New J. Phys.* **2018**, *20* (115003).

(41) Cassemiro, K. N.; Laiho, K.; Silberhorn, C. Accessing the Purity of a Single Photon by the Width of the Hong–Ou–Mandel Interference. *New J. Phys.* **2010**, *12* (113052), 1–15. https://doi.org/10.1088/1367-2630/12/11/113052.

(42) Atature, M.; Giuseppe, G. Di; Shaw, M. D.; Sergienko, A. V; Saleh, B. E. A.; Teich, M. C. Multiparameter Entanglement in Quantum Interferometry. *Phys. Rev. A* **2002**, *66* (023822), 1–15. https://doi.org/10.1103/PhysRevA.66.023822.

(43) Atature, M.; Giuseppe, G. Di; Shaw, M. D.; Sergienko, A. V; Saleh, B. E. A.; Teich, M. C. Multiparameter Entanglement in Femtosecond Parametric Down-Conversion ¨. *Phys. Rev. A* **2002**, *65* (023808), 1–4. https://doi.org/10.1103/PhysRevA.65.023808.

(44) Kim, Y.; Berardi, V.; Chekhova, M. V; Shih, Y. Anticorrelation Effect in Femtosecond-Pulse Pumped Type-II Spontaneous Parametric down-Conversion. *Phys. Rev. A* **2001**, *64*, 1–4. https://doi.org/10.1103/PhysRevA.64.011801.

(45) Kim, Y.; Grice, W. P. Generation of Pulsed Polarization-Entangled Two-Photon State via Temporal and Spectral Engineering. *J. Mod. Opt.* **2002**, *49* (14), 2309–2323. https://doi.org/10.1080/0950034021000011455.

(46) Grice, W. P.; Walmsley, I. A. Spectral Information and Distinguishability in Type-II down-Conversion with a Broadband Pump. *Phys. Rev. A* **1997**, *56* (2), 1627–1634.

(47) Takeuchi, S. Recent Progress in Single-Photon and Entangled- Photon Generation and Applications. *Jpn. J. Appl. Phys.* **2014**, *53* (030101).

(48) Kim, Y. Measuerement of One-Photon and Two-Photon Wave Packets in Spontaneous Parametric Downconversion. *J. Opt. Soc. Am. B* **2003**, *20* (9), 1959–1966.

(49) Loudon, R. *The Quantum Theory of Light*; Oxford University Press, 2000.

(50) Lucarini, B. V.; Saarinen, J. J.; Peiponen, K.; Vartiainen, E. M. *Kramers-Kronig Relations in Optical Materials Research*; Springer, 2005.

(51) Schlawin, F.; Mukamel, S. Two-Photon Spectroscopy of Excitons with Entangled Photons. *J. Chem. Phys.* **2013**, *139* (24). https://doi.org/10.1063/1.4848739.

(52) Gu, B.; Mukamel, S. Manipulating Two-Photon-Absorption of Cavity Polaritons by Entangled Light. *J. Phys. Chem. Lett.* **2020**, *11* (19), 8177–8182. https://doi.org/10.1021/acs.jpclett.0c02282.

6.6 Supplementary Information

Polarizer Phase Shift

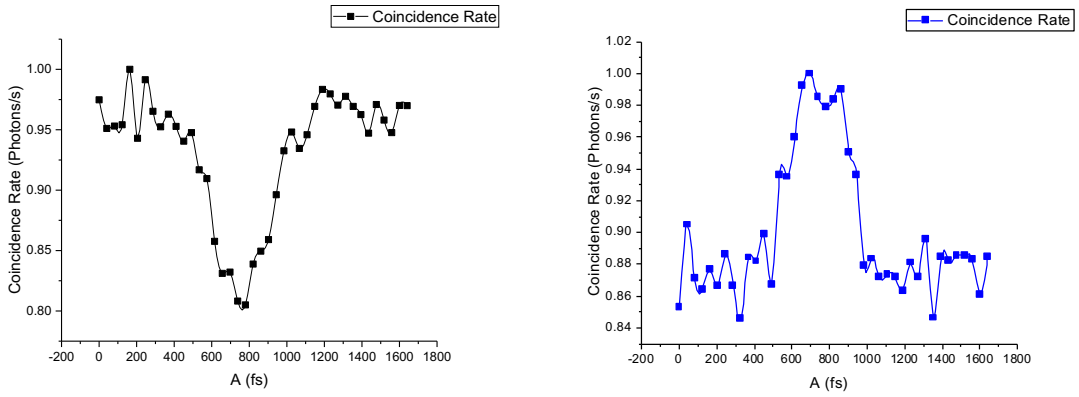

Figure 6.13 *HOM scans with polarizer phase turned showing a phase shift in the HOM scan.*

IR-140 linear Susceptibility

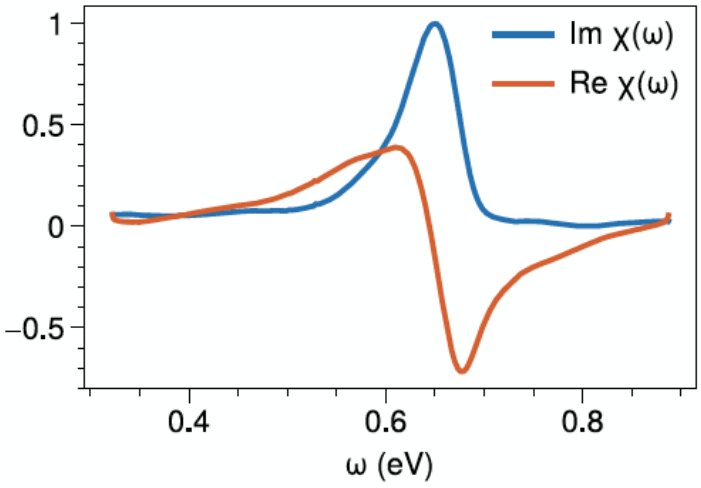

Figure 6.14 *Imaginary, Im $\chi(\omega)$, and real, Re $\chi(\omega)$, parts of the linear susceptibility of the IR-140 molecule The real part is obtained by Hilbert transform of the absorption data.*

Narrowband pump and broadband twin photons

In the limit of a narrowband pump ($\sigma_+ \to 0$) and broadband twin photons (i.e. σ_- is larger than the characteristic linewidth γ of the transmission function), Fourier transform of the HOM coincidence counting rate (Eq. 6.2) leads to

$$R(\tau) = -\frac{1}{2}\int d\Delta \beta^*(\Delta)\beta(-\Delta)T^*\left(\bar{\omega}-\frac{\Delta}{2}\right)T\left(\bar{\omega}+\frac{\Delta}{2}\right)e^{i\Delta\tau} = -\frac{1}{2}\int d\Delta\, T^*\left(\bar{\omega}-\frac{\Delta}{2}\right)T\left(\bar{\omega}+\frac{\Delta}{2}\right)e^{i\Delta\tau} \equiv -\frac{1}{2}T_W\left(\frac{\omega_p}{2},\tau\right) \quad \text{Eq. 6.12}$$

Eq. 6.12 shows that in this limit, the coincidence counting rate is determined by the Wigner transform of the transmission function. By scanning the pump frequency, it is possible to obtain the full $T_W(\omega,\tau)$. Note that the condition $\sigma_- \gg \gamma$ is not satisfied in the current experiment.

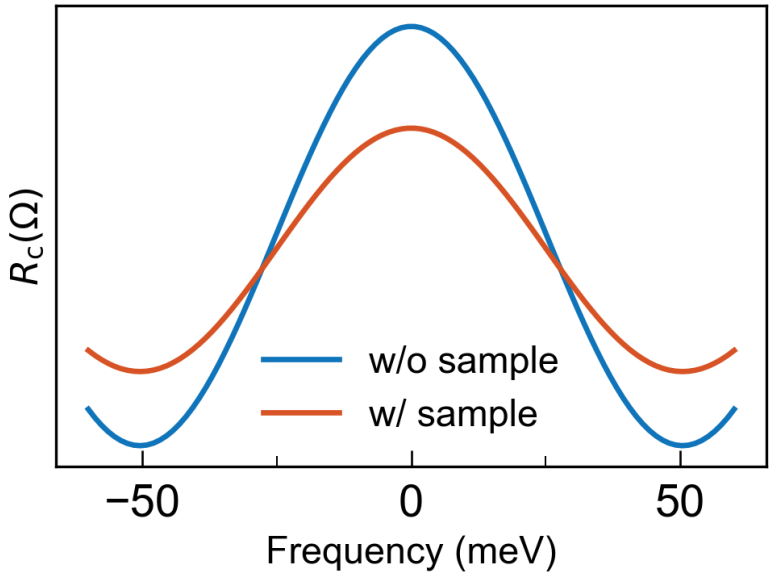

Figure 6.15 *Fourier transform of coincidence rates according to Eq. 8. We observe a difference in the frequency distributions and amplitude for the data with and without a sample.*

Chapter 7

Overall Summary and Future Directions

7.1 Overall Summary

Quantum entanglement which initially seemed a strange and evasive concept has now had significant impact on many fields, being used in optics, computing, metrology, communication and information science as a whole.[1–3] As the interest in the field grows, researchers have increasingly been searching for ways to take advantage of the unique properties offered by this quantum mechanic phenomenon. The strong correlations and temporal properties of light generated as quantum entangled pairs make them an evident avenue for spectroscopy. Early theoretical works showed that the high spatial and temporal correlations of entangled photon pairs would make them ideal for two-photon absorption spectroscopy.[4–6] The two-photon absorption (TPA) process involves the simultaneous absorption of two photons of lower energy, leading to a direct transition in the atom or molecule from the ground state to an excited state the sum of the energy of the photons. Thus, the correlations of entangled photons would allow the pair to be absorbed as if they were "single entity" with a linear dependence on the light intensity. The initial theory provided a simple probabilistic model, comparing entangled TPA (ETPA) to classical TPA cross-sections, but also provided a more nuanced derivation of the ETPA cross-sections due to the quantum interference of the entangled photons and the molecular intermediate states.[5] The time correlations of the entangled photon pair would also lead to time control which allows for selective population of different energy levels, and thus

different ETPA cross-sections attainable at the same wavelength by changing the interbeam delay or entanglement time.[5–8] Thus, information can be gained about the energy levels contributing to the ETPA of the sample under study.

While the theoretical work has been well developed and was studied in the 90s, experimental realizations were not seen until later and a lot is still left to be understood about these processes. In 1997, Georgiades *et al*[9] were successful in exciting a two-photon transition in atomic Cs using correlated nondegenerate downconverted photons generated by an optical parametric oscillator and the photocurrent due to fluorescence was observed.[9] Later, Dayan *et al* also showed that this two-photon absorption with low flux down converted light was possible by exciting atomic Rb measuring the resulting fluorescence.[10] An essential part of this work was that they proved the TPA origin by showing its dependence on the signal-idler delay.[10] Since then, members of the Goodson group have been able to observe the linear dependence of ETPA in larger organic molecules[11–14] which is a big step for employing entangled two-photon spectroscopy more widely. In these studies, different parameters, such as spatial phase-matching conditions and inter-beam time delay dependence were tested to prove the ETPA origin of the signal. Even more exciting was the observation of the resulting fluorescence from the ETPA excitation process which was also tested with spatial and temporal parameters.[15] This was another important demonstration of the ETPA process as emitted photons can only be detected if there is absorption. Furthermore, the ability to observe fluorescence from ETPA opens doors to imaging and microscopy with these low light intensities and the advantages of the control knobs provided by entangled light. A particular ETPA study by Upton *et al*[14] looked more closely at the ETPA process and the interference of different absorption pathways and how this relates to the observed signals. I wanted to build

on this work, to determine exact interactions and understand how ETPA was related to the structure of the molecule, hence expanding our knowledge of these structure-function relations with ETPA. Also, as more researchers become interested in fluorescence applications with entangled light, it is necessary to have a working ETPEF experiment that we can always rely on, as well as a firmer grasp on the ETPEF process and the molecular and experimental parameters needed to obtain it.

However, entangled two-photon absorption is not the only channel for spectroscopy utilizing quantum light. Many practical applications of quantum light in communication and metrology have involved interferometry.[3,16] Classically, interferometers are used for different types of spectroscopy, from Michelson interferometers used in Fourier Transform Infrared (FT-IR) spectroscopy[17] to Mach-Zehnder interferometry used for mid-infrared chemical sensing and photothermal spectroscopy[18,19] measuring optical phases. As quantum interferometers are more sensitive than their classical counterparts,[20] it becomes apparent that the seemingly untapped field of quantum interferometry for spectroscopy of organic and biological materials is one that should be explored. Currently, quantum interferometry has been used mainly in communication and computing via qubits and additionally for the measurement of optical thicknesses and refractive indices of optics and inorganic structures.[21–23] Most recently, in a study quantum interferometry was used to measure properties relating to the coherent excitation of inorganic structures.[24] The question remained whether this was an experimental method that could be applied to organic molecules, to excite them and obtain information about the molecular excitation. Therefore, this was a new form of spectroscopy with entangled photons in an interferometer that I wanted to investigate. The introduction chapter, Chapter 1, offers a comprehensive breakdown of quantum entanglement and how it

relates to electric fields and their correlations, as well as a background on the theoretical and experimental work done on ETPA thus far and the motivation for quantum interferometry for spectroscopy. In Chapter 2, the experimental techniques utilized are described alongside their theory. Overall, this thesis seeks to shed light on different ways in which entangled photon pairs can be utilized to understand the optical properties of molecules.

While it was known that ETPA could be measured via transmission and via fluorescence, a more in-depth analysis was needed on how the cross-sections measured with these two methods would scale, but also how they would scale compared to classical TPA. Particularly, in Chapter 3, by utilizing a set of organic chromophores with similar structures but different atomic substitutions that alter their structure-function properties, I was able to compare the linear, classical two-photon and entangled two-photon properties in these molecules with varying degrees of dipolar and quadrupolar character. Using steady-state absorption and fluorescence spectroscopy backed by quantum chemical calculations, I found that the optical properties of these 9-ringed benzodithiophene compounds are indeed altered by the substitution of a nitrogen (**9R-N**), sulfur (**9R-S**) or selenium (**9R-Se**) atom into the parent structure (**9R**) framework. The results of the measured entangled cross-sections using transmission and fluorescence methods scaled with the same trend for both methods, confirming the ETPA origin of the fluorescence observed and substantiating it as a viable method for spectroscopy and measuring optical properties. Interestingly, while entangled methods scaled similarly for the substituted compounds, it was clear that there was an enhancement in the entangled cross-sections of the parent structure (**9R**) compared to its classical cross-section and this was not seen with the other compounds. The inclusion of the

permanent dipole absorption pathway in the entangled cross-section or **9R** due to its dipolar character would result in an enhancement of the entangled cross-section. This pathway is not accessible for the other solely quadrupolar chromophores studied in the series. The enhancements in the 9R ETPA cross-section were experimentally observed due to the high sensitivity of entangled photons and their ability to resolve small contributions of different pathways due to the quantum interferences between energy states and the entangled photons. This work provides a basis for understanding the structure-function response of non-linear optical molecules excited by entangled light, and how molecules can be specially synthesized and developed to be selectively probed by entangled light.

I sought to obtain a better understanding of the entangled two-photon excited fluorescence process and also to ensure that the lab had a working ETPEF setup that was well characterized. This is detailed in Chapter 4 where I explore the experimental and molecular properties necessary for the observation of ETPEF. In addition to work done by myself and other researchers at the Goodson group, fluorescence induced by different forms of quantum light have been observed in the quantum optics and spectroscopy communities.[25,26] A comprehensive analysis of these observations was carried out and the dependence on the molecule's electronic states and transition dipole moment properties made clear. ETPEF setups must be very well isolated from spurious light and must incorporate efficient fluorescence methods in order it improve the signal to noise ratio of the measurements. I carried out quantum chemical electronic structure calculations to highlight the pathway dependence of ETPEF. It was shown that for the molecules investigated, those with small detuning energies that absorb via the virtual transition pathway showed enhanced ETPEF signals due to the coupling between these resonant intermediate states and the entangled photons. This enhancement was not

observed for compounds with larger detuning energies. This study confirmed that in order to observe good ETPED signals, compounds under study should have high transition dipole moments, small detuning energies and good quantum yields.

It has been theorized that the temporal correlations of entangled photons allow them to be used to elucidate information about the intermediate states and energy levels utilized in excitation processes.[6,27] This is very important for materials used for optical applications such as photovoltaics and organic light emitting diodes (OLED) as it gives a broader understanding of the optical properties of the molecule. In Chapter 5, I utilize the interbeam time-delay properties of entangled photons to observe different ETPA rates for a pair of perylene diimide (PDI) trimer systems that have been studied for their use toward photovoltaic applications.[28] The flexible π-bridge of one of the trimers, $\boldsymbol{\beta}$, led to it forming a twisted geometry while the rigid π-bridge of the second trimer, $\boldsymbol{\beta C}$, resulted in it having a primarily planar geometry. These compounds are interesting as it has previously been shown that the twisted nature of the $\boldsymbol{\beta}$ compound leads it to undergo intramolecular singlet exciton fission (iSEF) – the generation of two triplet excitons from one excited singlet exciton by the absorption of a single photon – while the planar trimer does not experience iSEF.[28] In chapter 5, linear and non-linear classical spectroscopy as well as entangled two-photon spectroscopy at different time delays were performed to provide a full picture of the optical properties of the two compounds. Mainly, ETPA at different time delays led to selective population that resulted in different ETPA signals and different cross-sections at varying delay times for both compounds. With this experimental data and information about the compounds' dipole moments and energy levels obtained from quantum chemical calculations, I was able to simulate more precise ETPA patterns with respect to time delay and using a Fourier transform, extract the intermediate or

virtual states contributing to ETPA. For both compounds, some of these were close to resonance with the entangled photons, leading to the relatively large entangled cross-sections observed ($x10^{-18}$ cm^2/molecule). For the twisted compound, some of these states coincided with transient species observed in transient absorption spectroscopy and coincided with stationary Born-Oppenheimer states of the molecule. These could be reasons for the enhancement of the compound's cross-section in relation to the planar compound in comparison to classical TPA. There is a possibility that for this twisted compound, the entangled photons could probe the energetically accessible double triplet state.

Chapter 6 considers a different form of entangled photon spectroscopy, where I examine the viability of quantum interferometry with a Hong-Ou-Mandel (HOM) interferometer to investigate the molecular properties of an organic dye. The two-photon interference in an HOM interferometer measures the indistinguishability of the entangled photon pair when they are incident at a 50/50 beam splitter and leads to a signature HOM "dip".[29] In the experiment, the entangled photons are separated into two pathways and then recombine at a beam splitter to two detectors which are connected in coincidence. By placing an organic sample, a resonant dye IR-140, in one path of the interferometer, I have been able to confirm that the coincidence counts and HOM dip are responsive to the dye, and that the sample causes an interference and phase shift to the propagating photons. The HOM dip holds information pertaining to the absorption of the studied sample and with fitting of the experimental data, it was possible to extract the molecular dephasing time of the coherent excitation. A dephasing time of **102 fs** was extracted, speaking to the femtosecond precision of the method and the ability to use it for time-resolved studies. The work in this chapter is the doorway towards using HOM interferometry as a spectroscopic method for sensitive organic and biological samples.

7.2 Future Directions

Future work in this field will involve exploring all these potential applications of entangled photon spectroscopy further. With work in this dissertation, the mechanisms of entangled two-photon absorption spectroscopy have become better understood by considering a variety of molecules and hopefully, this will contribute to further work carried out in this area. Particularly, work in the field of entangled two-photon fluorescence spectroscopy will have a lot of sought-after applications. Already, an entangled two-photon fluorescence microscope has been built and images obtained with an excitation intensity six orders of magnitude lower than what is necessary to image with classical light.[30] Many biophysicists are interested in this area of quantum imaging, so it is imperative to build on the research available with ETPEF, especially with biological materials. The recent work by Tabakaev *et al*[25] expanded the realm of ETPEF of organic molecules with SPDC photons beyond the Goodson group, and more of such experimental realizations are necessary by different researchers to obtain different outlooks on the experimental method. Conducting ETPEF with periodically-poled crystals will allow us to have a higher photon flux and therefore a potential increase in the fluorescence counts, making measurements easier. Similarly with fluorescence measured with squeezed light excitation,[26] conducting ETPEF measurements with a variety of quantum light sources is essential to determine what provides the best results while remaining in the low flux regime. This will be imperative towards the overall goal of quantum light fluorescence applications for sensitive materials.

While this thesis shows the potential of virtual state spectroscopy by using a small number of delay times to vary ETPA signals, it is clear that this is an untapped area where we can further our knowledge about the excitation processes in chromophores and the intermediate

states involved in these processes. It is therefore important for this work to be continued with better time resolution and more femtosecond precision. This can be done by inserting a delay stage in the entangled photon beam path to give minute femtosecond resolution, rather than the limited delays provided by fixed thickness quartz plates. This will offer an experimental view of the more complex nonmonotonic behavior of ETPA and provide a more accurate result of the virtual states involved in ETPA. Hence, this will give more information about the photophysical properties of molecules that can be used for optical applications. Furthermore, suggestions that the entangled photons may probe states involved in different processes should be explored. More analysis of virtual state spectroscopy and studying of such chromophores that exhibit interesting processes such as iSEF need to be done with entangled light in order to corroborate these suggestions and observe how entangled photons probe these particular states or processes.

A big part of this dissertation work was setting up and testing an HOM interferometer as an avenue for entangled photon spectroscopy. Work in this area had been suggested[3132,33] and similar work carried out on inorganic crystal structures[24] which are far easier to probe, but my experiment confirmed that this setup is sensitive to organic molecules and can be used to excite them and obtain molecular information. One way to expand on this work will be to conduct it with a continuous wave laser. This will not only make the setup easier to build, therefore making it easier to alter the setup if need be, but it will also improve visibility. With a greater depth of the HOM dip, it will be easier to observe minute changes captured in the sides of the dip. Additionally, the experiment can be applied to thin film organic samples to test how differing the optical thickness affects the results when extracting time-resolved data.

Most importantly, spectroscopy with HOM interferometry can be applied to higher order nonlinear measurements and this is surely the future of this method. By introducing an external laser pulse to produce a steady excitation in the molecule before interacting with the propagating photons, HOM spectroscopy can be used to measure nonlinear susceptibilities of molecules with high sensitivity and precision. The temporal delay between the laser pulses can also be controlled to obtain time-resolved information. Furthermore, in the future, it will be compelling to device a way to probe the sample under study with both photons of the entangled pair to understand the effect of the strong correlations in the two-photon interaction and obtain nonlinear information in this way. The frequency correlations of the photon pair can be altered using different wavelengths and different types of quantum light, to observe the effects of the light-matter interaction with different frequency correlations; essentially how this will affect the observed phase shifts and dip asymmetry. Ultimately this can be applied to biological materials with practical applications or quantum emitters to study susceptibilities, symmetry breaking and coherence in the nonlinear regime. The investigation in this dissertation has provided the groundwork on which these studies can grow.

References

(1) Xu, W.; Wang, T.; Wang, C. Efficient Teleportation for High-Dimensional Quantum Computing. *IEEE Access* **2019**, *7*, 115331–115338. https://doi.org/10.1109/ACCESS.2019.2934408.

(2) Pirandola, S.; Andersen, U. L.; Banchi, L.; Berta, M.; Bunandar, D.; Colbeck, R.; England, D.; Gehring, T.; Lupo, C.; Ottaviani, C.; Pereira, J. L.; Razavi, M.; Shaari, J. S.; Tomamichel, M.; Usenko, V. C.; Vallone, G.; Villoresi, P.; Wallden, P. Advances in Quantum Cryptography and Relays. *Adv. Opt. Photonics* **2020**, *12* (4), 1012–1236. https://doi.org/10.1109/ecoc.2006.4801410.

(3) Gisin, N.; Thew, R. Review1_Gisin_2007. *Nat. Photonics* **2007**, *1*, 165–171.

(4) Javanainen, J.; Gould, P. L. Linear Intensity Dependence of a Two-Photon Transition Rate. *Phys. Rev. A* **1990**, *41* (9), 5088–5091. https://doi.org/10.1103/PhysRevA.41.5088.

(5) Fei, H. B.; Jost, B. M.; Popescu, S.; Saleh, B. E. A.; Teich, M. C. Entanglement-Induced Two-Photon Transparency. *Phys. Rev. Lett.* **1997**, *78* (9), 1679–1682. https://doi.org/10.1103/PhysRevLett.78.1679.

(6) Saleh, B. E. A.; Jost, B. M.; Fei, H. B.; Teich, M. C. Entangled-Photon Virtual-State Spectroscopy. *Phys. Rev. Lett.* **1998**, *80* (16), 3483–3486. https://doi.org/10.1103/PhysRevLett.80.3483.

(7) Burdick, R. K.; Varnavski, O.; Molina, A.; Upton, L.; Zimmerman, P.; Iii, T. G. Predicting and Controlling Entangled Two-Photon Absorption in Diatomic Molecules Published as Part of The Journal of Physical Chemistry Virtual Special Issue " William M . Jackson Festschrift " . *J. Phys. Chem. A* **2018**, *122*, 8198–8212. https://doi.org/10.1021/acs.jpca.8b07466.

(8) Kang, G.; Avanaki, K. N.; Mosquera, M. A.; Burdick, R. K.; Villabona-monsalve, J. P.; Goodson III, T.; Schatz, G. C. Efficient Modeling of Organic Chromophores for Entangled Two-Photon Absorption. *J. Am. Chem. Soc.* **2020**, *10.1021/ja*. https://doi.org/10.1021/jacs.0c02808.

(9) Georgiades, N. P.; Polzik, E. S.; Kimble, H. J. Atoms as Nonlinear Mixers for Detection of Quantum Correlations at Ultrahigh Frequencies. *Phys. Rev. A* **1997**, *55* (3), 1605–1608.

(10) Dayan, B.; Pe'er, A.; Friesem, A. A.; Silberberg, Y. Two Photon Absorption and Coherent Control with Broadband Down-Converted Light. *Phys. Rev. Lett.* **2004**, *93* (2), 1–4. https://doi.org/10.1103/PhysRevLett.93.023005.

(11) Lee, D.; Goodson III, T. Entangled Photon Absorption in an Organic Porphyrin Dendrimer. *J. Phys. Chem. B* **2006**, *110*, 25582–25585. https://doi.org/10.1021/jp066767g.

(12) Harpham, M. R.; Süzer, Ö.; Ma, C. Q.; Bäuerle, P.; Goodson, T. Thiophene Dendrimers as Entangled Photon Sensor Materials. *J. Am. Chem. Soc.* **2009**, *131* (3), 973–979. https://doi.org/10.1021/ja803268s.

(13) Guzman, A. R.; Harpham, M. R.; Süzer, Ö.; Haley, M. M.; Goodson, T. G. Spatial Control of Entangled Two-Photon Absorption with Organic Chromophores. *J. Am. Chem. Soc.* **2010**, *132* (23), 7840–7841. https://doi.org/10.1021/ja1016816.

(14) Upton, L.; Harpham, M.; Suzer, O.; Richter, M.; Mukamel, S.; Goodson, T. Optically Excited Entangled States in Organic Molecules Illuminate the Dark. *J. Phys. Chem. Lett.* **2013**, *4* (12), 2046–2052. https://doi.org/10.1021/jz400851d.

(15) Varnavski, O.; Pinsky, B.; Goodson, T. Entangled Photon Excited Fluorescence in Organic Materials: An Ultrafast Coincidence Detector. **2017**, 6–11. https://doi.org/10.1021/acs.jpclett.6b02378.

(16) Giovannetti, V.; Lloyd, S.; MacCone, L. Quantum Metrology. *Phys. Rev. Lett.* **2006**, *96* (1), 13–16. https://doi.org/10.1103/PhysRevLett.96.010401.

(17) Ishida, H.; Ishino, Y.; Buijs, H.; Tripp, C.; Dignam, M. J. Polarization-Modulation Ft-Ir Reflection Spectroscopy Using a Polarizing Michelson Interferometer. *Appl. Spectrosc.* **1987**, *41* (8), 1288–1294. https://doi.org/10.1366/0003702874447167.

(18) Hayden, J.; Hugger, S.; Fuchs, F.; Lendl, B. A Quantum Cascade Laser-Based Mach–Zehnder Interferometer for Chemical Sensing Employing Molecular Absorption and Dispersion. *Appl. Phys. B Lasers Opt.* **2018**, *124* (2), 1–9. https://doi.org/10.1007/s00340-018-6899-8.

(19) Dong, J.; Yan, P.; Yang, L.; Zhang, Y.; Zhang, T.; Zhang, L.; Zhou, S.; Li, J. Dual-Wavelength Mach-Zehnder Interferometry-Assisted Photothermal Spectroscopy for

Characterization of Surface Contaminants. *Opt. Express* **2020**, *28* (20), 29865. https://doi.org/10.1364/oe.404924.

(20) Kaiser, F.; Vergyris, P.; Aktas, D.; Babin, C.; Labonté, L.; Tanzilli, S. Quantum Enhancement of Accuracy and Precision in Optical Interferometry. *Light Sci. Appl.* **2018**, *7* (3), 17163. https://doi.org/10.1038/lsa.2017.163.

(21) Zhang, Q.; Goebel, A.; Wagenknecht, C.; Chen, Y. A.; Zhao, B.; Yang, T.; Mair, A.; Schmiedmayer, J.; Pan, J. W. Experimental Quantum Teleportation of a Two-Qubit Composite System. *Nat. Phys.* **2006**, *2* (10), 678–682. https://doi.org/10.1038/nphys417.

(22) Lim, H. T.; Hong, K. H.; Kim, Y. H. Effects of Polarization Mode Dispersion on Polarization-Entangled Photons Generated via Broadband Pumped Spontaneous Parametric down-Conversion. *Sci. Rep.* **2016**, *6* (April), 1–7. https://doi.org/10.1038/srep25846.

(23) Abouraddy, A. F.; Nasr, M. B.; Saleh, B. E. A.; Sergienko, A. V.; Teich, M. C. Quantum-Optical Coherence Tomography with Dispersion Cancellation. *Phys. Rev. A* **2002**, *65* (5), 6. https://doi.org/10.1103/PhysRevA.65.053817.

(24) Kalashnikov, D. A.; Melik-gaykazyan, E. V; Kalachev, A. A.; Yu, Y. F.; Kuznetsov, A. I.; Krivitsky, L. A. Quantum Interference in the Presence of a Resonant Medium. *Sci. Rep.* **2017**, *7*, 1–8. https://doi.org/10.1038/s41598-017-11694-z.

(25) Tabakaev, D.; Montagnese, M.; Haack, G.; Bonacina, L.; Zbinden, H.; Thew, R. T. Energy-Time Entangled Two-Photon Molecular Absorption. *Phys. Rev. A* **2021**, *103* (033701), 1–5.

(26) Li, T.; Li, F.; Altuzarra, C.; Classen, A.; Agarwal, G. S. Squeezed Light Induced Two-Photon Absorption Fluorescence of Fluorescein Biomarkers Squeezed Light Induced Two-Photon Absorption Fluorescence of Fluorescein Biomarkers. *Appl. Phys. Lett.* **2020**, *116* (June), 1–5. https://doi.org/10.1063/5.0010909.

(27) Kojima, J.; Nguyen, Q. V. Entangled Biphoton Virtual-State Spectroscopy of the A 2Σ +- X 2Π System of OH. *Chem. Phys. Lett.* **2004**, *396* (4–6), 323–328. https://doi.org/10.1016/j.cplett.2004.08.051.

(28) Carlotti, B.; Madu, I. K.; Kim, H.; Cai, Z.; Jiang, H.; Muthike, A. K.; Yu, L.; Zimmerman, P. M.; Goodson, T. Activating Intramolecular Singlet Exciton Fission by Altering π-Bridge Flexibility in Perylene Diimide Trimers for Organic Solar Cells. *Chem. Sci.* **2020**,

11 (33), 8757–8770. https://doi.org/10.1039/d0sc03271a.

(29) Brańczyk, A. M. Hong-Ou-Mandel Interference. *arXiv* **2017**, 1–17.

(30) Varnavski, O. Two-Photon Fluorescence Microscopy at Extremely Low Excitation Intensity: The Power of Quantum Correlations. *J. Am. Chem. Soc.* **2020**, *142*, 12966–12975. https://doi.org/10.1021/jacs.0c01153.

(31) Dorfman, K. E.; Asban, S.; Gu, B.; Mukamel, S. Hong-Ou-Mandel Interferometry and Spectroscopy Using Entangled Photons. *Submiss.*

(32) Li, H.; Piryatinski, Srimath Kandada, A.R.; Silva, C.; Bittner, E. R. Photon Entanglement Entropy as a Probe of Many-Body Correlations and Fluctuations. *J. Chem. Phys.* **2019**, *150* (184106), 1–10. https://doi.org/10.1063/1.5083613.

(33) Szoke, S.; Liu, H.; Hickam, B. P.; He, M.; Cushing, S. K. Entangled Light-Matter Interactions and Spectroscopy. *J. Mater. Chem. C* **2020**, *Advance Ar*. https://doi.org/10.1039/d0tc02300k.